POLITECNICO DI MILANO

Dipartimento di Scienze e Tecnologie Aerospaziali

Doctoral Programme in Rotary Wing Aircraft

Computational fluid dynamic analysis of a L-shaped Gurney flap for vibration control

Doctoral dissertation of:
Valentina Motta
Matr. 785682

Advisor:
Prof. Giuseppe Quaranta
Tutor and Chair of the Doctoral Programme:
Prof. Luigi Vigevano

Year 2015 - XXVII Cycle

When you fall, get right back up. Just keep going, keep pushing it.

Lindsey Vonn

Acknowledgments

I wish to express my sincere gratitude to all the people who stayed closed to me during these three years.

At first I would like to express my gratefulness to Prof. Quaranta for his support and advice in the development of this thesis. With his experience and with patience he guided me through the difficulties I often encountered during my work. I'm very grateful for the manifold discussions I had with him, in which he constantly helped and encouraged me. I also wish to thank Prof. Guardone, who gave me his useful advice for a considerable part of this work. Moreover I would like to thank Dr. Le Pape, who kindly accepted to review this work.

I would like to express my thankfulness to my colleagues, who helped me in many situations and cheered my stay in office with their pleasantness. A special thanks goes to Andrea and Federica, who behaved as true friends in difficult moments.

A profound thank goes to my mum, my dad, my family and the people closest to me, for their constant presence. Finally my deepest gratitude goes to Federico, who has been by my side with his unwavering love.

Summary

This thesis deals with the computational fluid dynamic analysis of a L-shaped Gurney flap for rotorcraft applications. Steady and unsteady CFD computations, performed with a Reynolds-Averaged Navier-Stokes flow solver employing the overset mesh approach, are carried out to assess the behavior of such L-tab as a novel solution to balance the rotor loads and, at the same time, to reduce the blade vibration. The steady state characterization shows that the L-tab is potentially capable to enhance the lift and the lift to drag ratio, when downward deployed, and to effectively alleviate the static stall, when upward deflected. The results attained with steady state numerical simulations are also supported by experimental measurements performed on the same device. Numerical computations carried out for small amplitude oscillating motions, either of the blade –namely a NACA 0012 airfoil– or of the installed L-tab, allow to gain an insight into the shedding phenomena occurring past the movable device and into the generated multi-harmonic unsteady loads. Subsequently these simulations are used to develop a physically-based linear Reduced Order Model (ROM) in the frequency domain for the unsteady lift and pitching moment of a NACA 0012 airfoil, considering as input the pitch and plunge harmonic oscillations of the airfoil, together with the oscillations of the L-shaped Gurney flap. The aerodynamic assessment of the L-tab shows that the behavior of the loads can be predicted using an equivalent flat-plate model to represent the airfoil, composed of three segments: the first, representative of the fixed part of the airfoil, the second, representative of the longitudinal edge of the tab and the third, representative of the counter rotating vortical structures that appear behind the movable device. The same approach is used to model the static lift and moment enhancements as due to an equivalent camber modification effect. The strong connection of the parameters of the reduced order model with the physical quantities is highlighted, as well as its predictive capability for arbitrary parameters of the imposed motion laws. The ROM is then exploited to build up a three degrees of freedom linear aerostructural model for a blade equipped with a partial span L-tab. Additionally a physically based ROM and a related analytical aeroelastic model is developed in parallel for a classical trailing edge plain flap. This allows to compare the aerodynamic and aerostructural behaviors of the novel L-tab to those exhibited by a well known trailing edge configuration, as a classical plain flap is. A higher harmonic control algorithm is then applied to compute proper control laws of the L-tab, to reduce separately the N/rev harmonics of the rotating frame blade root vertical force, flapping and feathering moments. A significant reduction of the vibratory loads is obtained. Moreover, the attainment of comparable results with a well known trailing edge device, such the classical flap taken under consideration, is a further confirmation of the potential feasibility of this novel L-tab as an effective alternative mean for vibration reduction on rotor blades.

Sommario

La presente tesi riguarda l'analisi fluidodinamica computazionale di un Gurney flap a L (tab a L) per applicazioni su elicotteri. Impiegando un solutore delle equazioni mediate di Reynolds, che permette di trattare sistemi di griglie sovrapposte, vengono effettuate simulazioni CFD stazionarie e instazionarie per stimare il comportamento del presente tab a L, quale una possibile soluzione innovativa per bilanciare i carichi sul rotore e, allo stesso tempo, per ridurre le vibrazioni sulla pala. La caratterizzazione stazionaria mostra che il tab a L è potenzialmente in grado di aumentare la portanza e l'efficienza aerodinamica, quando estratto verso il basso, e di alleviare efficacemente lo stallo statico quando deflesso verso l'alto. I risultati ottenuti tramite le simulazioni stazionarie sono inoltre supportati da misurazioni sperimentali effettuate sullo stesso dispositivo. Simulazioni numeriche condotte per moti oscillatori di piccola ampiezza, della pala –un profilo NACA 0012– o del tab a L montato su questa, permettono di analizzare i fenomeni di shedding che avvengono dietro il dispositivo mobile e i carichi multi-armonici generati di conseguenza. Queste simulazioni sono in seguito utilizzate per sviluppare un modello di ordine ridotto fisicamente consistente, espresso nel dominio della frequenza, per la portanza e il momento instazionari di una sezione di pala con il tab a L, considerando come ingressi le oscillazioni in pitch e in plunge del profilo, insieme alla deflessione armonica del dispositivo mobile. A questo riguardo la caratterizzazione aerodinamica del tab a L mostra che il comportamento dei carichi può essere stimato utilizzando un modello analitico equivalente a lastra piana, composto da tre segmenti: il primo, rappresentativo della parte fissa del profilo, il secondo, rappresentativo del lato longitudinale del tab e il terzo, rappresentativo delle strutture vorticose controrotanti che appaiono dietro il dispositivo mobile. Lo stesso approccio è usato per modellare gli incrementi statici di portanza e momento, in termini di quelli generati da una modifica equivalente di curvatura. Viene dunque mostrata la stretta connessione dei parametri del modello di ordine ridotto con le quantità fisiche, così come le capacità predittive di questo per parametri arbitrari delle leggi di moto imposte. Il modello di ordine ridotto viene quindi utilizzato per definire un modello aerostrutturale lineare a tre gradi di libertà per una pala equipaggiata, su una frazione dell'apertura, con il tab a L. In aggiunta è sviluppato parallelamente un modello di ordine ridotto fisicamente consistente e un corrispondente modello aeroelastico per un flap classico di bordo di uscita. Risulta così possibile confrontare il comportamento aerodinamico e aerostrutturale del nuovo dispositivo con quello di una soluzione di bordo di uscita largamente impiegata, quale appunto un flap classico. Viene dunque applicato un algoritmo higher harmonic control per calcolare opportune leggi di controllo per il tab a L, volte a ridurre separatamente le armoniche N/rev della forza verticale e dei momenti di flappeggio e di pitch alla radice della pala, espressi nel sistema di riferimento rotante. Si ottiene in generale una riduzione significativa dei carichi vibratori. Inoltre, l'ottenimento di risultati comparabili con un dispositivo di bordo di uscita ben noto quale il flap classico considerato, è un'ulteriore conferma della potenziale applicabilità del presente tab a L, quale un'efficace soluzione alternativa per ridurre le vibrazioni sulle pale di elicottero.

Contents

Chapter 1

Introduction

The Gurney Flap (GF) was originally designed for the race car of Dan Gurney to increase the vehicle downforce generated by the rear inverted wing [1]. Since then, the GFs have also attracted much attention of aircraft and rotorcraft designers as a very effective high-lift device. Moreover, GFs are successfully applied in wind turbines and in turbomachinery.

The GF effectiveness stems directly from its extreme simplicity: a flat plate attached to the trailing edge (TE) and perpendicular to the chord line. On the contrary, classical high lift devices are very complex, both in terms of aerodynamics that governs their functioning and of mechanical systems necessary to activate them, requiring a high level of maintenance operations. Liebeck [2] was among the first to study the behavior of Gurney flaps for aeronautical applications. On the basis of his experimental studies, he found that two counter rotating vortices are generated behind the Gurney flap, since the flow is forced to turn around the perpendicular plate at the TE. The intersection point of the streamlines coming from the pressure and from the suction side, is shifted away from the TE. As a consequence, the location of the Kutta condition is shifted downstream the TE, resulting in a net effect in terms of load that is equivalent to what can be obtained by a longer effective chord and a more cambered airfoil. The interpretation proposed by Liebeck in Ref. [2] on the aerodynamic effects of GFs was confirmed by later studies. Experiments conducted on airfoils equipped with GFs highlighted the capability of these devices to significantly increase lift without severe drawbacks in terms of drag increment [3, 4, 5, 6, 7, 8, 9, 10]. Several numerical computations were also performed to investigate the behavior of GFs [11, 12, 13, 14, 9, 15]. These studies highlighted how such movable devices allow to increase the lift, and in particular the maximum lift, and the lift to drag ratio. Kentfield [3] developed a semi-empirical formulation to compute the lift and drag coefficients of airfoils equipped with a GF with respect to the clean configuration, as a function of the GF height.

Recently, large interest was directed toward movable aerodynamic surfaces for aerodynamic performance improvement, alleviation of vibratory loads, flutter suppression and modification of the vortical wake. Several authors worked on the application of movable trailing edge flaps on rotorcraft blades for vibratory load control, see Refs.[16, 17, 18, 19, 20], and for the mitigation of negative effect associated with dynamic stall, see Refs. [21, 22, 23]. Since a GF has considerably less inertia than a traditional flap, smaller forces are expected to be required to actuate the system. As a consequence, a larger bandwidth can be achieved together with a reduced modification of the structural stiffness of the blades.

Gerontakos and Lee [24] performed experimental measurements on a NACA 0012 section equipped with fixed GF-like strips both on the pressure and on the suction side of the airfoil. They showed that trailing edge strips are suitable to improve performance of oscillating airfoils, in dynamic stall conditions. Tang and Dowell [25] validated a numerical model of a fixed GF on an oscillating airfoil against the the experiments of Ref. [24]. Then they showed, through numerical computations, that an oscillating Gurney flap brings additional benefits for deep-stall cases. Moreover in Ref. [26] they carried out experiments on an oscillating NACA 0012 equipped with an oscillating GF, reaching the same conclusions of the numerical work, i.e. that an oscillating small strip located near the trailing edge can be used for active aerodynamic flow control of a wing.

Kinzel et al. [27] performed several steady and unsteady numerical simulations for various flow conditions over a S903 section equipped with GFs, referred to as Miniature Trailing edge Effectors (MiTEs). Such simulations gave an overview on the possible usage of MiTEs both to improve performance and to reduce vibratory loads on helicopter blades. Additionally, they investigated the effect of chordwise positioning of the GF, showing that increased upstream positioning enlarges the hysteresis loop, degrades the lift enhancement, increases drag and decreases the nose-down pitching moment. Similar limits were found also in Refs. [28, 14, 10, 29]. Matalanis et al. [30] carried out 2D and 3D simulations, together with experimental measurements, on a VR-12 section equipped with a deployable GF. They investigated the effects of the actuation frequency of the movable device on the vibratory moment coefficient, showing by CFD-CSD coupled analysis on a model of the UH-60A that significant reduction of vibratory loads can be achieved. Min et al. [31] by using CFD-CSD simulations, showed significant vibration reduction on the classical HART-II [32] test case with deployable GF. Liu et al. [33] investigated by numerical simulations the effect of several Gurney flap-like devices on a NACA 0012 airfoil. They used numerical CFD computations as a reference to develop a Reduced Order Model (ROM) for the unsteady loads generated by the airfoil section equipped with this movable device. This model was used within a comprehensive solver and an active control system was designed to effectively reduce vibratory loads on a helicopter rotor.

Despite the progress in the understanding the behavior of these movable devices, the integration of an active GF on a helicopter blade is still a very challenging design problem. In particular it is necessary to stow the deployable device, together with the actuation mechanism, at the TE, complying with weight and balance constraints related to the aeroelastic behavior of the blades. Moreover classical sliding actuation solutions, widely used for fixed wing GFs, are likely to undergo failures, under high centrifugal loads which affect rotor blades. Palacios et al. [34] carried out several experimental tests to investigate the operation of MiTEs under centrifugal loads comparable to those encountered on rotor blades. They found that indeed such devices are potentially capable to effectively operate in these conditions. Moreover the estimated power requirements of GF like devices were found significantly lower than those of classical plain flaps. Additionally they proposed a concept of a novel pneumatic actuation system exploiting the pressure radial gradients within the rotor blades. Such concept could avoid failures often occurring on commonly employed sliding actuation systems, when these operate under high centrifugal loads typical of rotorcraft environments.

In an attempt to overcome stowage and actuation issues at the same time Zanotti et al. [35, 36] proposed an L-shaped tab (L-tab), i.e. a combination between a TE spoiler, namely a classical split flap, and a GF, applied at the TE of a helicopter blade section. This solution has the additional advantage of locating the GF on the trailing edge, therefore maximizing its performance. An example sketch of a blade section equipped with such L-tab is reported in figure 1.1. The primary feature of this device consists of a twofold aerodynamic operation. Namely, when upward deflected it behaves as a classical GF therefore allowing to increase lift, without severe drawbacks in terms of drag rise. On the other hand, upward deflections of the movable device provide behaviors similar to those of a plain flap. Therefore load alleviations can be attained, for upward deflections of the tab, in terms of both lift and pitching moment magnitude, allowing to reduce issues typical of stall conditions. The baseline configuration for such device installed on a helicopter blade consists of an upward deflection of the L-tab such that the lower extreme of the vertical prong lies on the airfoil trailing edge. As a result the baseline section of the blade presents a slightly divergent trailing edge. With this regard several experimental tests, see Refs. [37, 38] have shown that divergent TE configurations, including those provided by GF-like devices, could be indeed appropriate for transonic flow conditions, being these latter not unusual for rotorcraft blade sections.

Notice also that, since the device lies entirely on the blade external surface, frequent issues concerning the lack of internal volumes on rotors are avoided. Moreover, since the L-tab is actually much thinner than a plain flap, significant reductions in terms of actuation power are expected. At the same time, failures under high centrifugal fields often affecting sliding actuation mechanisms, commonly used for deployable Gurney flaps [33], are prevented.

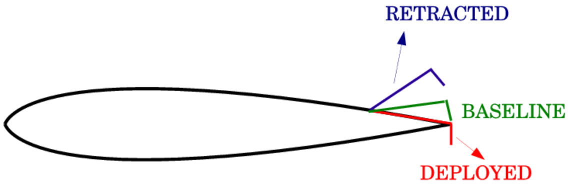

Figure 1.1: Sketch of a blade section equipped with the L-tab.

The experimental measurements carried out by Zanotti et al. showed that this novel L-shaped tab can be exploited to mitigate the negative effects of dynamic stall.

To verify the capabilities of this novel device also for steady state load balancing, to optimize the rotor asset according to the flight conditions, and for the control of vibratory loads far from those of dynamic stall, the behavior of the steady state and unsteady loads, these latter due to oscillations of the airfoil and of the L-tab, is investigated numerically by means of CFD.

A preliminary numerical assessment of the capabilities of this device has been performed. The analyses highlighted how the L-tab allows for the enhancement of performance both for small and high angles of attack in steady state conditions. With this regard part of the present work is dedicated to numerically investigate the aerodynamic behavior of L-tab in static conditions and for different freestream Mach numbers. Additionally, sensitivity analyses with respect to the geometrical configuration, are carried out. Numerical computations are performed for several angles of attack, each with various rotations of the L-tab. The validation of numerical results is performed through a time and space convergence analysis as well as by means of three dimensional simulations. Furthermore the reliability of the numerical investigation is supported by comparisons with experimental data. To this purpose steady state simulations are carried out on a NACA 23012 airfoil equipped with the L-tab under consideration. The numerical pressure distributions and the flow fields in the TE region are compared to the results of pressure measurements and PIV surveys on this latter configuration. The small angle of attack regime as well as the static light and deep stall conditions are taken under consideration. Likewise the phenomenon encountered in common GFs, two counter rotating vortical structures are developed past the vertical prong of the L-tab. Moreover the simulations show that for downward deflections of the tab a significant increase in lift coefficient is achieved, without severely affections on drag. For upward deflections of the tab the lift and the pitching moment magnitude are reduced and negative phenomena related to the static stall are effectively counteracted. It is found that for some geometrical configurations, the L-tab is even capable to delay the stall incoming.

On the other hand, simulations carried out for small amplitude oscillations of the blade section model equipped with the movable L-tab show the potential suitability of this TE device for vibration reduction on helicopter blades. In particular unsteady simulations are carried out at first for pitching or plunging oscillating motions of the airfoil with the L-tab in fixed position. These allow to gain an overview on the relation between the shedding phenomena of the counter rotating vortical structures past the L-tab and the motion of the airfoil. The affection of the steady state deflection of the L-tab on the unsteady airloads is investigated in detail. Secondly unsteady simulations are carried out for oscillating motions of the L-tab with the airfoil at constant angle of attack. Consistently the relation between the motion of the L-tab and the shedding frequency, with respect to that of the input motion, is taken under consideration. The features of the multi-harmonic hysteresis loops of the airloads –similar to those observed experimentally on harmonically deflected GFs installed on blade section models [27]– are also assessed.

Although effective, these simulations are computationally intensive, and as such are not effective during the design process and the development of control strategies. Thus, it is necessary to develop a Reduced Order Model (ROM) starting from CFD simulations.

In this context Liu and Montefort [39] proposed an analytical interpretation of steady effects of GFs on the basis of the thin airfoil theory. An extension of the thin-plate approach to the unsteady domain was proposed by Kinzel et al. [40]. The model was based on the formulation of Hariharan and Leishman [41], originally developed for airfoils equipped with a classical flap, and essentially it looks for an equivalent flap size which returns the indicial response that best approximates the indicial response of the GF obtained through a CFD computation. The formulation allows to keep into account the effects of the Mach number. These linear models are capable to capture the harmonic components of the aerodynamic loads. An extension was proposed in Ref. [42], to model also the non-harmonic disturbances visible in the results of CFD simulations.

A different approach is followed here, within the aim of developing a physically based linear ROM for the first harmonic of the unsteady lift and moment. Such approach does not require to run a CFD indicial response simulation, but relies on physical flow features, such as the mean size of the Counter Rotating Vortices structures (CRV) developed past the L-tab. Notice that the correct representation of the first harmonic is the primary interest of the ROM in view of the application of classical rotorcraft active control systems for vibration reduction.

The development of a ROM for a NACA 0012 section equipped with a TE L-tab, with the shape of the movable device adopted by Ref. [36] is discussed in detail. It will be shown in the following how the primary effect of the L-tab consists of a modification in the effective blade section mean line. As a consequence, similarly to the approach followed by other authors, a flat-plate approximation model can be employed effectively. In this case, the analytical formulation of Küssner and Schwarz [43] (KS) is selected to build the approximation, since it is capable to deal with arbitrarily shaped mean lines. As a result the ROM herein developed is found to correctly reproduce the equivalent mean line blade section equipped with the L-tab. In particular the inclination and the length of the Counter Rotating Vortices (CRV) past the L-tab, is accurately represented by the final segment of the mean line of the ROM. No attempt has been made to investigate the effect of Mach number at this stage, so low Mach number CFD simulations have been employed to identify the parameters of the ROM model. However, extensions to higher Mach could be straightforward using the identified equivalent flat-plate model in conjunction with the Hariharan and Leishman [41] formulation.

Additionally, such thin-line based formulation is used to perform a comparison between the unsteady airloads generated by the L-tab under consideration and those developed by a solution widely employed in literature, namely a classical trailing edge plain flap, both oscillating with the same law. With this regard a two segments piece-wise mean line ROM is used to represent the airfoil equipped with the plain flap. Such comparison is carried out for several reduced frequencies, ranging from 0 up to 0.6. In general the L-tab is found to provide larger lift for low reduced frequencies, namely smaller than 0.125, whereas a larger pitching moment is developed for reduced frequency k $\geq$ 0.0125.

The thin-line ROMs for the L-tab and the flap are then exploited to build an aeroelastic linear model consisting of a helicopter blade equipped with either the L-tab or the TE flap, both covering the 12% of the span. The aerostructural analytical model is developed according to classical formulations available in literature [44]. Namely, by starting from the flap and pitch equilibrium equations of the blade, a typical section aeroelastic model [45] with three DOFs is developed. In particular the model relates the blade root flapping, feathering and control surface hinge moments to the bending, pitching and TE device motions, being this latter the actual control input of the aerostructural system. Moreover, the aeroelastic equation for the blade root vertical force is added as output transformation.

The Higher Harmonic Control (HHC) approach [46], is herein employed to compute proper control laws for the L-tab and the TE flap respectively, with the aim to reduce the blade root loads at one specific harmonic a time. The HHC algorithm was first conceived to be applied directly on the non-rotating swashplate, but soon extended as the basis algorithm for independent controls applied in the rotating frame on each blade separately [47, 33]. Among these applications there is the Individual Blade Control (IBC), where each blade is controlled in the rotating frame [16], by either actuators located on the root, or actively controlled partial span trailing edge surfaces, which are indeed the solution adopted in this work.

The HHC approach has received considerable interest for rotorcraft applications, since found effective and simple at the same time. In fact, since disturbances on helicopters have specific and known frequencies, an effective vibration reduction can be achieved by directly imposing high gains at such frequencies. In other words this algorithm, which is conceived to reject disturbances at a specific frequency, results particularly suitable for rotorcraft, due to the highly tonal nature of the vibration, whose frequency is also known a priori. An extended review on literature concerning active control systems for rotorcraft applications, including of course the HHC, was given by Friedmann [16]. The most relevant theoretical, digital, experimental and numerical studies on the HHC algorithm are therein detailed and commented. Johnson [46] proposed a comprehensive study concerning specifically HHC algorithms. He highlighted that HHC algorithms share in general three features: a linear quasi-static, frequency domain model of the helicopter response; an identification procedure carried out by means of a least squares or a Kalman filter method; the usage of a quadratic form figure of merit.

The control approach employed in this work presents all of these three features and, as such, can be considered properly a HHC algorithm. In this case the quadratic-form figure of merit involves the rotating frame blade root bending and feathering moments, in addition to the vertical force. The expression of the cost function, as well as the consequent derivation of the control input at a specific frequency, are written according to the classical formulation of Johnson [46]. The uncontrolled rotating frame blade root harmonics of loads are extracted from data of the HART-II program [32]. The vibration reductions obtained with HHC control algorithms, applied to the models for the L-tab and for the TE flaps respectively, are then compared. Both the trailing edge solutions are found capable to significantly reduce the 2/rev 3/rev, 4/rev and 5/rev rotating frame blade root flapping moment and vertical force. As expected, the span-wise limited extension of the movable devices, i.e. 12% of the blade radius, does not allow to effectively control the blade root pitching moment, due to the high torsional stiffness of most rotors. A more effective action is expected by employing more than a single movable device on the blade, so that a larger portion of the span could be covered by control surfaces.

It's worth noting that vibration reduction capabilities of the L-tab are absolutely comparable with literature results concerning trailing edge control surfaces, employed to reduce vibratory loads on rotorcraft. In this context Milgram et al. [106] investigated the potentialities of plain trailing edge flaps in vibration reduction within a comprehensive rotorcraft analysis. The magnitude of the hub vertical 4/rev load was found reduced of 98% with flap control inputs at 4/rev. Moreover it was shown that also 3/rev flap inputs are capable to alleviate the 4/rev hub loads. Additionally it was found that the plain flap is still effective, if the blade torsional stiffness is reduced of 50%. Namely a 85% reduction of the 4/rev vertical shear in the fixed system was observed in this case. The aforementioned work of Min et al. [31] shows that a proper actuation of GF-like devices allows for reductions up to the 83% of the rotor 4/rev vibratory loads, without affecting the performance and the trim state. Moreover in Ref. [31] it was found that the 4/rev loads can be even virtually withdrawn, by optimizing the deployment of the appended device. Additionally, a simultaneous reduction of 4/rev and 8/rev vibratory loads can be achieved by individual control of multiple Gurney flaps distributed along blade span. The previously referenced work of Matalanis et al. [30] highlights that miniature trailing-edge effectors deployed sinusoidally at 4/rev frequency are capable to reduce approximately the 80% of the 4/rev integrated aerodynamic loads in the vertical direction. In this context it appears proper to recall also the aforementioned work of Liu et al. [33], in which the vibration reduction capabilities of a GF-like device installed on helicopter blades were evaluated. Open-loop control studies showed a 80% reduction of vertical shear, but at the same time other load components were found to grow. On the other hand a closed-loop control, characterized by a sum of harmonic inputs ranging from 2/rev to 5/rev, allows for a 92% reduction in all of the 4/rev shears and moments.

Overall the L-tab under consideration is found potentially capable to be effectively used for vibration reduction on rotor blades, in addition to performance improvement and dynamic stall alleviation, see for this latter application Refs. [35, 36]. The feasibility of this novel solution is also here supported by the reasonable agreement with the behavior exhibited by a well known trailing edge device, namely a classical plain flap.

Before focusing on the assessment of the behavior of the novel L-tab trailing edge solution, it appears proper to characterize clean blade section models with the same instruments employed hereafter for the movable device. Namely oscillating airfoils are taken under consideration and their behavior is investigated with numerical computations as well as with analytical low order models.

In general the accurate evaluation of the unsteady aerodynamic loads around aerodynamic lifting bodies is of paramount importance in the determination of dynamic structural loads and aeroelastic stability in fixed- and rotary-wing aircraft, turbo-machinery and wind turbines. With this regard a realistic prediction of unsteady loads is also mandatory to evaluate the propulsive efficiency of flapping motion see Refs. [48, 49, 50] and to design load-alleviation devices see e.g. Ref. [27]. To understand all the implications of unsteadiness in the design process, it is necessary to achieve a deep knowledge into the theoretical fundamentals of unsteady flows and in particular of periodic motions.

A large number of studies have been carried out to investigate the complex aerodynamics of airfoils in unsteady motion in different flow regimes. Kurosaka [51] applied the linearized theory to the prediction of unsteady loads around airfoils oscillating at high reduced frequencies in supersonic flows. The dynamic loading over airfoil at low Reynolds number (up to 40 000) and in the incompressible limit was studied by e.g. Anderson [50], that observed peculiar flow field features, including so-called leading edge vortices and large-scale vortical structure in the wake. Baik [52] successfully compared experimental results to linear theory predictions in these conditions, which are relevant to the understating of the propulsion of fish and cetaceans and of insect flight. In particular, Uldrick [53] investigated the effect of the airfoil thickness in swimming motion. At a larger angle of attack, so-called dynamic stall is possibly observed, see for example Ref. [54]. More recently, the boundary layer transition and separation was studied experimentally by Lee [55] at Re = 135 000 for an oscillating NACA 0012 airfoil. High reduced frequency effects were measured for the NACA 0012 airfoil at Re = 12 600 by Bohl [56]. The reader is referred to the review of the work of McCroskey [57] for further details.

Physical models of different complexity have been proposed and validated through experiments and, more recently, by numerical simulations. The cornerstone models for unsteady aerodynamics were developed by Wagner [58] in the time domain, and by Theodorsen [59] for unsteady aerodynamic forces in the frequency domain. Relevant contributions to the field were given by e.g. Küssner [60] and Cicala [61]. Garrick [62] demonstrated the equivalence between the Theodorsen's frequency domain function and the indicial response function developed by Wagner for the transient response of an impulsively started airfoil. Most mathematical models moves from the small perturbation hypothesis, which is justified by the fact that the surface of aerodynamic lifting bodies can be approximated by the corresponding lifting flat-plate with zero thickness see Ref. [45], chapter 5. In accordance to the small perturbation hypothesis, the aerodynamic solution was obtained by Wagner [58] and Theodorsen [59] as a linear combination of elementary solutions corresponding to the separate contributions of the body angle of attack, camber and thickness distribution, under the further assumption that the coupling among these terms is negligible. In particular, by using conformal mapping techniques, Theodorsen derived the analytical expression of the unsteady lift of a two-dimensional flat-plate moving in an inviscid incompressible flow, written in terms of three contributions: quasi-steady aerodynamics, the so-called added mass, and the wake unsteady contribution. Küssner and Schwarz [43], already mentioned in the above, were able to obtain the pressure distribution along the chord for an arbitrary spatial and temporal distribution of the velocity boundary condition on the airfoil, thus opening the way to the possibility of studying variable shape airfoils, see e.g. Ref. [63]. Starting from these seminal works several authors developed more complex models to account for e.g. the flow compressibility, see for extensive reviews Refs. [64, 45]. These models, with slight modifications, are currently being successfully applied to fixed-wing [45, 64] and rotary-wing [65, 66] aircraft design.

Extensions of the Theodorsen's theory were proposed to keep into account the effect of airfoil thickness, of primary interest in the present work. These research activities were motivated by the limits of the linearity assumption and by the fact that the thin-airfoil theory exploited by Theodorsen is clearly unreliable in the airfoil nose region [67]. Küssner [68] developed a very elegant mathematical theory to account for the effect of the finite airfoil thickness. By resorting to conformal mapping techniques, Küssner computed a set of modified Theodorsen's functions for Joukowsky airfoils. McCroskey [69] developed a formulation for airfoils in unsteady motion, starting from the thin-airfoil theory, but keeping into account also the thickness and the camber, to evaluate the pressure distribution. The boundary velocity was expressed as the sum of three contributions. The camber and the thickness contributions are coincident with those obtained from the steady-flow theory, see e.g. Ref. [70]. The third term, which is a function of the angle of attack, accounts for the flow unsteadiness. The unsteady term depends actually on the ratio between the unsteady and the quasi-steady solution for a flat-plate. While being an extension of the Theodorsen's approach, in Ref. [69] the effects of unsteadiness is still restricted to the contribution of the angle of attack only. Additionally Goldstein and Atassi [71] showed that the effects of thickness, camber and angle of attack cannot simply be superimposed for the computation of the response of an airfoil to an incident gust. They developed a second order approximation that leads to a complex analytical expression for the unsteady lift, but in their analysis the effect of thickness on the unsteady lift was neglected because, according to the authors themselves, the "airfoil thickness probably has only an unimportant influence on the unsteady lift". A second order expansion was developed by Van Dyke [72] for an oscillating airfoil in a supersonic flow. Glegg [73] developed a theory based on the conformal mapping and on the Blasius theorem, to evaluate the unsteady loading of an arbitrary thickness airfoil resulting from an airfoil-vortex interaction, highlighting significant effects due to thickness.

The availability of computational fluid dynamics (CFD) tools, ousted almost completely the analytical formulations, also due to the high degree of complexity reached by these latter, see Ref. [71]. Several panel methods, to compute numerically the unsteady incompressible potential flow around a moving airfoil, are presented in the textbook by Katz and Plotkin [74]. A more refined approach capable of taking into account also compressibility effects was proposed by Morino [75, 76]. As the computational power increased, numerical simulations based on e.g. the finite volume or finite elements discretization of the Euler or Reynolds–Averaged Navier–Stokes (RANS) equations, were used to study unsteady aerodynamic phenomena. With this regard, for example, Ref. [77] reports the results of CFD computations performed indeed on a NACA 0012 airfoil, undergoing at the same time pitch and plunge oscillations. Notwithstanding the advantages related to the use of a more complete physical model, several aspects may affect the reliability of numerical results, including the influence of the grid resolution or of the time integration scheme.

Overall the understanding of the influence of airfoil thickness on the unsteady aerodynamic loads is still unsatisfactory, though the capability of predicting the aerodynamic loads in these conditions is of paramount importance in e.g. fixed- and rotary-wing design.

This is even more important for this specific work, concerning the assessment of a novel trailing edge device installed on oscillating sections. Indeed, to correctly figure out the affection of the present L-tab on blade sections, the comprehension of the phenomena occurring on the baseline airfoil in oscillating motion is mandatory. Consistently with such remark the initial part of the work is aimed to provide a comprehensive description, under both a qualitative and a quantitative point of view, of the aerodynamic loads dependence on the airfoil thickness, for small amplitude oscillations and in the low Mach limit. In these conditions, a linear and incompressible behavior can be expected. A CFD solver for RANS/Euler's equations –the same then employed for simulations on the L-tab– is used to compute the aerodynamic flow-field, avoiding the derivation of a complex analytical or semi-analytical solution of the potential problem. Namely the second chapter of the work is dedicated to the characterization of the unsteady geometrical effects of oscillating airfoils, i.e. blade section models, on the resulting airloads. In particular the quantitative evaluation of unsteady thickness effects, neglected by most analytical models, highlights that these phenomena are actually relevant in affecting the airloads developed on oscillating sections. A modification of the classical oscillating flat plate Theodorsen's model [59], accounting for unsteady thickness effects, is developed on the basis of well tested numerical computations on 4%,12%,18% and 24% thick airfoils. A significant improvement in predicting the loads hysteresis cycles is observed by employing this thickness accounting linear model, in place of the original flat plate formulation. Applications of this new model to aeroelastic computations concerning the prediction of the flutter onset on a typical section approximation are also reported. It is found that the employment of a aerodynamic transfer matrix, which accounts for unsteady thickness effects, significantly affects the computed flutter velocity. In particular the flat plate assumption appears not always conservative in predicting the onset of the aeroelastic instabilities. Having gained some additional information on the behavior of oscillating sections, it is possible to get more clearly the phenomena directly induced by the L-tab, which are indeed the focus of this thesis.

The work is structured as follows. Chapter 2 deals with the characterization of simple blade section models in harmonic motion. At first the well-known linear theory results for oscillating airfoils are recalled, to underline the interplay between the airfoil thickness and the boundary conditions of the potential problem at the body interface. A brief overview of the considered computational model is then given and its suitability for the problem under study is assessed. Subsequently the results of the numerical simulation for symmetrical four-digit NACA airfoils are presented and an explanation of the dependence of aerodynamic loads on the airfoil thickness is provided. As a result a modification to the flat-plate Theodorsen model, which accounts for the thickness effects in the computation of the unsteady aerodynamic loads, is proposed. The significant improvements with respect to the classical Theodorsen's formulation in computing the hysteresis cycles of finite thickness and slightly cambered airfoils are pointed out. The application of the thickness accounting analytical formulation to the flutter prediction on a typical section aeroelastic model is also reported.

Chapter 3 concerns the steady characterization of the L-tab. The geometrical features and the numerical model for the L-tab equipped NACA 0012 section are initially illustrated. The computational domain, the grid realization and the numerical solver are briefly described. The convergence analysis, both in time and in space, performed for low angles of attack as well as for static stall conditions is discussed. Comparisons with experimental data taken from literature on a NACA 0012 section with and without a classical TE Gurney flap are also included, to support the reliability of the numerical results. Subsequently the results of steady state numerical simulations, performed at small angles of attack, are reported. The force coefficients, obtained for different deflections of the L-tab and for the clean NACA 0012 airfoil, are compared end extensively discussed. Additionally a Mach number sensitivity analysis is reported, allowing for an estimation of L-tab the span-wise operation on actual rotor blades environments. Static stall computations are then reported. The potential capabilities of upward deflections of the L-tab in alleviating the static stall negative effects are highlighted. Furthermore, computations carried out by doubling the L-tab chord-wise length, highlight how the stall onset can be even shifted to angles of attack α larger than 18 degrees. A whole section is then dedicated to the comparisons between numerical results and experimental data achieved at the Politecnico di Milano wind tunnel on the same L-shaped device. Comparisons are performed in terms of loads and near body flow field on a L-tab equipped NACA 23012 blade section. Finally, results of three-dimensional computations performed on a span-wise uniform blade model featuring the L-tab under consideration are discussed. It is shown that, at least for small angles of attack, the flow is substantially two-dimensional, therefore further confirming the feasibility of 2D computations, to characterize the L-tab. Moreover, the three-dimensional computations highlight again the two counter-rotating vortical structures past the vertical prong of the L-tab, which are consistent in shape and extension with those captured by experimental flow field visualizations and observed with 2D simulations.

Chapter 4 concerns the unsteady characterization of the L-tab. At first oscillating motions of the airfoil in pitch or plunge with the L-tab in fixed position are taken under consideration. The convergence of the unsteady solution with respect to the number of time-steps per period and with respect to the number of oscillation cycles is checked. The flow field and the unsteady airloads achieved for reduced frequencies in the range [0.1 0.6] at several angular positions of the L-tab, as well as with the clean NACA 0012, are reported and discussed. The motion related shedding phenomena of the two counter rotating vortical structures past the L-tab, and their affection on the unsteady airloads are investigated in detail. The same approach is adopted for small amplitude oscillations of the L-tab with the airfoil at fixed angle of attack. Again the motion related shedding phenomena, affecting the resulting airloads are taken under consideration. Overall it is found that the alternate downstream convection of the CRV generates oscillations in the unsteady airloads. By the way such oscillations are much smaller, namely at least two orders of magnitude lower, with respect to the first harmonic component, which additionally is by far the main concern when dealing with active control systems for vibration reduction on rototcraft. Moreover it is shown that the frequency of such oscillations is not an integer multiple of the rotor angular velocity, therefore potential resonance phenomena are avoided. The first harmonic of the unsteady airloads, generated by pitching or plunging oscillations of the airfoil or harmonic motions of the L-tab, is then extracted and compared for different input motion laws.

Chapter 5 presents the derivation of the Reduced Order Model (ROM) for the blade section equipped with the L-tab. At first the analytical formulation of Küssner and Schwarz [43] (KS), which is the basis of the ROM, is briefly introduced. The application of such theory to this specific L-tab equipped blade section in then detailed. Namely the development of the equivalent geometry, with the aim to correctly reproduce the mean line modifications induced by the L-tab, is illustrated. The identification procedure, carried out to compute the geometrical and motion parameters of the KS equivalent mean line is also described, specifically for steady state positions of the airfoil and L-tab and for oscillating motions of the movable device. The derivation of the ROM for several fixed positions of the L-tab at constant angles of attack is then presented. It is shown how the ROM is capable to correctly reproduce and predict the steady airloads, as well as the mean line modifications introduced by the L-tab. For periodic motions, either of the airfoil or of the L-tab, the first harmonic of the unsteady airloads is the main concern for active control systems aiming to reduce vibratory loads on rotor blades. Being the vibration reduction the ultimate purpose of the present work, the ROM is thought to reproduce indeed the first harmonic of the unsteady lift and moment coefficients. For unsteady motions of the airfoil, with the L-tab at constant rotation, a simple oscillating flat plate model is found appropriate, since the steady position of the L-tab appears not affecting the first harmonic of the aerodynamic loads. The chord of the equivalent flat plate model is actually rescaled by taking into account the mean enlargement effect induced by the CRV. Subsequently, the ROM for oscillating motions of the L-tab developed at several reduced frequencies is described in detail. The feasibility of the ROM in correctly reproducing the first harmonic of unsteady airloads, as well as in capturing the mean line shape during the oscillation cycle is highlighted. Again the predictive capabilities of the ROM, both in terms of aerodynamic forces and equivalent geometry, for arbitrary reduced frequencies in the range [0.1 0.6] are demonstrated. Finally a physically based ROM for a blade section equipped with a trailing edge plain flap is developed. The aerodynamic performance provided by a widely employed solution as a classical plain flap is, are an useful term of comparison to ultimately check the feasibility of the results attained with the L-shaped novel configuration. The range of the the movable devices motion frequencies where the L-tab appears to perform better than the plain flap and vice versa are also shown.

Chapter 6 reports the aeroelastic characterization of a blade section model equipped with either the L-tab or the aforementioned TE plain flap. The analytical derivation of the three Degrees Of Freedom (DOFs) aerostructural system, employing the typical section model, is discussed. At the beginning of the chapter, the results of simulations carried out on a blade section oscillating at the same time in pitch, in plunge and with the L-tab harmonically moving are compared, in terms of the airloads first harmonic, with the forces computed as the simple summation of the corresponding single-DOF ROMs. The reasonable agreement between the CFD and the ROMs ultimately confirms how the whole blade model, undergoing together pitch and plunge oscillations, in addition to L-tab harmonic deflections, behaves linearly in terms of the loads generated. Then the development of the aerodynamic transfer matrices for the blade model, with the L-tab or the plain flap as control surfaces, is discussed. Subsequently the assembling of the mass and stiffness matrices is described. The resulting three equations aerostructural system relates the rotating frame blade root flapping moment, feathering moment and vertical shear, to the blade bending and pitching angles and to the deflection of the control surface. It is shown how the first two equations of the aeroelastic system are actually used to compute the control input, whereas the third, related to the hinge moment is kept separated, since it concerns the evaluation a posteriori of the feasibility of the hinge moment developed by the control system, in terms of the actuation system provided performance. The computation of the control input, by means of the Higher Harmonic Control algorithm, is reported. After a brief overview on the main features of such algorithm, the control inputs attained at four different frequencies, integer multiples of the rotor angular velocity, are compared to the corresponding uncontrolled loads. It is shown how both the L-tab and the TE flap are potentially capable to reduce almost the 100% of the vertical force and the flapping moment at 2/rev and 3/rev. An effective reduction of such loads is attained also at 4/rev. It is remarked how probably multi-harmonic control inputs, also according to literature results, would be probably effective in reducing even the 5/rev vibratory loads. Finally it is shown that, with regard to the blade root feathering moment, the substantial ineffectiveness, both of the L-tab and of the TE plain flap, is likely due to the limited span-wise extension of the control surfaces. In fact, since the torsional stiffness of common blades is much larger than the bending counterpart, the local pitch induced by the control surfaces is not propagated along the span, with consequent low effectiveness in controlling the feathering moment. It is remarked that, by the way, this issue could be easily overcome by distributing several control surfaces along the span. Overall it is shown that the L-tab is potentially a promising solution in alleviating vibratory loads on rotor blades, in addition to improving performance and, as shown in Ref. [35], alleviating dynamic stall phenomena.

Chapter 7 contains final remarks to the present work, as well as possible future developments.

Chapter 2

Unsteady geometrical effects on aerodynamic loads of rotor blades

---

Numerical computations are herein used as reference to gain an insight into the unsteady effects of the blade section geometrical properties on the time-dependent aerodynamic loads. Namely, the thickness and the camber of the blade section airfoil are analytically assessed in section 2.1. It is shown how, for classical aerodynamic sections, the thickness is prevailing, with respect to the camber, in the affection of the unsteady airloads. In this context the formulation of the linear Theodorsen's model [59], for the computation of the unsteady loads on oscillating flat plates, is taken under consideration. Specifically, starting from the same hypotheses of the Theodorsen's model, the unsteady contribution of the thickness to the local loads is analytically derived. It is found that the thickness may play a quite considerable role in affecting the pressure distribution, especially in the nose area. Such contribution is proportional to the thickness times its spacial derivative, therefore becoming more significant for thicker airfoils. Accordingly, the CFD results reported in sections 2.2 and 2.3 confirm how the computed aerodynamic loads undergo a shift, with respect to the flat plate solution, which grows with the airfoil thickness. Additionally, analyses in the frequency domain highlight how the error of the flat plate model, in computing the aerodynamic loads, gets higher for increasing values of the reduced frequency. In section 2.4 a modification of the classical Theodorsen's model is developed, which takes into account the unsteady effects of the airfoil thickness in the airloads computation. Such model is in fact found to perform much better, with respect to the original flat plate formulation, in predicting the unsteady airloads on arbitrarily thick airfoils –in the range 4-24%–, even for high reduced frequencies. An application of the developed model to a simple typical section aeroelastic problem is then reported in section 2.5. Significant differences in the prediction of the flutter onset are encountered, if the present thickness-accounting model is used, instead of the flat plate formulation, to compute the aerodynamic transfer matrix. Further remarks and conclusions are reported in section 2.6

2.1 Review of the linear theory for oscillating airfoils

With regard to the formulation of linear theories for steady and unsteady airfoils, most mathematical models moves from the small perturbation hypothesis. Such assumption is justified if one considers that the surface of aerodynamic lifting bodies can be approximated by the corresponding lifting flat-plate with zero thickness, as it is explained, for example, in the textbook of Bisplinghoff [45], chapter 5. In accordance to the small perturbation hypothesis, the aerodynamic solution was obtained by Wagner [58] and Theodorsen [59] as a linear combination of elementary solutions corresponding to the separate contributions of the body angle of attack, camber and thickness distribution, under the further assumption that the coupling among these terms is negligible. In particular, by using conformal mapping techniques, Theodorsen [59] derived the analytical expression of the unsteady lift of a two-dimensional flat-plate moving in an inviscid incompressible flow, written in terms of three contributions: quasi-steady aerodynamics, the so-called added mass, and the wake unsteady contribution. In this regard Küssner and Schwarz [43] were able to obtain the pressure distribution along the chord for an arbitrary spatial and temporal distribution of the velocity boundary condition on the airfoil, thus opening the way to the possibility of studying variable shape airfoils, see e.g. the work of Gennaretti [63]. McCroskey [69] proposed an extension of the Theodorsen's model, capable to take into account the steady effects of thickness and camber in the computation of unsteady loads over oscillating airfoils.

Among the linear models, the Theodorsen's formulation is among the most extensively used to compute aerodynamic loads on helicopter blade sections. The classical Theodorsen's linear theory for plunging and pitching airfoils, moves from the hypothesis of irrotational and incompressible flow. Under these assumptions, the point-wise value of the velocity vector $\boldsymbol{V}(\boldsymbol{x},t)$ is written as the sum of the constant free-stream velocity U_∞ –the x-axis is parallel to the free-stream velocity– and the perturbation velocity $\boldsymbol{v}(\boldsymbol{x},t)$, i.e. $\boldsymbol{V}(\boldsymbol{x},t) = U_\infty \hat{\boldsymbol{\imath}} + \boldsymbol{v}(\boldsymbol{x},t)$, where $\hat{\boldsymbol{\imath}}$ is the x-axis unit vector. The perturbation velocity is the gradient of a scalar function $\varphi(\boldsymbol{x},t)$, termed the perturbation potential, i.e. $\boldsymbol{v}(\boldsymbol{x},t) = \boldsymbol{\nabla}\varphi(\boldsymbol{x},t)$. Within the linear theory, the perturbation velocity is assumed to be small with respect to the free-stream velocity, namely $|\boldsymbol{v}|/U_\infty \ll 1$. By combining the velocity potential definition and the continuity equation for incompressible flows, the well-known Laplace equation is obtained as

$$\nabla^2 \varphi = 0, \tag{2.1}$$

which is to be made complete by suitable initial and boundary conditions.

At the body surface, the boundary condition is the well-known impermeability or slip condition, namely, $\boldsymbol{V} \cdot \boldsymbol{n} = \boldsymbol{v}_{\mathrm{B}} \cdot \boldsymbol{n}$, with $\boldsymbol{v}_{\mathrm{B}}$ local velocity of the solid surface. In terms of velocity potentials, the boundary condition is written as a Neumann condition as follows, see the textbook of Katz and Plotkin [74], Chapter 2:

$$\frac{\partial \varphi}{\partial n} = \left(\boldsymbol{v}_{\mathrm{B}} - U_\infty \hat{\boldsymbol{\imath}} \right) \cdot \boldsymbol{n}, \tag{2.2}$$

where $\boldsymbol{n}$ is the normal unit vector from the body surface and $\partial/\partial n = \boldsymbol{n} \cdot \boldsymbol{\nabla}$.

Sufficiently far from the airfoil, the so-called boundary condition at infinity is enforced as

$$\lim_{r \to \infty} \boldsymbol{v}(r) = o(r^{-1})$$

with r distance from the airfoil.

The boundary conditions along the wake are obtained by imposing the conservation of mass and momentum across the surface of discontinuity as

$$\begin{aligned} \Delta \left(\frac{\partial \varphi}{\partial n} \right) &= 0 \\ \Delta \varphi(\boldsymbol{x}_{\mathrm{W}}, t) &= \Delta \varphi(\boldsymbol{x}_{\mathrm{TE}}, t - t_c), \end{aligned}$$

where the symbol Δ indicates the difference between the two sides of the wake, $\boldsymbol{x}_{\mathrm{TE}}$ is the coordinate vector of the trailing edge, t_c is the convection time and the wake is described by the function $\boldsymbol{x} = \boldsymbol{x}_{\mathrm{W}}(s_w, t)$, being s_w the curvilinear coordinate along the wake. At the trailing edge, one also has to explicitly impose the well known Kutta condition, see the work of Morino [78], pp. 1213–1214. It is not obvious that the Kutta condition for steady flows could be extended to unsteady flows as well. Experimental studies indicated that in fact the streamlines do not leave parallel to the trailing edge at reduced frequencies above 0.6. However, for small-amplitude oscillations the pressure distribution and the lift are not affected significantly by such misalignment, so for practical purposes the unsteady Kutta condition is equivalent to the steady one, fixing the rear stagnation line to start at the trailing edge, see Chapter 3 of the textbook of Katz and Plotkin [74].

From the potential equation (2.1), it is apparent that at larger times, when the transitory regime from initial conditions can be assumed to be terminated, the flow unsteadiness and possible non-linear terms can be introduced only by the displacement of the solid boundary, as duly detailed in the following.

2.1.1 Boundary conditions at the airfoil surface

The boundary condition at the body surface (2.2) is herein discussed. For simplicity, we start by considering the airfoil upper surface. The coordinate vector of each point along the upper surface is given by

$$\boldsymbol{\sigma}(s,t) = \boldsymbol{\sigma}_{\mathrm{ca}}(s) + \boldsymbol{\sigma}_{\mathrm{th}}(s) + \boldsymbol{\sigma}_{\mathrm{ds}}(s,t) = \boldsymbol{\sigma}_{\mathrm{st}}(s) + \boldsymbol{\sigma}_{\mathrm{ds}}(s,t), \tag{2.3}$$

where s is the curvilinear coordinate and where the flow direction is aligned with the x coordinate axis. The initial shape of the airfoil $\boldsymbol{\sigma}_{\mathrm{st}}$ at $t = 0$ is expressed as the sum of two terms: the mean line camber $\boldsymbol{\sigma}_{\mathrm{ca}}$ and the thickness $\boldsymbol{\sigma}_{\mathrm{th}}$. The quantity $\boldsymbol{\sigma}_{\mathrm{ds}}$ is the local surface displacement due to the airfoil motion.

The normal outward vector along the airfoil surface reads

$$\boldsymbol{n}(s,t) = -\frac{\partial \boldsymbol{\sigma}(s,t)}{\partial s} \times \hat{\boldsymbol{k}} = \boldsymbol{n}_{\mathrm{st}}(s) + \boldsymbol{n}_{\mathrm{ds}}(s,t), \tag{2.4}$$

where $\hat{\boldsymbol{k}}$ is the unit vector of the z-axis normal to the airfoil plane. The normal unit vector $\hat{\boldsymbol{n}}$ therefore reads

$$\hat{\boldsymbol{n}}(s,t) = \frac{\boldsymbol{n}}{|\boldsymbol{n}|} = \frac{\boldsymbol{n}_{\mathrm{st}} + \boldsymbol{n}_{\mathrm{ds}}}{|\boldsymbol{n}_{\mathrm{st}} + \boldsymbol{n}_{\mathrm{ds}}|}. \tag{2.5}$$

The module of the normal vector $\boldsymbol{n}$ is

$$\begin{aligned} |\boldsymbol{n}_{\mathrm{st}} + \boldsymbol{n}_{\mathrm{ds}}| &= \sqrt{|\boldsymbol{n}_{\mathrm{st}}|^2 + |\boldsymbol{n}_{\mathrm{ds}}|^2 + 2\,\boldsymbol{n}_{\mathrm{st}} \cdot \boldsymbol{n}_{\mathrm{ds}}} \\ &= |\boldsymbol{n}_{\mathrm{st}}| \sqrt{1 + 2\,\frac{\boldsymbol{n}_{\mathrm{st}} \cdot \boldsymbol{n}_{\mathrm{ds}}}{|\boldsymbol{n}_{\mathrm{st}}|^2} + \frac{|\boldsymbol{n}_{\mathrm{ds}}|^2}{|\boldsymbol{n}_{\mathrm{st}}|^2}} \\ &\simeq |\boldsymbol{n}_{\mathrm{st}}| \left[1 - \frac{\boldsymbol{n}_{\mathrm{st}} \cdot \boldsymbol{n}_{\mathrm{ds}}}{|\boldsymbol{n}_{\mathrm{st}}|^2} - \frac{1}{2} \frac{|\boldsymbol{n}_{\mathrm{ds}}|^2}{|\boldsymbol{n}_{\mathrm{st}}|^2} \right]^{-1} \end{aligned}$$

where in the last relation, the expansion $(1+\epsilon)^{1/2} \simeq (1-\epsilon/2)^{-1}$, valid for $\epsilon \ll 1$, is used. By considering only the first order displacement terms in (2.5), the linearised form of the normal unit vector reads

$$\hat{\boldsymbol{n}} \simeq \frac{\boldsymbol{n}_{\mathrm{st}} + \boldsymbol{n}_{\mathrm{ds}}}{|\boldsymbol{n}_{\mathrm{st}}|} \left(1 - \frac{\boldsymbol{n}_{\mathrm{st}} \cdot \boldsymbol{n}_{\mathrm{ds}}}{|\boldsymbol{n}_{\mathrm{st}}|^2} \right) \simeq \frac{\boldsymbol{n}_{\mathrm{ds}}}{|\boldsymbol{n}_{\mathrm{st}}|} + \left(1 - \frac{\boldsymbol{n}_{\mathrm{ds}} \cdot \boldsymbol{n}_{\mathrm{st}}}{|\boldsymbol{n}_{\mathrm{st}}|^2} \right) \hat{\boldsymbol{n}}_{\mathrm{st}}. \tag{2.6}$$

where in the last expression the second order term $\boldsymbol{n}_{\mathrm{ds}}(\boldsymbol{n}_{\mathrm{ds}} \cdot \boldsymbol{n}_{\mathrm{ds}})$ is neglected.

The expression (2.6) of the normal unit vector is now used to compute the normal component of the body displacement velocity as

$$\boldsymbol{v}_{\mathrm{B}} \cdot \hat{\boldsymbol{n}} = -\frac{\partial \boldsymbol{\sigma}}{\partial t} \cdot \left(\frac{\partial \boldsymbol{\sigma}}{\partial s} \times \hat{\boldsymbol{k}} \right) \simeq -\frac{\partial \boldsymbol{\sigma}_{\mathrm{ds}}}{\partial t} \cdot \hat{\boldsymbol{n}}, \tag{2.7}$$

where the velocity of the body is expressed in terms of the body displacement as $\boldsymbol{v}_{\mathrm{B}} = \partial \boldsymbol{\sigma}/\partial t = \partial \boldsymbol{\sigma}_{\mathrm{ds}}/\partial t$. By substituting (2.7) and the fluid velocity $\boldsymbol{V} = U_\infty\, \hat{\boldsymbol{\imath}} + \boldsymbol{\nabla}\varphi$, into the boundary condition (2.2) one obtains

$$\begin{aligned}\frac{1}{U_\infty}\frac{\partial\varphi}{\partial n} &= -\hat{\boldsymbol{n}}\cdot\hat{\boldsymbol{i}} + \frac{1}{U_\infty}\frac{\partial\boldsymbol{\sigma}_{\mathrm{ds}}}{\partial t}\cdot\hat{\boldsymbol{n}} \\ &= -\left[\frac{\boldsymbol{n}_{\mathrm{ds}}}{|\boldsymbol{n}_{\mathrm{st}}|} + \left(1 - \frac{\boldsymbol{n}_{\mathrm{ds}}\cdot\boldsymbol{n}_{\mathrm{st}}}{|\boldsymbol{n}_{\mathrm{st}}|^2}\right)\hat{\boldsymbol{n}}_{\mathrm{st}}\right]\cdot\hat{\boldsymbol{i}} + \frac{1}{U_\infty}\frac{\partial\boldsymbol{\sigma}_{\mathrm{ds}}}{\partial t}\cdot\hat{\boldsymbol{n}}_{\mathrm{st}} \\ &= \theta_{\mathrm{st}}(s) + \theta_{\mathrm{ge}}(s,t) + \theta_{\mathrm{ki}}(s,t), \end{aligned} \tag{2.8}$$

where the following definitions have been introduced

$$\theta_{\mathrm{st}}(s) = -\hat{\boldsymbol{n}}_{\mathrm{st}}\cdot\hat{\boldsymbol{i}}, \tag{2.9}$$

$$\theta_{\mathrm{ge}}(s,t) = -\left[\frac{\boldsymbol{n}_{\mathrm{ds}}}{|\boldsymbol{n}_{\mathrm{st}}|} - \frac{\boldsymbol{n}_{\mathrm{ds}}\cdot\boldsymbol{n}_{\mathrm{st}}}{|\boldsymbol{n}_{\mathrm{st}}|^2}\hat{\boldsymbol{n}}_{\mathrm{st}}\right]\cdot\hat{\boldsymbol{i}}, \tag{2.10}$$

$$\theta_{\mathrm{ki}}(s,t) = \frac{1}{U_\infty}\frac{\partial\boldsymbol{\sigma}_{\mathrm{ds}}}{\partial t}\cdot\hat{\boldsymbol{n}}_{\mathrm{st}} \tag{2.11}$$

The function θ_{st} is the local angle of attack at $t = 0$, θ_{ge} is the geometric angle of attack due to the airfoil displacement, and θ_{ki} is the kinematic angle of attack, resulting from the body velocity. Notice that θ_{st} is constant, whereas θ_{ge} and θ_{ki} depend on time.

If only plunge and pitch movement around the point $(x_0, 0)$ are considered, for small angles of rotation the displacement vector $\boldsymbol{\sigma}_{\mathrm{ds}}$ reads

$$\boldsymbol{\sigma}_{\mathrm{ds}} = \begin{Bmatrix}0\\1\end{Bmatrix} h(t) + \begin{Bmatrix}-\boldsymbol{\sigma}_{\mathrm{st}}^{(y)}\\ x - x_0\end{Bmatrix}\alpha(t), \tag{2.12}$$

where the superscript (y) indicates the y-component of a vector, $h = h(t)$ is the y displacement due to the plunge motion, $\alpha = \alpha(t)$ is the angle of attack. For small airfoil displacements, $s \sim x$ and one has

$$\frac{\partial\boldsymbol{\sigma}_{\mathrm{st}}}{\partial s} = \frac{\partial\boldsymbol{\sigma}_{\mathrm{st}}}{\partial x}\frac{\partial x}{\partial s} + \frac{\partial\boldsymbol{\sigma}_{\mathrm{st}}}{\partial y}\frac{\partial y}{\partial s} \simeq \frac{\partial\boldsymbol{\sigma}_{\mathrm{st}}}{\partial x}.$$

Moreover, according to the hypothesis of small perturbation that is usually valid for standard airfoils outside the nose area, one also has

$$\frac{\partial\boldsymbol{\sigma}_{\mathrm{ca}}^{(y)}}{\partial s} \ll 1,\ \frac{\partial\boldsymbol{\sigma}_{\mathrm{th}}^{(y)}}{\partial s} \ll 1 \quad \Rightarrow \quad \frac{\partial\boldsymbol{\sigma}_{\mathrm{st}}^{(x)}}{\partial x} \simeq 1,\ \frac{\partial\boldsymbol{\sigma}_{\mathrm{st}}^{(y)}}{\partial x} \ll 1.$$

Therefore, from definition (2.4), one immediately obtains

$$\boldsymbol{n}_{\mathrm{st}}(s) = \left\{\begin{matrix}-\dfrac{\partial\boldsymbol{\sigma}_{\mathrm{st}}^{(y)}}{\partial x}\\ 1\end{matrix}\right\},\quad |\boldsymbol{n}_{\mathrm{st}}| \simeq 1,\qquad \boldsymbol{n}_{\mathrm{ds}}(s,t) = \left\{\begin{matrix}1\\ -\dfrac{\partial\boldsymbol{\sigma}_{\mathrm{st}}^{(y)}}{\partial x}\end{matrix}\right\}\alpha(t),\quad |\boldsymbol{n}_{\mathrm{ds}}| \simeq \alpha(t) \tag{2.13}$$

By substituting the above expressions into (2.9) and (2.10), the sum of the initial and geometric angle of attack reads

$$\theta_{\mathrm{st}} + \theta_{\mathrm{ge}} = \frac{\partial\boldsymbol{\sigma}_{\mathrm{st}}^{(y)}}{\partial x} + \left[1 + \left(\frac{\partial\boldsymbol{\sigma}_{\mathrm{st}}^{(y)}}{\partial x}\right)^2\right]\alpha(t) \simeq \frac{\partial\boldsymbol{\sigma}_{\mathrm{st}}^{(y)}}{\partial x} + \alpha(t), \tag{2.14}$$

where only first-order terms have been retained. It is remarkable that, according to the small perturbation theory, the unsteady contribution to the sum of the initial and geometric angle of attack does not depend on the airfoil thickness. The linearised body velocity vector is

$$\frac{\partial\boldsymbol{\sigma}_{\mathrm{ds}}}{\partial t} = \begin{Bmatrix}0\\1\end{Bmatrix}\frac{\mathrm{d}\,h(t)}{\mathrm{d}\,t} + \begin{Bmatrix}-\boldsymbol{\sigma}_{\mathrm{st}}^{(y)}\\ x - x_0\end{Bmatrix}\frac{\mathrm{d}\,\alpha(t)}{\mathrm{d}\,t}, \tag{2.15}$$

and therefore the kinematic angle of attack reads

$$\theta_{\mathrm{ki}} = \frac{1}{U_\infty}\left[\frac{\mathrm{d}\,h(t)}{\mathrm{d}\,t} - (x-x_0)\frac{\mathrm{d}\,\alpha(t)}{\mathrm{d}\,t} + \boldsymbol{\sigma}_{\mathrm{st}}^{(y)}\frac{\partial \boldsymbol{\sigma}_{\mathrm{st}}^{(y)}}{\partial x}\frac{\mathrm{d}\,\alpha(t)}{\mathrm{d}\,t}\right]. \tag{2.16}$$

Therefore, under the small perturbation hypothesis, the boundary condition (2.2) can be written as

$$\frac{\partial \varphi}{\partial n} = U_\infty\frac{\partial \boldsymbol{\sigma}_{\mathrm{st}}^{(y)}}{\partial x} + U_\infty \alpha(t) + \frac{\mathrm{d}\,h(t)}{\mathrm{d}\,t} - (x-x_0)\frac{\mathrm{d}\,\alpha(t)}{\mathrm{d}\,t} + \boldsymbol{\sigma}_{\mathrm{st}}^{(y)}\frac{\partial \boldsymbol{\sigma}_{\mathrm{st}}^{(y)}}{\partial x}\frac{\mathrm{d}\,\alpha(t)}{\mathrm{d}\,t}. \tag{2.17}$$

The difference of the normal derivative of the potential between the upper and lower surface of the airfoil, namely,

$$\Delta\left(\frac{\partial \varphi}{\partial n}\right) = U_\infty\,\Delta\big[\theta_{\mathrm{st}}(s) + \theta_{\mathrm{ge}}(s,t) + \theta_{\mathrm{ki}}(s,t)\big]. \tag{2.18}$$

is now computed. By recalling that on the lower surface of the airfoil the boundary coordinates are given by $\boldsymbol{\sigma}^- = \boldsymbol{\sigma}_{\mathrm{ca}} - \boldsymbol{\sigma}_{\mathrm{th}} + \boldsymbol{\sigma}_{\mathrm{ds}}$, one immediately obtains

$$\tfrac{1}{2}\Delta\big[\theta_{\mathrm{st}}(s) + \theta_{\mathrm{ge}}(s,t)\big] = \frac{\partial \boldsymbol{\sigma}_{\mathrm{ca}}^{(y)}}{\partial x} + \alpha(t) \tag{2.19}$$

and the difference of the kinematic angle of attack is

$$\tfrac{1}{2}U_\infty \Delta\theta_{\mathrm{ds}}(s,t) = \frac{\mathrm{d}\,h(t)}{\mathrm{d}\,t} - (x-x_0)\frac{\mathrm{d}\,\alpha(t)}{\mathrm{d}\,t} + \boldsymbol{\sigma}_{\mathrm{th}}^{(y)}\left[\frac{\partial \boldsymbol{\sigma}_{\mathrm{ca}}^{(y)}}{\partial x} + \frac{\partial \boldsymbol{\sigma}_{\mathrm{th}}^{(y)}}{\partial x}\right]\frac{\mathrm{d}\,\alpha(t)}{\mathrm{d}\,t}. \tag{2.20}$$

In standard shape airfoil, one can usually assume

$$\frac{\partial \boldsymbol{\sigma}_{\mathrm{ca}}^{(y)}}{\partial x} \ll \frac{\partial \boldsymbol{\sigma}_{\mathrm{th}}^{(y)}}{\partial x} \tag{2.21}$$

and therefore, relation (2.18) simplifies to

$$\tfrac{1}{2}\Delta\left(\frac{\partial \varphi}{\partial n}\right) = U_\infty\frac{\partial \boldsymbol{\sigma}_{\mathrm{th}}^{(y)}}{\partial x} + U_\infty \alpha(t) + \frac{\mathrm{d}\,h(t)}{\mathrm{d}\,t} - (x-x_0)\frac{\mathrm{d}\,\alpha(t)}{\mathrm{d}\,t} + \boldsymbol{\sigma}_{\mathrm{th}}^{(y)}\frac{\partial \boldsymbol{\sigma}_{\mathrm{th}}^{(y)}}{\partial x}\frac{\mathrm{d}\,\alpha(t)}{\mathrm{d}\,t}. \tag{2.22}$$

By neglecting the thickness effects, namely, by assuming $\boldsymbol{\sigma}_{\mathrm{th}} \equiv \mathbf{0}$, Theodorsen [79] derived the well-known model for an oscillating flat plate reported in section 2.1.2, see also the textbook of Katz and Plotkin [74]. In deriving his model for the unsteady aerodynamic loads, McCroskey [69] computed the camber and thickness velocity contributions using the steady theory. Moreover, he took into account the steady non-linear velocity contributions close to the airfoil leading edge and neglected the unsteady contribution from the thickness. To the author knowledge, the last unsteady term in (2.17), which is identically zero for a flat plate, has been neglected in all analytical and semi-analytical solutions of the potential flow equations, though its presence is fully justified within the small perturbation theory.

Ultimately, under the assumption (2.21), the potential difference across the airfoil contains an unsteady term that is proportional to the airfoil thickness and to its first order spatial derivative, thus indicating that the airfoil thickness may produce a non-negligible contribution to the aerodynamic loads within the small perturbation theory. This contribution has been neglected in previous studies and it is the focus of the present analysis. It is remarkable that if the rotation center x_0 is close to the point of maximum airfoil thickness—as it is the case in most aerodynamic applications—the sign of $-(x-x_0)$ is equal to that of $\boldsymbol{\sigma}_{\mathrm{th}}^{(y)}\partial\boldsymbol{\sigma}_{\mathrm{th}}^{(y)}/\partial x$ and therefore the inclusion of the last term in (2.18) results in an increase of the module of the flat-plate contribution to the potential difference across the airfoil.

2.1.2 Theodorsen's model for oscillating airfoils

For later convenience, the main results of the Theodorsen's [59] solution for a flat-plate, i.e. $\boldsymbol{\sigma}_{\mathrm{ca}} \equiv \boldsymbol{\sigma}_{\mathrm{th}} \equiv \mathbf{0}$, subject to harmonic motions of airfoil plunge and pitch, is briefly recalled. In the model, both the airfoil and the wake are represented by a vortex sheet, with the shed wake extending as a planar surface from the trailing edge downstream to infinity, i.e. , $\boldsymbol{x}_{\mathrm{W}} = (s, \boldsymbol{x}_{\mathrm{TE}}^{(y)}), \forall s > \boldsymbol{x}_{\mathrm{TE}}^{(x)}, t > 0$.

The solution is given by Theodorsen in terms of the transfer function between the forcing movements (plunge h and pitch α) and the aerodynamic response (lift and pitching moment) at a given reduced frequency $k = \omega b/U$, with ω oscillation frequency and b the airfoil semi-chord, as

$$C_L(k) = \pi b \left[\frac{\ddot{h}}{U_\infty^2} + \frac{\dot{\alpha}}{U_\infty} - \frac{ba}{U_\infty^2}\ddot{\alpha}\right] + 2\pi C(k)\left[\frac{\dot{h}}{U_\infty} + \alpha + \frac{b}{U_\infty}\left(\frac{1}{2} - a\right)\dot{\alpha}\right], \tag{2.23}$$

for the lift coefficient C_L and

$$C_m(k) = -\frac{1}{2}\pi b \left[\frac{1}{2U_\infty^2}\ddot{h} + \frac{1}{U_\infty}\dot{\alpha} + \frac{b}{2U_\infty^2}\left(\frac{1}{4} - a\right)\ddot{\alpha}\right]. \tag{2.24}$$

for the moment coefficient C_m with the respect to the quarter-chord $c/4$ point. The parameter a is the position of the rotation center with respect to the mid-chord, made dimensionless with the semi-chord b.

The lift coefficient (2.23) is written as the sum of two terms. The first is the so-called non-circulatory part and corresponds to the added mass. It accounts for the pressure forces required to accelerate the fluid near the airfoil. The second term is called the circulatory part and it is multiplied by the complex Theodorsen's function $C(k) \in \mathbb{C}$.This term is in fact the sum of the quasi-steady lift:

$$C_{L_{\mathrm{qs}}} = 2\pi \left[\frac{\dot{h}}{U_\infty} + \alpha + \frac{b}{U_\infty}\left(\frac{1}{2} - a\right)\dot{\alpha}\right]$$

and the lift attenuation due to the shedding of vorticity into the wake that is equal to $(1 - C(k))C_{L_{\mathrm{qs}}}$. It is interesting to note that the moment coefficient with respect to $c/4$ does not depend on the circulatory part but only on the added mass effect. The complex function $C(k)$ is defined as

$$C(k) = \frac{H_1^{(2)}(k)}{H_1^{(2)}(k) + \mathrm{j}H_0^{(2)}(k)}, \tag{2.25}$$

where $H_1^{(2)}$ and $H_0^{(2)}$ are Hankel functions that involve Bessel's functions of the first and of the second kind, see the work of Theodorsen [59].

The C_L curve (2.23) as a function of the angle of attack α is shown in figure 2.1 for three values of the reduced frequency k, namely, 0.1, 0.3 and 0.5, against their steady state counterpart, i.e. $C(k) = 1$, $k = \omega = 0$. The curve in figure 2.1 is drawn by recalling that the real part of $C_L(k)$ represents the portion of the harmonic load that oscillates in phase with the input, while the imaginary part represents the one that is in quadrature (i.e. 90 deg. delay). As it is well known, an hysteresis cycle is observed, together with a reduction of the maximum value of the lift coefficient with increasing reduced frequencies. Figure 2.1 also shows that, for low reduced frequency values, the orientation of the cycle is counter-clockwise, while for higher frequencies it is clockwise. This effect can be noticed more clearly by considering the diagrams of the magnitude and the phase of the lift coefficient of equation (2.23), shown in figures 2.2(a) and 2.2(b). Notice that in the present work the magnitude of the lift and of the moment coefficients are always computed and represented as the corresponding transfer function, unless otherwise specified. That is, these quantities are scaled with respect to the amplitude of the input motion law, of course in the frequency

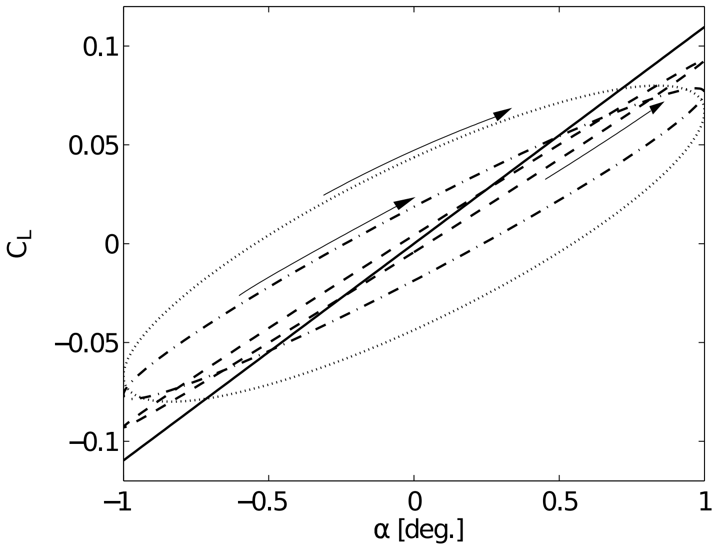

Figure 2.1: Lift coefficient curve due to a pitch oscillation for the steady case (solid line) and the unsteady case at three different reduced frequencies: $k = 0.1$ dashed line, counter-clockwise; $k = 0.3$ dot-dashed line, clockwise; $k = 0.5$ dotted line, clockwise

.

domain. Since the imposed motion is always a sinusoidal law, such scaling factor is directly the oscillation amplitude. Therefore, at $k = 0$, the module of the lift coefficient is expected to be equal to the slope of the C_L-α curve which, for a steady flat plate, is 2π. Figure 2.2(a) clearly shows that 2π is indeed the value of the lift magnitude at $k = 0$. At low reduced frequency the lift is rotating counter-clockwise (phase negative) due to the dominant action of the circulatory contribution. Instead, for higher reduced frequencies, the dominant apparent mass contribution, proportional to the airfoil acceleration, causes the anticipation (phase positive) of the lift. In particular, the phase curve, figure 2.2(b), shows a change of slope followed by a point where the phase curve crosses the zero value at $k = 0.144$, which is referred to in the following as the *phase inversion* point. In this situation the amplitude of the hysteresis cycle is null. For larger values of k, the cycle orientation is clockwise.

By taking the above Theodorsen's result as the baseline, the effects of a non-zero airfoil thickness on the aerodynamic loads are assessed in the following for pitching movement only. A similar behavior, to be eventually characterized in a future work, is expected for plunge motions. To avoid the analytical or semi-analytical solution of the potential equation (2.1) with the boundary conditions (2.17), a finite volume CFD solver based on RANS/Euler's equation models is used to compute the aerodynamic loads, without introducing any significant undue simplification when compared to a wind tunnel test campaign.

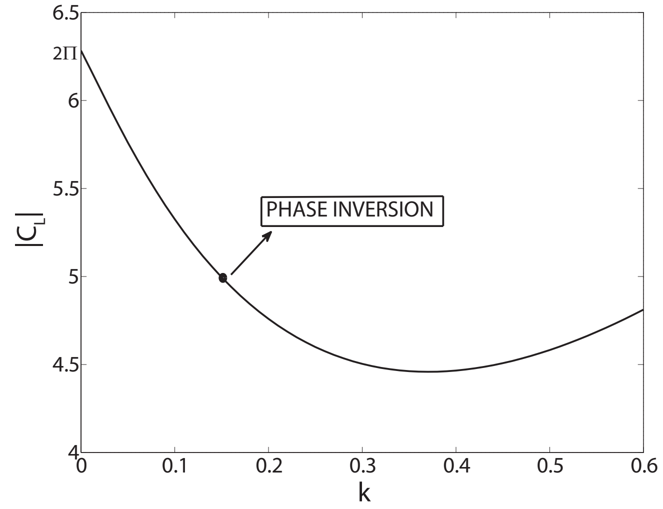

(a) Magnitude

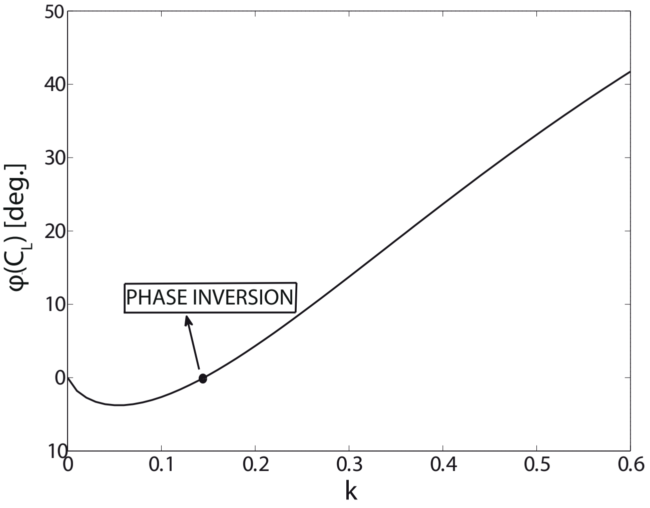

(b) Phase

Figure 2.2: Lift coefficient at various reduced frequencies for a pitch oscillation of amplitude equal to one degree.

2.2 Numerical simulation of oscillating airfoils

Numerical simulations for unsteady oscillations of a pitching airfoil are carried out using the ROSITA flow solver, see the work of Biava [80], a finite volume Euler/RANS solver for moving, overset, multi-block grids. The equations of motion are discretized in space by means of a cell-centered finite-volume implementation of either the Roe's scheme or the Jameson's one, with scalar and matricial numerical viscosity. Second order accuracy in space in smooth flow regions is obtained by Monotonic Upstream-Centered Scheme for Conservation Laws (MUSCL) extrapolation [81, 82], using the modified version of the Van Albada limiter introduced by Venkatakrishnan [83]. The viscous terms are computed by applying the Gauss theorem and using a centered approximation scheme. The time integration is carried out with a dual-time formulation, employing a second order backward differentiation formula (BDF) to approximate the time derivative and a fully unfactored implicit scheme in the pseudo-time. The generalized conjugate gradient (GCG), in conjunction with a block incomplete lower-upper preconditioner, is used to solve the resulting linear system. Details of the implementation can be found in the works of Biava [80, 84, 85].

Unsteady computations are performed to simulate the behavior of a symmetrical airfoil pitching around its $c/4$ point, approximately the aerodynamic center of the airfoil. The general form of the harmonic law used in this case is

$$\alpha = \alpha_0 + \alpha_m \sin(\omega t), \tag{2.26}$$

where α_0 is the mean angle, α_m is the maximum magnitude of the oscillation and ω is the circulatory frequency. To assess the reliability of the ROSITA unsteady solutions, a comparison with the Theodorsen's model, as well as with numerical and experimental data, is performed.

Figure 2.4(a) reports the lift hysteresis curves obtained by for the NACA 0012 at $k = 0.4$, $\mathrm{M} = 0.1$, $\mathrm{Re} = 10^6$, $\alpha_0 = 0$ deg. and $\alpha_m = 6.7$ degrees. The experimental results for this case were provided by Halfman [86], and were then used as a benchmark for numerical computations by Jameson [87]. Additionally viscous and inviscid fluid simulations are carried out with the ROSITA solver for comparison. The viscous fluid simulation requires a finer grid (a $[400 + 80] \times 70$ C-type structured mesh, with 400 elements over the airfoil, 80 elements along the wake and 70 elements in the normal directions), accounting for the boundary layer. With this regard the Spalart-Allmaras [88] turbulence model is used to represent the Reynolds stress tensor of the RANS. For inviscid computations it is possible to use a coarser grid (a $[300+60]\times 40$ C-type structured mesh), hence reducing significantly the computational burden. The viscous results show a somewhat higher error, probably due to the still insufficient grid refinement. Since here the primary interest is investigating a phenomenon where viscosity is expected to have a limited impact, the inviscid set of equation is chosen, to reduce the computational costs. Additionally, for the attached flow conditions herein considered, the viscosity is expected to have effects which are overall equivalent to an increase of the airfoil thickness. This further addresses toward performing inviscid computations, being indeed the specific purpose of this chapter the evaluation of thickness effects on the unsteady airloads. Figure 2.3 represents the computational grid adopted for the present inviscid computations, on the NACA 0012 airfoil. Similar grids are realized for the other airfoils herein considered. The grid has extension of 20 chords far from the body. Refinements are realized in the wake region, which significantly affects the unsteady loads, object of the present study, as well as close to the solid body, to enhance the accuracy of the numerical results.

In figure 2.4(b) the Theodorsen's model shows low accuracy in terms of the hysteresis amplitude. The model of McCroskey [69], including a steady-state correction for thickness effects, does not show significant improvements over the Theodorsen's model in reproducing the experimental results of Halfman [86].

The difference of the pressure coefficient between the upper and lower side of the airfoil is computed for the same test case. Figure 2.5 compares the results obtained by means of ROSITA with those obtained by using the formulation of Küssner and Schwarz

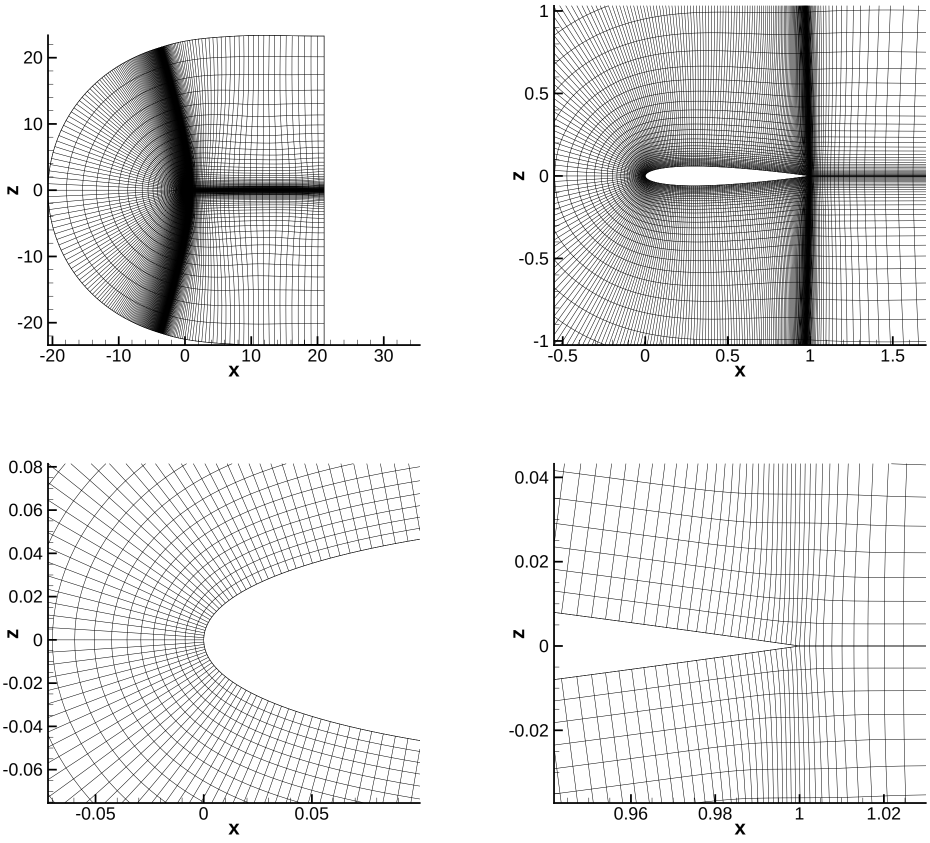

Figure 2.3: Computational grid realized for the inviscid computations around the NACA 0012 airfoil. Both the overall computational domain and details of the wake and the near body regions are shown.

[43], which provides the local load distributions within the Theodorsen approach, and the formulation presented by McCroskey [69], that includes the thickness effects in the reference flow. Significant differences of the thin-airfoil solutions with respect to the CFD are visible not only in the nose area, where these discrepancies are expected due to the flat-plate approximation, but also in the central part of the airfoil. In particular, both models over-estimate the magnitude of aerodynamic forces, as it is apparent from the instantaneous load distribution at $\alpha = 0$ deg. in the upstroke phase (figure 2.5(a)) and at $\alpha = -4.14$ deg. in the downstroke phase (figure 2.5(b)). Figure 2.6 reports the pressure coefficient difference in the frequency domain. Whereas for the real part (figure 2.6(a)) a fairly good agreement is found, with differences being limited to the nose region, the McCroskey model fails to capture the in-quadrature component (figure 2.6(b)).

Overall results in figures 2.4, 2.5 and 2.6 highlight that both the Küssner and the McCroskey models fail to accurately predict the aerodynamic loads for airfoils of finite thickness, in terms of local distributions and integral forces. As a consequence, only the CFD code ROSITA is used in the following to quantify the thickness contribution, avoiding the employment of the McCroskey model.

A second numerical test at a higher Mach number is considered. The conditions are: $k = 0.0814$, $\mathrm{M} = 0.755$, $\alpha_0 = 0.016$ deg. $\alpha_m = 2.51$ degrees. These test conditions were taken as benchmark in the work by Venkatakrishnan & Mavriplis [83] and are extracted from the report VV. AA. (1982) [89]. Figure 2.7 shows a good overlapping between the ROSITA computations and the numerical simulations of Venkatakrishnan & Mavriplis

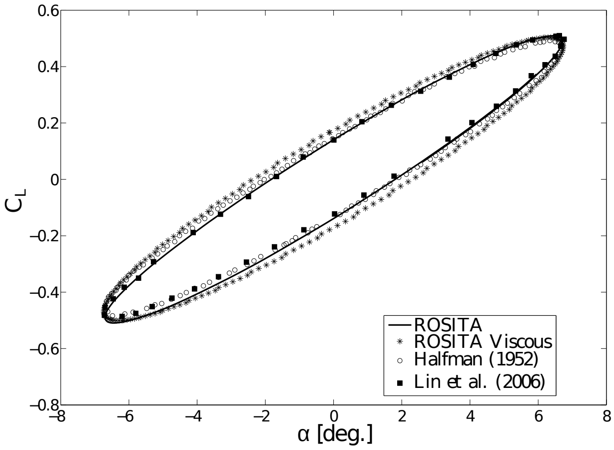

(a) Comparison with the experiments of Halfman [86] and with the numerical computations of Lin et al. [87]

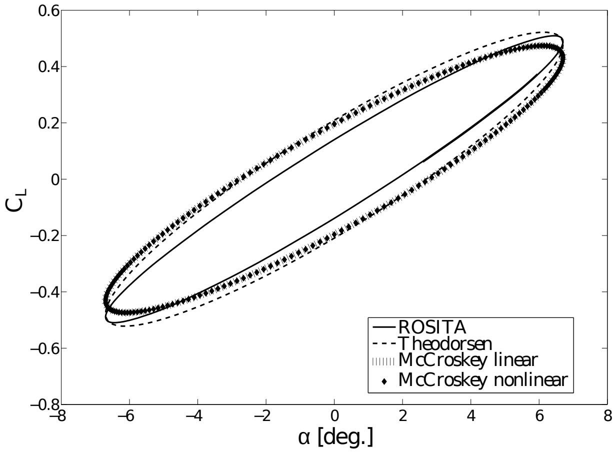

(b) Comparison with the analytical models of Theodorsen [79] and McCroskey [69]

Figure 2.4: Lift coefficient history for the NACA 0012 airfoil with $k = 0.4$, $\mathrm{M} = 0.1$, $\mathrm{Re} = 10^6$, $\alpha_0 = 0$ deg. and $\alpha_m = 6.7$ deg.

[83]. However, the accuracy with respect to the experimental data is poorer, probably due to an offset in the mean angle of attack.

The dependence of the numerical results on both the grid spacing Δx and the time step Δt is assessed for different reduced frequencies. Simulations are performed at all the possible combinations of the parameters reported in Table 2.1 and oscillation law $\alpha = \sin(\omega t)$ degrees. Figure 2.8 shows the C_L amplitude and phase for the points listed in the test matrix computed for the NACA 0004 airfoil together with the Theodorsen's model curves. The solid line is the baseline solution computed over a $[300+60]\times 40$ C-type structured mesh with 200 time steps for each period. The NACA 0004 is chosen due to the very low thickness (4%), which resembles the Theodorsen's flat-plate model. Each marker in figure 2.8 represents a simulation point. At low reduced frequency values, the simulations results are more scattered, thus indicating a strong grid/time step dependence that is not observed at higher reduced frequencies. This is not surprising since for $k \to 0$ one should have $\Delta x, \Delta t \to 0$. Numerical results are deemed to be satisfactory for the purposes of the present investigation, since they accurately reproduce the flat plate results at the frequencies of interest. The accuracy of the numerical simulations is confirmed by

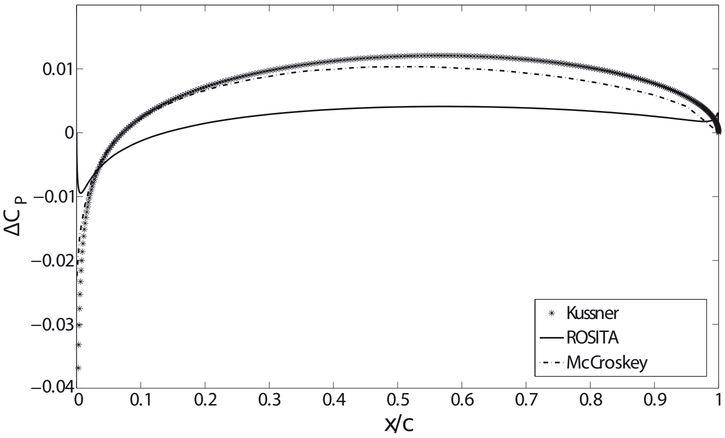

(a) Upstroke, $\alpha = 0$ deg.

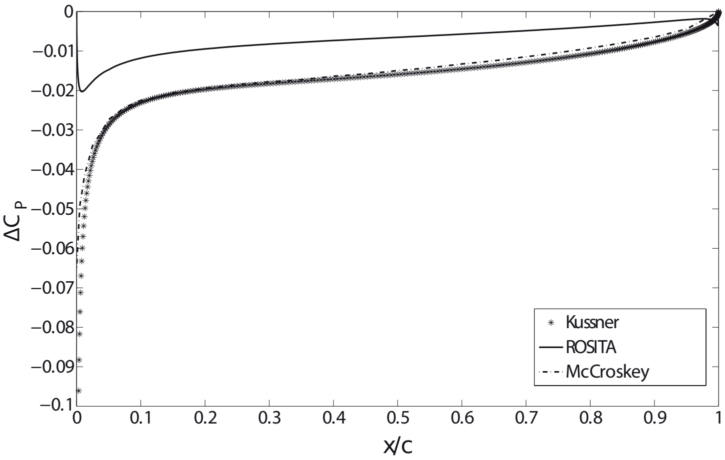

(b) Downstroke, $\alpha = -4.14$ deg.

Figure 2.5: Difference of the pressure coefficient magnitude between the upper and lower side of the airfoil for the NACA 0012 airfoil with $k = 0.4$, $\mathrm{M} = 0.1$, $\mathrm{Re} = 10^6$, $\alpha_0 = 0$ deg. and $\alpha_m = 6.7$ degrees. Distributions in the upstroke phase and at $\alpha = 0$ deg. (a) and in the downstroke phase at $\alpha = -4.14$ deg. (b).

the C_L hysteresis curve shown in figure 2.9, which is almost independent from the grid spacing and from the time step.

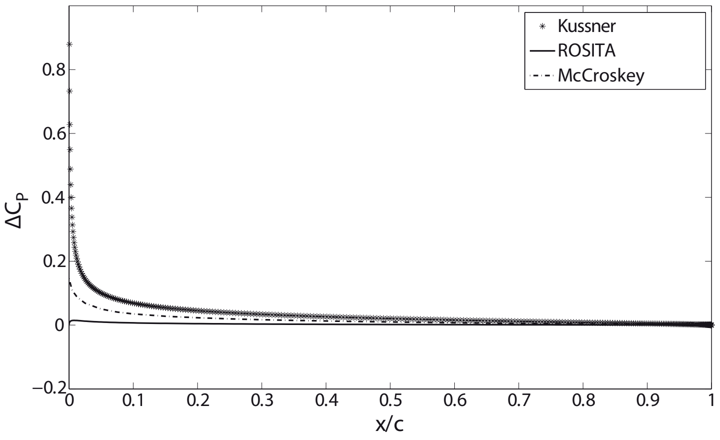

(a) Real part

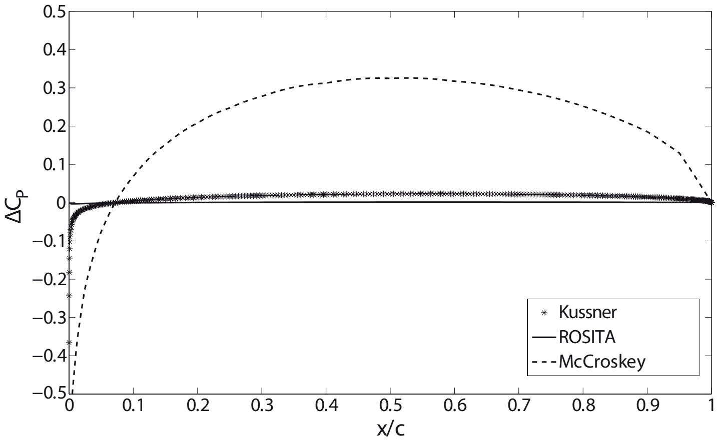

(b) Imaginary part

Figure 2.6: Difference of pressure coefficient between the upper and lower side of the airfoil for the NACA 0012 airfoil with $k = 0.4$, $\mathrm{M} = 0.1$, $\mathrm{Re} = 10^6$, $\alpha_0 = 0$ deg. and $\alpha_m = 6.7$ deg. in the frequency domain: real (a) and imaginary (b) parts.

C-type grids:	$[212 + 40] \times 28$, $[300 + 60] \times 40$, $[424 + 80] \times 56$
Time steps per period:	100, 200, 400
Reduced frequency k:	0.025, 0.01, 0.1

Table 2.1: Test matrix used to study the numerical convergence of the solution. All the twentyseven combinations of the parameters were considered in the simulations reported in figure 2.8.

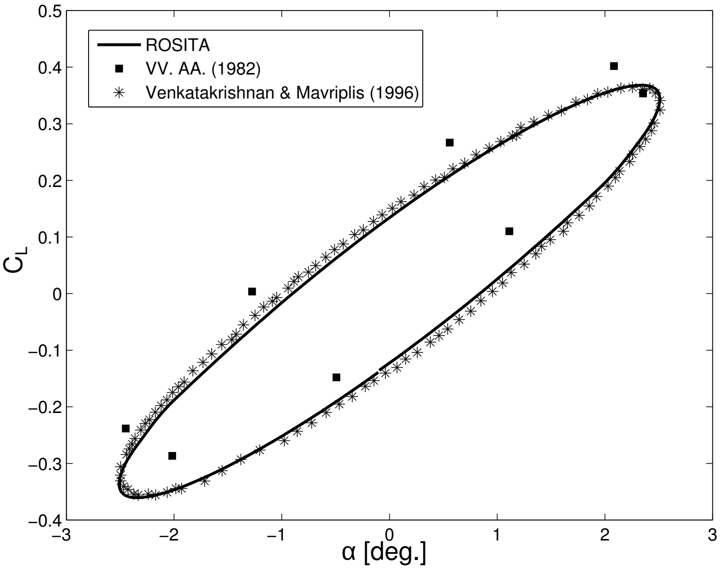

Figure 2.7: Lift coefficient history for the NACA 0012 airfoil with $k = 0.0814$, $\mathrm{M} = 0.755$, $\alpha_0 = 0.016$ deg., $\alpha_m = 2.51$ degrees Comparison with data of Refs. [89] and [83].

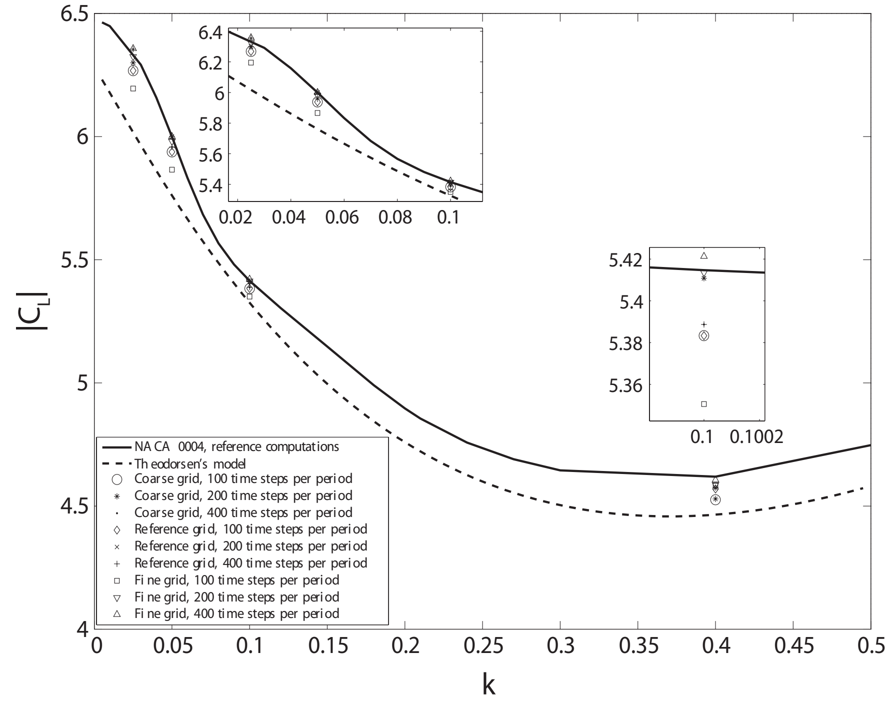

(a) Amplitude

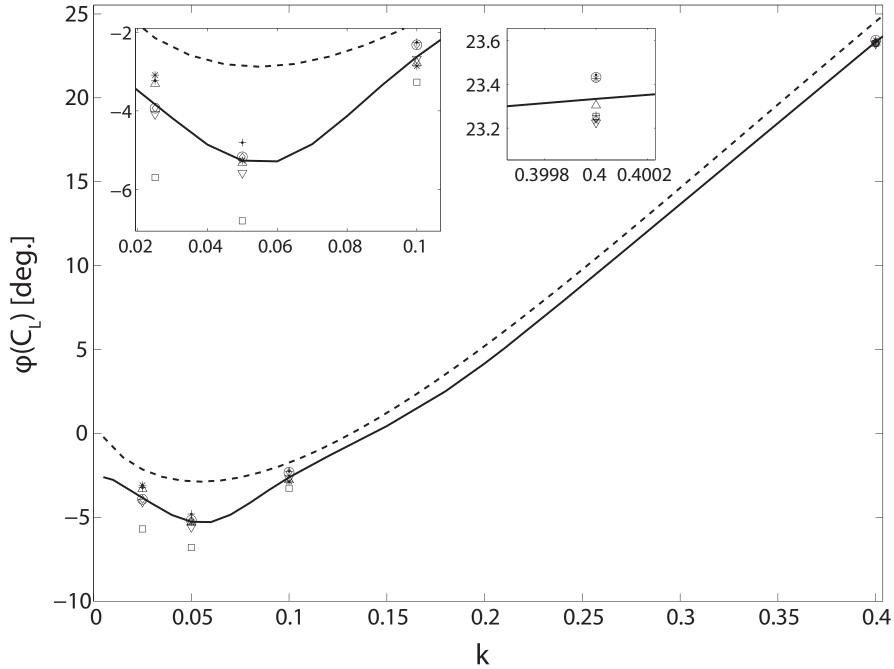

(b) Phase

Figure 2.8: Amplitude and phase of the C_L transfer function for the NACA 0004 airfoil (—) against the prediction from the Theodorsen model (- - -), $\alpha = \sin(\omega t)$ degrees. The markers correspond to results obtained for the different grid resolutions and time steps per period listed in Table 2.1.

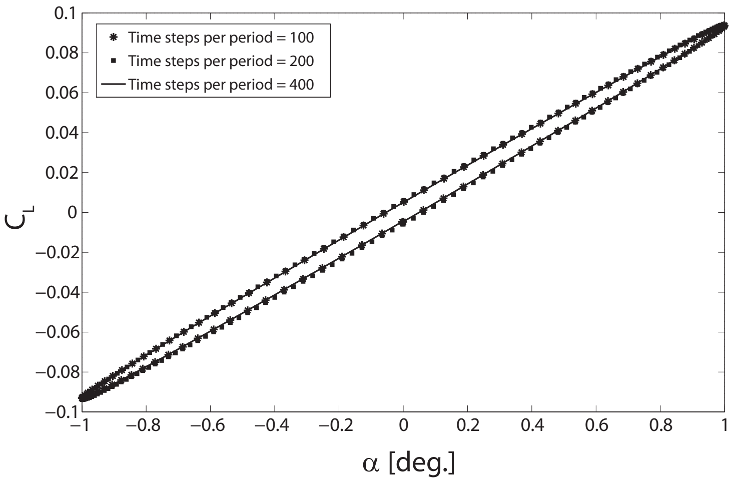

(a) Time convergence

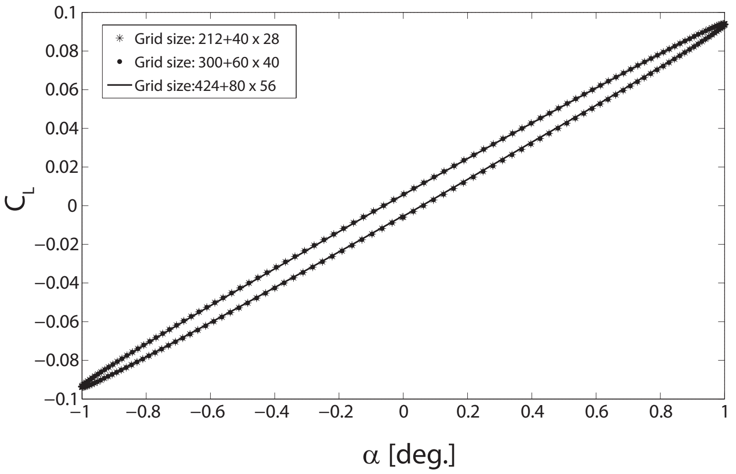

(b) Space convergence

Figure 2.9: Convergence of the numerical solution in the time domain for the NACA 0004 airfoil, $k = 0.1$, $\alpha = \sin(\omega t)$ degrees.

2.3 Aerodynamic loads for zero and finite thickness sections oscillating in pitch

To investigate numerically the unsteady effects of the airfoil thickness on the developed airloads, unsteady inviscid simulations are carried out on four symmetrical sections, namely the NACA 0004, the NACA 0012, the NACA 0018 and the NACA 0024 airfoil, each at several reduced frequencies. Therefore, the maximum thickness ranges from 4% to 24% of the airfoil chord. Values of k between 0.01 and 0.75 are used in the input motion laws. The Mach number is M = 0.117, which corresponds to an almost incompressible flow. The mean angle of attack is $\alpha_0 = 0$ degrees, whereas the oscillation amplitude is $\alpha_m = 1.0$ degree. In the following the results of few tests are discussed to expose the modification of unsteady loads induced by the airfoil thickness.

The results obtained at a reduced frequency below the phase inversion point namely at $k = 0.1$, are shown in figure 2.10. The hysteresis curve of the NACA 0004 is almost indistinguishable from those computed using the Theodorsen's method. By increasing the airfoil thickness, the amplitude of the hysteresis cycle is found to grow. The opposite behavior is experienced for reduced frequencies above the phase inversion point, namely at $k = 0.5$, as shown in figure 2.11. In this case the increase of thickness causes a reduction of the amplitude of the counter-clockwise hysteresis cycles. Notice that several analyses are performed by doubling the amplitude of the pitch motion from 1 deg. to 2 deg. A linear dependence of the lift coefficient is observed, thus empirically confirming the problem linearity, as shown in appendix A.

The aerodynamic behavior of thick airfoils can be explained by recalling equation (2.22), where the airfoil thickness is found to enhance the unsteady contribution of the flat-plate model. During the down-stroke phase $\frac{d\alpha}{dt} > 0$, i.e. on the airfoil reference system there is an increment of the induced angle of attack. The last two terms of equation (2.22), featuring the same sign, are positive and therefore increase the potential difference between the upper and the lower surface. Being the last term of equation (2.22) proportional to the airfoil thickness, it results that, for thicker sections, there is a larger increase of the difference of potential and, in turn, of the lift developed. This in indeed consistent with the behavior exhibited by the hysteresis loops in figures 2.10 and 2.11.

At the maximum and minimum angles of attack ($\alpha = \pm 1$ deg.), where $d\alpha/dt = 0$ and the thickness-related term in (2.17) is zero, figure 2.12 shows that the overall effect of thickness is almost null. This indicates that the main effect of thickness is due to the kinematic angle of attack and not to the geometric angle of attack. Additionally, the above suggeststhat the main effect is related to the circulatory part of the lift rather than to the added mass, which is proportional to the airfoil acceleration. Therefore, the variation in the angle of attack is a local instantaneous effect and the velocity difference across the upper and lower boundary, instantaneously results in a pressure difference.

For the upstroke the situation is opposite. Namely in the reference frame of the airfoil $\frac{d\alpha}{dt} < 0$. As a result the last two terms of equation (2.22) are negative and therefore decrease the difference of potential between the upper and the lower side. Being the last term of equation (2.22) proportional to the airfoil thickness, it results that, for thicker sections, a larger decrease in the potential difference is encountered. As a consequence, during the upstroke, the lift developed by thick airfoils is lower with respect to that generated by a flat plate. This is again consistent with the behavior exhibited by the curves in figures 2.10 and 2.11.

Figure 2.13 shows the pressure coefficient C_p on the NACA 0024 airfoil and the flat-plate model at different angles of attack along one oscillation cycle for a reduced frequency of $k = 0.5$, above the phase inversion condition. The C_p for the flat-plate are computed using the model developed by Küssner and Schwarz [43]. In particular, differences between the flat-plate model and the thick airfoil C_p distribution are always observed in the leading edge area, where ,as expected, the flat-plate approximation is not accurate, see also the work of Barger [67]. However, significant differences in the C_p distribution on the upper and lower side are clearly visible when $\alpha = 0$ (upstroke and down-stroke), i.e. when the

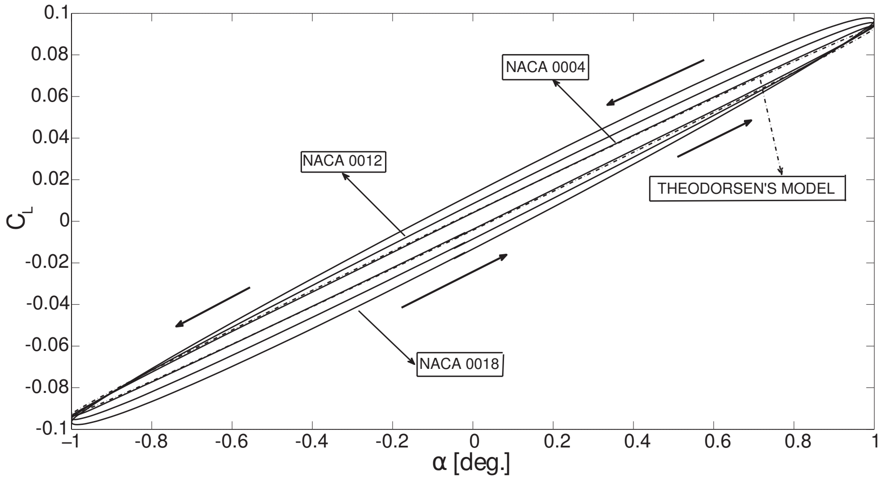

Figure 2.10: Lift coefficient hysteresis curve below the phase inversion point, $k = 0.1$.

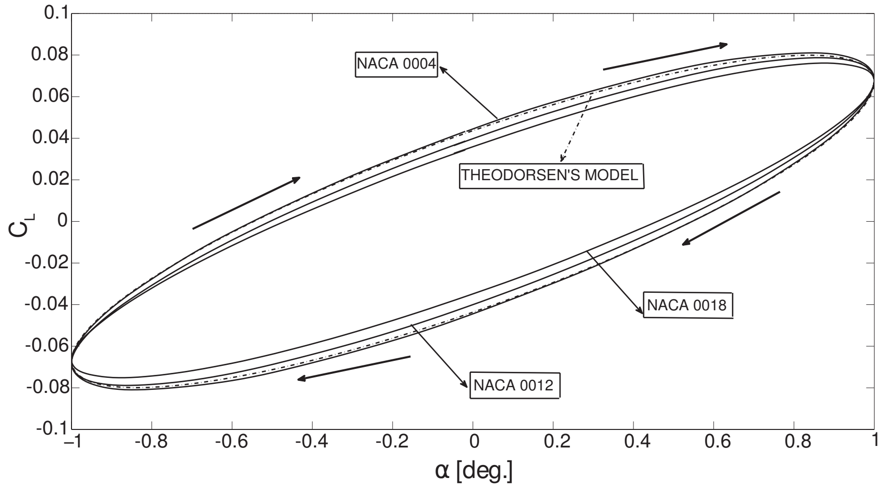

Figure 2.11: Lift coefficient hysteresis curve above the phase inversion point, $k = 0.5$.

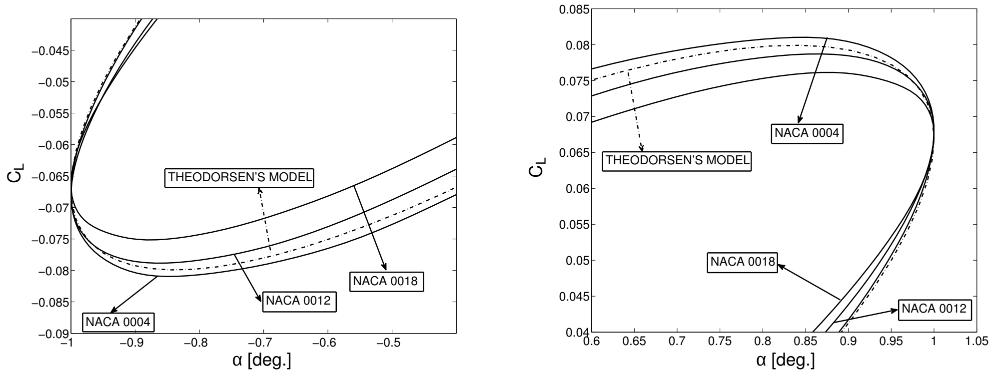

(a) Minimum

(b) Maximum

Figure 2.12: Lift coefficient hysteresis curve nearby the minimum (a) and the maximum (b) angle of attack, $k = 0.5$.

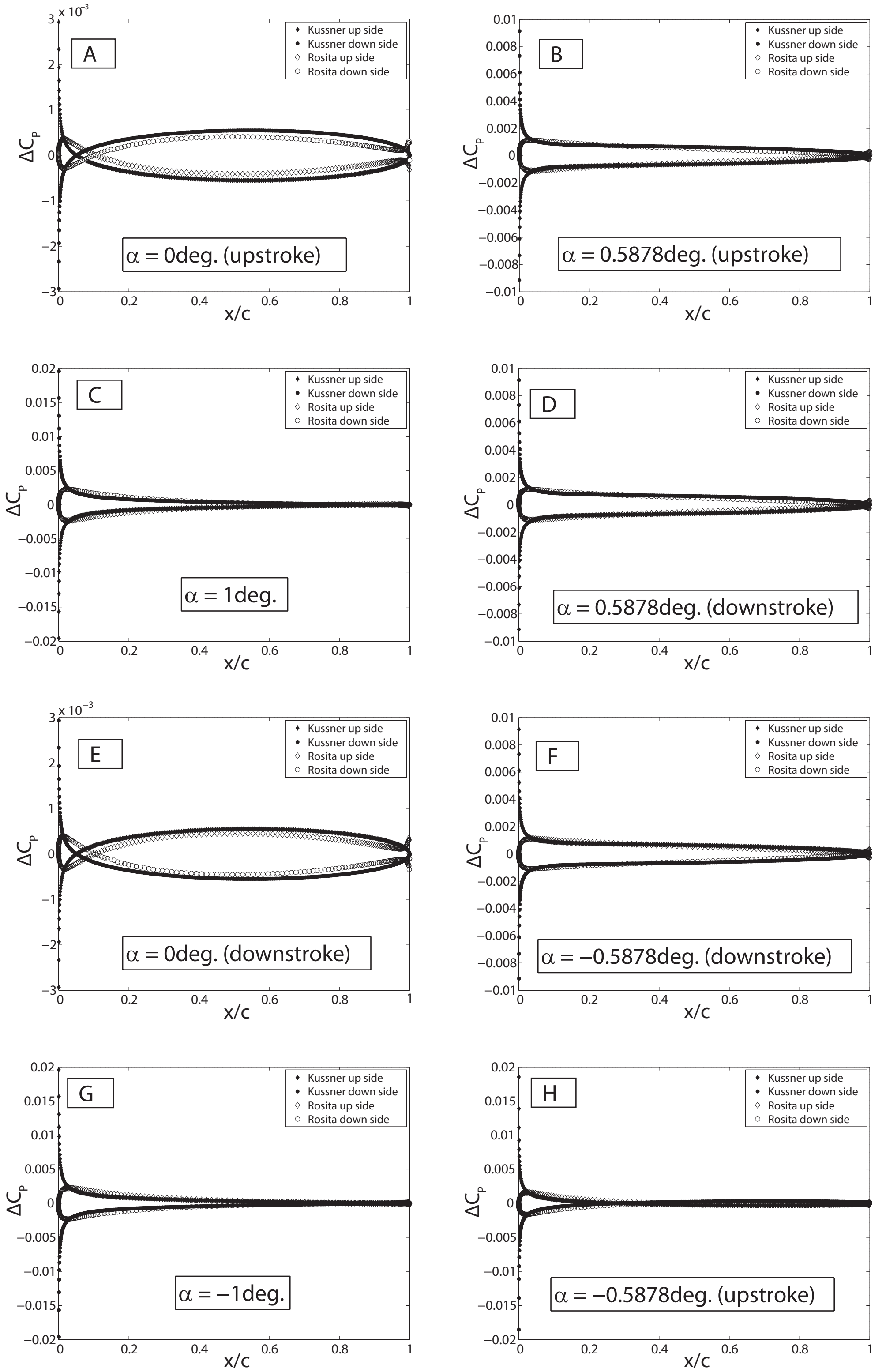

Figure 2.13: Pressure coefficient distribution along the hysteresis curve. Comparison of the Küssner solution for the flat-plate with the numerical results obtained on the NACA 0024 airfoil.

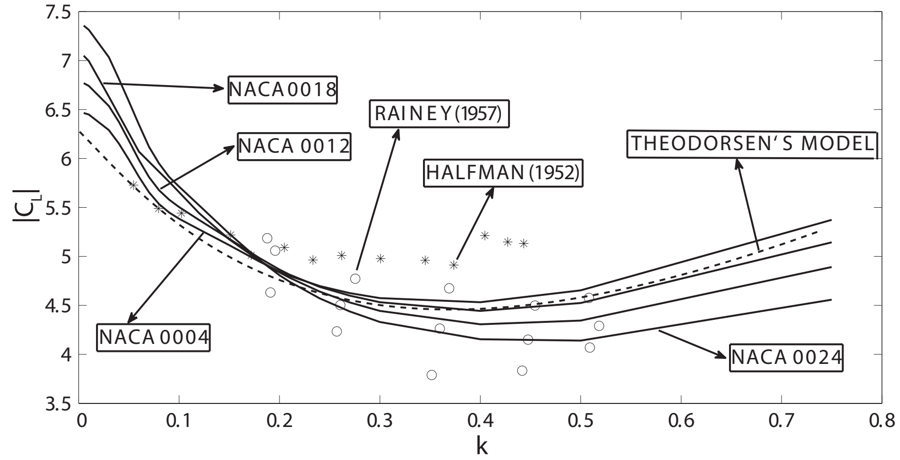

Figure 2.14: Numerical lift coefficient magnitude versus k compared to the Theodorsen's model and to the experimental data by Halfman [86] and Rainey [90].

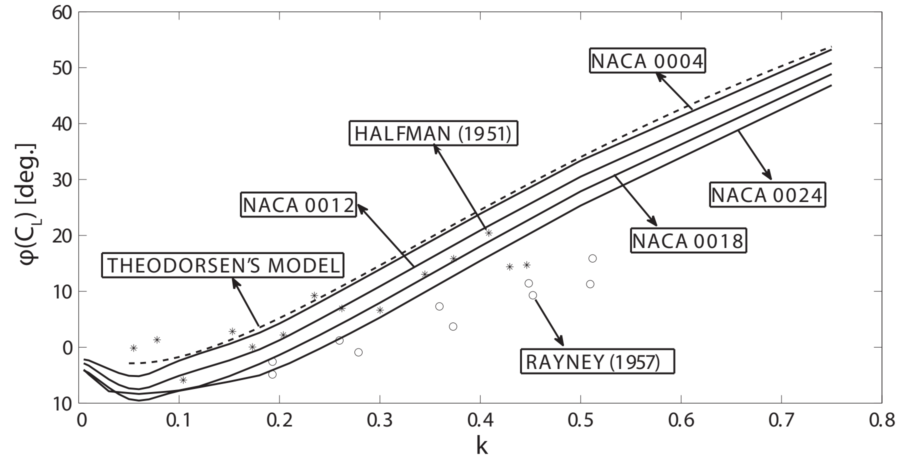

Figure 2.15: Numerical lift phase angle versus k compared to the Theodorsen's model and to the experimental data by Halfman [86] and Rainey [90].

angular velocity is maximum, while at $\alpha = \pm 1$ deg. the difference are limited to the nose area. The discrepancies at the trailing edge are related to the fact that, differently from the method of Küssner and Schwarz [43] where the Kutta condition is explicitly imposed, in the CFD solver the fulfilment of the Kutta conditions, both steady and unsteady, is indirectly obtained by the introduction of the artificial viscosity in the inviscid flow equations.

Figures 2.14 and 2.15 show the effects of the thickness in terms of the amplitude and the phase of the lift coefficient transfer function. Both the amplitude and the phase retain a qualitative dependence on the reduced frequency which is similar to the flat-plate case, cd. figures 2.2(a) and 2.2(b). However, the amplitude increases at small k by increasing the thickness and decreases at large reduced frequency, while the phase curves shift to the right, moving the phase inversion point to higher values of k as the thickness is increased. This behavior is in accordance with the previous remarks on the lift coefficient hysteresis curve. Indeed, because of the amplification of the lift coefficient hysteresis due to thickness, the phase inversion is observed at larger k.

By recalling that the lift magnitude is normalized with respect to that of the input motion, see figure 2.2(a), the module depicted in figure 2.14 evaluated at $k = 0$, is equal to

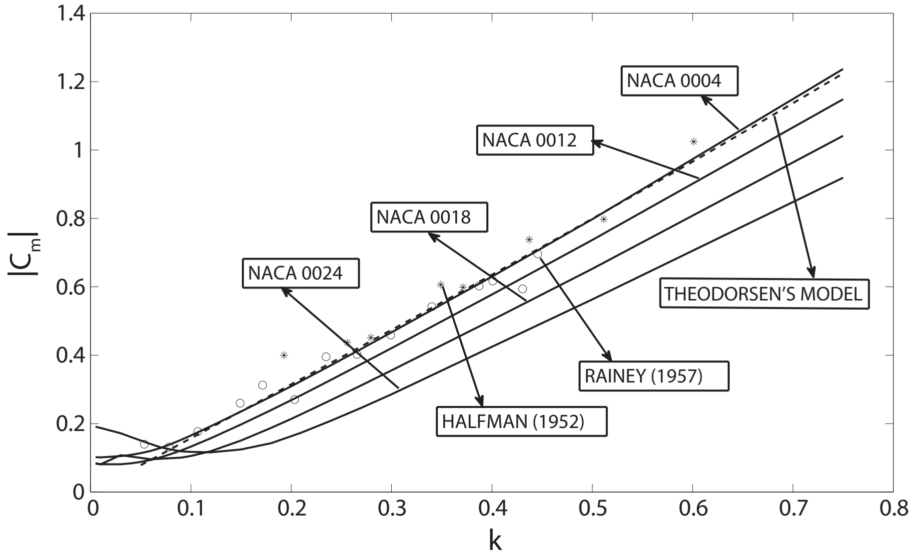

Figure 2.16: Moment coefficient magnitude versus k compared to the Theodorsen's model and to experimental data.

the slope of the steady C_L-α curve. Moreover, according to the flat plate model, such value is 2π. For airfoils of larger thickness an increase in the value of the lift magnitude at $k = 0$ is observed. This is in agreement with the classical steady state aerodynamics of thick Joukowsky airfoils, where the lift coefficient slope follows the law $C_{L_\alpha} = 2\pi(1 + 0.77t/c)$, with t the maximum airfoil thickness, see for instance the textbook of Currie [91], chapter 4. This correction is valid for small pertubations so that $\sin\alpha \sim \alpha$.

The amplitude and the phase of the moment coefficient transfer function are shown in figures 2.16 and 2.17, together with the results from Theodorsen's theory. Notice that in the present chapter the moment coefficient is always computed with respect to the aerodynamic center, which for a flat plate is located at $c/4$. In this case the disagreement with respect to the Theodorsen's model can be explained by the fact that the aerodynamic center location is not at $c/4$ (a well known fact already suggested by Leishman[66] in his textbook, pp.437-438). As a consequence, the circulatory part of the lift has an influence on the moment, showing a dependency of this quantity on the airfoil thickness as well.

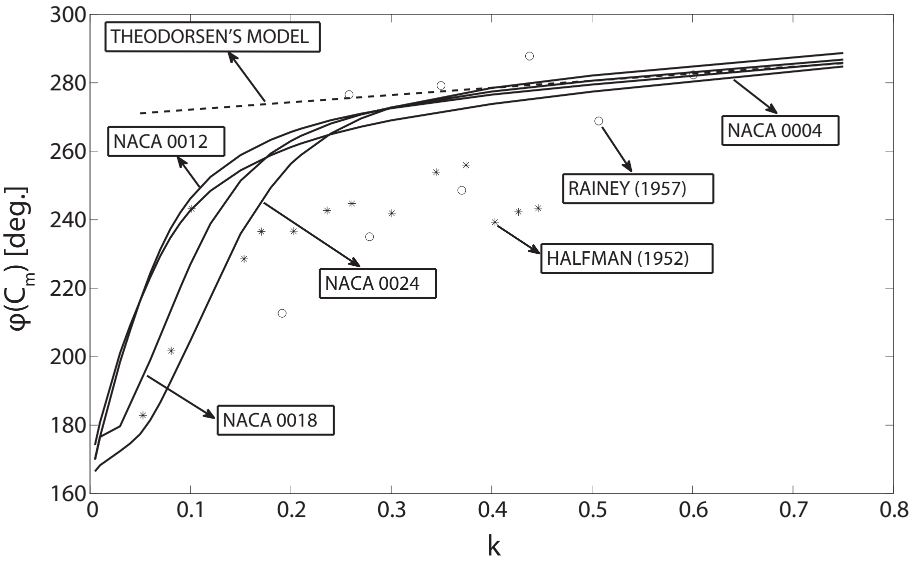

Figure 2.17: Moment coefficient phase angle versus k compared to the Theodorsen's model and to experimental data.

2.4 Modified Theodorsen's model for thick airfoils

The numerical experiments conducted exploiting the capabilities of the CFD indicate that the thick airfoils behave similarly to the flat-plate Theodorsen's model. In fact, even though the values of the specific points related to each thick airfoil in figures 2.14–2.17 are different, the trends of the lift and moment with respect to k are quite similar and there is not a radical change of behavior with respect to the flat-plate model. However, the curves in the figures 2.14–2.17 show clearly that the larger is the thickness the greater is the difference with respect to the flat-plate model. Additionally, looking at the results presented in figure 2.12, it is possible to infer that, by modifying the airfoil thickness, it is mainly the input-output relationship that changes and not the states of the aerodynamic unsteady phenomenon herein investigated.

Using these hints it is possible to set up a single baseline analytical model that may be a good candidate to fit all the results of the numerical simulations obtained for the thick airfoils analyzed in the previous sections. In particular, it can be assumed that the Theodorsen's function $C(k)$, equation(2.25), does not change for thick airfoils. On the other hand, to change the input-output relationship all of the coefficients related to the pitch kinematics in equations(2.23) and (2.24) should be modified, using scaling factors which are not dependent on the reduced frequency but only on the airfoil thickness.

Under these assumptions, the lift and moment frequency response functions, due to pitch movements of thick airfoils, may be modeled by the following modified Theodorsen's expression:

$$\begin{aligned} C_L(k, s_m) &= \pi b \left[P_1^L(s_m) \frac{\dot{\alpha}}{U} - P_2^L(s_m) \frac{ba\ddot{\alpha}}{U^2} \right] + \\ & \quad +2\pi C(k) \left[P_3^L(s_m)\alpha + P_4^L(s_m) b \left(\frac{1}{2} - a \right) \frac{\dot{\alpha}}{U} \right], \qquad (2.27) \\ C_m(k, s_m) &= -\frac{1}{2}\pi b \left[P_1^m(s_m) \frac{1}{U}\dot{\alpha} + P_2^m(s_m) \frac{b}{2U^2} \left(\frac{1}{4} - a \right) \ddot{\alpha} \right], \qquad (2.28) \end{aligned}$$

where s_m is used as a parameter to identify the airfoil thickness. The parameters P_1^L and P_2^L and P_1^m and P_2^m, that depend from the airfoil thickness, are used to fit the added mass

Table 2.2: Fitted coefficients for the modified Theodorsen's formula (2.27) and (2.28) of the lift and moment coefficients of thick airfoils, respectively.

max thickness %	P_1^L	P_2^L	P_3^L	P_4^L	P_1^m	P_2^m
4	0.9659	1.0687	1.0111	1.0627	1.0194	0.8932
12	1.2449	0.9045	1.0393	0.7001	0.9416	0.8934
18	1.6232	0.7431	1.0623	0.2536	0.8502	0.8596
24	1.7637	0.6671	1.0567	-0.902e-2	0.7427	0.8476

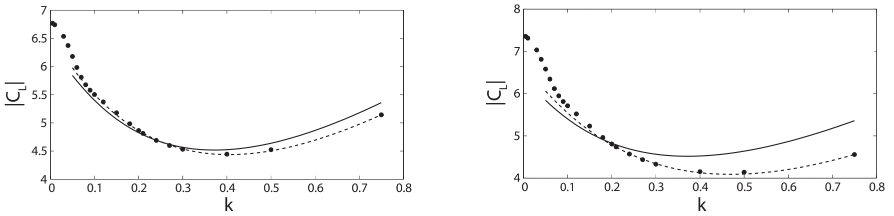

(a) NACA 0012, lift coefficient magnitude (b) NACA 0024, lift coefficient magnitude

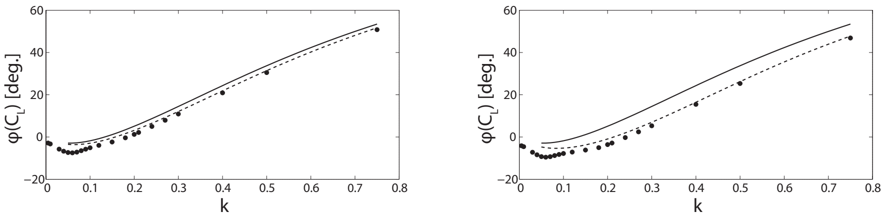

(c) NACA 0012, lift coefficient phase (d) NACA 0024, lift coefficient phase

Figure 2.18: Lift coefficient magnitude and phase used to compute the modified Theodorsen's models. Dots: CFD computations; solid line: classical Theodorsen's model; dashed line: modified Theodorsen's model.

terms for the lift and the moment. The parameters P_3^L and P_4^L, that depends as well from the airfoil thickness, are used to fit the circulatory part of the lift. No tentative is done to include in this modified Theodorsen's model the effect on the aerodynamic moment due to the shift of the aerodynamic center, since this effect can be modeled easily by simply considering that the moment of equation (2.28) is the one computed around the effective aerodynamic center of the airfoil.

2.4.1 Determination of the P coefficients for four thick airfoils

Using the results of the numerical simulations presented in sections 2.2 and 2.3, it is possible to test the capability of the proposed modified Theodorsen's model to fit adequately the behavior of thick airfoils. At the same time, it is possible to compute the values of the coefficients P_i^L and P_i^m for the four NACA airfoils considered, i.e. the symmetrical airfoils with maximum thickness equal to 4%, 12%, 18% and 24%. A weighted least squares fitting procedure is used to compute the values of the P coefficients, considering seventeen reduced frequencies ranging from $k = 0.05$ to $k = 0.75$. Notice that higher weights are associated to the points with larger reduced frequency, since these are affected by a smaller numerical error. The coefficients obtained are reported in table 2.2.

Figures 2.18 and 2.19 show the results of the numerical CFD computations together with the curves obtained using the fitted modified Theodorsen's formulation for the magnitude and the phase of the lift and moment, related to the NACA 0012 and the NACA

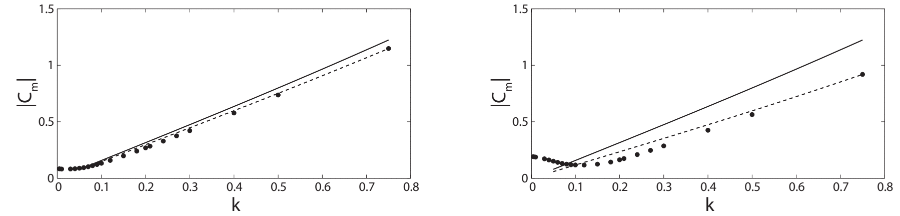

(a) NACA 0012, moment coefficient magnitude (b) NACA 0024, moment coefficient magnitude

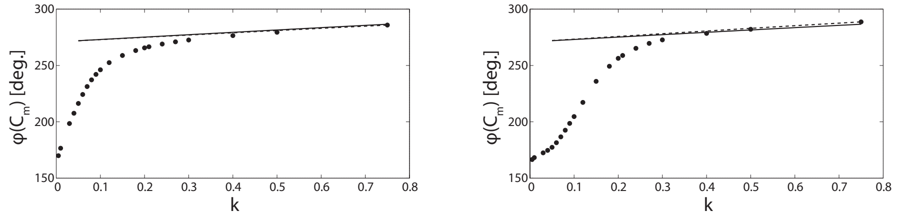

(c) NACA 0012, moment coefficient phase (d) NACA 0024, moment coefficient phase

Figure 2.19: Moment coefficient magnitude and phase used to compute the modified Theodorsen's models. Dots: CFD computations; solid line: classical Theodorsen's model; dashed line: modified Theodorsen's model.

0024 airfoils. The curves related to the classical Theodorsen's model are also reported. Notice that a significant improvement in reproducing the numerical results is found by applying the fitting procedure. Indeed the curves of the fitted Theodorsen's formulation undergo the desired shift with respect to the classical flat plate model, resulting almost overlapped to the numerical results.

2.4.2 Computation of the P coefficients for arbitrary thickness

It is possible to extend the results obtained for the four airfoils involved in the the fitting procedure to the case of an arbitrary thickness, using an interpolation of the already computed coefficients.

A fourth order polynomial is used to interpolate the P_i^L and P_i^m coefficients with respect to the maximum thickness.

The expressions obtained, plotted in figure 2.20, are the following

$$\begin{aligned}
P_1^L(s_m) &= 1 - 2.09 s_m + 25.73 s_m^2 + 160.94 s_m^3 - 735.68 s_m^4, && (2.29)\\
P_2^L(s_m) &= 1 + 3.93 s_m - 64.71 s_m^2 + 244.47 s_m^3 - 280.08 s_m^4, && (2.30)\\
P_3^L(s_m) &= 1 + 0.31 s_m - 1.65 s_m^2 + 24.26 s_m^3 - 77.97 s_m^4, && (2.31)\\
P_4^L(s_m) &= 1 + 4.17 s_m - 68.51 s_m^2 + 75.45 s_m^3 + 269.26 s_m^4, && (2.32)\\
P_1^m(s_m) &= 1 + 1.32 s_m - 24.64 s_m^2 + 98.24 s_m^3 - 154.77 s_m^4, && (2.33)\\
P_2^m(s_m) &= 1 - 4.92 s_m + 71.09 s_m^2 - 403.38 s_m^3 + 756.28 s_m^4. && (2.34)
\end{aligned}$$

In order to validate the obtained interpolation formulae, the NACA 0020 and the NACA 23012 airfoils are chosen as test cases, each of them oscillating with unitary amplitude and zero mean value at several reduced frequencies. The NACA 23012 is selected also to test the reliability of the proposed formulation on slightly cambered airfoils.

The hysteresis curves for C_L and C_m, computed with the new formulation, are compared to the numerical results and to the classical Theodorsen's model. For brevity, only a case at $k = 0.5$ is herein reported. Figures 2.21 and 2.22, highlight a better accordance of the modified models for the C_L with the numerical tests, with respect to the flat plate Theodorsen's model. An increase of the accuracy can also be observed in figures 2.23 and 2.24, where the C_m hysteresis curves are reported.

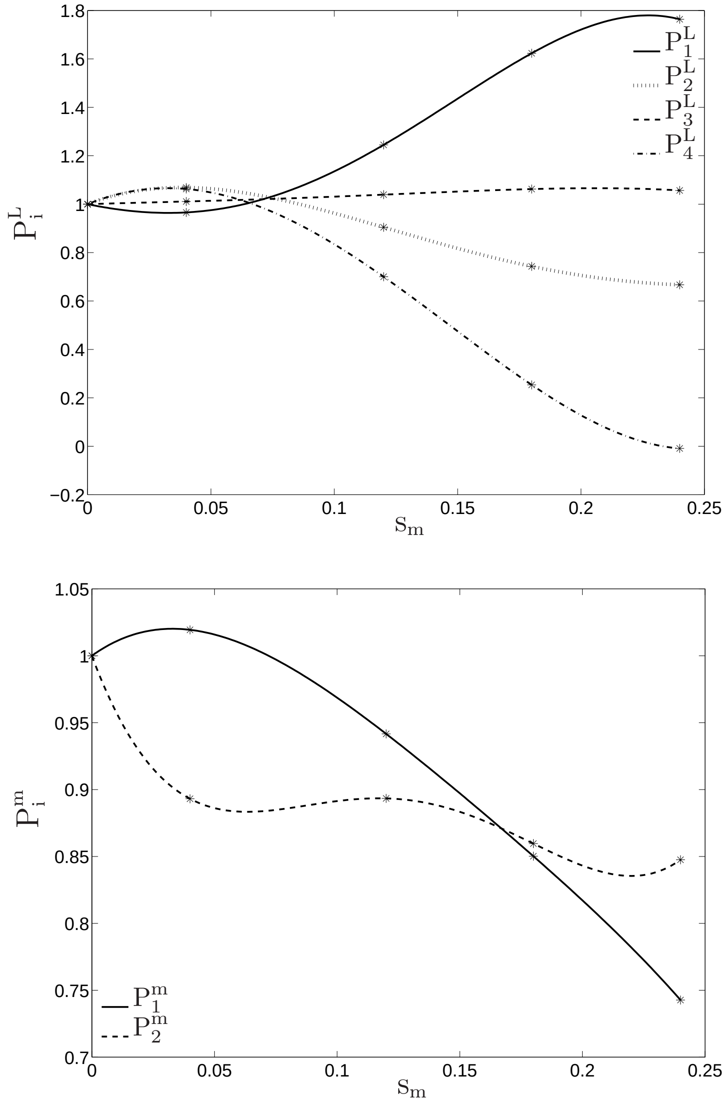

Figure 2.20: Polynomial interpolation of the coefficients versus the airfoil thickness of the modified Theodorsen's model.

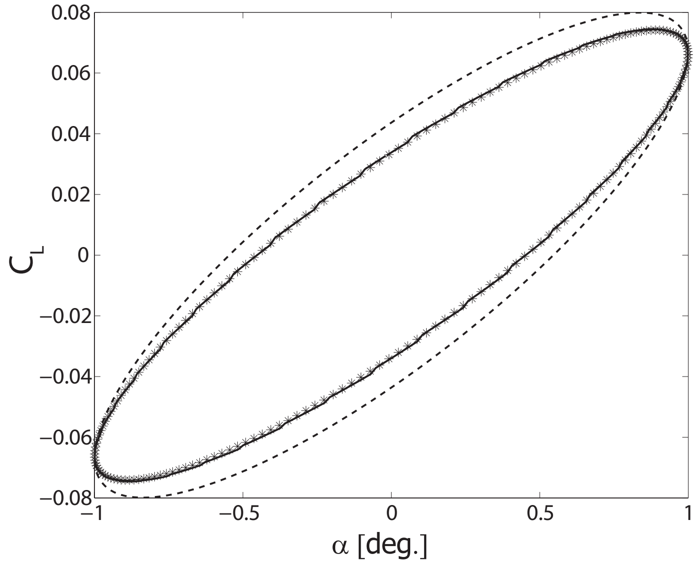

Figure 2.21: NACA 0020 C_L hysteresis curves at $k = 0.5$. Stars: CFD computations; dashed line: classical Theodorsen's model; solid line: modified Theodorsen's model.

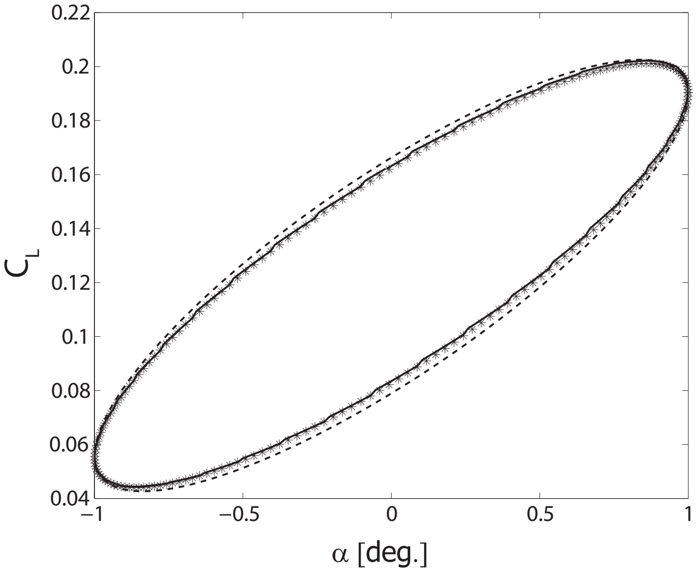

Figure 2.22: NACA 23012 C_L hysteresis curves at $k = 0.5$. Stars: CFD computations; dashed line: classical Theodorsen's model; solid line: modified Theodorsen's model.

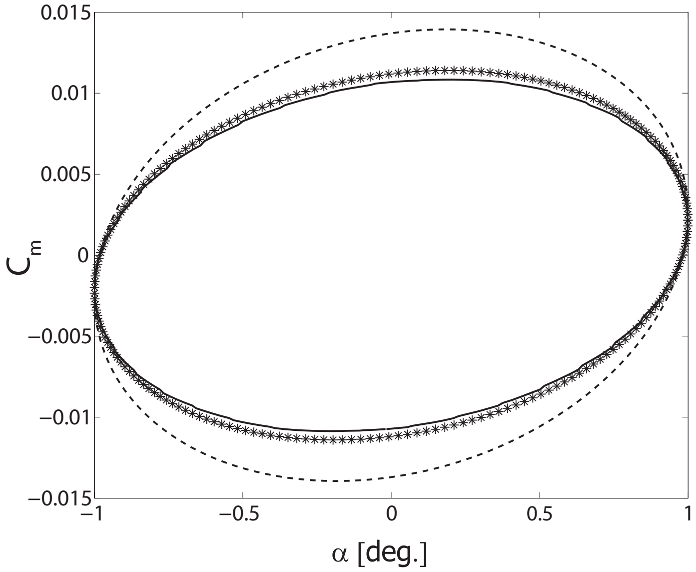

Figure 2.23: NACA 0020 C_m hysteresis curves at $k = 0.5$. Stars: CFD computations; dashed line: classical Theodorsen's model; solid line: modified Theodorsen's model.

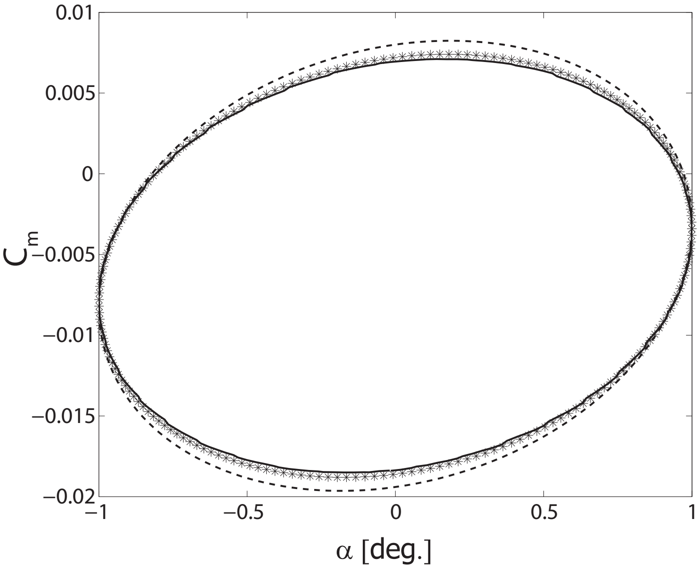

Figure 2.24: NACA 23012 C_m hysteresis curves at $k = 0.5$. Stars: CFD computations; dashed line: classical Theodorsen's model; solid line: modified Theodorsen's model.

2.5 Aeroelastic stability analysis for a typical section

It is interesting to investigate the effects of airfoil thickness on the flutter onset of a typical section model exploiting the modified Theodorsen's model discussed in the previous section. The aeroelastic model is built up by considering an airfoil with chord $c = 2b$ suspended in an incompressible fluid at speed U with two degrees of freedom: a bending h positive downward and a twisting α positive nose-up, as shown in figure 6.1. These two displacements are resisted by a pair of equivalent springs, with stiffness constants denominated k_h and k_α, respectively.

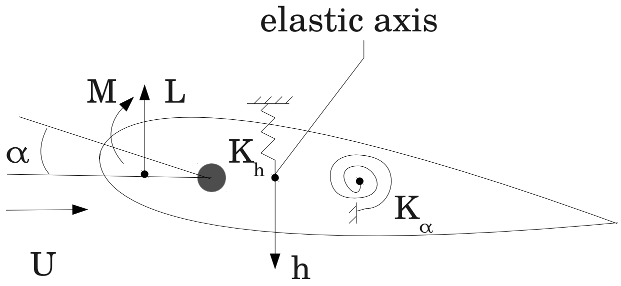

Figure 2.25: Sketch of a typical section model with pitch and plunge motions.

The equations of motion of this system can be found in several classical textbooks on aeroelasticity, e.g. those of Bisplinghoff [45] or Fung [64], and read

$$\begin{cases} m\ddot{h} + S\ddot{\alpha} + K_h h = -L \\ I\ddot{\alpha} + S\ddot{h} + K_\alpha \alpha = M \end{cases} \tag{2.35}$$

where m is the total mass, S is static moment about the elastic axis, and I is the mass moment of inertia about the elastic axis. L and M are the aerodynamic lift and moment about the elastic axis, respectively.

In this case a frequency domain approach can be easily employed to solve for the flutter speed, since the analytical frequency response functions of the lift and the aerodynamic moments are known, i.e. eqs. (2.27) and (2.28).

By introducing the following non-dimensional coefficients

$$\mu = \frac{m}{\pi\rho b}, \quad \text{mass ratio, } \rho \text{ air density} \tag{2.36}$$

$$x_\alpha = \frac{S}{mb}, \quad \text{non-dimensional position of the center of mass} \tag{2.37}$$

$$r_\alpha = \sqrt{\frac{I}{mb^2}}, \quad \text{non-dimensional radius of gyration} \tag{2.38}$$

$$\omega_h = \sqrt{\frac{K_h}{m}}, \tag{2.39}$$

$$\omega_\alpha = \sqrt{\frac{K_\alpha}{I}}, \tag{2.40}$$

it is possible to write the frequency domain aeroelastic model as

$$\mathbf{Z} \begin{Bmatrix} \overline{h}/b \\ \overline{\alpha} \end{Bmatrix} = \mathbf{0}. \tag{2.41}$$

Table 2.3: Parameters of the typical section flutter computations.

Test	μ	a	x_α	r_α
1	3	-0.3	0.2	0.5
2	3	-0.3	0.0	0.5
3	20	-0.2	0.0	0.5

The coefficients of the matrix $\mathbf{Z}$ are

$$a_{11} = -\mu + \mu\frac{\omega_h^2}{\omega^2} - 1 + \frac{\mathrm{j}2C(k)}{k} \tag{2.42}$$

$$a_{12} = -\mu x_\alpha + \frac{\mathrm{j}}{k}P_1^L + aP_2^L + \frac{2C(k)}{k^2}\left[P_3^L + \mathrm{j}k\left(\frac{1}{2} - a\right)P_4^L\right] \tag{2.43}$$

$$a_{21} = -\mu x_\alpha + a - \frac{\mathrm{j}2C(k)}{k}\left(\frac{1}{2} + a\right) \tag{2.44}$$

$$\begin{aligned} a_{22} = & -\mu r_\alpha^2 + \mu r_\alpha^2\frac{\omega_\alpha^2}{\omega^2} + \frac{\mathrm{j}}{k}P_1^m - \frac{1}{2}\left(\frac{1}{4} - a\right)P_2^m + \\ & - \left(\frac{1}{2} + a\right)\left(\frac{\mathrm{j}}{k}P_1^L + aP_2^L\right) - \left(\frac{1}{2} + a\right)\frac{2C(k)}{k^2}\left[P_3^L + \mathrm{j}k\left(\frac{1}{2} - a\right)P_4^L\right]. \end{aligned} \tag{2.45}$$

The flutter condition can be computed by solving the complex nonlinear equation $|\mathbf{Z}| = 0$. Following the same procedure described in the textbook of Fung [64], pp. 212–225, it is possible to solve this nonlinear system by assigning the parameters μ, a, x_α, r_α and k and computing the values of the structural frequency ratio ω_h/ω_α and of the dimensionless flutter speed $U_f/b\omega_\alpha = k\omega/\omega_\alpha$.

Three test cases are considered here, chosen among those presented in the textbook of Bisplinghoff [45], pp. 538–539. The values of the assigned parameters are those shown in table 2.3.

In the test case 1, figure 2.26 (a), significant reductions in the dimensionless flutter speed are visible for thick airfoils, if the structural frequency ratio lies in the interval $0.5 < \omega_h/\omega_\alpha < 1.2$. These flutter points are characterized by large reduced frequencies, figure 2.26 (b), in the interval $1.3 < k < 2.2$. In this range even the 4% thick airfoil shows visible differences with respect to the flat plate. For lower structural frequency ratio, the flutter speed is in any case smaller for thick airfoils, when compared to the results of the flat plate model.

The test case 2 differs from the first case for the static unbalance term. This leads to flutter points characterized by lower reduced frequencies with respect to case 1, see figure 2.27 (b). Figure 2.27 (a) shows how by increasing the airfoil thickness, the flutter boundary moves to the right, i.e. toward higher structural frequency ratios. As a consequence, there are several structural frequency ratios where only some of the thick airfoils herein considered show a flutter point with a low dimensionless flutter speed.

The test case 3 investigates the effect of thickness on the flutter speed for large mass ratio values. Figure 2.28 (a) shows how the variation of flutter speed due to thickness becomes smaller in percentage if compared to what happens in case 1, unless large structural frequency ratio are considered.

In general it is possible to say that in all cases shown in figures 2.26-2.28, the differences due to thickness are smaller for lower reduced frequencies. Additionally, in many situations the prediction given by the flat plate model is un-conservative, i.e. it is characterized by a flutter speed higher than what predicted by the thick airfoil model.

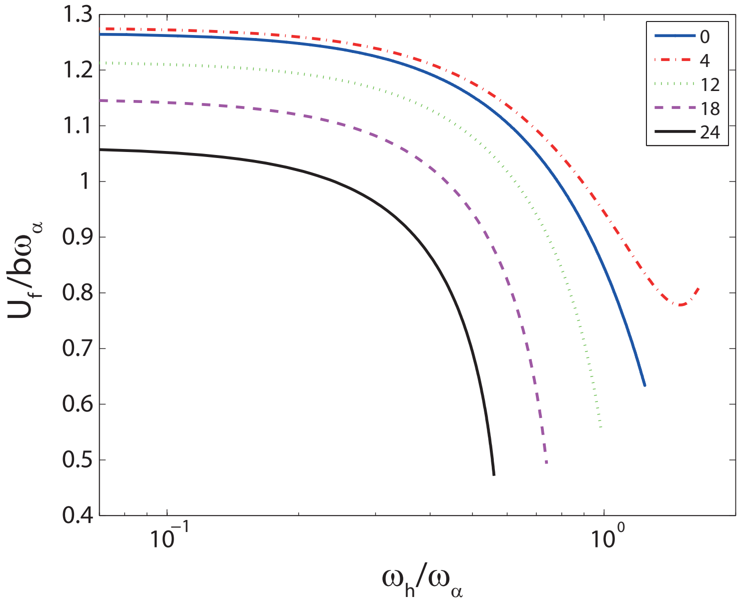

(a)

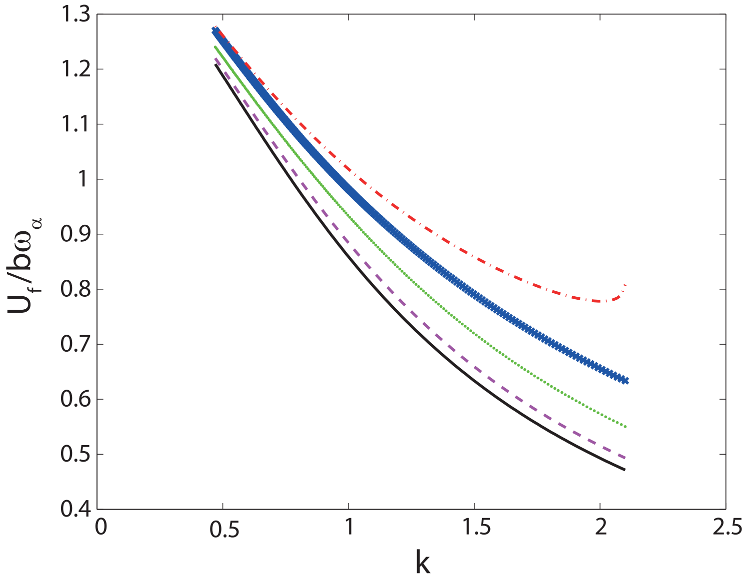

(b)

Figure 2.26: Case 1 of table 2.3: dimensionless flutter speed versus the structural frequency ratio (a), and reduced frequency (b), for airfoils with $0, 4, 12, 18, 24\%$ maximum thickness.

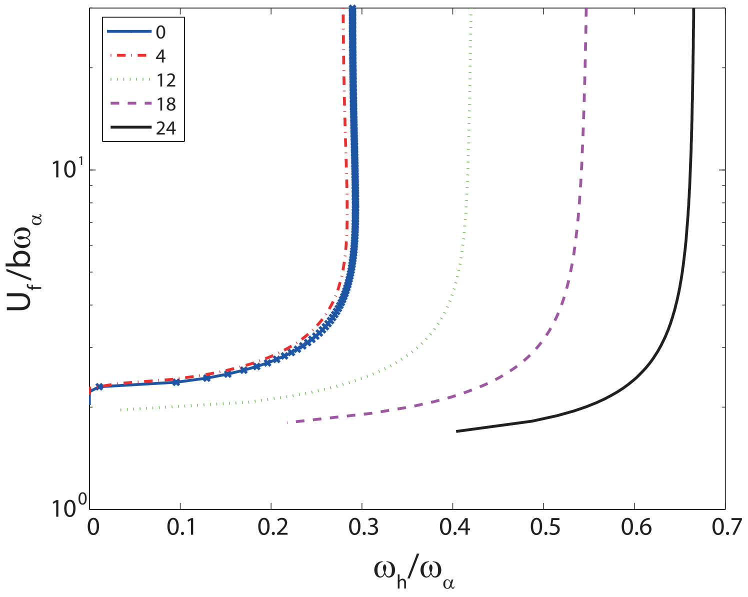

(a)

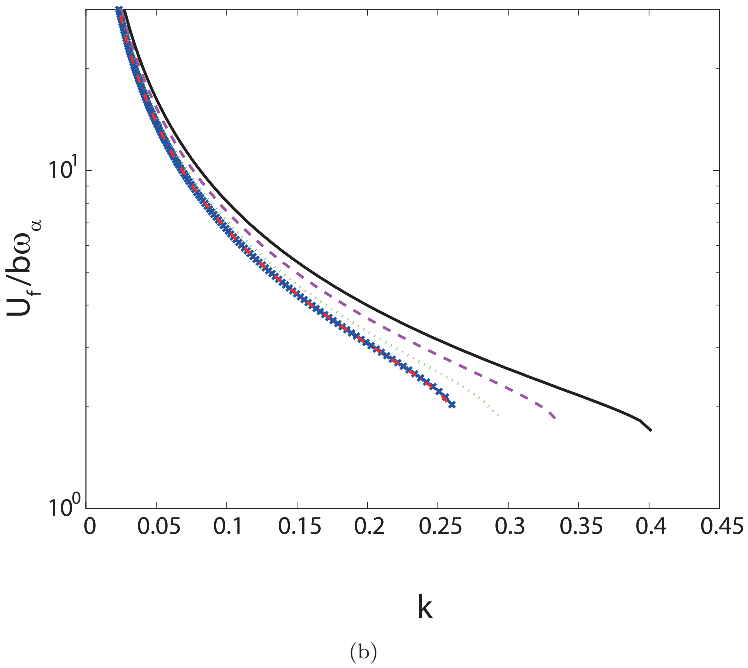

(b)

Figure 2.27: Case 2 of table 2.3: dimensionless flutter speed against frequency ratio (a), and reduced frequency (b), for airfoils with variable thickness.

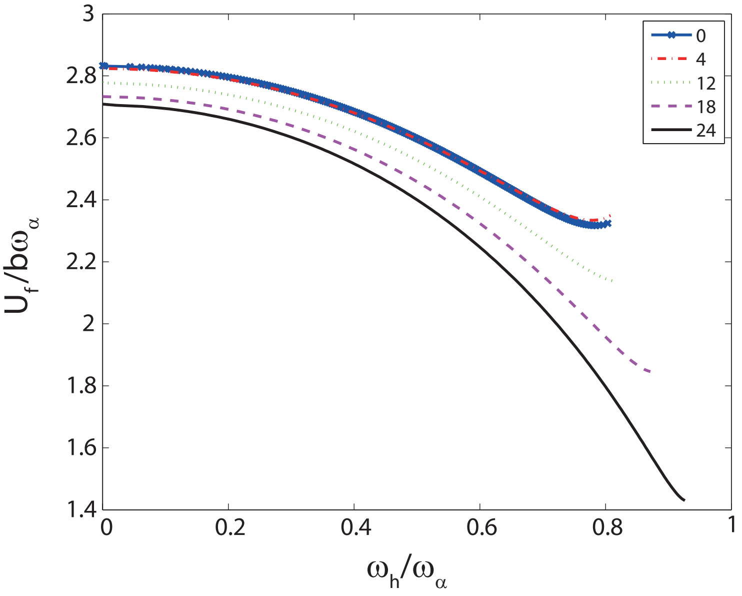

(a)

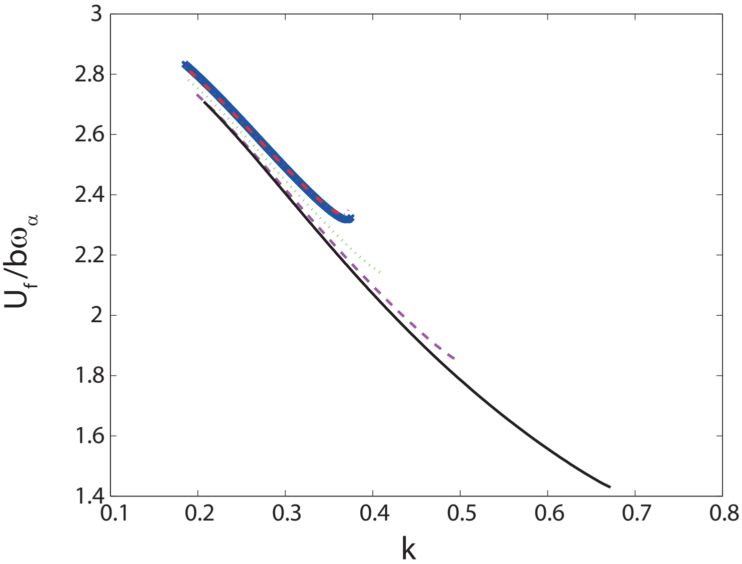

(b)

Figure 2.28: Case 3 of table 2.3: dimensionless flutter speed against frequency ratio (a), and reduced frequency (b), for airfoils with variable thickness.

2.6 Concluding remarks

The effects of the airfoil thickness on the aerodynamic loads generated by an harmonic motion are investigated numerically. As expected from a detailed analysis of the boundary conditions, a dependency of the linearised lift and moment coefficient on the thickness is observed for the case of pitch movements.

Numerical results obtained using the flow solver ROSITA show a significant dependency of the loads from the thickness. In particular, the inversion reduced frequency—at which the phase inversion of the lift-coefficient curve occurs—depends significantly on the thickness of the airfoil. The amplitude of the lift hysteresis cycle is larger for thicker airfoils, for reduced frequencies below the inversion frequency, and smaller for reduced frequencies above it. This modification results in a shift of the phase inversion point towards higher reduced frequencies for thicker airfoils.

A fitting procedure is then applied to the computed loads of oscillating thick airfoils to identify a modified Theodorsen's linear model that accounts for the airfoil thickness. The flat-plate Theodorsen's model is used as a starting point.

The fitting procedure is applied on four different airfoils. The coefficients obtained for every airfoil, are used for a subsequent interpolation useful to define expressions valid for airfoils of arbitrary thickness. The improvement in the computed loads obtained using the modified model instead of the classical flat-plate model is in many cases relevant.

The simple thickness-dependent linear model herein presented, appears to be suitable for many applications, involving aerodynamic and aeroelastic computations. As an example, the application to the flutter problem of a typical section model is reported, showing the significant impact on flutter speed that the modified Theodorsen's formulation may have. The highlighted changes show how it could be important to assess the flutter stability using numerical models that can keep into account the airfoil and wing thicknesses, and not only by means of equivalent flat-plate models.

Of course, a complete validation of these results may require an experimental campaign with several airfoils of different thickness. Moreover, the linear model herein derived, could be potentially useful to improve simple methods for the computation of unsteady loads on any system dealing with small amplitude oscillating quasi-two dimensional flows, such as wind turbines or helicopter rotors, being these latter the concern of this thesis.

Chapter 3

Steady state aerodynamic assessment of a blade section with a L-shaped Gurney flap

---

The aerodynamic performance of a novel trailing edge L-shaped tab design is herein characterized numerically. This device is primarily thought to allow for a shape adaptation of rotorcraft blades according to the current flight condition, as well as to be used as an active control for performance enhancement and vibration reduction. The present chapter is focused on the first of the three possible targets just listed. Overall the operation of the L-tab is found to be twofold. On one side, when the device is downward deployed, it acts as a Gurney flap, allowing for a significant increase in the aerodynamic lift, without severe drawbacks in terms of drag rise. On the other side, when it is deflected upward, it behaves as a classical flap and it is found capable to significantly alleviate the negative effects of stall conditions. The geometrical features of the L-tab are detailed in section 3.1. The computational geometry and the the flow solver, which are employed for the numerical characterization of the L-tab, are also described in section 3.1. The convergence analyses, both in time and in space, are also therein reported. Additionally, comparisons with experimental data from literature are provided. Simulations carried out on a L-tab equipped NACA 0012 airfoil, at several angles of attack in the linear and in the stall regime, are reported in sections 3.2 and 3.3, respectively. Moreover in section 3.2 a Mach number sensitivity analysis, for small angles of attack, is reported, to assess the behavior of the L-tab with respect to the compressibility effects. In section 3.3 the aerodynamic loads achieved by doubling the L-tab chord-wise length, highlight how such longer geometrical configuration is potentially capable to even delay the static stall incoming. The reliability of the numerical computations is further supported by comparisons with pressure measurements and PIV surveys, presented in section 3.4. The feasibility of the two-dimensional flow assumption is also verified by means of 3D numerical computations, that are reported in section 3.5. The load distribution, and the flow field at several span-wise sections, are therein compared to 2D results. Finally, general remarks to the steady state assessment of the L-tab are reported in section 3.6.

3.1 Geometry of the L-tab and numerical model

The numerical assessment for the steady-state and unsteady behavior of the L-tab employes the finite volume solver ROSITA [80], already introduced in chapter 2. Since the wake has to be correctly captured, viscous computations are herein performed. It appears useful to recall that, for viscous fluids, ROSITA solves the RANS equations, modeling the Reynolds stress tensor with the turbulent viscosity transport equation of Spalart and Allmaras [92]. This section contains a description of the geometrical model used for the computations on the L-tab. Details concerning the realization of the computational grid for the tab are also provided. To demonstrate the reliability of the numerical computations, convergence analyses are reported. Additionally, comparisons with experimental data taken from literature for classical GFs are provided. This latter comparison appears useful to demonstrate that, when deployed, the present tab acts indeed as a classical Gurney flap.

There is a general agreement, see e.g. Refs. [2, 25, 33], on the fact that the primary effects induced by GFs consist of a modification in the effective camber line, with respect to the clean airfoil. Results reported in previous works [15, 93] and detailed in this and in the following chapter, highlight that the main affection of the present L-tab GF results in a change in the mean line actual shape. As a consequence, since the purpose of this numerical assessment is to investigate the physical phenomena induced specifically by the L-tab, it appears convenient to use a symmetrical section as clean airfoil. Indeed this allows to immediately get the camber modification effects typical of this movable device.

Figure 3.1(a) shows a schematic view of the L-tab geometry located at the airfoil trailing edge. The L-tab chord-wise length is equal to 10%c, while the height of the tab is equal to 1.33%c. A detail in the TE region of the employed numerical geometry is reported figure 3.1(b). Notice that the L-tab downward deployed actually protrudes 1.01%c from the airfoil pressure side, being the geometry of the clean airfoil cut slightly upstream the trailing edge. Notice that the resulting size of the tab vertical prong is consistent with the GF heights found in literature, that commonly range from 1%c to 2.5%c. A second configuration, similar to the first, but with chord-wise length of the L-tab equal to 20%c, is also built. This allows to investigate the affection of the tab length on the flow field and on the developed airloads. The *baseline* configuration conceived for the L-tab is meant when the device is upward rotated so that the end of its vertical prong lies almost on the suction side corner of the trailing edge. This configuration is attained with an upward rotation of the L-tab corresponding to approx. four degrees. Therefore the baseline shape of the resulting blade section resembles that of a divergent trailing edge solution, widely employed for applications concerning transonic flows, which are indeed not unusual conditions for rotorcraft environments. With this regard works published in literature [37, 38] report the comparison between divergent trailing edge and Gurney flap solutions operating in transonic conditions. It appears useful to highlight that the employment of the present L-tab is thought to be a choice to be done in the preliminary steps of the blade design process, so that the rotor performance can be optimized with respect to this trailing edge configuration.

A comparison is also carried out with a no-slotted geometrical configuration, for the L-tab downward deployed. This allows for a preliminary assessment of the the numerical slot effects, both on the flow field and on the airloads.

A comparison with steady state experimental measurements attained on a NACA 23012 section equipped with the L-tab is then proposed. To foster the consistency with the experimental model, a computational grid employing a NACA 23012 airfoil as clean section is also built.

In order to deal with parts in relative motion, a system of two overlapped multi-block structured grids is realized. The former background C-type grid of 51659 elements extends from the blade section up to the far-field, and is reported in figures 3.2(a) and 3.2(b), where the entire airfoil and a detail of the trailing edge region are shown, respectively. In particular 412 elements are located on the airfoil, 30 elements along the boundary layer, 159 along the wake and 40 along the radial direction, from the end of the boundary layer up to the far-field. The latter overlapping 45281 elements grid is just around the L-tab and it has rectangular shape. This latter grid has width of approx. three times the length of the tab and height of approx. twice the length of the movable device. Namely 230 elements are located on the L-tab, 25 elements along the L-tab boundary layer, 25 elements in

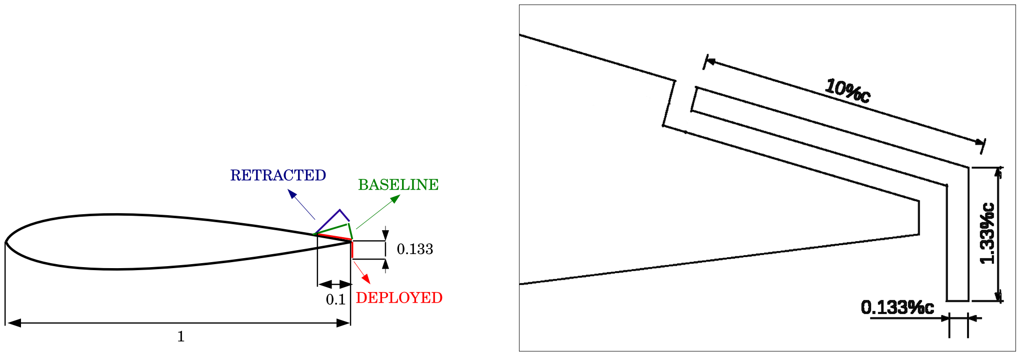

(a) Schematic of the L-tab Gurney flap (b) Computational geometry for the 10%c L-tab

Figure 3.1: Geometrical model for the L-tab equipped blade section.

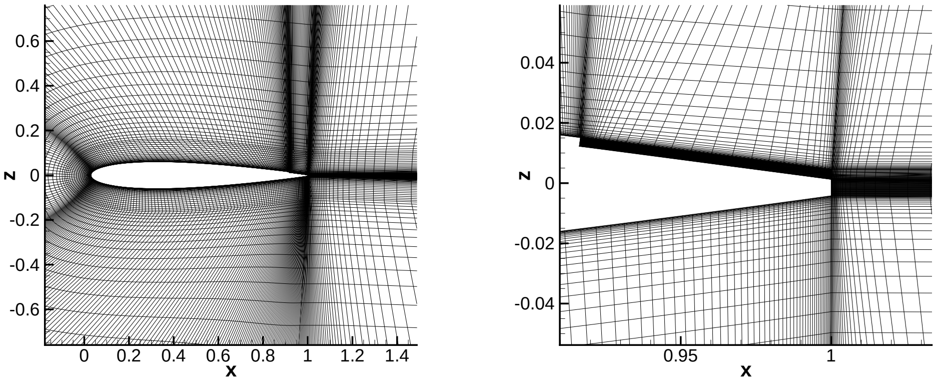

(a) (b)

Figure 3.2: Background C-type 51659 elements reference grid, realized from the airfoil up to the 25c extended far-field.

the longitudinal and transverse directions, from the end of the boundary layer up to the domain extremes. The entire overlapping grid is shown in figure 3.3(a), whereas a detail of the trailing edge area is reported in figure 3.3(b). The elements of the two grids are refined in the trailing edge region, to accurately capture the expected high gradients of the flow passing through the slot between the airfoil and the L-tab, see figures 3.2(b) and 3.3(b). Refinements are of course realized also along the solid walls, to correctly reproduce the boundary layer. With this regard the first cells on the solid bodies have height of $2 \cdot 10^{-5}$ chords, to keep unitary the y^+ parameter.

As just mentioned, the numerical geometry is built to always grant a finite slot between the L-tab and the airfoil, so that the correct functioning of the grid overlapping scheme [80] is ensured. The two overlapped grids are coupled by the numerical solver through the Chimera algorithm [80], with a second order interpolation. Therefore two layers of cells for each of the interpolating grids are employed. Figures 3.4(a) and 3.4(b) represent the computational domain in the trailing edge region, resulting from the interpolation procedure of the background and of the overlapping grids, with the L-tab downward deployed and upward deflected, respectively.

The steady-state simulations are carried out at Reynolds number $\mathrm{Re} = 1 \cdot 10^6$, whereas three values of the Mach number, i.e. $\mathrm{M} = 0.117$, $\mathrm{M} = 0.5$, and $\mathrm{M} = 0.7$, are considered. This allows to preliminarily assess the behavior of the present L-tab on rotor blade environments in forward flight conditions, often characterized by compressible or supersonic

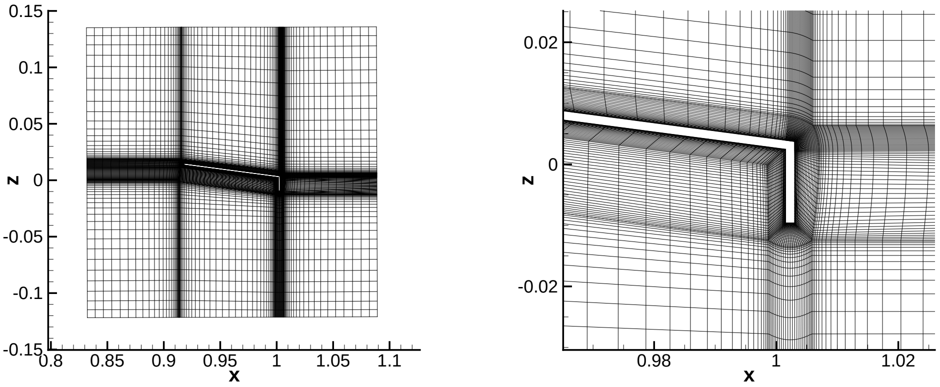

(a) (b)

Figure 3.3: Overlapping rectangular 45281 elements grid, surrounding the movable L-tab.

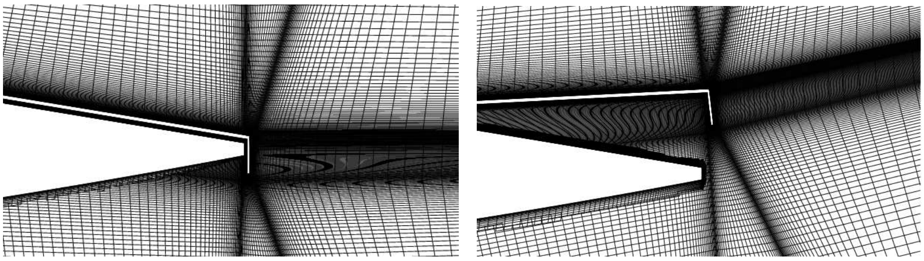

(a) (b)

Figure 3.4: Computational grid for the L-tab downward deployed (a) and for the L-tab 9 deg. upward deflected (b) after the interpolation procedure, $\alpha = 0$ degrees.

flows.

It appears also useful to remark that, with regard to the force coefficients, the pitching moment will be expressed with respect to the quarter-chord in this chapter, unless otherwise specified. Moreover for the present work, $\beta = 0$ deg. will be associated to the L-tab completely downward deployed. Positive values of β will be used to indicate upward rotations of the L-tab.

3.1.1 Convergence analyses for the numerical model

Convergence analyses with respect to the pseudo-time and spatial resolution are performed, both at small angle of attack and in the stall regime. It is proper to remark that of course 2D computations in stall conditions are meant to provide just qualitative results. In order to accurately capture the flow field and the airloads for massively separated flows, 3D time accurate computations, without Reynolds average operations, should be performed. By the way 2D computations in stall conditions, widely employed in literature –see e.g. Refs. [94, 25, 33, 34]–, are useful to gain a preliminary overview on the general behavior of the flow. The downward deployed configuration is selected for the convergence analyses, since the flow conditions are found to be the most critical, among all of the possible configurations. Indeed, when the L-tab is completely downward deployed, the fluid through the slot, which in this specific configuration presents the minimum cross section, reaches its maximum speed, with consequent not negligible gradients in the other flow quantities. Moreover the L-tab portion protruding from the pressure side of the airfoil determines a stagnation point and a recirculating flow region, which in turn further enhances the complexity of the flow field.

Tables 3.1(a) and 3.1(b) report a pseudo-time and space convergence study, for the the airfoil at $\alpha = 0$ deg. and with the L-tab downward deployed, i.e. $\beta = 0$ degrees. In this configuration the solver is found to reach the convergence in 5000 pseudo-time iterations, with the 51659+45181 elements reference grid. The spatial convergence is analyzed by halving and doubling the number of the grid elements, respectively. No significant modifications in the computed airloads are found by refining the grid with respect to the reference, whereas larger differences appear with the coarser grid. As a consequence the 51659+45181 elements grid is selected for the present computations.

Table 3.1: Pseudo-time and space convergence analyses, $\alpha = 0$ degrees, $\beta = 0$ degrees, $\mathrm{M} = 0.117$, $\mathrm{Re} = 1 \cdot 10^6$.

(a) Steady state convergence

P-T steps	C_L	C_m	C_D
5000	0.1468	-0.0686	0.0090
10000	0.1451	-0.0679	0.0089
40000	0.1450	-0.0679	0.0086

(b) Spatial convergence

Elements	C_L	C_m	C_D
coarse	0.3001	-0.1262	0.0087
reference	0.1468	-0.0686	0.0090
fine	0.1483	-0.0636	0.0082

Table 3.2(a) reports the results obtained within the stall regime, namely at $\alpha = 20$ degrees, with the L-tab downward deployed. The convergence in deep stall conditions is investigated as well, since severe non-linearities may affect the flow field when massive separations occur. For stall conditions it appears reasonable to enlarge the acceptable gaps for the convergence analysis. The convergence to steady state is achieved in 10000 iterations, instead of the 5000 required for small angles of attack. On the other hand the computations carried out to study the spatial convergence highlight how the reference grid, adopted for small angles of attack, is still feasible for the stall regime as well, see table 3.2(b).

The convergence to a steady state, is also verified by means of unsteady computations carried out at $\beta = 0$ degrees. Such simulations are performed in order to look for eventual non negligible unsteadiness of the phenomena related to the movable device. The results

Table 3.2: Pseudo-time and space convergence analyses, $\alpha = 20$ degrees, $\beta = 0$ degrees, M $= 0.117$, Re $= 1 \cdot 10^6$.

(a) Steady state convergence

P-T steps	C_L	C_m	C_D
5000	0.9944	-0.4145	0.3790
10000	0.8845	-0.3622	0.3449
40000	0.8979	-0.3701	0.3476

(b) Spatial convergence

Elements	C_L	C_m	C_D
coarse	0.9645	-0.3942	0.3481
reference	0.8845	-0.3622	0.3449
fine	0.8466	-0.3732	0.3465

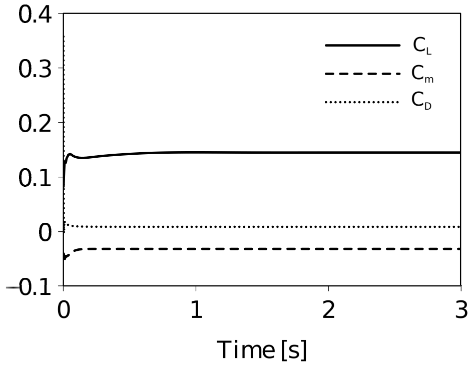

Figure 3.5: Time history of the force coefficients with the L-tab downward deployed, i.e. $\beta = 0$ degrees, at $\alpha = 0$ degrees, M $= 0.117$ and Re $= 1 \cdot 10^6$.

reported in figure 3.5, show the time histories of the aerodynamic loads, at $\alpha = 0$ degrees. At small angle of attack, no unsteady phenomena significantly affect the flow field. In this regard the results of a frequency analysis, reported in section 3.2, will show how unsteady shedding phenomena are encountered only at high frequency, i.e. ~ 50 Hz, which is approx. the shedding frequency of a square cylinder at Re $\approx 1 \cdot 10^6$ [95]. As a consequence the assumption of steady behavior in the mean flow is further validated. No unsteady computations are performed for stall conditions at this step since these would require an excessive computational burden to reach the convergence –i.e. much more than three seconds lasting simulations– in the context of the preliminary investigation here reported.

Validation tests carried out on the aforementioned double chord-wise length L-tab are hereinafter briefly recalled, since such longer configuration will be extensively treated in the following chapters. The convergence with respect to the pseudo-time is investigated by varying the number of iterations for the implicit integration scheme. Table 3.3(a) shows that the convergence with respect to the pseudo time is achieved with 5000 iterations for steady state computations. Namely the difference between the lift, drag and moment coefficients, computed with respect to the reference 10000 iterations, is always smaller than 1.2%.

The spatial convergence is analyzed by halving and doubling the number of the grid elements with respect to the reference mesh of 124601 elements. Table 3.3(b) reports the sensitivity of the aerodynamic loads to the spatial resolution of the grid. By doubling the refinement with respect to the reference grid, the maximum difference in the aerodynamic loads is for the drag coefficient and it is equal to 8% with respect to the reference 124601 elements and 5000 pseudo time steps test case. Much smaller differences are found for the lift and moment coefficients. With regard to the convergence in stall conditions, the reference grid with 10000 pseudo-time iterations is found appropriate, see tables 3.4(a) and 3.4(b).

The geometrical configuration with the 20 %c-long L-tab downward deployed is selected

Table 3.3: Pseudo-time steps and spatial resolution convergence analysis performed in terms of the aerodynamic loads on the 20%c-long L-tab at $\alpha = 0$ deg. and $\beta = 0$ degrees. The number of pseudo-time steps is fixed at 5000; M = 0.117, Re = $1 \cdot 10^6$.

(a) 20%c-long L-tab, pseudo-time steps convergence analysis

P-T steps	C_L	C_m	C_D
5000	0.1468	-0.0686	0.0090
10000	0.1451	-0.0679	0.0089
40000	0.1450	-0.0679	0.0089

(b) 20%c-long L-tab, space convergence analysis

Elements	C_L	C_m	C_D
coarse	0.3001	-0.1262	0.0087
reference	0.1468	-0.0686	0.0090
fine	0.1383	-0.0636	0.0082

Table 3.4: Pseudo-time steps and spatial resolution convergence analysis performed on aerodynamic loads at $\alpha = 20$ deg. and with the tab downward deployed for the 20%c-long L-tab. The number of pseudo-time steps is fixed at 10000; M = 0.117, Re = $1 \cdot 10^6$.

(a) 20%c-long L-tab, pseudo-time steps convergence analysis

P-T steps	C_L	C_m	C_D
5000	0.9546	-0.04021	0.3676
10000	0.8581	-0.3513	0.3346
40000	0.8709	-0.3589	0.3371

(b) 20%c-long L-tab, space convergence analysis

Elements	C_L	C_m	C_D
coarse	0.9356	-0.3823	0.3377
reference	0.8581	-0.3513	0.3346
fine	0.8541	-0.3341	0.3370

for the convergence analyses, consistently with the approach followed for the shorter movable device. Since the L-tab is expected to generate unsteady phenomena on the flow field, the convergence to a steady state, for time-independent configurations, is verified by means of unsteady computations. Figure 3.6 shows how a steady state solution is reached for each of the force coefficients at low incidence. Again no unsteady computations are performed in stall conditions, for the huge computational burden which would be required, excessive for the preliminary investigation herein reported.

3.1.2 Comparison with experimental data for a classical GF

A preliminary validation of the numerical computations for the 20%c-long L-tab with the experimental data of Ref. [28] is reported hereinafter. Further validations with experimental data measured specifically on the L-tab are detailed in section 3.4. Both the clean

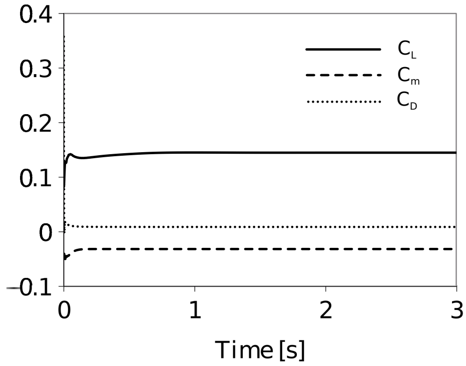

Figure 3.6: Time history of the force coefficients with the 20%c-long L-tab downward deployed, i.e. $\beta = 0$ degrees, at $\alpha = 0$ degrees, M = 0.117, Re = $1 \cdot 10^6$.

airfoil and the configuration with the L-tab downward deployed are taken under consideration. Li [28] performed several measurements on a NACA 0012 section, both clean and equipped with a trailing edge GF with height equal to 1.5%c. To attain a proper validation of the present numerical results, a specific computational model is realized for a new geometry, consisting of a NACA 0012 section with a L-tab device protruding 1.5%c from the airfoil TE pressure side, thus more closely resembling that of Li [28]. All the remaining geometrical parameters for this test model, as well as the elements distribution for the computational grids, are kept unchanged with respect to those related to the reference 1.3%c L-tab. Notice that comparisons for upward deflections of the L-tab are not feasible, since the resulting configuration of the upward deflected L-tab is quite novel and, to the authors knowledge, no suitable experimental data, except for those reported in section 3.4, are available so far. Moreover no comparisons with experimental data for unsteady motions of the airfoil or the tab are retained feasible, due to the substantial lack of measurements in the small perturbation regime –as already stated by Friedmann [33]– and also because, as just mentioned, the present configuration is somehow novel in literature. Figures 3.7(a) and 3.7(b) report the comparison between the pressure coefficient related to the current computations and to the experimental measurements of Li [28], at angle of attack $\alpha = 4$ degrees. A very good agreement is found between the numerical and the experimental data, both for the clean NACA 0012 airfoil and for the section equipped with the L-tab downward deployed. In particular the peaks in the leading edge region, which primarily affect the resulting aerodynamic loads, are very well captured by the numerical computations. For the section with the L-tab downward deployed, the behavior in the trailing edge area is accurately captured as well. The local mismatches between the CFD and the experiments in this region are probably due to differences in the geometrical features of the two trailing edge devices under consideration.

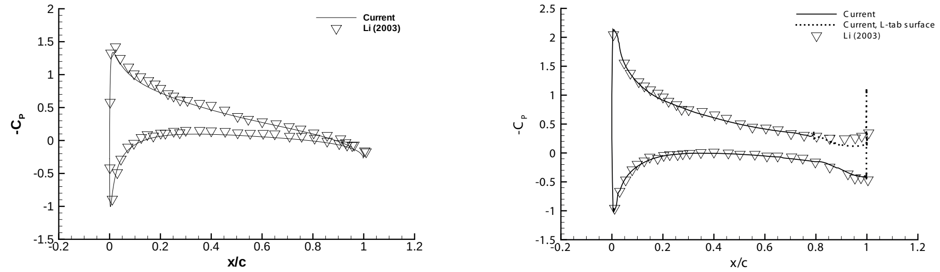

(a) NACA 0012 clean airfoil

(b) NACA 0012 with L-tab/GF downward deployed

Figure 3.7: Comparison of the steady state pressure distribution at $\alpha = 4$ deg. for the current numerical computations and the experiments of Li [28] at $\mathrm{Re} = 2.1 \cdot 10^6$ and $U_\infty = 30\mathrm{m/s}$ on the NACA 0012 section without and with a trailing edge GF.

Figure 3.8 reports the lift, quarter-chord moment and drag coefficients from the current numerical computations and from the experiments of Li [28] on the clean NACA 0012 section. A very good agreement is found between the numerical and the experimental data for each of the force coefficients in the linear range. Namely, within attached flow conditions, the maximum difference in lift is lower than 4%, whereas the maximum errors for the pitching moment and for the drag coefficients lie below 8% and 4%, respectively. An expected mismatch in the stall onset prediction is observed between the numerical and the experimental results. Such discrepancy is attributable to the lack of accuracy typical of most RANS solvers at high angles of attack. Figure 3.9 reports the lift, quarter-chord moment and drag coefficients, from the current numerical computations and from the experiments of Li [28], for the configuration with the trailing edge device downward deployed. A very good agreement is found between the numerical and the experimental data for each of the force coefficients, including the drag. Namely for attached flow conditions the maximum difference in lift is lower than 3%, whereas the maximum errors for the pitching moment and drag coefficient are smaller than 6% and 5%, respectively. As anticipated in the above the disagreement encountered between the numerical and the experimental results in terms of the stall onset prediction, for the clean airfoil as well as for the section with the trailing edge device, may be due to the assumption of fully turbulent flow and to limitations related to the RANS turbulent models of the computations. With this regard it appears useful to recall that also e.g. Friedmann [33] and Palacios [34] found discrepancies between their CFD computations and experimental data. In particular Friedmann [33] compared its CFD results to the experiments of Li [28], the same used to check the numerical computations of this work. Overall the good agreement observed in terms of both the local and the resulting loads computed numerically, with respect to experimental data from literature, gives reasonable feasibility to the numerical results reported in the following.

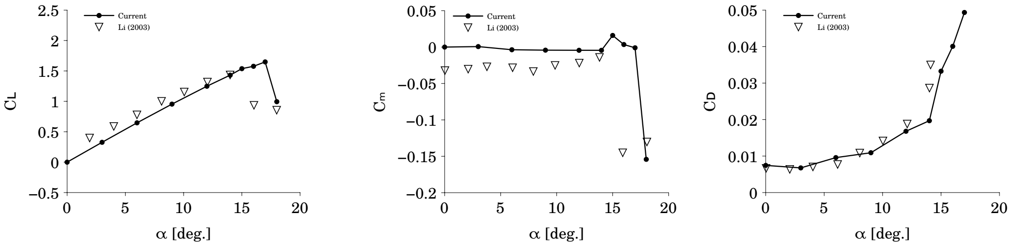

(a) Lift coefficient

(b) Quarter-chord moment coefficient

(c) Drag coefficient

Figure 3.8: Comparison of the steady state force coefficients for the current numerical computations and the experiments of Li [28] at Re $= 2.1 \cdot 10^6$, $U_\infty = 30$m/s on the NACA 0012 section.

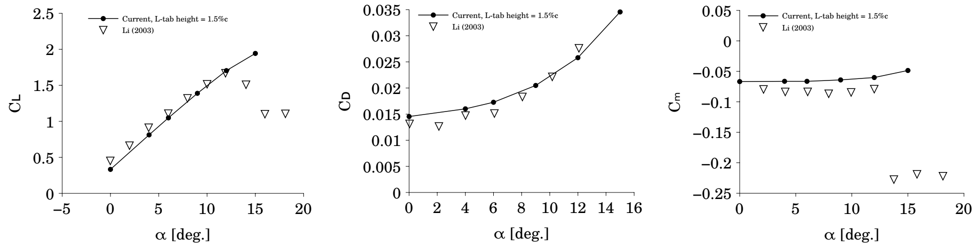

(a) Lift coefficient

(b) Drag coefficient

(c) Quarter-chord moment coefficient

Figure 3.9: Comparison of the steady state force coefficients for the current numerical computations and the experiments of Li [28] at Re $= 2.1 \cdot 10^6$, $U_\infty = 30$m/s on the NACA 0012 section with the L-tab/GF downward deployed.

3.1.3 Sensitivity to the slot between the L-tab and the airfoil

Most CFD results on GFs available in literature, see e.g. Refs. [25, 30, 34], employ computational grids with no slots between the control surface and the airfoil. Since the grid of the present work is conceived to always present a finite slot between the airfoil and the L-tab, it appears proper to estimate the effects of such a gap on the numerical solution. A comparison between the loads computed employing the reference slotted grid and one without slot between the airfoil and the tab is here reported. Notice that the slot effects are expected to be primarily due to the stagnation area developed between the vertical prong of the airfoil and the pressure side of the airfoil. Therefore the comparison

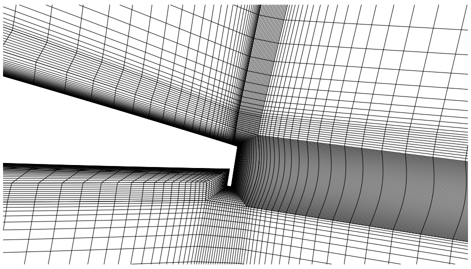

Figure 3.10: Computational domain close to the trailing edge for the no slotted configuration of the L-tab equipped blade section. This numerical geometry doesn't require the realization of separate overlapping grids.

between the slotted and the no-slotted computational models is performed when the L-tab is completely downward deployed, i.e. when the stagnation area is more extended and the most significant suction effects are encountered. On the other hand, when the L-tab does no longer protrude from the airfoil pressure side, a recirculating flow area, with expected smaller effects on the loads distribution, appears between the tab and the airfoil suction side.

A detail of the no slotted geometry in the trailing edge region is reported in figure 3.10. Notice that, since the airfoil and the L-tab are modeled as a single solid body, no overlapped grids are required. The 10%c slotted L-tab is used as a reference for the present purpose.

Figure 3.11 reports the aerodynamic loads computed both on the slotted and on the no-slotted configurations, at angles of attack ranging between $\alpha = -3$ deg. and $\alpha = 20$ degrees. For low angles of attack a behavior similar to the slotted configuration is observed.

On the contrary, a remarkably different behavior is observed at medium to high angles of attack. Namely the no-slotted configuration significantly anticipates the prediction of the stall onset, which is found well below 15 degrees, see figure 3.11. It appears proper to recall that this latter result is perfectly consistent with CFD computations of other authors, e.g. Refs. [33, 34], performed indeed on a NACA 0012 section equipped with no-slotted GF like devices. Both Liu [33] and Palacios [34] found an anticipation of the stall onset with respect to the experimental data used for comparison. The two authors explained this mismatch with the inaccuracy of the turbulence modeling in capturing viscosity-dominated effects and with the intrinsically three-dimensional nature of the flow for medium-high angles of attack, which of course is not accounted for when performing 2D computations. The results concerning the slotted configuration exhibit a delay in the stall onset with respect to the no-slotted counterpart, highlighting how the slot somehow keeps the flow attached. This is probably due to suction phenomena numerically observed in the slot, where the high pressure fluid of the airfoil lower side moves to the upper side, with effects that can be roughly assimilated to the blowing of the boundary layer. Of course the suction phenomena just mentioned are likely to be in large part numerical effects. Indeed, as mentioned in the above, two-dimensional CFD RANS computations are not expected to provide quantitatively accurate results at medium-high angles of attack. To investigate the actual effects of the slot between the airfoil and the tab, much more refined simulations, probably unsteady, should be performed. In particular very fine grid, with a resolution comparable to that of the boundary layer, should be realized in the slot between the airfoil and the tab. Additionally a very refined space resolution on the airfoil suction side nearby the should be adopted. This would significantly increase the computational burden and lies beyond the preliminary purposes of this investigation. By the way the present results suggest how it could be interesting to experimentally investigate the slot effects on a blade model equipped with the L-tab, since the gap is expected to actually

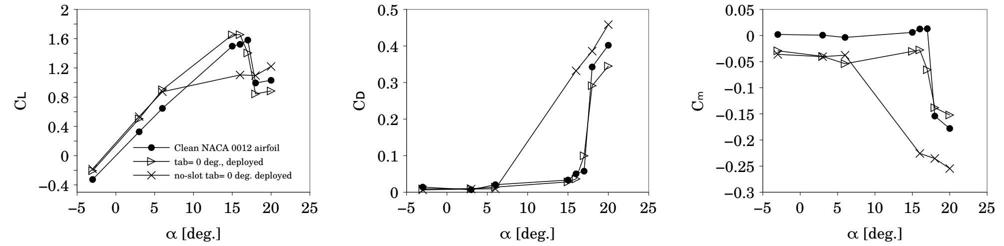

(a) Lift coefficient

(b) Drag coefficient

(c) Quarter-chord moment coefficient

Figure 3.11: Force coefficients for the slotted and the no-slotted geometries of the L-tab, together with the results for clean NACA 0012 airfoil. Mach number M = 0.117, Reynolds number Re = $1 \cdot 10^6$.

affect the flow behavior, especially at medium-high angles of attack.

It appears also proper to remark that the agreement of the loads computed with the slotted and the no-slotted configuration for small angles of attack –which in turn resemble other no-slotted numerical computations found in literature [33, 34]– is ultimately an additional confirmation of the reliability of the present CFD simulations.

3.2 Steady state computations at small angles of attack

Steady state computations at small angles of attack are carried out at Re = $1 \cdot 10^6$ and M = 0.117. Moreover computations are performed at M = 0.5 and M = 0.7, to get a preliminary estimation of the Mach number sensitivity of the movable device.

An assessment of the phenomena related to the L-tab can be attained with an insight into the features of the flow field. Figure 3.12 shows the contours of the Mach number together with the streamlines close to the trailing edge, computed with the L-tab both downward deployed (a) and upward deflected (b).

Two counter-rotating vortical structures (CRV) are clearly visible just behind the L-tab. Since the transverse edge of the L-tab seems to behave as a bluff body, it appears interesting to evaluate the shedding frequency, if eventually present, of the related vortical structures. The shedding frequency f_s is herein estimated through unsteady numerical computations for fixed configurations of the airfoil and of the L-tab. In particular the Fourier transformation is applied to the time histories of the computed aerodynamic loads. The spectrum of the force coefficients is attained by applying a Hann windowing to the reference time history and by using several repetitions of the original signal, to avoid leakage phenomena. Figures 3.13(a) and 3.13(b) show the lift coefficient spectra achieved for 2.322 seconds lasting unsteady simulations at $\alpha = 0$ deg. for $\beta = 0$ deg. (a) and $\beta = 4$ deg. (b). Notice that the star symbol used as a superscript for the variable $|C_L(f)|$ indicates that the magnitude of the lift coefficient in the frequency domain has not been scaled with respect to the amplitude of the input motion law. Since sinusoidal motion laws are herein taken under consideration, such scaling factor is directly the oscillation amplitude. Two peaks are clearly visible in the lift coefficient spectra. The secondary peak in the spectrum identifies the shedding frequency. Such peak is found to lie in the range 54-60 Hz. This confirms that, also for the present L-shaped GF, secondary unsteady phenomena occur at a specific fixed frequency, at least for this regime of Reynolds number. In terms of the Strouhal number St, the non-dimensional shedding frequency is found equal to St = $f_s h/U = 0.15$, where h is the non-dimensional height of the L-tab. Such value is very close to the Strouhal number typical of a rectangular cylinder at Reynolds Re = $1 \cdot 10^6$, corresponding to St = 0.16, see for instance the work of Sarioglu [95]. Notice that a similar value of the mean Strouhal number, i.e. approx. 0.2, was also computed by Dowell [25]

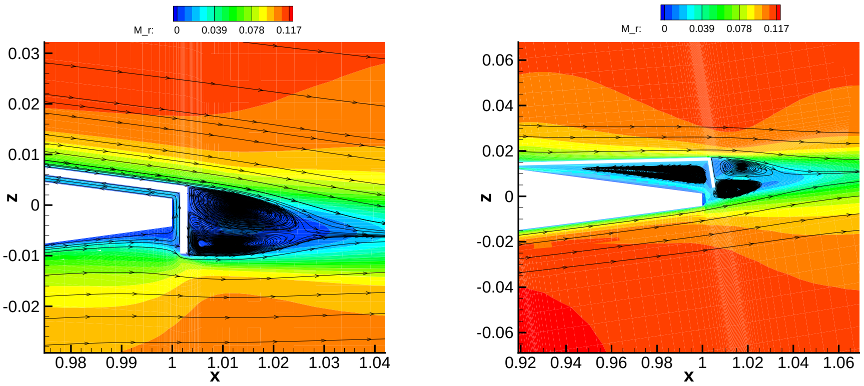

(a) $\beta = 0$ deg.

(b) $\beta = 6$ deg.

Figure 3.12: Mach number flow field and streamlines close to the trailing edge of the L-tab equipped blade section, $\alpha = 0$ degrees, freestream Mach number $\mathrm{M} = 0.117$, Reynolds number $\mathrm{Re} = 1 \cdot 10^6$.

for a blade section equipped with a GF-like device. No further secondary peaks are herein observed in the spectrum, therefore confirming that no other unsteady phenomena affect the flow field. The assumption of steady on average flow, for the present computations, is further validated at least at low angle of attack.

It appears proper to remark that the generation of two counter rotating vortical structures is a well known phenomenon occurring on GF-like devices and it is extensively treated in literature, see e.g. Refs. [25, 33]. The widespread accepted explanation of what occurs lies in the the consideration that the fluid, encountering the vertical edge of the Gurney flap, is forced to turn around it. This leads to the generation of the two counter-rotating vortical structures just mentioned. The primary effect of these vortical structures is a modification in the effective mean line. Indeed the CRV cause a shift of the Kutta condition application point, downstream with respect to the trailing edge. An equivalent longer and more cambered airfoil, with additionally a consequent shift of the zero lift angle, results from such modifications in the flow field. Therefore the curves of the aerodynamic loads versus the angle of attack are expected to shift according to the rotation of the L-tab.

Figures 3.12(a) and 3.12(b) are also helpful to understand what occurs in the slot between the L-tab and the airfoil. In particular when the L-tab is downward deployed, the lower side high pressure fluid enters the slot between the L-tab and the airfoil. This fluid moves towards the suction side of the section. On the other hand, when the L-tab is upward deflected, a recirculating flow region clearly appears between the movable device and the airfoil. As a consequence, when the L-tab is downward deployed, the flow across the slot may give a contribution in increasing the aerodynamic loads. Indeed such flow yields a difference of pressure between the lower and the upper side of the L-tab streamwise edge. On the other hand, when the L-tab is upward deflected, the region between the L-tab and the airfoil suction side is filled with almost stagnating fluid. Therefore no additional contributions to loads are expected. Of course, as anticipated in section 3.1, much more refined numerical computations, in addition to experimental tests, are mandatory to understand the actual affection of the slot between the airfoil and the tab, with respect to no-slotted configurations.

With the aim to investigate the local effects of the L-tab, the pressure coefficient C_P along the blade section model is computed. Figure 3.14 shows the comparison between the pressure coefficient at angle of attack $\alpha = 6$ degrees, with the L-tab both downward deployed (blue long-dashed line and dark blue dashed line) and upward deflected (light green dash-dot line and dark green dash-dot-dot line), together with the results obtained for the clean airfoil (red solid line). It is remarkable how the L-tab, for subsonic flows,

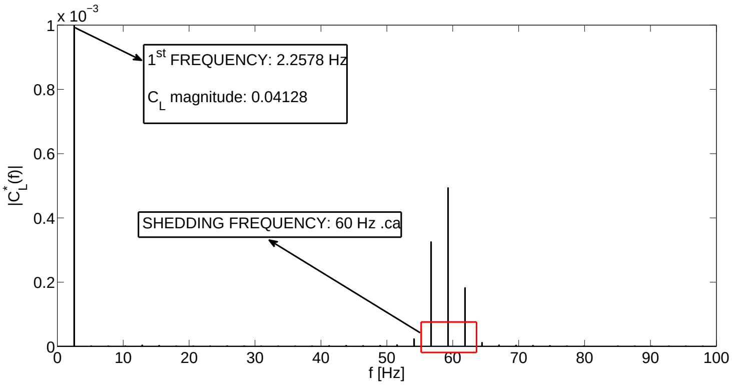

(a) $\beta = 0$ deg.

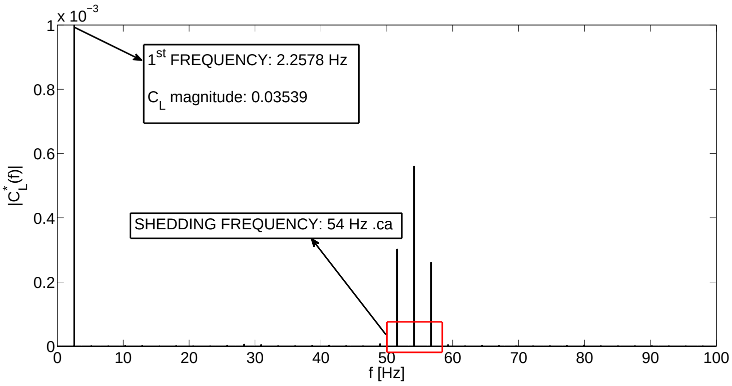

(b) $\beta = 4$ deg.

Figure 3.13: Lift coefficient spectra for unsteady computations on fixed configurations of both the L-tab and the airfoil; $\alpha = 0$ degrees, freestream Mach number $\mathrm{M} = 0.117$, Reynolds number $\mathrm{Re} = 1 \cdot 10^6$.

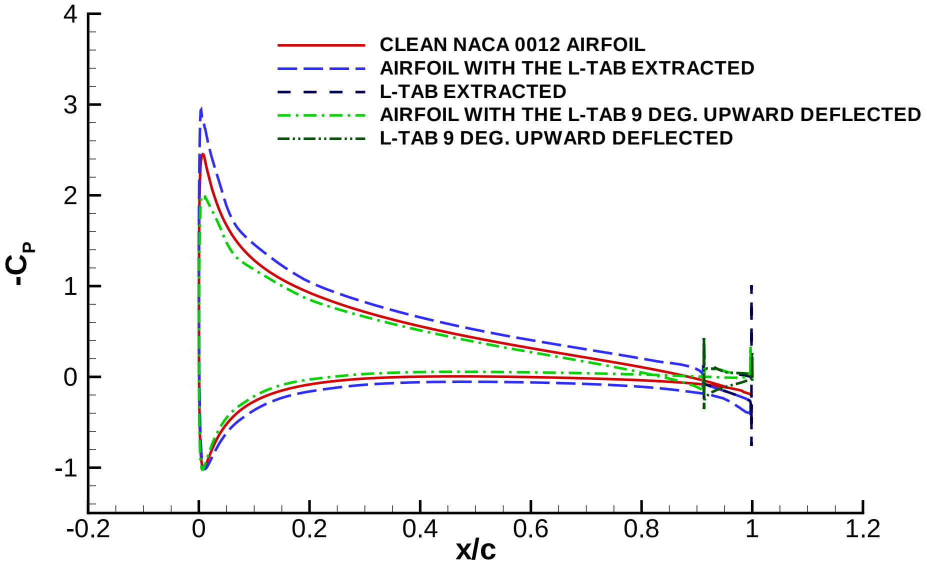

Figure 3.14: Pressure coefficient distribution for the upward/downward deflected L-tab equipped section and for the clean airfoil, $\alpha = 6$ degrees, M $= 0.117$, Re $= 1 \cdot 10^6$; red solid line: clean NACA 0012 airfoil; blue long-dashed line and dark blue dashed line: L-tab deployed, airfoil and movable device edges; light green dash-dot line and dark green dash-dot-dot line: L-tab upward deflected, airfoil and movable device edges.

affects the pressure distribution along the entire blade section, up to the leading edge. In particular the area subtended by the C_P curve of the clean airfoil is larger than the one obtained with the L-tab upward deflected and smaller than the one related to the downward deployed movable device . This is consistent with the interpretation given in the above, according to which the effects of the L-tab on the distribution of loads are equivalent to what one would attain with a longer and more cambered airfoil. That is, the primary effects of the L-tab are in fact related to a change in the shape of the mean line.

Moreover the C_P curves allow for an useful insight into the behavior of the aerodynamic loads. In particular the extension of the area subtended by the pressure coefficient curve is an indication of what occurs in terms of integral quantities.

Figure 3.15 shows the behavior of the force coefficients at low angles of attack, for various rotations of the L-tab. The baseline configuration, with the L-tab 9 deg. upward deflected, is represented by the square markers. The corresponding curves for the clean NACA 0012 geometry are also reported. It can be firstly noticed that the C_L-α curve slope, see figure 3.15(a), with the L-tab installed on the blade section, is larger or almost equal with respect to the clean airfoil curve. In particular the lift curves exhibit a downward vertical shift, as the L-tab is deflected upward, since the zero lift angle gets positive. On the other hand, when the L-tab is downward deployed, the zero lift angle gets negative and an upward shift of the C_L-α curve is encountered.

Figure 3.15(b) reports the drag coefficient for several rotations of the L-tab. Overall no severe penalization, in terms of drag rise with respect to the clean airfoil, are encountered. It appears useful to remark that the present findings, concerning the behavior of the drag coefficient, are partially supported by the unsteady experimental results of Ref. [35, 36] in which, in the upstroke phase of the airfoil oscillation, the measured pressure drag exhibits similar behaviors to those herein computed numerically. For few configurations figure 3.15(b) shows a light decrease in drag with the L-tab installed on the blade. This is in agreement with other results in literature on TE devices. For upward deflections of the

L-tab, the movable device acts similarly to classical TE flaps. With this regard Cusher [96] gave an extended review on TE flap-like configurations capable to reduce the drag with respect to the clean configuration, including devices not dissimilar to the present L-tab. Additionally, on the basis of various experimental results, Giguère [11] provided a detailed explanation of the physical mechanisms, which, even at low angles of attack, could yield drag reductions with respect to the clean airfoil, if properly sized GFs are employed. According to Giguère, benefical effects could be attained with GFs, in terms of both pressure drag and skin-friction drag. In particular, Giguère infers that the skin friction drag could be reduced with the addition of GFs, being the flow forced to separate from the lower surface, with the consequent generation of a recirculation region in front of the flap. However such drag reduction is expected to be quite low, since an efficient GF has to be small enough to lie entirely within the boundary layer, as recommended by several authors [2, 97, 98, 4, 99]. With regard to the pressure drag Giguère recalls that the Gurney flap is submerged in a shear layer where the flow is dominated by viscous effects. Therefore, as it was first suggested by Liebeck [2], two counter rotating vortical structures may be generated past the trailing edge. If such structures are steady on average, i.e. an attached bubble exists, these allow for a reduction of the wake thickness behind the airfoil. The achievement of a thinner wake leads in turn to lower drag values. Moreover Giguère inferred that these phenomena could grant a smaller drag for a given lift coefficient, as well as for a given angle of attack. Furthermore the experimental data of Cole [29] show that, for some specific configurations, lower drag coefficients could be attained with GFs installed on the airfoil. Actually the opposite was found by employing other airfoil-GF configurations, leading Cole to conclude that the performance and effectiveness of GFs installed on aerodynamic sections is strongly dependent on the shape of the movable device and of the clean airfoil which is used. Jeffrey [13] and Traub [100] also found drag reductions with respect to the clean configuration, for medium to high angles of attack. They both inferred that such effects may be due to the reduction in the displacement thickness of the boundary layer, induced by the GFs. Nevertheless it appears proper to remark that detailed insights into the behavior of the drag coefficient lie out from the concerns of the present work. Moreover more complex computations should be proper to accurately capture the behavior of the drag coefficient. Overall figure 3.15(b) is primarily meant to show that this novel L-tab is not expected to yield important drawbacks in terms of drag and therefore enhancing its potential suitability for fixed- and rotary wing- aircraft applications.

The pitching moment coefficient C_m is computed with respect to the airfoil quarter chord, i.e. approx. the aerodynamic center of the NACA 0012 airfoil, see figure 3.15(c). As expected this quantity appears to be almost constant for the clean airfoil. On the other hand, with the L-tab installed, the C_m slightly changes with the angle of attack. The behavior of the pitching moment is affected by the change in the effective camber as well. Indeed such a modification leads to a chord-wise shift of the aerodynamic center. In particular it is found that, with upward deflections of the movable device, the C_m is larger than for the clean airfoil. That is, the upward deflection of the movable device reduces the pitching moment magnitude. On the contrary, when the L-tab is downward deployed, the pitching moment curve lies below that of the clean airfoil.

The aerodynamic efficiency, namely the lift to drag ratio $E = C_L/C_D$, is shown in figure 3.15(d). Such quantity behaves according to the lift and the drag coefficients just discussed.

3.2.1 Sensitivity to the Mach number

With the aim to have a general perspective on the Mach number sensitivity, simulations at freestream Mach numbers of M = 0.5 and M = 0.7 are performed. In particular the downward deployed L-tab configuration is compared to the clean airfoil at freestream Mach number M = 0.117 and M = 0.7, in terms of pressure distribution, flow field and force coefficients. The airloads computed at M = 0.117, M = 0.5 and M = 0.7 respectively,

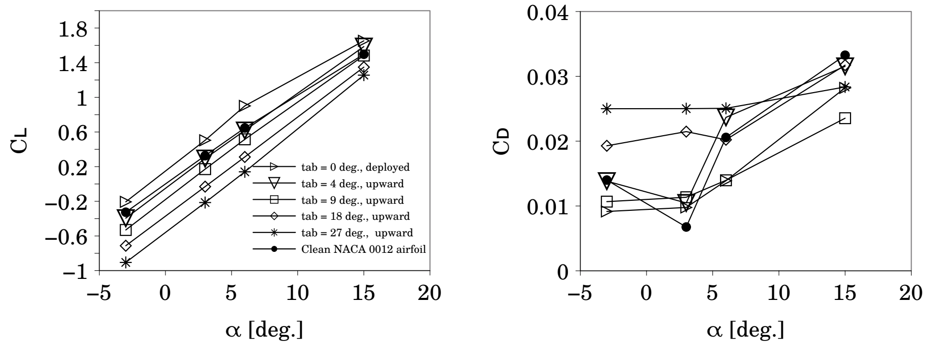

(a) Lift coefficient

(b) Drag coefficient

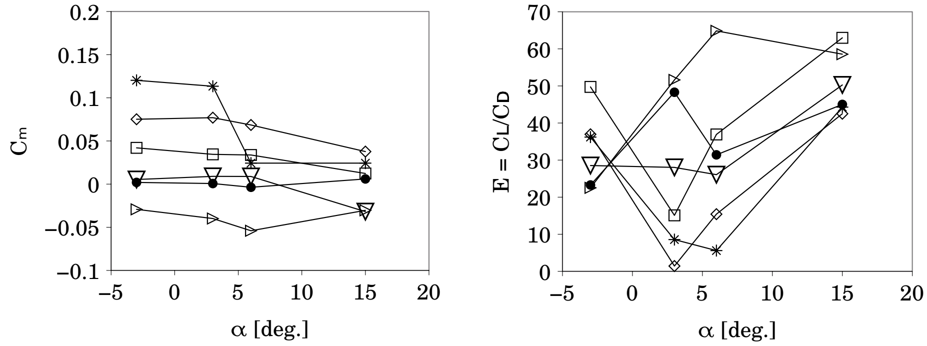

(c) Quarter-chord moment coefficient

(d) Lift to drag ratio

Figure 3.15: Force coefficients and aerodynamic efficiency –namely lift to drag ratio $E = C_L/C_D$, for several rotations of the L-tab together with the clean airfoil, at small angles of attack; M = 0.117, Re $= 1 \cdot 10^6$.

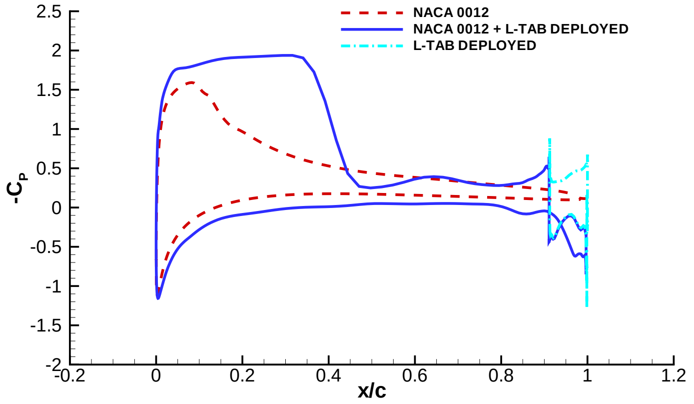

Figure 3.16: Pressure coefficient on the blade section for the clean airfoil (red dashed line) and for the L-tab equipped section (blue solid line + cyan dash-dot line), $\alpha = 6$ deg. and $\beta = 0$ deg. at freestream Mach number $\mathrm{M} = 0.7$, $\mathrm{Re} = 1 \cdot 10^6$.

with the L-tab downward and upward deflected, as well as with the clean airfoil, are also reported. The purpose of such investigation is to assess how the L-tab operates on actual rotor blades, often featuring a transition from subsonic to transonic flow, moving from the root to the tip. In particular the freestream Mach number $\mathrm{M} = 0.7$, is meant to realistically reproduce the supersonic region onset, which is typical of the blade tips in forward flight conditions. As a consequence, a drastic change in the flow field is expected at freestream Mach number of $\mathrm{M} = 0.7$, with respect to $\mathrm{M} = 0.117$. With this regard it appears also useful to remark that trailing edge control surfaces are usually located approx. at the 75% of the blade span, see e.g. Ref. [33]. As a result, according to Ref. [44] p. 296, the operating Mach number at such fraction of the span, is usually not larger than 0.7. This confirms the appropriateness of the Mach number range selected for this preliminary sensitivity study.

Figure 3.16 reports the comparison between the pressure coefficient distribution along the chord, for the clean NACA 0012 airfoil and for the blade section equipped with the L-tab downward deployed, at freestream Mach number $\mathrm{M} = 0.7$. A drastic change is clearly visible between the pressure distribution of the clean airfoil and of the L-tab equipped section. In particular the intensity of the shock is found to be significantly larger, with the movable device installed. Moreover the high-suction region, i.e. the supersonic region, appears to be more extended with respect to the clean section. Additionally, behind the shock, the pressure coefficient on the L-tab equipped section assumes almost the same values of the clean configuration, where a less intense discontinuity is observed. Therefore no local losses in the overall aerodynamic loads, due to the shock compression, are expected with respect to the clean section. As a consequence larger values of the lift coefficient are realistic for the section equipped with the L-tab downward deployed, if compared to those provided by the clean airfoil. The opposite, with respect to the deployed configuration, is likely to occur for upward deflections of the L-tab.

Figure 3.17 reports the Mach number flow field achieved with freestream Mach number $\mathrm{M} = 0.7$, for the clean airfoil, figure 3.17(a), and for the section equipped with the L-tab downward deployed, figure 3.17(b). Consistently with the pressure coefficient, the flow field highlights how the velocity peak area is more extended with the L-tab deployed than for the clean section. This allows to attain larger values of lift, which is in fact one of the operations of the L-tab. Furthermore the flow field confirms how the shock occurring on the section with the downward deployed L-tab is more intense with respect to the clean airfoil.

Notice that the upper side, downstream the super-velocity area, undergoes a flow

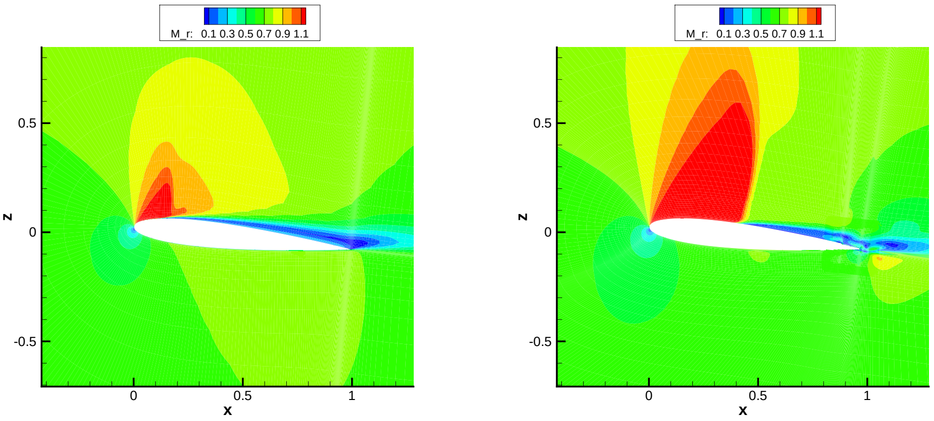

(a) Clean NACA 0012 section

(b) L-tab equipped NACA 0012 section, $\beta = 0$ deg.

Figure 3.17: Mach number flow field at freestream Mach number $\mathrm{M} = 0.7$, Reynolds number $\mathrm{Re} = 1 \cdot 10^6$ and angle of attack $\alpha = 6$ degrees.

separation for both the clean and the L-tab equipped configurations. In particular the separated flow region, has almost the same extension for the deployed L-tab configuration and for the clean section. No significant growths of skin-friction drag are expected on the blade section equipped with the L-tab. On the other hand, the L-tab downward deployed is expected to yield higher values of pressure drag with respect to the the clean configuration. This is due to the stronger compression occurring downstream the shock, on the L-tab equipped section.

With regard to the pressure side, the flow keeps subsonic and the differences between the clean and the L-tab equipped section are qualitatively the same to those encountered at low Mach number. Namely on the lower side the L-tab yields higher pressure and lower velocity, with respect to the clean airfoil. The pressure coefficient, as well as the flow field, related to upward deflections of the L-tab are not herein discussed, for brevity purposes. A behavior specular to what seen for the downward deployed movable device is observed. The pressure coefficient and the flow field for freestream Mach number $\mathrm{M} = 0.5$ are not reported as well, being the results qualitatively similar to those attained at $\mathrm{M} = 0.117$.

Figure 3.18 shows the force coefficients computed at $\alpha = 6$ deg. versus the freestream Mach number, with the L-tab both downward deployed and upward deflected, as well as for the clean NACA 0012 airfoil. The lift coefficient, figure 3.18(a), behaves according to what observed in terms of the pressure distribution. Namely, the large suction area observed at $\mathrm{M} = 0.7$ on the deployed L-tab equipped section, allows for an increase of the resulting load, despite the re-compression behind the shock. On the contrary, this does not occur for the clean airfoil. Indeed the suction region of the nose is found not enough extended, to counteract the shock induced re-compression. As a consequence, a light decrease in the lift coefficient, with respect to $\mathrm{M} = 0.117$ and to $\mathrm{M} = 0.5$, where the flow field is still entirely subsonic, is found. The L-tab upward deflected leads to a further reduction of the suction intensity on the upper side. The lift coefficient vs. Mach number curve results almost parallel to the corresponding of the clean airfoil, with an additional shift to down, due to the aforementioned increase in the zero lift angle.

The drag coefficient, shown in figure 3.18(b), behaves according to what observed in the flow field at $\mathrm{M} = 0.7$. That is, since a stronger re-compression occurs with the L-tab downward deployed, rather than with the clean airfoil, a significantly larger drag increase is found for the section equipped with the movable device. At $\mathrm{M} = 0.5$ there are no significant changes in the drag coefficient, for each of the three configuration therein depicted. A slight decrease is found for the clean airfoil between $\mathrm{M} = 0.117$ and $\mathrm{M} = 0.5$, which is not surprising, in that analogous results were reported by Abbott [70] in his textbook, pp. 283-287. The upward deflected L-tab configuration, at M = 0.117 and M = 0.5, behaves qualitatively likewise the clean airfoil, in terms of lift coefficient. On the other hand, at M = 0.7, the L-tab upward deflected configuration exhibits a smaller drag, with respect to the clean section. Indeed the loads reduction, caused by upward deflections of the L-tab, further reduces the shock intensity and the consequent pressure drag which is generated.

The quarter-chord pitching moment coefficient is reported in figure 3.18(c). At first notice that, with the L-tab upward deflected, the negative nose-up pitching moment keeps always positive. That is, the L-tab upward deflected is stabilizing for the blade section, as expected. For the clean airfoil the pitching moment gets negative at M = 0.7. On the other hand, with the L-tab downward deployed, the moment coefficient is found to be always negative. In particular the shift of this quantity between M = 0.117 and M = 0.5 is found to be almost the same for the section with the L-tab downward deployed and for the clean airfoil. At M = 0.7 the supersonic region on the leading edge area gives an additional contribution to the pitching moment, which undergoes a significant increase in magnitude, both for the downward deployed L-tab configuration and for the clean airfoil. As expected, the shock fosters the nose-up pitching moment, giving a non-stabilizing contribution to the blade pitch. In particular the growth in magnitude is found to be larger with the L-tab downward deployed. With the L-tab upward deflected, the pitching moment coefficient is almost unchanged between M = 0.117, M = 0.5 and M = 0.7.

The lift to drag ratio $E = C_L/C_D$, reported in figure 3.18(d), behaves according to what seen in terms of the lift and drag coefficients. As expected, due to the drag growth, the lift to drag ratio in general decreases between M = 0.117 and M = 0.7. Nevertheless at M = 0.5, the lift growth, together with no significant changes in drag, lead to a light increase of efficiency, for the L-tab upward deflected configuration and for the clean airfoil. Moreover, for the upward deflected configuration, a lower loss in efficiency is found at M = 0.7, since a less strong re-compression is encountered on the upper side, past the shock.

Overall, as anticipated in the above, the drag increase is a common issue to all of the high-lift devices, which are specifically designed to enhance the normal force. Moreover, the behavior of the flow field and of the aerodynamic loads just discussed, are similar to those concerning other GF-like devices in transonic flows, available in literature. Similar results were found, for instance, by Li [101] and by Yu [102]. In general the L-shaped GF is found capable to effectively operate also in compressible and transonic flow conditions, typically encountered on rotor blade environments. Indeed the computations performed at M = 0.7 highlight that, when downward deployed, the L-tab is still capable to significantly increase the lift coefficient. Additionally, upward deflections of the L-tab at M = 0.7, are found to allow for effective load alleviations, consistently with the behavior encountered at low Mach number.

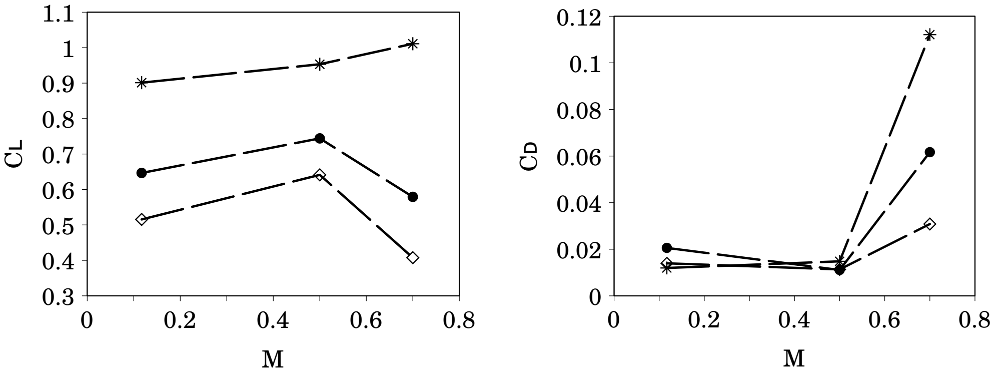

(a) Lift coefficient

(b) Drag coefficient

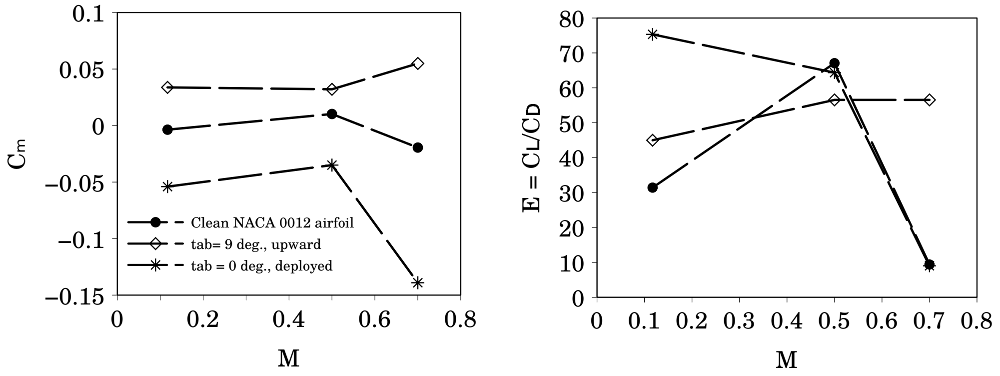

(c) Quarter-chord moment coefficient

(d) Lift to drag ratio

Figure 3.18: Force coefficients and aerodynamic efficiency –namely lift to drag ratio $E = C_L/C_D$– vs. freestream Mach number, for the clean airfoil and for the L-tab equipped section. Reynolds number $\text{Re} = 1 \cdot 10^6$ and angle of attack $\alpha = 6$ degrees.

3.3 Steady state computations in stall conditions

The effects of the L-tab in static stall conditions are investigated by means of numerical computations at high/stall angles of attack. Such simulations are carried out at a Mach number of M = 0.117. Several rotations of the movable device are considered to this purpose. Figure 3.20 shows the aerodynamic loads and the lift to drag ratio in stall conditions. Notice that for angles of attack smaller than the stall value, the behavior encountered is qualitatively similar to what occurs at low incidence. Therefore the present section is primarily focused on the investigation of the L-tab behavior after the stall onset.

Figure 3.19 shows the non-dimensional velocity magnitude field at $\alpha = 18$ deg., with the movable device 9 deg. upward deflected, compared to the clean airfoil. The velocity is made dimensioneless with respect to the freestream sound speed $c_{\text{ref}} = 346$ m/s. The reduction of the separated flow area achieved through the movable device is clearly visible. Moreover the nose suction area with the L-tab upward deflected is found to be more extended than the one related to the clean airfoil, thus helping in achieving higher values of lift, see the squared marker at $\alpha = 18$ deg. in figure 3.20(a).

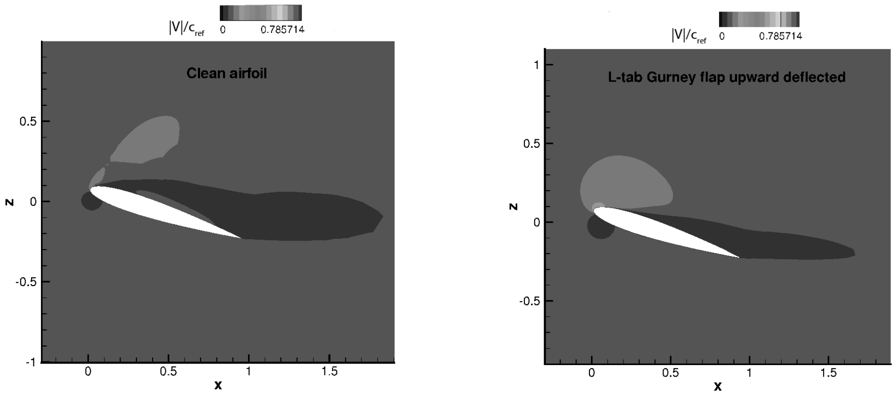

(a) Clean NACA 0012 airfoil (b) Blade section with the L-tab, $\beta = 9$ deg.

Figure 3.19: Non-dimensional velocity magnitude field at angle of attack $\alpha = 18$ degrees. The velocity is made non-dimensional with respect to the freestream sound speed $c_{\text{ref}} = 346$ m/s; freestream Mach number M = 0.117, Reynolds number $\text{Re} = 1 \cdot 10^6$.

The lift coefficient is reported in figure 3.20(a). Notice at first that the computed stall onset occurs at approx. $\alpha = 17$ degrees for the clean airfoil, as well as for upward deflections of the L-tab. On the other hand, with the L-tab downward deployed, the stall is found to be slightly anticipated, namely between $\alpha = 16$ deg. and $\alpha = 17$ degrees. In can be also observed that the L-tab upward deflected allows for an increase of the post-stall lift, with respect to the clean airfoil, up to the 20%. Therefore a proper actuation of the movable device could be very helpful in alleviating part of the stall issues. With this regard figure 3.20(b) shows that the L-tab is also capable to significantly reduce the drag rise related to the stall separation. Indeed upward deflections of the L-tab show a much less extended recirculating flow area, as it can be clearly seen in figure 3.20(b). The present movable device results beneficial also in terms of the moment coefficient, which is reported in figure 3.20(c). In particular the L-tab upward deflected leads to a drastic reduction in the pitching moment magnitude for post-stall angles of attack, with a stabilizing effect on the blade section. Namely upward deflections of the tab allow for pitching moment magnitude reductions higher than the 80%. The lift to drag ratio is shown in figure 3.20(d) and it is primarily affected by the drastic effects of the L-tab on the drag coefficient. That is, a larger lift to drag ratio is achieved with the L-tab upward deflected, if compared to the clean airfoil, therefore helping in reducing power requirements and operation costs.

It appears useful to remark again that, of course, the numerical investigation of the

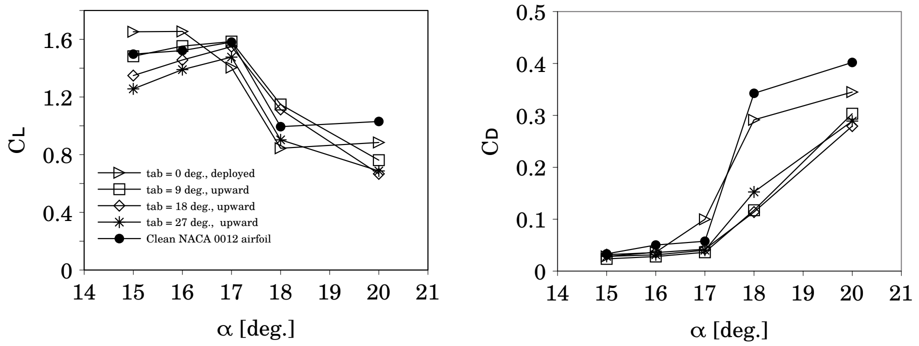

(a) Lift coefficient (b) Drag coefficient

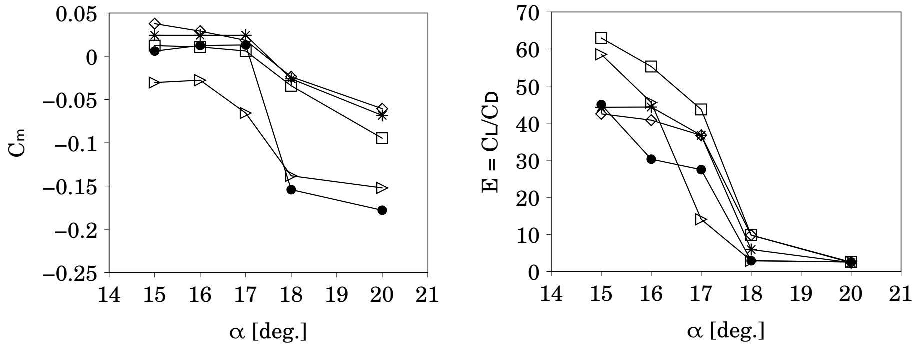

(c) Quarter-chord moment coefficient (d) Lift to drag ratio

Figure 3.20: Force coefficients and lift to drag ratio vs. α for the $10\%c$ L-tab at high/stall angles of attack; freestream Mach number $\mathrm{M} = 0.117$, Reynolds number $\mathrm{Re} = 1 \cdot 10^6$.

stall behavior with 2D RANS computations has to be meant as merely qualitative, since separated flows are intrinsically three-dimensional and most turbulence models are likely to fail in capturing the actual behavior of the vortical structures. Nevertheless a much finer discretization, aiming to increase the accuracy, would require a rise in the computational burden, excessively time-consuming within the aims of this preliminary study. Moreover 2D steady-state RANS computations are often used in literature for numerical assessments of both clean and trailing edge devices equipped sections, in static and dynamic stall conditions, see again Refs. [25, 33, 34]. Therefore 2D steady-state RANS simulations are retained appropriate to assess at least the qualitative behavior of this novel L-shaped tab in stall conditions.

3.3.1 Sensitivity to the L-tab chord-wise length

In order to evaluate an eventual improvement of its effectiveness, a L-tab with double chord-wise length, i.e. $20\%c$ long, is tested. The distinguishing mark of this geometrical modification, with respect to the reference size, lies in the location of tab hinge along the chord. Therefore the difference between these two solutions is not merely limited to the larger circular arch achieved for equal rotations of the L-tab. Indeed, in the present case, the L-tab hinge is in general located upstream with respect to the re-compression region of the suction side. As a consequence, an upward deflection of this longer movable device is expected to be more effective on the flow separation, potentially leading to a local reattachment of the flow. Since the main concern of the present sensitivity study is to enhance the performance of the L-tab on the flow separation, only the results achieved for high/stall angles of attack are herein discussed.

The flow fields of the non-dimensional velocity magnitude obtained at $\alpha = 18$ deg.

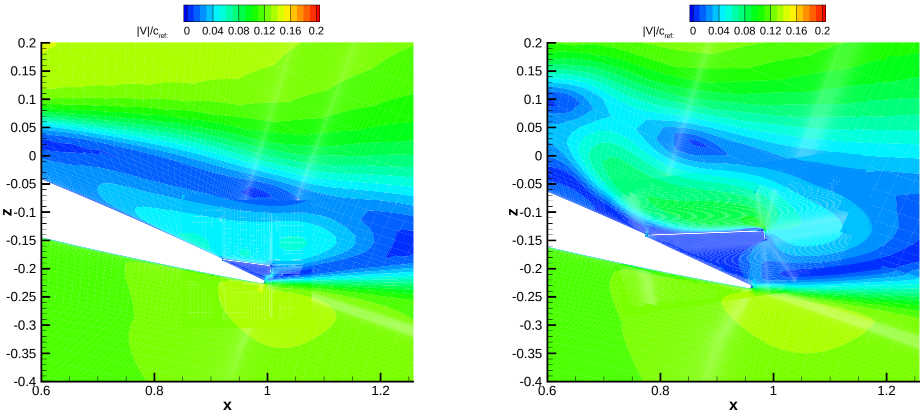

(a) 10%c long L-tab

(b) 20%c long L-tab

Figure 3.21: Flow field of the non-dimensional velocity magnitude for the reference and the double-length L-tab, $\alpha = 18$ deg. and $\beta = 27$ degrees; freestream Mach number $\mathrm{M} = 0.117$, Reynolds number $\mathrm{Re} = 1 \cdot 10^6$.

and $\beta = 27$ deg., for the 10%c and the 20%c L-tab, are reported in figure 3.21. The velocity is made non-dimensional with respect to the freestream sound speed $c_{\mathrm{ref}} = 346$ m/s. Notice that, with the shorter tab, the flow is completely separated, whereas with the longer configuration, a region of reattachment is observed, therefore reducing the lift coefficient losses typical of the stall conditions.

The force coefficients and the lift to drag ratio, achieved with the 20%c L-tab, are reported in figure 3.22. Notice that, with the present double-length L-tab, the static stall behavior appears improved with respect to the shorter device, see figure 3.20. Positive effects are found for each of the aerodynamic quantities. In particular simulations carried out at $\beta = 18$ deg. and $\beta = 27$ deg. highlight how the stall onset may be even delayed to higher angles of attack, see figure 3.22(a). Figure 3.22(b) shows the improvements achieved in terms of drag reduction with the longer L-tab. In particular for $\alpha = 18$ deg. and $\beta = 27$ degrees, since the stall hasn't occurred yet, approx. a 75% drag reduction is attained with respect to the clean section, see also figure 3.20(b) for comparison. Furthermore, a more effective operation, with respect to the 10%c long L-tab, is encountered in terms of the pitching moment coefficient, reported in figure 3.22(c). The behavior of the lift to drag ratio, represented in figure 3.22(d), follows from what observed with regard to the lift and drag coefficients.

Figure 3.23 shows the results of a preliminary optimization study for the lift coefficient developed at high angle of attack, namely $\alpha = 18$ degrees, with respect to the L-tab deflection. As shown in the above, the double length L-tab provides larger lift, with respect to the 10%c long one, for equal rotation angles of the TE device. Notice that, with the longer tab a high peak in effectiveness is found for $\beta = 27$ degrees. Indeed, for $\beta = 27$ deg. the improvements provided are so important, that the L-tab action results in a stall onset delay, as shown in figure 3.22(a). On the other hand, a lower effectiveness is in general observed by employing the shorter tab.

Overall the longer tab appears to be more effective at high/stall angles of attack, even allowing for a delay in the stall onset. In turn the drag coefficient is of course much lower, for the conditions where the flow is kept attached. This yields an increase of the lift to drag ratio as well, with consequent potential advantages in terms of power requirements and fuel consumption. Additionally, if the stall is avoided, the magnitude of the pitching moment coefficient is kept low as well. This means that the pitching moment can act positively on the aerodynamic damping. Therefore, a more effective counteraction of the blade torsion can be achieved, thus potentially delaying the incoming of aeroelastic

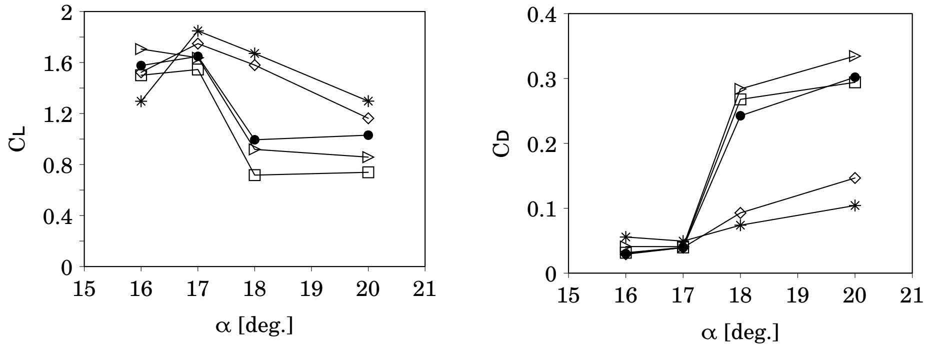

(a) Lift coefficient

(b) Drag coefficient

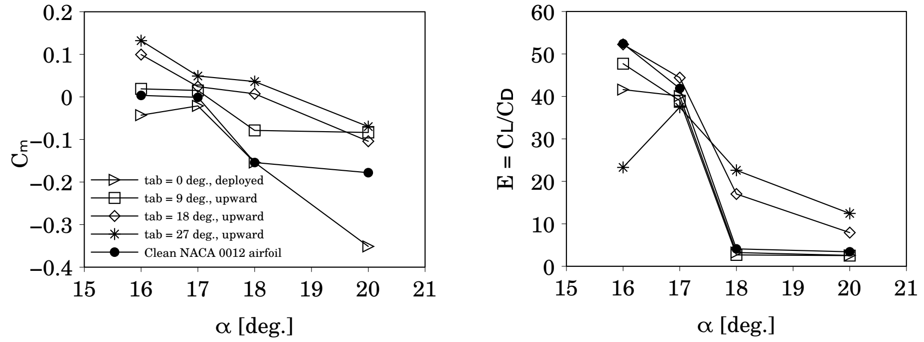

(c) Quarter-chord moment coefficient

(d) Lift to drag ratio

Figure 3.22: Force coefficients and lift to drag ratio $E = C_L/C_D$ for the 20%c L-tab at high/stall angles of attack; freestream Mach number M = 0.117, Reynolds number $\mathrm{Re} = 1 \cdot 10^6$.

instabilities as well. However, for small angles of attack, the 10%c L-tab, behaves similarly to the 20%c movable device. With this regard, not negligible advantages, with respect to the longer configuration, are expected in terms of the actuation power requirements and operating costs. Therefore the selection of the chord-wise length of the L-tab requires to take into account several aspects at the same time. The ultimate choice has to be made with additional insights into the behavior of the movable device, including more detailed sensitivity studies to the L-tab chord-wise length.

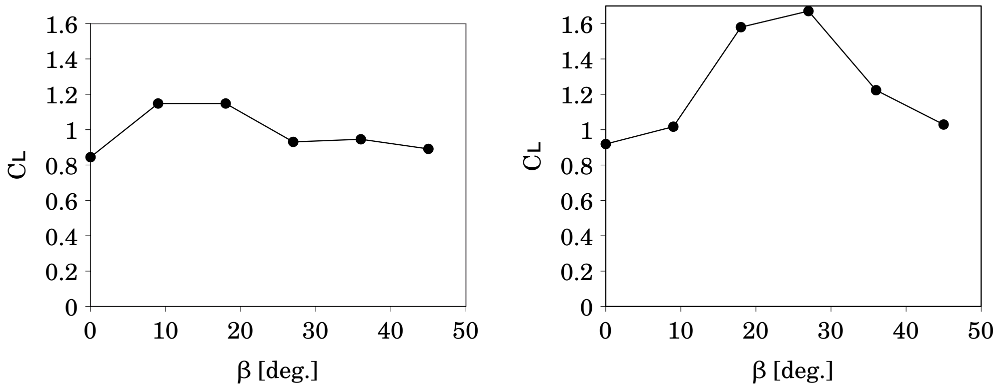

(a) 10%c long L-tab

(b) 20%c long L-tab

Figure 3.23: Lift coefficient computed at $\alpha = 18$ deg. with the 10%c L-tab and with the 20%c L-tab, respectively; freestream Mach number $\mathrm{M} = 0.117$, Reynolds number $\mathrm{Re} = 1 \cdot 10^6$.

3.4 Comparison with experimental results

The reliability of the numerical model is also tested by means of comparisons with experimental results attained on the same L-shaped GF.

Pressure measurements and PIV surveys in steady conditions are carried out on a blade section model equipped with the L-tab. The experimental model of the L-tab is made in carbon fiber with a chord-wise length equal to 8.33%c and a height equal to 1.33%c. The test campaign is conducted in the 1.5m×1m low-speed closed-return wind tunnel of the Aerodynamics Laboratory of the Dipartimento di Scienze e Tecnologie Aerospaziali (DSTA). The measurements reported in this work are provided by the experimental fluid dynamics group of DSTA. The experimental rig used for this activity is suitable for tests on oscillating airfoils successfully used to study the retreating blade dynamic stall. Moreover, the same experimental rig is employed to investigate the effects of the L-tab in fixed positions for deep dynamic stall conditions [103]. The NACA 23012 section model, completely in aluminium, has a chord of 0.3 m and a span of 0.93 m (aspect ratio 3.1), see figure 3.24.

The NACA 23012 airfoil is selected for the experimental activity since, being a typical helicopter blade section, it was object of experimental investigations about the dynamic stall process [35]. The model central section is interchangeable depending on the measurement technique involved. In particular, one central section is equipped with 21 pressure taps positioned along the midspan airfoil contour (see Ref. [35] for the taps distribution

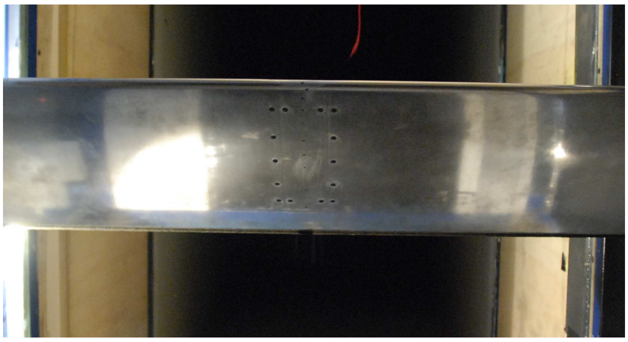

Figure 3.24: NACA 23012 blade section model inside the Politecnico di Milano wind tunnel.

along the chord). A different central section without taps is used to perform PIV surveys in the model midspan plane. Pressure measurements are carried out using a 32 ports PSI scanner system (1 psi F.S.). The 2D PIV surveys are carried out at the TE region where the L-tab is installed. The PIV system uses a Nd:Yag double pulsed laser with 200 mJ output energy and a double shutter CCD camera with a 12 bit, 1952×1112 pixel array. The correlation of the image pairs is carried out using a smaller interrogation window of 8×8 pixels. The PIV velocity fields are phase averaged over 100 image pairs. More details about the experimental set up can be found in Ref. [35].

The tests include steady state conditions reproducing both pre-stall and post-stall conditions with the L-tab fixed in two different positions. When deployed, the tab is attached to the airfoil upper surface so that the end prong protrudes at the airfoil TE. In retracted position the tab features a deflection angle of $\beta = 9.1$ deg. The tests are carried out at freestream velocity of 30 m/s, corresponding to $\mathrm{Re} = 6 \times 10^5$ and $\mathrm{M} = 0.09$. The numerical simulations are performed on a 2D computational grid specifically built up on a NACA 23012 section with a L-shaped GF of the same size of the experimental model. To account for the rotation of the tab with respect to the airfoil, a system of two overlapped multi-block structured grids is realized, consistently with the approach illustrated in the above for the NACA 0012 section. The comparison between numerical and experimental results with the L-tab is carried out in pre-stall and post-stall conditions at the same effective angle of attack, taking into account the induced incidence effect, since, of course, the experimental model has finite span. A quantitative validation of the numerical model is carried out by the comparison of the C_P distribution measured on the airfoil surface. Moreover, the flow fields computed at the trailing edge region are compared with PIV results to investigate specifically the phenomena occurring nearby the L-shaped tab.

Pre-stall condition

The comparison in pre-stall condition is carried out at the effective angle of attack, i.e. by taking into account the wall induced incidence effect. The effective angle of attack corresponds to 7.3 deg. for the L-tab deployed configuration and to 7.7 deg. for the retracted L-tab configuration, when the experimental model is rotated of 9 deg. with respect to the quarter-chord. The induced angle of attacks are attained by comparing the lift coefficient curves numerically computed and experimentally attained by integrating the measured pressure distribution. Such comparisons are performed for the clean NACA 23012 section, for the blade with the L-tab downward deployed and for the blade with the L-tab upward deflected, respectively. In fact the induced angle of attack is found slightly different for each of these geometrical configurations.

Figure 3.4 shows the comparison between the experimental and numerical C_P distributions in the tested pre-stall condition. A very good matching of the computed and measured C_P over the upper and the lower surface of the airfoil is obtained at the same effective angle of attack, for both the L-shaped tab configurations tested. Notice that also the C_P nose peaks are well captured by the CFD. This quantitative comparison confirms the reliability of the numerical model for the main scope of the work, which indeed consists in the investigation of the behaviour of the novel L-shaped tab in attached flow conditions.

The comparison of the velocity fields past the trailig edge is presented in Figs. 3.26(a) and 3.26(b). These report the velocity magnitude contours as well as the in-plane streamlines patterns. For the test configuration with the tab deployed reported in figure 3.26(a), the PIV survey confirms the generation of two counter-rotating vortical structures behind the end prong of the tab. The numerical flow field at the same effective angle of attack shows similar flow structures, but some differences can be observed in the extent of the wake behind the tab. These discrepancies could be mainly related to the fact that the comparison is performed between the PIV phase averaged experimental flow field for the experimental case and the numerical solution obtained with Reynolds averaged computations. In order to capture the same unsteady flow field near the trailing edge shown by the phase-averaged PIV data, a time resolved CFD solution should have to be averaged over a quite longer period of calculation. This is not feasible considering the available

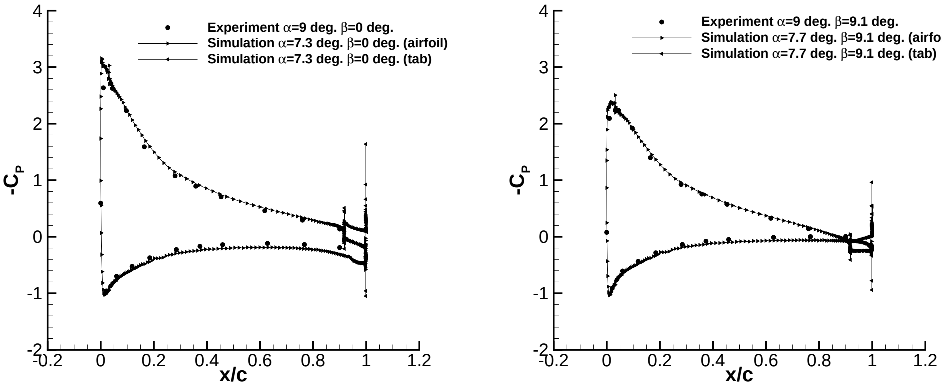

(a) $\alpha = 7.3$ deg. and $\beta = 0$ deg.

(b) $\alpha = 7.7$ deg. and $\beta = 9.1$ deg.

Figure 3.25: Comparison of experimental and numerical C_P distribution in pre-stall condition. Mach number M = 0.09, Reynolds number Re = $6 \cdot 10^5$.

computational resources and the scope of this work. Moreover, it has to be pointed out that the differences observed in the wake region could be also related to the lower accuracy of the PIV data in a flow region characterised by very low velocities. Another aspect to be taken into account is that the reconstruction of very small vortical structures as those typical of the present test cases is a very challenging activity considering the resolution of the available PIV camera. Additionally the numerical solver requires the employment of a slotted configuration of the airfoil/L-tab system, to deal with arbitrary rotations of the TE device. The slot between the airfoil and the tab is expected to induce local modifications in the flow field, though the global effects in terms of loads are negligible at low angle of attack. This is indeed consistent with the comparison of the pressure coefficient computed on the numerical slotted geometry and on the experimental no-slotted model.

With the retracted tab, the PIV results show a structure similar to the one observed for the deployed tab. In this case a quite bigger closed cell turning counterclockwise is observed (see figure 3.26(b)). The numerical flow field obtained in this configuration shows a very similar flow structure behind the end prong of the tab. Moreover, also the extent of the wake is better captured by the simulation with respect to the deployed tab configuration. Indeed, when the L-tab is upward deflected, the effect of the slot on the counter-rotating vortical structures is expected to be lower.

Post-stall condition

The comparison in post-stall condition is carried out at the effective angle of attack of 18 deg. for both the L-tab configurations.

Figure 3.27 shows the comparison between the experimental and the numerical C_P distributions in the tested post-stall condition. A quite good agreement between the computed and measured C_P over the upper surface of the airfoil can be observed for both the L-tab configurations. On the other hand discrepancies are encountered on the lower surface of the airfoil. This quantitative comparison indicates that for the post-stall condition the accuracy of a two-dimensional model for the simulation of the flow is lower with respect to the attached conditions, as remarked in the above.

This consideration is confirmed by the comparison of the flow fields at the trailing edge region. In particular, with the tab both deployed and retracted, the phase averaged experimental as well as the Reynolds averaged numerical flow fields show a separation region at the trailing edge characterized by a large vortical structure behind the end prong of the tab (see figures 3.28(a) and 3.28(b)).

The experimental and the numerical flow fields exhibit streamlines with reasonably

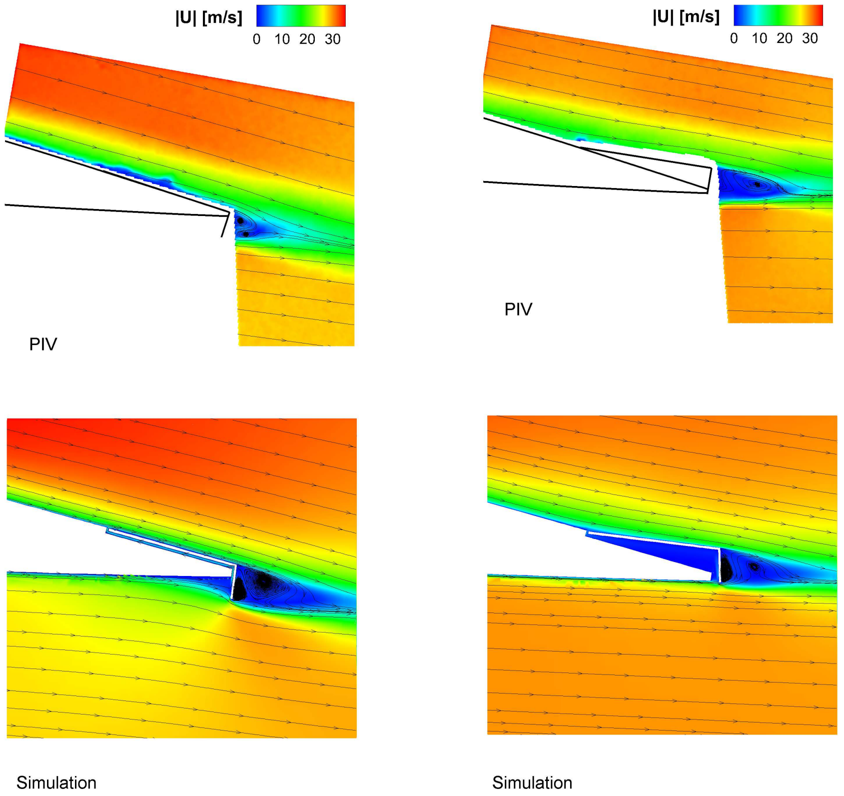

(a) α = 7.3 deg. and $\beta = 0$ deg. (b) α = 7.7 deg. and $\beta = 9.1$ deg.

Figure 3.26: Comparison of the velocity magnitude contours in pre-stall condition. Mach number M = 0.09, Reynolds number Re $= 6 \cdot 10^5$.

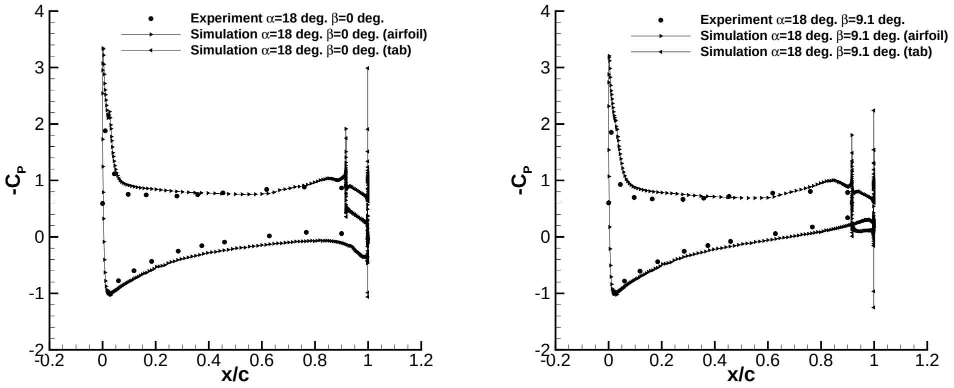

(a) α =18 deg. and $\beta = 0$ deg. (b) α =18 deg. and $\beta = 9.1$ deg.

Figure 3.27: Comparison of experimental and numerical C_P distribution in post-stall condition. Mach number M = 0.09, Reynolds number Re $= 6 \cdot 10^5$.

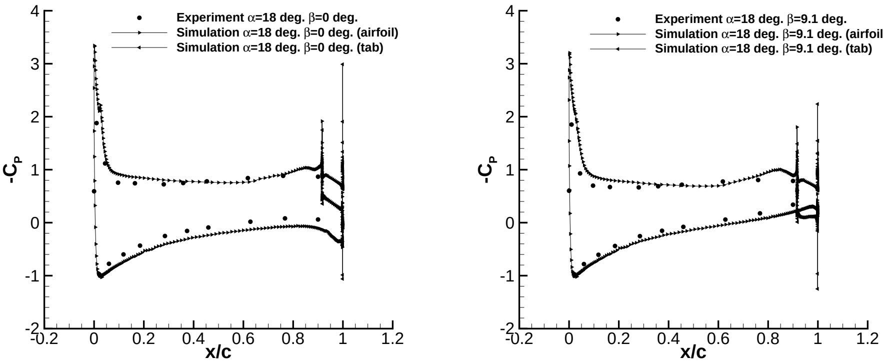

(a) α =18 deg. and β = 0 deg.

(b) α =18 deg. and β = 9.1 deg.

Figure 3.28: Comparison of experimental and numerical C_P distribution in post-stall condition. Mach number M = 0.09, Reynolds number Re = $6 \cdot 10^5$.

similar behavior, in particular in the shape and extension of the counter-clockwise vortical structure. Also the stream traces of the clockwise vortical structure related to the separation bubble numerically computed are remarkably parallel to the experimental counterparts. As a result the numerical mean inclination of the wake, significantly affecting the resulting airloads, is found in good agreement with the experiments. Nevertheless, the quantitative comparison of the velocity values in the investigated flow fields confirms some discrepancies between the and experiments results. These differences are mainly related to the aforementioned limitations of a two-dimensional model for the reproduction of massively separated flows. However, the comparison of both the C_P distributions and of the flow fields shows that an acceptable level of confidence can be obtained with the present numerical model for the investigation of the L-shaped tab functioning, even at angles of attack around the stall condition.

The overall reasonable matching with the experimental measurements, reported in this section, is an important validation of the present numerical results, which represent the elemental basis of the whole work. Additionally the agreement with the experiments suggests that no significant three-dimensional phenomena affect the flow field, at least for attached flow conditions. As a consequence two-dimensional numerical computations appear in fact appropriate, to investigate the L-tab behavior in this regime.

3.5 Three dimensional steady state computations

In order to further validate the feasibility of two-dimensional computations, preliminary three-dimensional steady state numerical simulations are carried out on a model of finite span. With this purpose a blade section model with span length of two chords is realized. The L-tab is supposed to be installed along the whole span. The geometrical properties of the model are thought to be span-wise uniform. Figures 3.29(a) and 3.29(b) report the geometrical model for the three dimensional solid body.

A system of two multi-block structured grids is realized around the blade model, with the same approach adopted for the 2D geometry. That is a C-type background grid, extending from the airfoil up to the far-field at twenty-five chords is realized, see figure 3.30(a). Consistently a small overlapping fine rectangular grid, surrounding the L-tab, is built, see figure 3.30(b). The cells on the span sections are located according to the two-dimensional model, in terms of number, as well as of spatial distribution, see section 3.1. Twenty elements with uniform spacing are realized along the span direction, yielding a span-wise spatial resolution of 0.1 chords. As a result the 3D background and overlapping

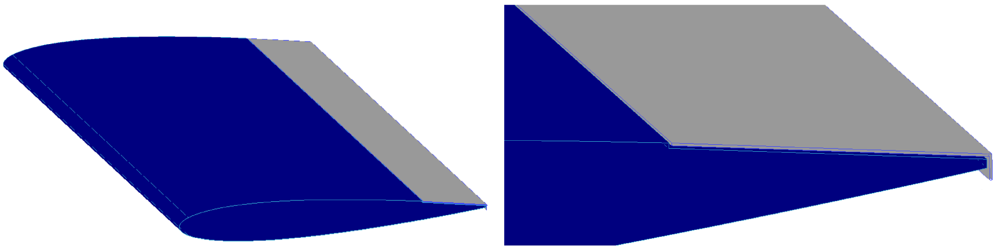

(a) (b)

Figure 3.29: Geometrical model for the three-dimensional computations, complete solid body (a) and detail of the trailing edge (b).

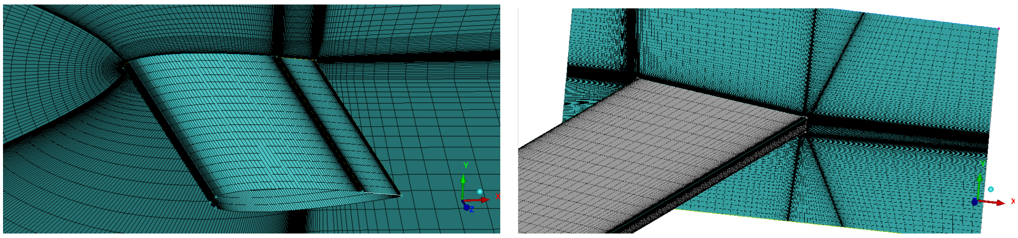

(a) (b)

Figure 3.30: Details of the three dimensional computational grid, airfoil (a) and L-tab (b).

grids are composed of approx. one million of cells each, being the total volumes equal to 2 378 325, with the tagging procedure to be performed. Slip symmetry boundary conditions are applied on the side walls of the model. Notice that the span-wise discretization of the grid is consistent with those employed in some other works for similar CFD simulations. In Ref. [104] a comparable spacing is used for the reference grid realized for three-dimensional dynamic stall computations. In Ref. [104] refinement studies of the span-wise spatial resolution of the grid are also reported. It is shown that, especially in the upstroke phase of the oscillation, which at low angles of attack provides loads not dissimilar to the steady state counterparts, the resulting forces do not change if the spatial resolution of the grid is enhanced, with respect to the reference. This confirms that the span-wise spatial resolution of the grid here selected is appropriate for the present three-dimensional computations at low angles of attack on the L-tab equipped blade model.

The 3D simulations herein reported are carried out at $\mathrm{Re} = 1 \cdot 10^6$, $\mathrm{M} = 0.117$, $\alpha = 0$ deg. and $\beta = 0$ degrees. The configuration with the L-tab downward deployed is selected, since, as reported in section 3.1, it appears the most critical for the flow close to the tab.

Figure 3.31 reports the pressure coefficient C_P extracted at four sections along the model span, compared to the two-dimensional results. Notice that, both on the airfoil and on the L-tab, the 3D sectional pressure coefficient results overlapped to the corresponding 2D curves.

The Mach number flow field close to the trailing edge is extracted at several sections along the span and compared to the 2D results as well, see figure 3.5. No significant differences are in fact encountered in the trailing edge flow field, by moving along the span. Moreover the trailing edge flow field appears to be very similar to that attained with the 2D computations.

The good matching between the 3D sectional results and the 2D computations is an useful confirmation of the feasibility of the two-dimensional flow hypothesis of the present work. A further validation of this elemental assumption can be achieved by looking at the velocity component parallel to the pitch axis, i.e. the span direction. By considering several slices along the span is it found that the transverse velocity keeps everywhere lower than $\sim 10^{-3}$, that is the 10% of the vertical component and the 1% of the horizontal component.

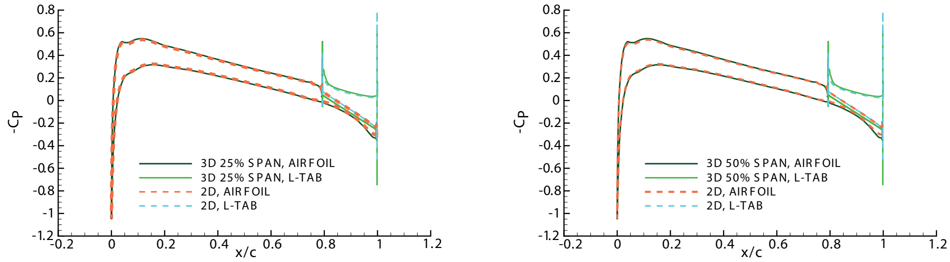

(a) 25% span (b) 50% span

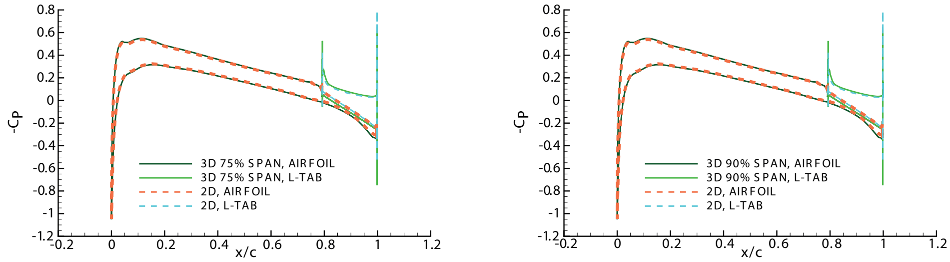

(c) 75% span (d) 90% span

Figure 3.31: Pressure coefficient at several sections along the span together with the corresponding 2D; Re $= 1 \cdot 10^6$, M $= 0.117$, $\alpha = 0$ deg. and $\beta = 0$ degrees.

These findings, which take into account even the sign of the transverse velocity and not merely its magnitude, show that the transverse velocity is in fact negligible with respect to the two remaining components. For brevity purposes the images of the transverse velocity component are not herein reported.

Figure 3.33(a) reports the streamlines close to the solid body. These are found to be almost parallel to the chord of the model, along the entire span, both on the upper and on the lower side. The absence of significant three-dimensional phenomena affecting the flow field is therefore further confirmed. Figure 3.33(b) reports the streamlines close to the vertical edge of the L-tab. Almost the same counter rotating vortical structures of the two-dimensional computations are observed, see figure 3.12 for comparison. This latter is a remarkable result in the context of the present work, since the aerodynamic loads generated by the L-tab are interpreted as a direct consequence of the counter rotating vortical structures developed close to the trailing edge.

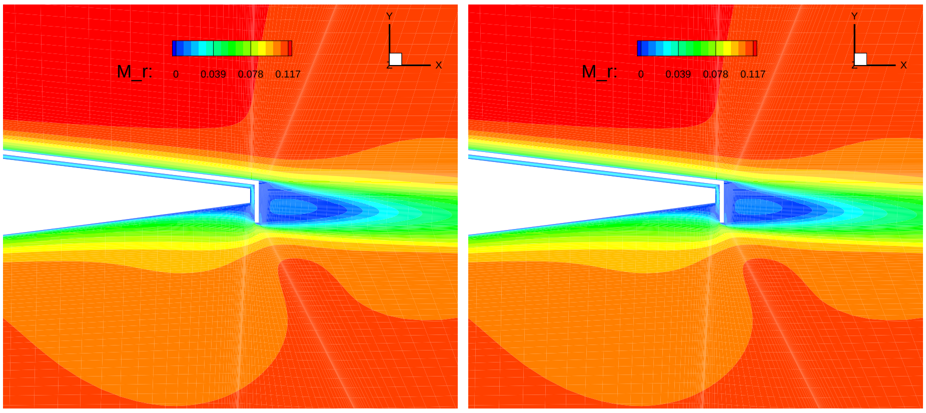

(a) 25% span (b) 50% span

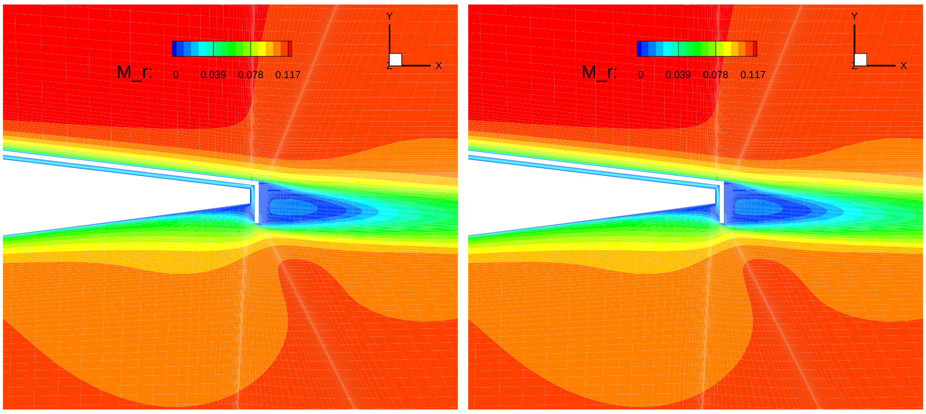

(c) 75% span (d) 90% span

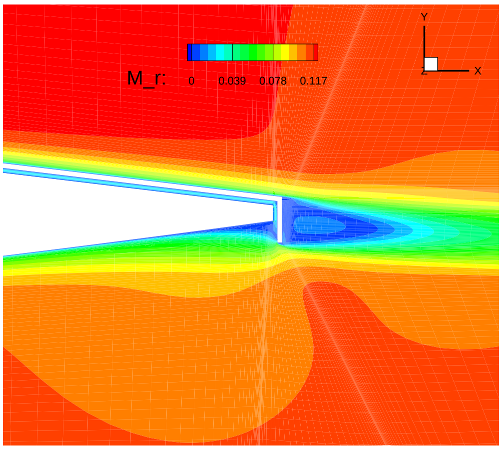

(e) 2D

Figure 3.32: Trailing edge Mach number flow field at several sections along the span, together with the corresponding 2D; $\mathrm{Re} = 1 \cdot 10^6$, $\mathrm{M} = 0.117$, $\alpha = 0$ deg. and $\beta = 0$ degrees.

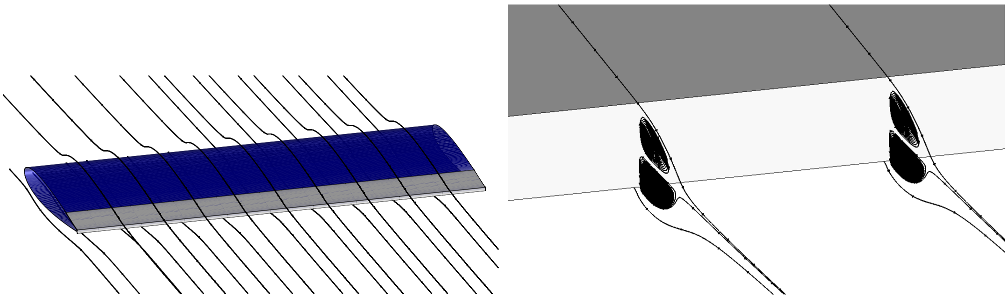

(a) (b)

Figure 3.33: Streamlines close to the body, whole model (a) and detail of the trailing edge (b); Re $= 1 \cdot 10^6$, M $= 0.117$, $\alpha = 0$ deg. and $\beta = 0$ degrees.

3.6 Concluding remarks

A numerical assessment of an innovative L-shaped tab installed on a NACA 0012 airfoil is reported in this chapter.

Steady state computations are carried out, both at small angle of attacks and in deep stall conditions. Configurations with several rotations of the movable device are considered. To achieve a preliminary estimation of the span-wise effectiveness of the L-tab on rotor blades, a Mach number sensitivity analysis is performed.

The present aerodynamic steady state characterization highlights how beneficial effects can be achieved with the L-tab both downward deployed and upward deflected. Advantages are meant in an adaption of the section camber to the flight conditions for helicopter rotors. The upward deflection of the present device can alleviate the stall drawbacks. On the other hand, a downward deployment could be exploited to keep the load balance between the retreating and the advancing side of the blade azimuth, beyond the operating ranges of the helicopter cyclic pitch. Additionally no losses in effectiveness are encountered when the L-tab operates in compressible and transonic flow conditions, typical of rotor blade tips.

Very promising results in the stall regime are attained by doubling the L-tab chordwise length. Such longer configuration is found more effective in deep stall conditions, whereas no significant improvements are achieved at small angles of attack.

The reliability of the numerical models is tested by comparisons with experimental results obtained for a NACA 23012 equipped with the same L-tab, both at small and post-stall angles of attack. The comparisons in terms of loads distributions and velocity fields show a good agreement between the simulations and the experimental data, thus strongly validating the numerical investigations reported in this work.

Additionally the matching with respect to the experimental results, as well as with respect to the 3D computations, suggests how the flow keeps almost 2D when the L-tab is installed, at least for attached conditions. As a consequence the assumption of two-dimensional behavior is found appropriate to investigate the L-tab. This finding ultimately confirms the reliability of the 2D computations carried out in this work.

The steady state investigation on the L-tab operation is also staple with regard to the unsteady characterization reported in the next chapters. Since harmonic motions will be taken under consideration, the mean behavior in terms of flow field and aerodynamic loads will be inferred from the steady state assessment herein discussed.

Chapter 4

Unsteady aerodynamic assessment of a blade section with a L-shaped Gurney flap

The L-tab introduced in chapter 3 is herein characterized for small amplitude oscillating motions, within the ultimate aim to realize an active control system, capable to reduce vibration on rotor blades. The small perturbation regime allows to assume the behavior of the system as linear. By the way, the 20 %c-long L-tab –more effective in improving performance at medium/high angles of attack– is employed, to ensure a better performance also in terms of static load balancing, which is indeed another target of the movable device. In section 4.1 harmonic pitch or plunge oscillations of the clean airfoil, with the L-tab at various fixed rotations, are studied. In section 4.2 harmonic deflections of the L-tab, with the airfoil at constant angle of attack, are investigated. The flow field and the airloads are characterized, for reduced frequencies ranging from 0.1 to 0.6. The flow field shows the two Counter Rotating Vortical structures (CRV) developed behind the L-tab, already highlighted by the steady state computations, see chapter 3. Such CRV are observed when the airfoil is in motion, as well as when the L-tab is harmonically deflected. Additionally, for unsteady motions either of the airfoil or of the tab, one of the CRV is found to detach from the trailing edge, being then shedded downstream. A new vortical structure is anon generated past the L-tab. The oscillations observed in the hysteresis cycles of the resulting multi-harmonic aerodynamic loads, are interpreted as a consequence of such detachments. The frequency analyses of the numerical airloads highlight an almost constant ratio between the shedding and the motion frequencies. Moreover the value of such ratio is approx. the same for pitch, plunge and tab oscillations. It is shown how, by the way, the magnitude of these secondary harmonics is much lower than the amplitude of the component at the same frequency of the motion. Moreover the response at the same frequency of the tab activation is by far the main concern for the Higher Harmonic Control (HHC) algorithm classical formulation, which is indeed employed in this work. Therefore, the first harmonic component is extracted from the unsteady loads and investigated at several reduced frequencies. For pitch and plunge motions of the airfoil, the prevailing effects on the first harmonic are attributed to the airfoil thickness, rather than to the modification of the mean line shape induced by L-tab rotation. On the contrary, for oscillating motions of the L-tab, the first harmonic of the airloads is found deeply affected by the mean line modifications induced by the movable device. Concluding remarks to the general unsteady assessment are reported in section 4.3.

4.1 Pitching and plunging airfoil with the L-tab in fixed position

4.1.1 Numerical simulations for pitching and plunging motions

Numerical simulations are carried out for a L-tab equipped NACA 0012 section, oscillating in pitch with respect to the quarter of chord. Computations are also performed for harmonic plunge motions of the airfoil. The freestream Mach number is set to $\mathrm{M} = 0.117$ and the Reynolds number is fixed at $\mathrm{Re} = 1 \cdot 10^6$.

Oscillations with zero mean value and amplitude of one degree are considered, whereas for the plunge motion the amplitude is set equal to $h/c = 0.01$. Therefore, in the present case, the equivalent angle of attack [105] $\alpha_{\mathrm{eq}} = \dot{h}/U$, grows linearly with the reduced frequency. It results that, for $k = 0.1$ $\alpha_{\mathrm{eq}} = 0.0573$ degrees, whereas for $k = 0.6$ one gets $\alpha_{\mathrm{eq}} = 0.3438$ degrees. However, the change in the equivalent angle of attack is not influential for the present purpose, since the behavior of the system is supposed to be linear.

To check the reliability of the numerical results for unsteady pitch and plunge motions, a convergence analysis is carried out in terms of resolution in the real-time. The test case for the convergence study is the configuration with the L-tab downward deployed, i.e. $\beta = 0$ deg., consistently with the considerations reported in chapter 3. The reduced frequency selected for the convergence analysis is $k = 0.4$, both for pitch and for plunge oscillations. This specific reduced frequency is selected for the convergence analyses, since it lies approx. in the middle of the range of k values considered in this work. Figures 4.1(a) and 4.1(b) show the time history of lift and moment coefficients, along twelve oscillation cycles, each with 200 time steps per period, for the airfoil in pitch with motion law $\alpha = \sin(\omega t)$ degrees. The time histories of the airloads achieved after six cycles with 400 time steps per period are also reported. A regular periodic trend is observed after six oscillating cycles with 200 time steps. Moreover no significant changes are observed for six cycles performed with 400 time steps per period. Consistently, figures 4.1(c) and 4.1(d) show the time histories of the lift and moment coefficients achieved for plunging motions of the airfoil, with motion law $h/c = 0.01 \sin(\omega t)$. Regularity and periodicity is observed after six oscillation cycles with 200 time step per period, as well. Therefore six cycles with 200 time steps each, are appropriate to perform numerical simulations of the airfoil in pitch or in plunge, with the tab in fixed position.

The steady state assessment reported in chapter 3 highlights that two Counter Rotating Vortical structures (CRV) are generated close to the transverse prong of the L-tab. These structures are found to modify the effective camber of the airfoil, therefore significantly affecting the aerodynamic loads. Consistently the flow field past the trailing edge is investigated for unsteady motions of the airfoil, to look for analogous trailing edge vortical structures.

Figures 4.2 and 4.3 report the near-wake flow field at various instants during the pitching oscillation cycle, namely at $k = 0.1$ and $k = 0.6$, for $\beta = 0$ degrees. The two CRV encountered in the steady state computations are still clearly visible. Additionally, the detachment and the downstream shedding of one of the CRV occurs during the oscillation cycle. A new vortical structure is anon generated past the L-tab. It is expected that such shedding is responsible of oscillatory behaviors in the generated airloads. Analogous phenomena are encountered for all of the reduced frequencies and the tab rotations taken into account in this work. The related images are herein omitted for brevity purposes.

Figures 4.4 and 4.5 report the near-wake flow field at various instants during the plunge oscillation cycle, at $k = 0.1$ and $k = 0.6$ at $\beta = 0$ degrees, respectively. The two CRV observed in the steady state computations, as well as for pitching motions of the airfoil, are still clearly visible. The detachment and the downstream shedding of one among the CRV, during the oscillation cycle, is again observed. Similarly a new vortical structure is then generated past the L-tab. Consistently, it is expected that such shedding is responsible of oscillatory behaviors in the unsteady airloads. Also for the plunging

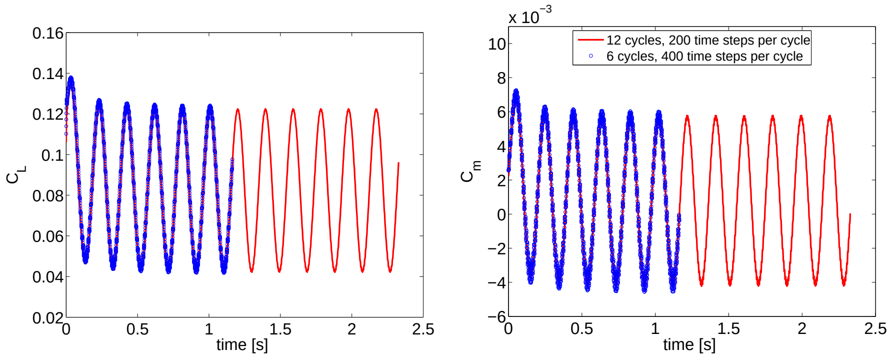

(a) Pitch, lift coeff. (b) Pitch, mid-chord moment coeff.

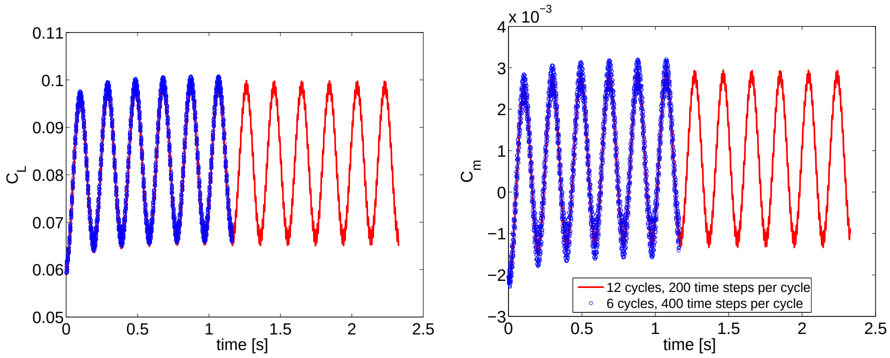

(c) Plunge, lift coeff. (d) Plunge, mid-chord moment coeff.

Figure 4.1: Time history of the force coefficients for the pitching/plunging NACA 0012 section, equipped with the L-tab at constant deflection; $k = 0.4$, $\beta = 0$ degrees, M $= 0.117$, Re $= 1 \cdot 10^6$.

motion analogous phenomena are encountered for each of the reduced frequencies and the tab rotations taken into account. The shedding observed for pitch and plunge oscillations, appears a consequence of the airfoil motion. It is additional with respect to the bluff body convection phenomena reported in chapter 3. These aspects will be discussed with more detail hereinafter.

As anticipated in the above, the shedding phenomena occurring during the pitching and the plunging oscillations are expected to cause oscillatory behaviors in the unsteady aerodynamic loads. With this regard figure 4.6 reports the lift and moment coefficient hysteresis curves achieved with pitching motions of the airfoil for $\beta = 0$ degrees, at $k = 0.1$ and $k = 0.6$, respectively. Figure 4.7 reports the same quantities resulting from plunging oscillations of the airfoil, again for $\beta = 0$ degrees, at $k = 0.1$ and $k = 0.6$, respectively. Clearly visible oscillations are encountered at $k = 0.1$, as well as at $k = 0.6$, both for pitch and plunge motions. Such oscillations in the unsteady airloads are observed for all of the reduced frequencies and the L-tab rotations taken under consideration in this work. The oscillatory behavior of the loads indicates that the response of the aerodynamic system, to single-frequency motion laws, is in fact multi-harmonic. That is, the unsteady airloads result from a composition of a primary harmonic component, namely at the same frequency of the forcing motion, and at least one further component at higher frequency, consequence of the CRV shedding. With this regard the Fourier transform is applied to the unsteady loads to pick out the single harmonics components. The first harmonic extracted from the unsteady airloads is also reported in figures 4.6 and 4.7.

To better understand the nature of the shedding phenomena herein discussed, a spectral analysis is carried out. With this purpose the unsteady airloads achieved for several reduced frequencies at $\beta = 0$ degrees, are investigated in the frequency domain. The

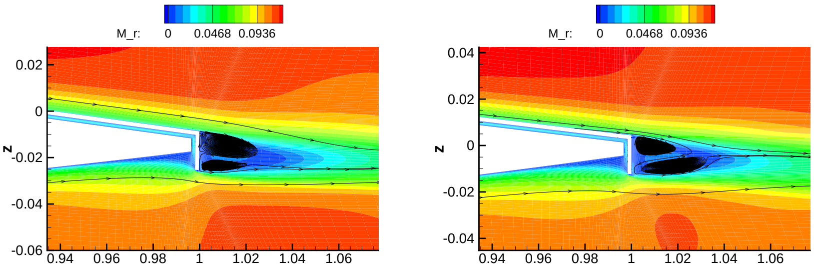

(a) $\alpha = 1$ deg. (b) $\alpha = 0$ deg. downstroke

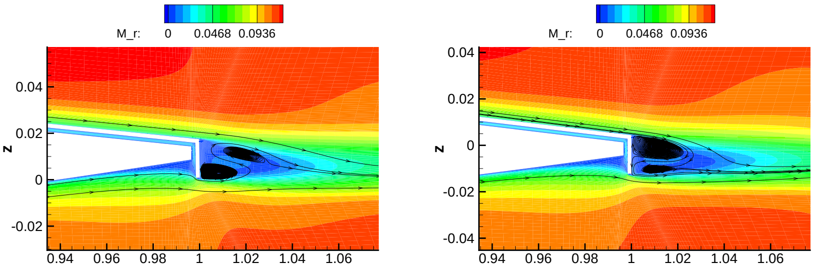

(c) $\alpha = -1$ deg. (d) $\alpha = 0$ deg. upstroke

Figure 4.2: Near-wake Mach number flow field and streamtraces during the pitch oscillation cycle at $k = 0.1$, $\beta = 0$ degrees, freestream Mach number $\mathrm{M} = 0.117$ and Reynolds number $\mathrm{Re} = 1 \cdot 10^6$.

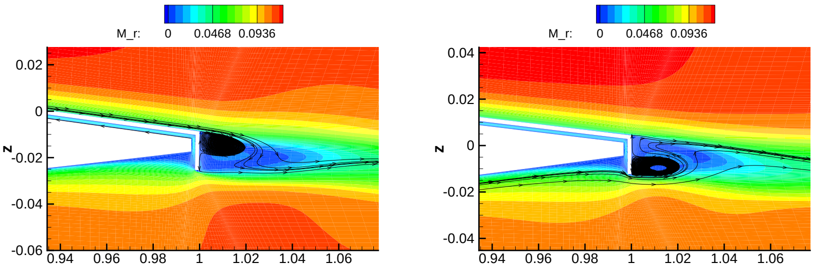

(a) $\alpha = 1$ deg. (b) $\alpha = 0$ deg. downstroke

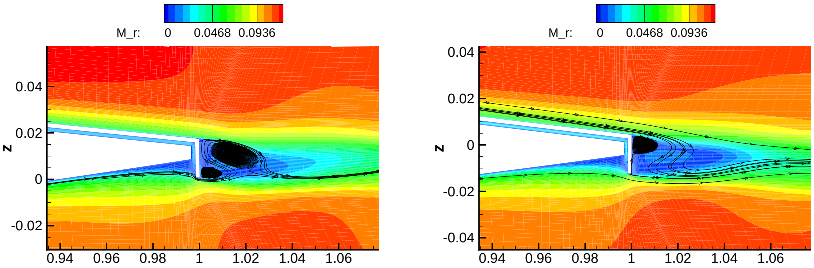

(c) $\alpha = -1$ deg. (d) $\alpha = 0$ deg. upstroke

Figure 4.3: Near-wake Mach number flow field and streamtraces during the pitch cycle at $k = 0.6$, $\beta = 0$ degrees, freestream Mach number $\mathrm{M} = 0.117$ and Reynolds number $\mathrm{Re} = 1 \cdot 10^6$.

motion reduced frequencies, taken into account for this purpose, are $k = 0.1$, $k = 0.2$, $k = 0.4$, $k = 0.6$, both for pitch and plunge oscillations. The motion laws have zero mean value, whereas the amplitude is $\alpha = 1$ deg. for pitch oscillations and $h/c = 0.01$ for plunge

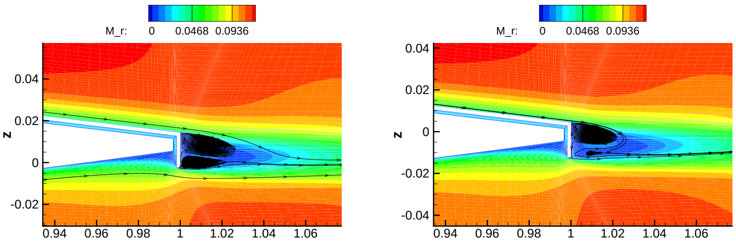

(a) $h/c = 0.01$ (b) $h/c = 0$ downstroke

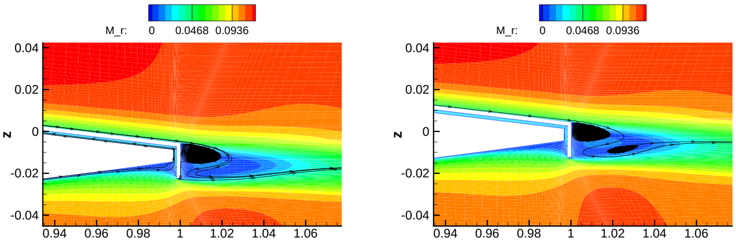

(c) $h/c = -0.01$ (d) $h/c = 0$ upstroke

Figure 4.4: Near-wake Mach number flow field and streamtraces during the plunge cycle at $k = 0.1$, $\beta = 0$ degrees, freestream Mach number $\mathrm{M} = 0.117$ and Reynolds number $\mathrm{Re} = 1 \cdot 10^6$.

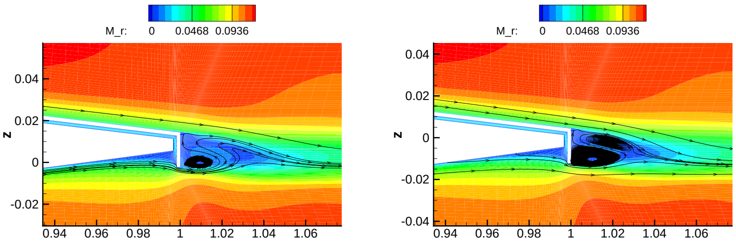

(a) $h/c = 0.01$ (b) $h/c = 0$ downstroke

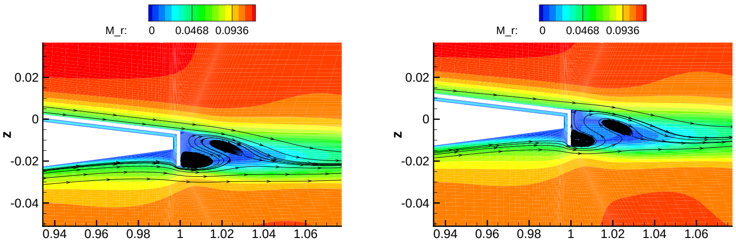

(c) $h/c = -0.01$ (d) $h/c = 0$ upstroke

Figure 4.5: Near-wake Mach number flow field and streamtraces during the plunge cycle at $k = 0.6$, $\beta = 0$ degrees, freestream Mach number $\mathrm{M} = 0.117$ and Reynolds number $\mathrm{Re} = 1 \cdot 10^6$.

oscillations, respectively. The spectral analysis carried out for fixed positions of the airfoil and of the tab, reported in chapter 3, highlights that not significant changes are found in the bluff body-like shedding phenomena, if the rotation of the movable device is changed. Therefore just one rotation of the L-tab is used for this preliminary spectral analysis, where the airfoil moves and the tab is in fixed position.

The Fourier transformation is applied to the unsteady numerically computed airloads. To avoid leakage effects the Hann window is applied and to enhance the frequency res-

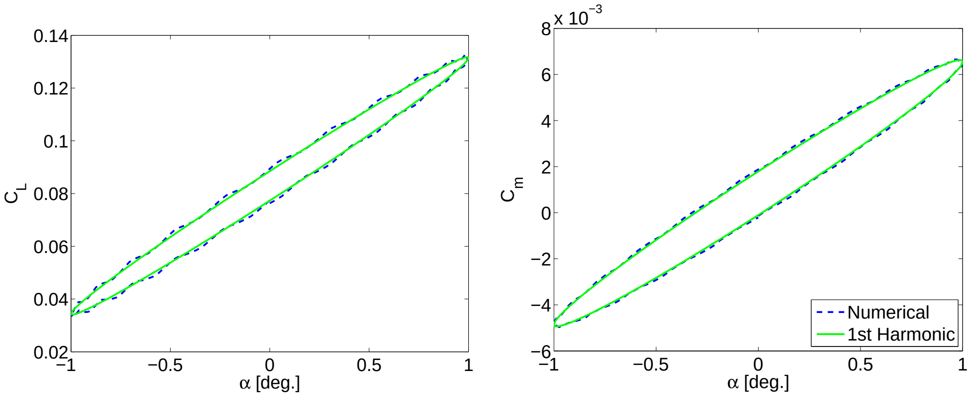

(a) $k = 0.1$, lift coeff.

(b) $k = 0.1$, mid-chord moment coeff.

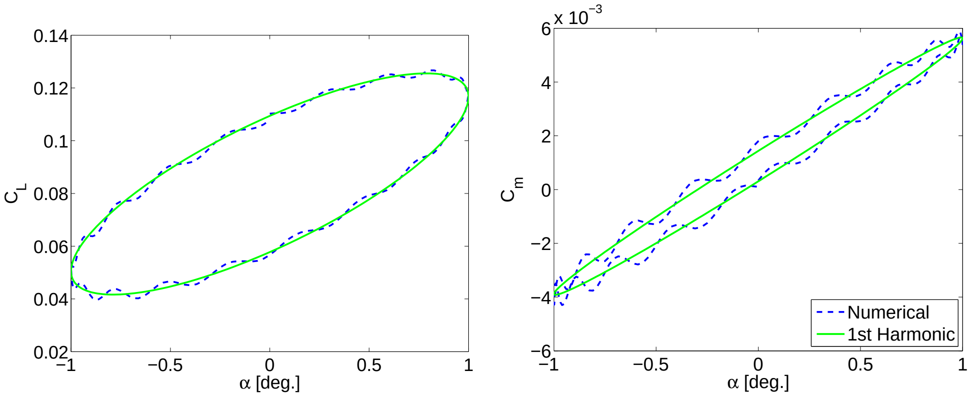

(c) $k = 0.6$, lift coeff.

(d) $k = 0.6$, mid-chord moment coeff.

Figure 4.6: Lift and moment coefficients together with their first harmonic component, for the pitch motion, $\beta = 0$ deg., M $= 0.117$, Re $= 1 \cdot 10^6$.

olution several repetitions of the signal are taken. The spectra of the lift coefficient are reported in figures 4.8 and 4.9. Two peaks are clearly visible, namely that corresponding to the input motion frequency and one at higher frequency, which may be associated to the motion-related shedding. It appears useful to recall that the star symbol used as a superscript for the variable $|C_L|$ indicates that the magnitude of the lift coefficient in the frequency domain has not been scaled with respect to the amplitude of the input motion law. Dealing with sinusoidal forcing inputs, such scaling factor is directly the oscillation amplitude.

Tables 4.1(a) and 4.1(b) report the computed shedding frequencies f_2 together with the motion frequencies f_1. The corresponding amplitudes of the two peaks are also reported. These values are extracted from figures 4.8 and 4.9, therefore these represent an approximation of the exact peaks of the spectra. The shedding frequency is found to grow almost linearly with the input frequency f_1. Indeed the ratio between the motion shedding frequency and the motion frequency, red colored in the tables, is found to lie always in the range 18-27, i.e. it keeps almost constant. Notice that almost the same number of oscillations can be observed in the loads hysteresis cycles reported in figures 4.6 and 4.7. It will be shown how the ratio f_2/f_1 will be almost the same also for oscillating motions of the tab, with the airfoil at constant angle of attack. Such finding appears to be useful when dealing with load control on helicopter blades. Indeed, for a selected actuation frequency, a small amplitude response of the system has to be expected also at a ~ 22 times larger frequency. It appears useful to remark that, with 200 time steps per period, employed for the unsteady numerical computations, there is sufficient frequency resolution

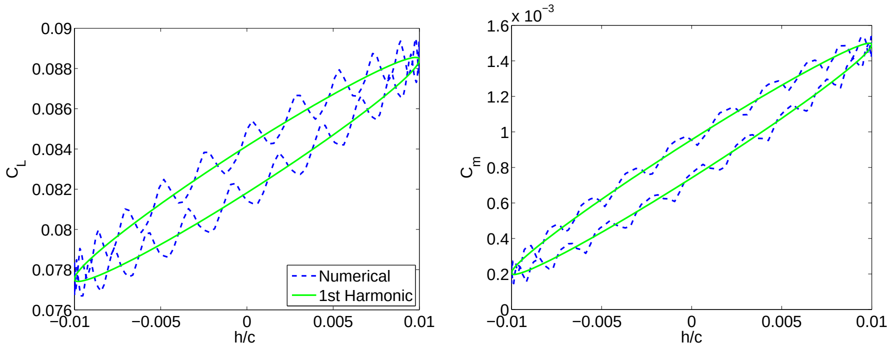

(a) $k = 0.1$, lift coeff. (b) $k = 0.1$, mid-chord moment coeff.

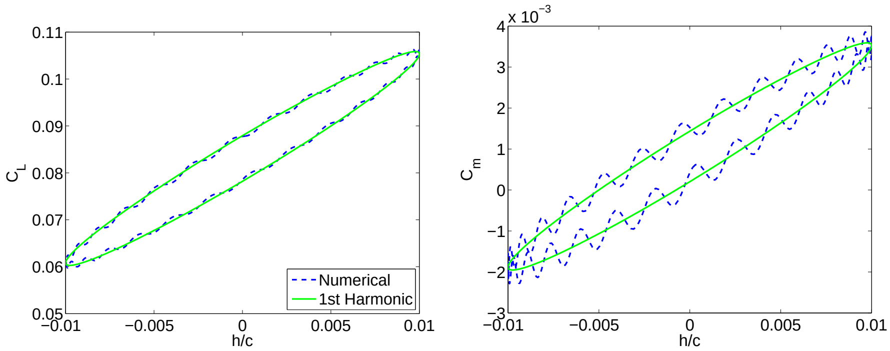

(c) $k = 0.6$, lift coeff. (d) $k = 0.6$, mid-chord moment coeff.

Figure 4.7: Lift and moment coefficients together with their first harmonic component, for the plunge motion, $\beta = 0$ deg., M $= 0.117$, Re $= 1 \cdot 10^6$.

–ten times the frequency of the shedding– to capture such oscillations, which indeed are not a result of aliasing or other sampling errors effects. Moreover the convergence analyses reported in figure 4.1, confirms that the analyzed numerical solution is regular and periodic, thus dispelling possible doubts related to a not converged numerical solution. By the way tables 4.1(a) and 4.1(b) indicate that the shedding frequency is never exactly an integer multiple of that of the motion. Therefore the motion-induced shedding is not expected to yield issues caused by resonance effects. Moreover, with regard to the amplitude of the first and of the second harmonic components, it is found that of course the latter is much lower with respect to the primary one. In particular the ratio between the amplitude of the first and of the second harmonic components appears to decrease with growing motion frequencies. Actually more detailed investigations should be performed to find out how the amplitude of the secondary harmonic is affected by the motion frequency. Nevertheless, such investigations lie out from the main purposes of this work. Indeed the present unsteady characterization is thought to be addressed to the design of an HHC-like active control system on a helicopter blade, where the main concern is the response at the same frequency of the input signal. This preliminary spectral spectral analysis is used to estimate the frequencies of the secondary harmonics and their ratio with respect to the motion frequency. Moreover it is verified that the oscillations encountered in the hysteresis curves of the airloads are in fact a consequence of high frequency caused by motion-related shedding phenomena. Consistent results are attained from the spectral analyses carried out in terms of the moment coefficient. These are herein omitted, not yielding any additional finding.

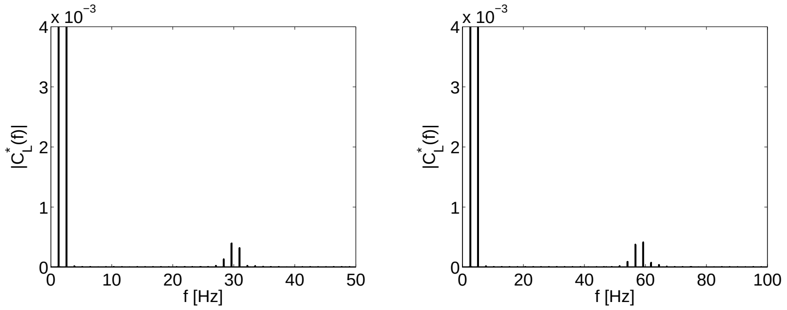

(a) $k = 0.1$ (b) $k = 0.2$

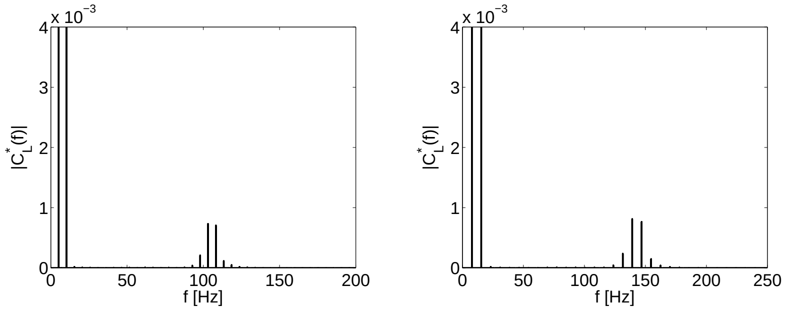

(c) $k = 0.4$ (d) $k = 0.6$

Figure 4.8: Lift coefficient spectra for the airfoil oscillating in pitch; $\beta = 0$ degrees, $\mathrm{M} = 0.117$, $\mathrm{Re} = 1 \cdot 10^6$.

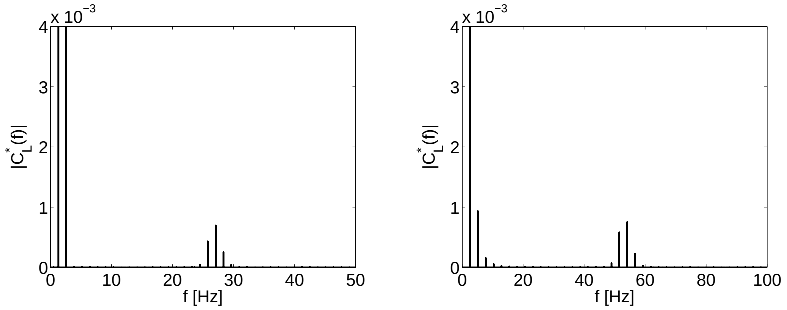

(a) $k = 0.1$ (b) $k = 0.2$

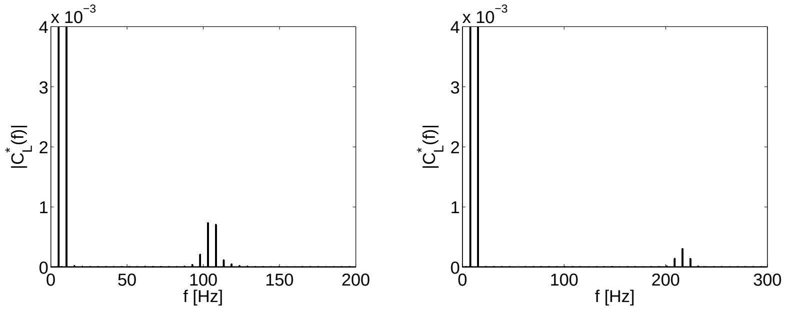

(c) $k = 0.4$ (d) $k = 0.6$

Figure 4.9: Lift coefficient spectra for the airfoil oscillating in plunge; $\beta = 0$ degrees, $\mathrm{M} = 0.117$, $\mathrm{Re} = 1 \cdot 10^6$.

Table 4.1: First and second harmonic components of the lift coefficient, together with the corresponding frequencies, for the pitch and the plunge motions; $\mathrm{M} = 0.117$, $\mathrm{Re} = 1 \cdot 10^6$.

(a) Airfoil in pitch

k	f_1 [Hz]	f_2 [Hz]	$\mathrm{f}_2/\mathrm{f}_1$	$\lvert C^*_L(\mathrm{f}_1)\rvert$	$\lvert C^*_L\lvert\mathrm{f}_2)\rvert$	$\lvert C^*_L(\mathrm{f}_1)\rvert/\lvert C^*_L(\mathrm{f}_2)\rvert$
0.1	1.289	29.64	~23	0.05041	0.0003954	127.49
0.2	2.578	59.29	~23	0.04636	0.0004132	112.20
0.4	5.155	108.3	~21	0.03949	0.0007032	56.16
0.6	7.733	139.2	~18	0.03321	0.0007640	43.46

(b) Airfoil in plunge

k	f_1 [Hz]	f_2 [Hz]	$\mathrm{f}_2/\mathrm{f}_1$	$\lvert C^*_L(\mathrm{f}_1)\rvert$	$\lvert C^*_L(\mathrm{f}_2)\rvert$	$\lvert C^*_L(\mathrm{f}_1)\rvert/\lvert C^*_L(\mathrm{f}_2)\rvert$
0.1	1.289	27.87	~21	0.04923	0.0006952	70.81
0.2	2.578	54.13	~24	0.04256	0.0007517	56.62
0.4	5.155	103.1	~20	0.03949	0.0007310	54.02
0.6	7.733	216.5	~27	0.03321	0.0007640	43.46

4.1.2 Characterization of the first harmonic component of the pitch/plunge airloads

Since the ultimate aim of this work is the design of a HHC control system, the first harmonic of the unsteady loads is the component of primary interest. This subsection is aimed to gain a more detailed investigation specifically in terms of the first harmonic of the airloads.

Figures 4.10 and 4.11 report the first harmonic component of the lift and moment coefficients for the pitching motion of the airfoil, at several reduced frequencies. On each of the images, the curves related to the section equipped with the L-tab, in three different fixed positions, are depicted. The hysteresis curves of the clean NACA 0012 airfoil are reported as well. Moreover the unsteady aerodynamic loads, computed with the flat plate Küssner Schwarz [43] (KS) model, applied to a straight one-piece mean line, are reported. Such formulation, analytically equivalent to the Theodorsen's model [59], is also the basis on which the reduced order model for the L-tab equipped section is developed, see chapter 5. Notice that actually, to account for the chord enlargement effects induced by the L-tab the reference length of the flat plate model is properly rescaled. Namely the chord of the flat plate model is rescaled according to the mean enlargement observed for steady state computations, corresponding to approx. 5%c.

Notice at first that the hysteresis curves related to the various deflections of the L-tab result to be overlapped, for both the pitch and the plunge motion. This occurs for the lift and moment coefficients and for each of the reduced frequencies herein considered. Hence the deflection of the L-tab does not seem to affect the first harmonic of aerodynamic loads. On the contrary significant steady effects of the L-tab are illustrated in chapter 3. The previous subsection highlights some minor effects on superior harmonics, but it is remarked that these do not concern the realization of a HHC control system. Regarding the clean section, the lift and moment coefficients of the NACA 0012 airfoil show only slight differences with respect to the curves of the L-tab equipped section. Such differences are probably related to the aforementioned chord enlargement induced by the CRV past the L-tab, of course absent on the clean airfoil.

A slightly larger mismatch is encountered, in terms of lift coefficient, between all of these numerical curves with respect to the flat plate KS model. This may be attributed to unsteady thickness effects, see chapter 2, which in fact are not accounted for in the KS model. These latter are far from being striking results, in that similar behaviors are widely described in literature. In this context Leishman reported very similar findings in some of his works [105, 66]. An analogous interpretation can be given to what observed in terms of the moment coefficient. Notice that, for the pitch motion, the numerical hysteresis curves are quite similar to those of the KS formulation. Larger differences are observed between the numerical pitching moment and the the same quantity, computed with the KS model, for the plunge motion. Very similar mismatches, between analytical flat plate models and measured data were highlighted by Leishman [105, 66]. He also attributed such discrepancies primarily to thickness effects. A further source of errors between the pitching moment, computed with flat plate formulations and with numerical or experimental results, is represented by the shift of the aerodynamic center occurring on finite thickness sections, with respect to the quarter-chord.

Overall the differences herein encountered, between the KS model and the numerical results, appear mostly related to unsteady thickness effects. For non symmetrical airfoils of course some affection is expected in terms of unsteady camber effects, as well. By the way, in chapter 2, it is shown how the camber affection on the unsteady airloads is significantly lower, with respect to that of the thickness. Consistently, no significant camber effects, induced by the L-tab, are observed on the first harmonic of the airloads. All these remarks find confirmation in what found by Leishman [105], which directly used, as inputs for his analytical flat plate model, the static lift curve slope and the location of the aerodynamic center, taken from literature data on finite thickness airfoils.

A brief additional remark concerns the direction of the hysteresis loops reported in figures 4.10 and 4.11. The behavior exhibited by such curves is consistent with that discussed in chapter 2, with regard to clean airfoils in oscillating motion. Namely the direction of the hysteresis loops is counter-clockwise (CCW) for $k < 0.2$, both for pitch and plunge motions of the airfoil, with the L-tab at arbitrary constant deflection angle. That is, the phase of the unsteady lift and moment coefficients is negative in such range of k. As a result, the unsteady airfoil behavior is in lag with respect to the steady counterpart. The opposite occurs for $k > 0.2$, where the phase of the lift and moment coefficients gets positive and the direction of the hysteresis loops is clockwise (CW). Therefore the unsteady loads are in lead, for equal angles of attack, with respect to the steady counterpart.

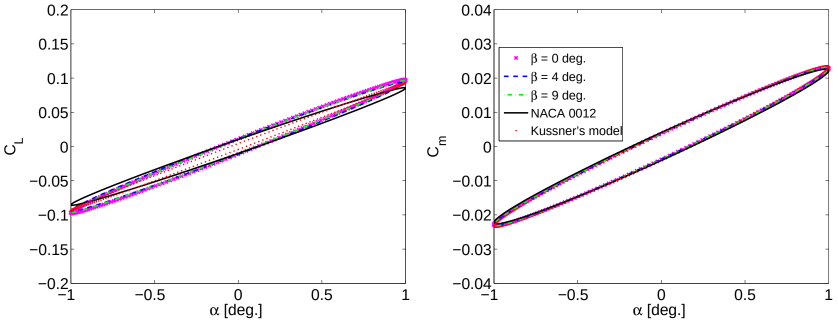

(a) $k = 0.1$, lift coeff., CW

(b) $k = 0.1$, mid-chord moment coeff., CW

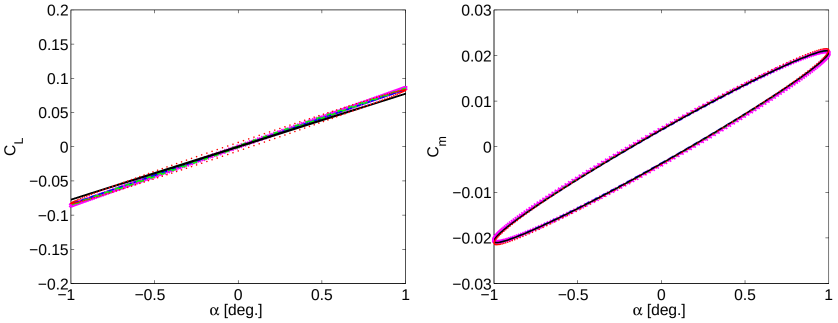

(c) $k = 0.2$, lift coeff., CCW

(d) $k = 0.2$, mid-chord moment coeff., CCW

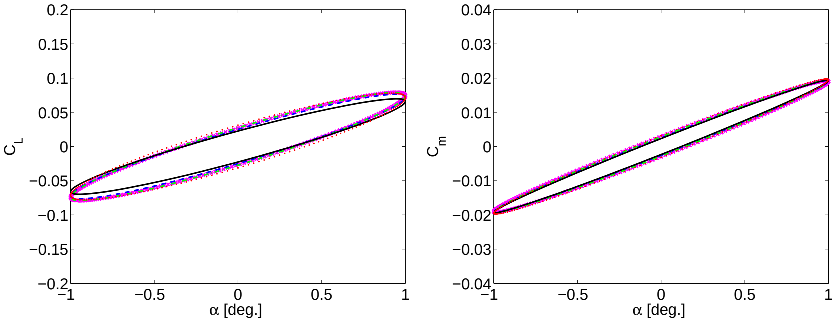

(e) $k = 0.4$, lift coeff., CCW

(f) $k = 0.4$, mid-chord moment coeff., CCW

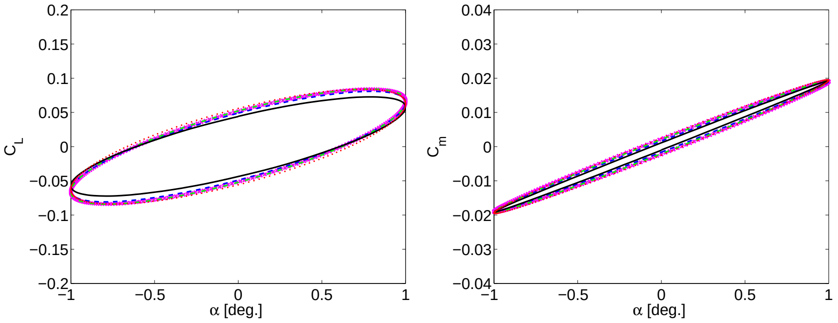

(g) $k = 0.6$, lift coeff., CCW

(h) $k = 0.6$, mid-chord moment coeff., CCW

Figure 4.10: First harmonic of the lift and moment coefficients, developed by pitch motions, for various deflections of the L-tab, together with the oscillating flat plate Küssner's model; $\mathrm{M} = 0.117$, $\mathrm{Re} = 1 \cdot 10^6$. The hysteresis curves for the NACA 0012 airfoil are also reported. The directions of the hysteresis loops are additionally shown.

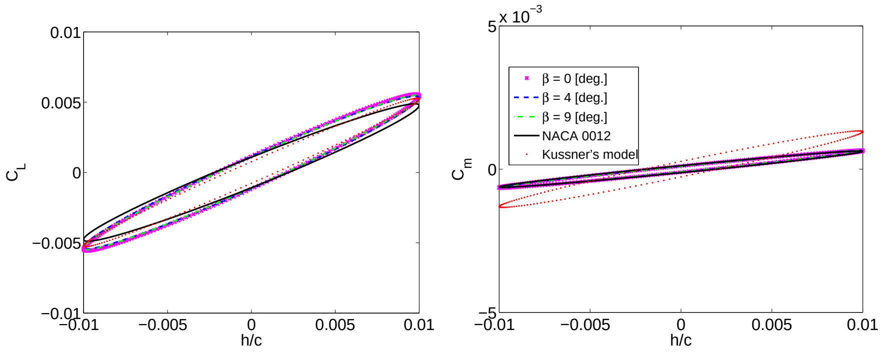

(a) $k = 0.1$, lift coeff., CW (b) $k = 0.1$, mid-chord moment coeff.

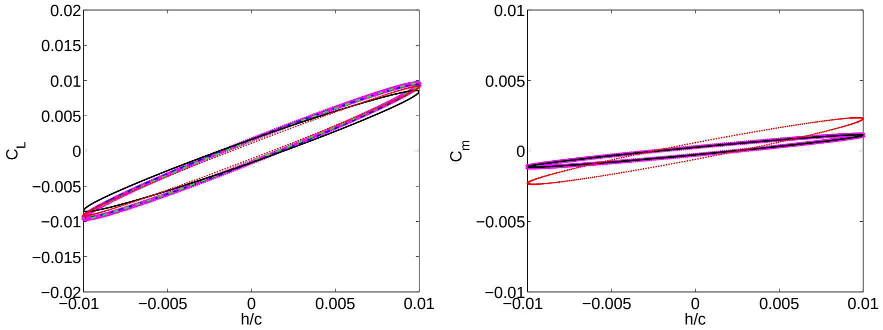

(c) $k = 0.2$, lift coeff., CW (d) $k = 0.2$, mid-chord moment coeff.

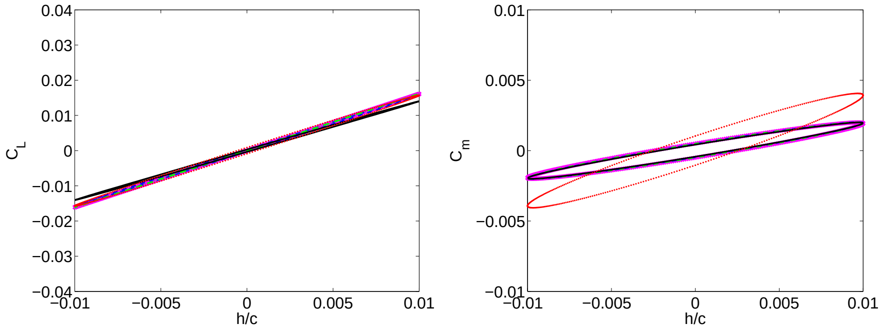

(e) $k = 0.4$, lift coeff., CCW (f) $k = 0.4$, mid-chord moment coeff.

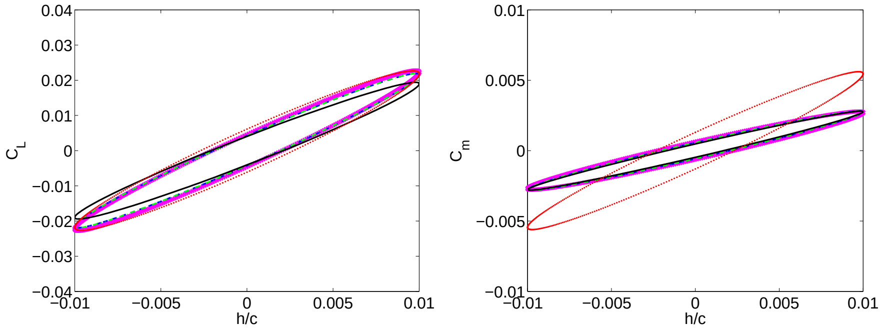

(g) $k = 0.6$, lift coeff., CCW (h) $k = 0.6$, mid-chord moment coeff., CCW

Figure 4.11: First harmonic of the lift and moment coefficients, developed by plunge motions, for various deflections of the L-tab, together with the oscillating flat plate Küssner's model; $\mathrm{M} = 0.117$, $\mathrm{Re} = 1 \cdot 10^6$. The hysteresis curves for the NACA 0012 airfoil are also reported. The directions of the hysteresis loops are additionally shown.

4.2 Steady airfoil with harmonically oscillating L-tab

4.2.1 Numerical simulations for steady airfoil with harmonically oscillating L-tab

The system of overlapped grids allows to simulate the relative motion of the L-tab and the airfoil. The ROSITA solver uses the Chimera algorithm [80] to calculate the resulting computational domain at each of the time steps, according to the motion law which is imposed. The reference motion law of the tab reads $\beta = 1 + 1\,\sin(\omega t)$ degrees, whereas the reduced frequencies taken under consideration are $k = 0.1$, $k = 0.2$, $k = 0.4$ and $k = 0.6$. The airfoil is kept at zero angle of attack, whereas the Mach number and the Reynolds number are fixed to $\mathrm{M} = 0.117$ and $\mathrm{Re} = 1 \cdot 10^6$, respectively. The reliability of numerical computations is checked by means of convergence analyses with respect to the resolution in the real time. Figure 4.12 shows the time history of the aerodynamic loads after twelve oscillation cycles, at $k = 0.4$. The time history of the aerodynamic loads achieved with a double time resolution, i.e. with 400 time steps per period, is also depicted. A periodic and reasonably regular trend is already visible after the third oscillation cycle. Moreover no significant differences are encountered in the time histories achieved by doubling the number of time steps per period. Therefore six cycles lasting numerical simulations with 200 time steps per period are retained appropriate, for conservativeness, to perform reasonably accurate numerical simulations of the L-tab in harmonic motion.

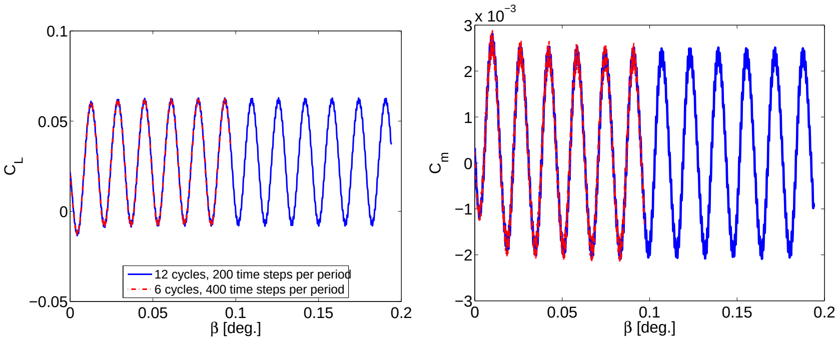

(a) Lift coeff. (b) Mid-chord moment coeff.

Figure 4.12: Time history of the force coefficients for the oscillating L-tab; $k = 0.4$, $\alpha = 0$ degrees, $\mathrm{M} = 0.117$, $\mathrm{Re} = 1 \cdot 10^6$.

The flow past the L-tab is again taken under consideration, to investigate the features of the CRV for this specific motion. Figures 4.13 and 4.14 report the near-wake flow field, together with the streamlines, at four instants during the cycle, for $k = 0.1$ and $k = 0.6$, respectively. Similarly to what seen for pitch and plunge motions of the airfoil, the alternate detachment of one among the CRV is observed. Consequent oscillations in the unsteady loads are expected, and a frequency analysis is proper to investigate the corresponding harmonic components.

Figure 4.15 shows the hysteresis cycles of the lift and of the moment coefficients achieved for oscillating motions of the tab at $k = 0.1$ and at $k = 0.6$. As expected an oscillatory behavior is observed, confirming how the airloads result in fact from the composition of at least two harmonics.

Therefore the Fourier transform is applied to the computed unsteady airloads, to identify the single harmonic contributions and the associated frequencies. The Hann window is applied, to avoid leakage effects, whereas several repetitions of the signal are taken to enhance the frequency resolution. Figure 4.16 shows the spectra of the lift coefficient for

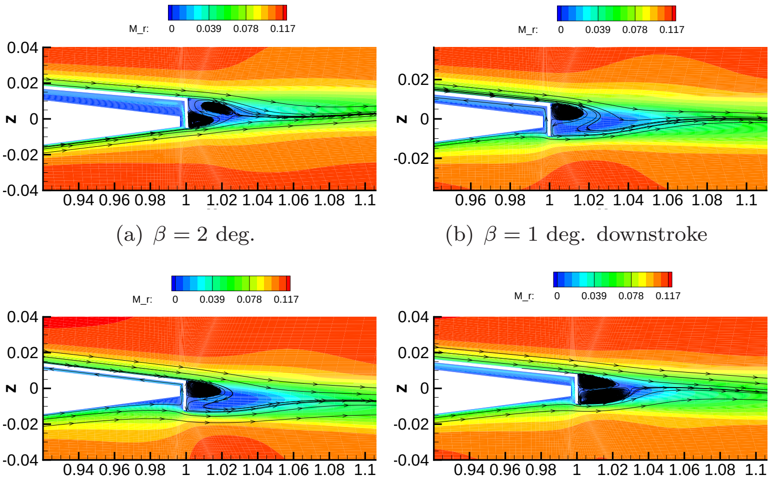

(a) $\beta = 2$ deg.

(b) $\beta = 1$ deg. downstroke

(c) $\beta = 0$ deg.

(d) $\beta = 1$ deg. upstroke

Figure 4.13: Near-wake Mach number flow field and streamtraces during the L-tab oscillation cycle, at $k = 0.1$; $\alpha = 0$ degrees, freestream Mach number $\mathrm{M} = 0.117$ and Reynolds number $\mathrm{Re} = 1 \cdot 10^6$.

several reduced frequencies of the input motion. Similarly to pitch and plunge oscillations of the airfoil, two peaks are clearly visible. These are the harmonic at the same frequency of the motion law and the harmonic related to the CRV shedding phenomena, consequence of the tab movement, see figures 4.13 and 4.14.

The frequencies of the peaks in the lift coefficient spectra, as well as the corresponding amplitudes are reported in table 4.2. Consistently with the approach adopted for pitch and plunge motions, such values are extracted from figure 4.16, therefore these represent an approximation of the exact peaks of the spectra. The same considerations of the previous section can be drawn from the values reported in table 4.2. Namely, the shedding frequency f_2 depends linearly on the motion frequency f_1. Moreover, the ratio between the shedding and the motion frequency keeps almost constant, since it lies in the range 18-24, for all of the k in input. It is also remarkable that very similar values in the ratios between f_2 and f_1 are encountered for pitch and plunge motions of the airfoil, with the tab in fixed position. That is, when actuating at a certain frequency f_1, again the system responds at f_1 and at a $f_2 \sim 22 f_1$. It appears proper to remark that the 200 time steps per period, employed for the unsteady computations, provide adequate resolution to capture such secondary oscillations, without incurring in sampling errors. Moreover, the time resolution sensitivity analysis, reported in figure 4.12, ensures that such oscillations are do not rise from a non converged numerical solution. The ratio of the amplitudes, i.e. $|C_L(f_1)|/|C_L(f_2)|$, appears to decrease with growing values of the reduced frequency, as observed for pitch and plunge motions. It's worth noting that more detailed investigations are required, to better understand the relative behavior of the amplitudes. By the way such insights lie out from the main concerns of the present work and therefore are left as a future development.

Additionally, computations are also performed by changing the motion law of the movable device, in terms of amplitudes and mean values. This allows to preliminary investigate the sensitivity of the shedding frequency –it has been proved that the second harmonic is indeed related to the CRV detachments– also to these parameters of the motion law. Tables 4.3(a)–4.3(c) report the main results of the spectral analysis, carried out on the computed unsteady loads, for three further motion laws. The reduced frequency ranges again from 0.1 to 0.6. It is remarkable that the ratio between the shedding frequency f_1 and the primary frequency f_2 still lies in the range 18-25. This further confirms the regularity of the shedding frequency, with respect to the input motion law. That is, when

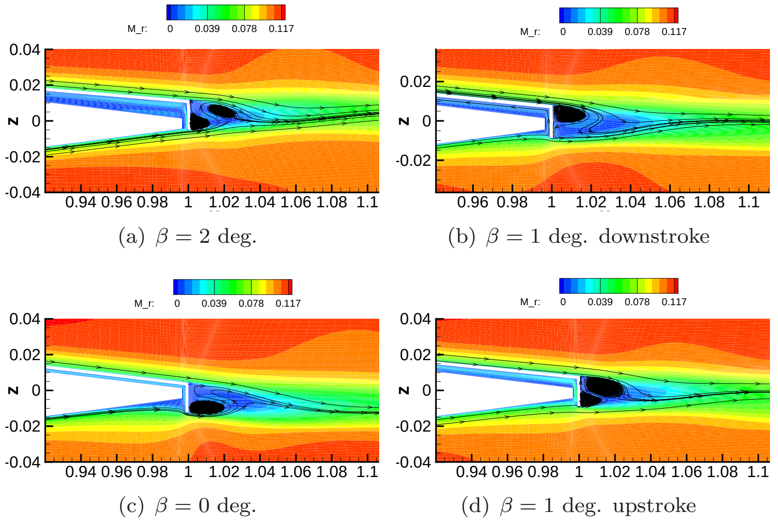

(a) $\beta = 2$ deg.

(b) $\beta = 1$ deg. downstroke

(c) $\beta = 0$ deg.

(d) $\beta = 1$ deg. upstroke

Figure 4.14: Near-wake Mach number flow field and streamtraces during the L-tab oscillation cycle, at $k = 0.6$; $\alpha = 0$ degrees, freestream Mach number $\mathrm{M} = 0.117$ and Reynolds number $\mathrm{Re} = 1 \cdot 10^6$.

actuating the tab at a certain frequency, both the movable device and the airfoil respond also at frequencies which are always $\sim$ 22 times the forcing value. Again, it is proper to remark that the amplitudes of the secondary oscillations in the unsteady airloads, are much smaller than the first harmonic component. Moreover tables 4.2, 4.3(a), 4.3(b) and 4.3(c) show how the shedding frequency is not actually an exact integer multiple of that of the motion. Therefore, also for oscillating motions of the L-tab, resonance phenomena, due to coupling with the blade frequencies, are prevented.

Finally, it appears useful to remark that such oscillations in the unsteady airloads are far from being novel, in that similar behaviors were found both experimentally [26, 27, 34] and numerically [25, 33, 34] on GF-like devices harmonically deployed, installed on blade section models.

4.2.2 Characterization of the first harmonic component of the moving L-tab airloads

Consistently with the steps followed in section 4.1, an overview on the effects of the oscillating L-tab on the first harmonic of the unsteady airloads is herein reported. It has been shown that the primary effect of the L-tab on airloads is determined by the CRV generated past its vertical prong, which ultimately modify the effective camber. Therefore, somehow different behaviors of the hysteresis cycles, for growing k, are expected with respect to classical symmetrical airfoils in oscillating motion. The images in figure 4.17 report the first harmonic of the lift and moment coefficients, achieved for oscillating motions of the L-tab, at various reduced frequencies, with the airfoil at zero angle of attack, together with their steady counterpart. Both the slope and the amplitude of the hysteresis loops are significantly affected by the reduced frequency. Additionally, a reduction of the maximum value of the lift coefficient with increasing reduced frequencies is observed. Figure 4.17 also shows that the orientation of the hysteresis cycles is counter-clockwise, for k ranging from 0.1 to 0.6. The same occurs in terms of the moment coefficient. Therefore, in the range $0.1 \leq k \leq 0.6$, leading effects, with respect to the steady counterpart, are encountered by harmonically deflecting the L-tab.

By following the approach used to investigate the behavior of oscillating airfoils in chapter 2, it appears useful to look at the diagrams of the magnitude and of the phase of the lift coefficient. Figure 4.18 reports the magnitude and the phase of the first harmonic

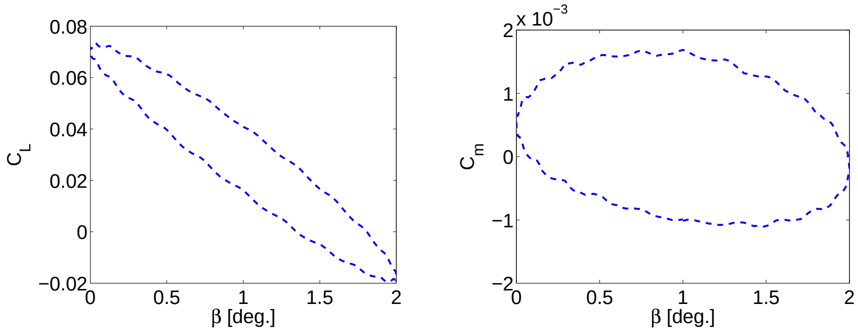

(a) $k = 0.1$, lift coeff.

(b) $k = 0.1$, mid-chord moment coeff.

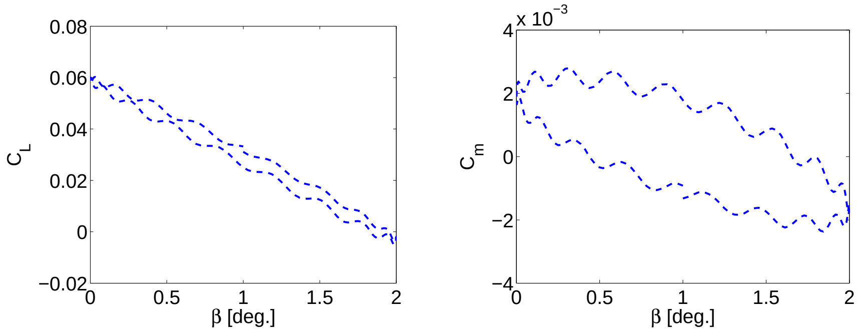

(c) $k = 0.6$, lift coeff.

(d) $k = 0.6$, mid-chord moment coeff.

Figure 4.15: Hysteresis curves of the lift and moment coefficients, for oscillating motions of the L-tab; $\alpha = 0$ degrees, $\mathrm{M} = 0.117$, $\mathrm{Re} = 1 \cdot 10^6$.

of the lift coefficient versus the L-tab motion reduced frequency. The qualitative behavior of the magnitude is similar to that observed for oscillating airfoils. That is, the magnitude decreases from $k = 0.1$ to $k = 0.4$, keeping almost constant for larger reduced frequencies. On the other hand, as anticipated, the phase keeps positive, namely in the range 110-175 degrees, for $0.1 \leq k \leq 0.6$. Differently, for symmetrical airfoils in oscillating pitch motion, the lift coefficient phase is found to get positive at reduced frequency between 0.1 and 0.3, depending on the thickness of the section, as reported in chapter 2. Namely, for lower k, the lift coefficient phase of oscillating symmetrical airfoils is negative, therefore the unsteady loads are in lag with respect to their static counterpart. The inversion phase of oscillating airfoils results from the combination of effects related to the acceleration of the fluid nearby the body and to the wake convection, see chapter 2 and the textbook of Leishman [66], chapter 8. For the L-tab in oscillating motion, the generation and the shedding of the two CRV play a primary role in balancing these phenomena, deeply affecting the behavior of the lift phase. Therefore, to accurately reproduce the effects induced by the oscillating L-tab, the unsteady effects of the CRV on the camber line have to be taken into account.

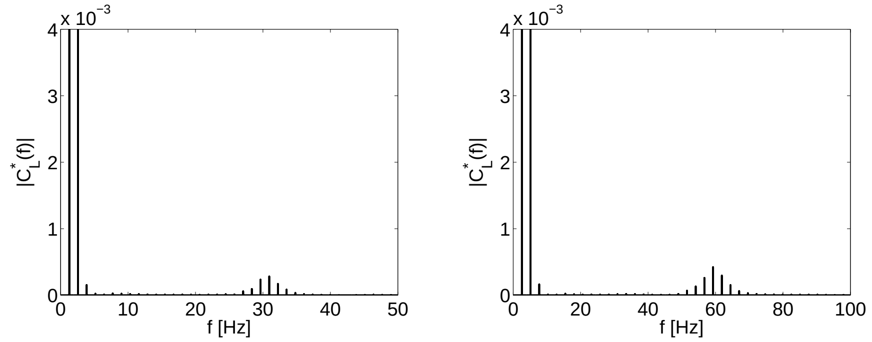

(a) $k = 0.1$

(b) $k = 0.2$

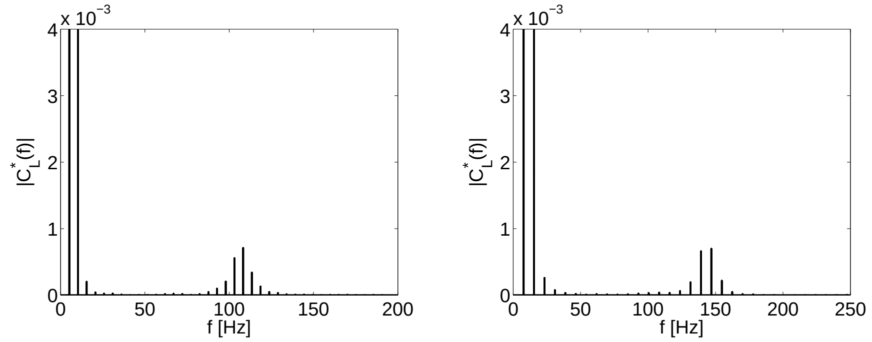

(c) $k = 0.4$

(d) $k = 0.6$

Figure 4.16: Lift coefficient spectra for oscillating motions of the L-tab; $\alpha = 0$ degrees, $\mathrm{M} = 0.117$, $\mathrm{Re} = 1 \cdot 10^6$.

Table 4.2: First and second harmonic components of the lift coefficient, together with the corresponding frequencies, for oscillating motions of the L-tab; $\alpha = 0$ degrees, $\mathrm{M} = 0.117$, $\mathrm{Re} = 1 \cdot 10^6$.

k	$\mathrm{f_1}$ [Hz]	$\mathrm{f_2}$ [Hz]	$\mathrm{f_2/f_1}$	$\lvert C_L^*(\mathrm{f_1})\rvert$	$\lvert C_L^*(\mathrm{f_2})\rvert$	$\lvert C_L^*(\mathrm{f_1})\rvert/\lvert C_L^*(\mathrm{f_2})\rvert$
0.1	1.289	30.93	~24	0.02356	0.0002823	83.46
0.2	2.578	59.29	~23	0.02119	0.0004204	50.40
0.4	5.153	108.3	~21	0.02006	0.0007097	28.27
0.6	7.733	146.9	~19	0.02047	0.0006967	29.38

Table 4.3: First and second harmonic components of the lift coefficient with the corresponding frequencies for diverse oscillating motions of the tab; $\alpha = 0$ degrees, $\mathrm{M} = 0.117$, $\mathrm{Re} = 1 \cdot 10^6$.

(a) $\beta = 2 + 2\sin(\omega t)$ deg.

k	f_1 [Hz]	f_2 [Hz]	f_2/f_1
0.1	1.289	32.22	~25
0.2	2.578	64.44	~25
0.4	5.153	108.3	~21
0.6	7.733	162.4	~21

(b) $\beta = 2 + 1\sin(\omega t)$ deg.

k	f_1 [Hz]	f_2 [Hz]	f_2/f_1
0.1	1.289	28.35	~24
0.2	2.578	56.71	~22
0.4	5.153	108.3	~21
0.6	7.733	146.9	~19

(c) $\beta = 2 + 1\sin(\omega t)$ deg.

k	f_1 [Hz]	f_2 [Hz]	f_2/f_1
0.1	1.289	29.64	~24
0.2	2.578	56.71	~22
0.4	5.153	108.3	~21
0.6	7.733	139.2	~18

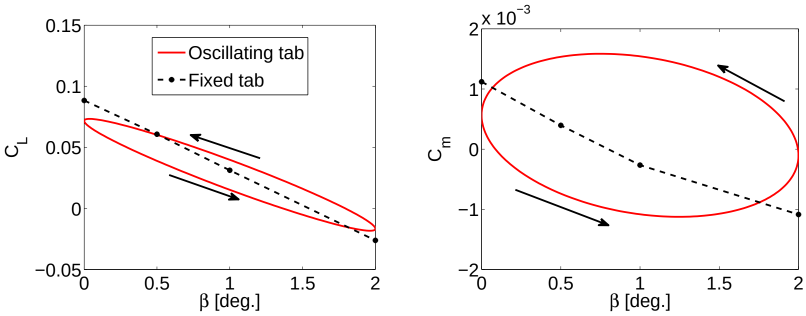

(a) $k = 0.1$, lift coeff. (b) $k = 0.1$, mid-chord moment coeff.

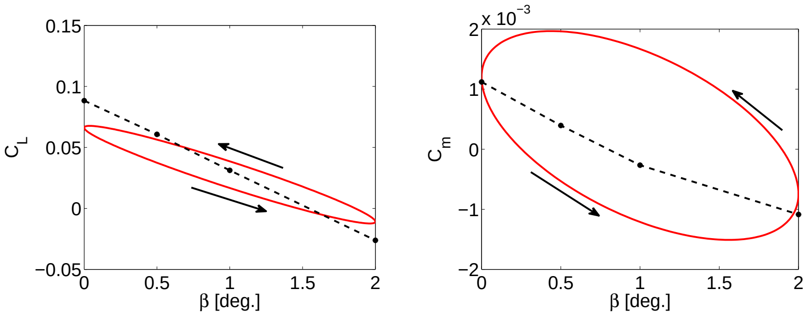

(c) $k = 0.2$, lift coeff. (d) $k = 0.2$, mid-chord moment coeff.

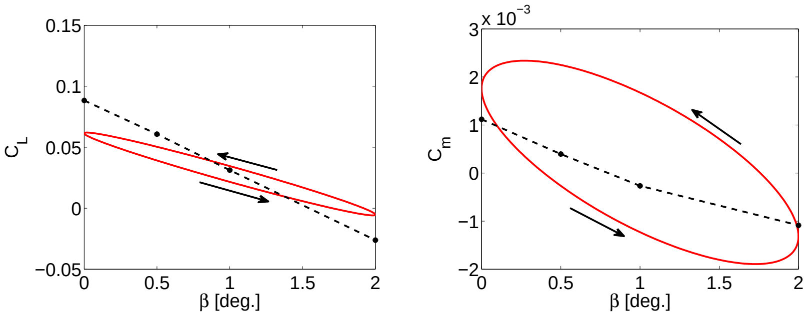

(e) $k = 0.4$, lift coeff. (f) $k = 0.4$, mid-chord moment coeff.

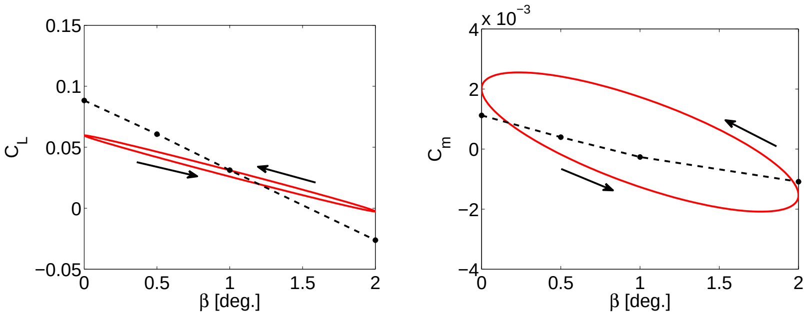

(g) $k = 0.6$, lift coeff. (h) $k = 0.6$, mid-chord moment coeff.

Figure 4.17: First harmonic of the lift and moment coefficients for the oscillating L-tab, at various reduced frequencies; $\beta = 1 + 1\sin(\omega t)$ degrees, $\alpha = 0$ degrees, $\mathrm{M} = 0.117$, $\mathrm{Re} = 1 \cdot 10^6$.

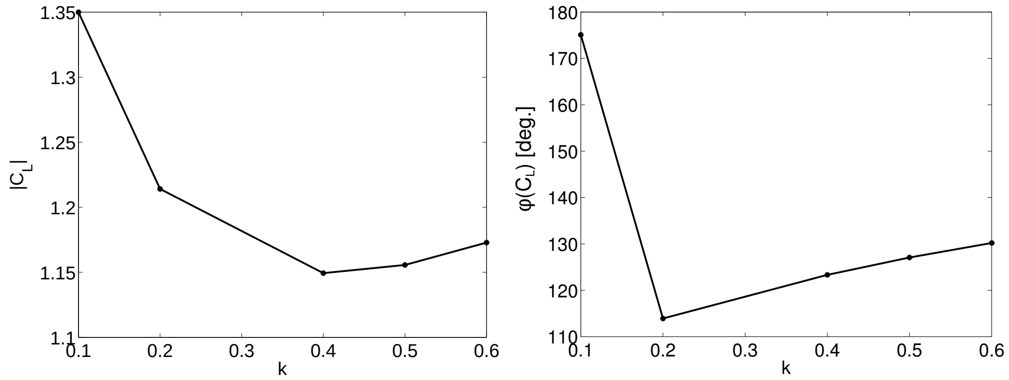

(a) Magnitude

(b) Phase angle

Figure 4.18: Magnitude and phase of the first harmonic of the lift coefficient, for several reduced frequencies; $\beta = 1 + 1\sin(\omega t)$ degrees, $\alpha = 0$ degrees, $\mathrm{M} = 0.117$, $\mathrm{Re} = 1 \cdot 10^6$.

4.3 Concluding remarks

The unsteady aerodynamic behavior of a NACA 0012 blade section equipped with the L-tab is characterized numerically. The 20%c long L-tab is herein taken under consideration, since while at low angles of attack it exhibits a behavior similar to the 10%c long configuration, significantly better performance are granted at medium and high values of α, see chapter 3. Therefore 20%c long L-tab could be more effectively employed for the manifold applications concerning rotorcraft, especially in forward flight conditions. The flow field past the movable device, as well as the aerodynamic forces, are investigated at several reduced frequencies in the range $k = [0.1\ 0.6]$. At first, pitch and plunge motions of the airfoil, for various fixed rotations of the L-tab, are considered. The motion pitching law reads $\alpha = \sin(\omega t)$ degrees. On the other hand the plunging motion law reads $h/c = 0.01 \sin(\omega t)$. Convergence analyses in the real time are performed to verify the reliability of the numerical results. The near wake flow field, at several instants during the oscillation cycles, highlights the detachments of one among the CRV, both for pitch and plunge motions. A new vortical structure is soon generated past the vertical prong of the tab. Such CRV shedding phenomena are found to cause oscillations in the hysteresis cycles of the aerodynamic loads, since the value of the circulation follows the vortex detachments. With this regard, a frequency analysis performed on the unsteady multi-harmonic airloads highlights two peaks in the lift coefficient spectra. The primary peak is of course at the same frequency of the input motion, whereas the frequency of the secondary peak is found to be dependent on that of the input motion. In particular, the ratio of the frequencies of the second and the first peak in the lift spectra is found to lie in the range 18-27, for any of the input motion k and both for pitch and plunge oscillations. Such information could be helpful during the design of control systems on helicopter blades. Indeed for a selected actuation frequency, a response of the system has to be expected also at a ~ 22 times larger frequency. With this regard, it is highlighted how, actually, such shedding frequencies are never exact integer multiples of those of the corresponding motions. Therefore, potential issues concerning resonance phenomena should be avoided. Moreover, it is shown that the amplitude of the secondary oscillations is in general much lower than that of the first harmonic counterpart. Notice that, since Higher Harmonic Control (HHC) algorithms, like the one which will be presented in chapter 6, deal primarily with the response of the system at the same frequency of the input, it is found proper to focus with more detail on the first harmonic of unsteady loads. The first harmonic of the lift and moment coefficients is extracted for various rotations of the L-tab and at several reduced frequencies of the airfoil in pitch and in plunge. The comparison of the resulting hysteresis loops highlights that the L-tab doesn't affect significantly the first harmonic of the unsteady loads, both for pitch and plunge motions of the airfoil.

Secondly the behavior of the of the blade section kept at constant angle of attack, with the L-tab harmonically oscillating is investigated. Again convergence analyses in the real time are performed to insure the reliability of the numerical results. The reference motion law of the L-tab reads $\beta = 1 + 1 \sin(\omega t)$ degrees. Reduced frequencies in the range [0.1 0.6] are considered, whereas the airfoil is kept at angle of attack of zero degrees. The near wake flow field highlights again the detachment and the subsequent regeneration of one among the CRV, during the oscillation cycle. Consistently the resulting unsteady airloads are found multi-harmonic and corresponding oscillating hysteresis loops are observed. The frequency analyses of the aerodynamic forces again highlight two peaks in the computed spectra, the former at the same frequency of the input motion and the latter related to the CRV shedding, which ultimately leads to time-varying circulation values. The ratio between the secondary and the primary peaks frequencies is found in the range 19-24, regardless to the input reduced frequency. The same ratio is evaluated by changing the parameters of the motion law. Values in the range 18-25 –which actually are not integer multiples of the motion frequency– are found again. This confirms the regularity of the shedding frequency with respect to the motion law. That is, when the tab is actuated at a certain frequency, both the movable device and the airfoil respond at frequencies which are always $\sim$ 22 times the forcing value. Actually the frequency of such secondary oscillations is not exactly an integer multple of the rotor angular velocity, therefore potential issues concerning resonance phenomena are again avoided. Consistently with the aim to realize a HHC control system, the first harmonic of unsteady airloads is then investigated with more detail. In particular both the amplitude and the slope of the corresponding hysteresis loops are found to change significantly according to the L-tab reduced frequency. The path of the corresponding hysteresis loops is found to be counter-clockwise for all of the k in the range [0.1 0.6]. That is, the unsteady loads appear to be always in lead with respect to their steady counterpart, unlike what observed in chapter 2 on oscillating airfoils, for $k \lessapprox 0.2$. The CRV generated past the vertical prong of tab, which are of course absent on classical airfoils, appear to play a significant role in affecting the first harmonic of the airloads. Indeed substantial differences are encountered in the behavior of the load hysteresis curves, achieved for harmonic motions of the L-tab, with respect to pitch or plunge airfoils oscillations, see again chapter 2. In particular, in order to realistically capture the effects of the L-tab on the first harmonic of the aerodynamic loads, it appears mandatory to take into account the unsteady phenomena induced by the CRV, at least those in the near body region.

It appears proper to remark that the assessment of the unsteady behavior in compressible and transonic flow conditions is left as a future development to this work. By the way the effect of the Mach number on oscillating motions either of the airfoil or of the L-tab can be led back to literature results. In the textbook of Leishman [66], Chapter 8, it is shown how the computation of the unsteady airloads for arbitrarily shaped thin lines in compressible flow conditions by means of indicial concepts is straightforward, once the incompressible behavior is known. Additionally, since it is found that the L-tab acts substantially by inducing modifications in the mean line shape, the thin line-based extension proposed by Leishman is appropriate for the present movable device, as well.

Chapter 5

Reduced order model for a blade section with the L-tab

A physically based Reduced Order Model (ROM) is developed for the blade section equipped with the L-tab [93]. The linear analytical thin line formulation of Küssner and Schwarz (KS) [43] is used as a benchmark for the derivation of the ROM. Indeed this model is capable to deal with arbitrarily shaped mean lines, therefore allowing to take into account the camber modifications caused by the movable device, discussed in chapters 3 and 4. The equivalent geometry of the ROM, presented in section 5.1, is built up as a three segments piece-wise mean line, where the first piece is thought to represent the airfoil, the second is meant to reproduce the longitudinal edge of the tab and the third deals with the CRV past the movable device. The geometrical and motion parameters of the equivalent mean line are found by means of an optimization algorithm, which minimizes the difference between the airloads achieved with numerical simulations and those computed with the KS based analytical formulation. Under the small perturbation hypothesis, the L-tab equipped blade section is represented as a linear system of three Degrees Of Freedom (DOFs), namely the pitch and plunge motions of the airfoil and the rotation of the movable device. In section 5.2 a ROM is developed for various fixed positions of the tab, at constant zero angle of attack, to reproduce the phenomena related to the steady mean term of the L-tab DOF. Section 5.3 illustrates how the KS model for a flat plate in oscillating motion –with the tab in arbitrary fixed position– is appropriate for the pitch and plunge DOFs, since no significant camber modification effects are observed on the first harmonic of the corresponding unsteady airloads, as illustrated in section 4.1. The only aspect to be here taken into account consists of a rescaling of the reference chord of the flat plate model, according to the mean enlargement induced by the CRV. The derivation of the ROM for the oscillating L-tab, reported in section 5.4, follows an approach analogous to that adopted for fixed positions of movable device. Overall the ROMs are found to correctly reproduce and predict the steady airloads or the first harmonic of the unsteady lift and moment coefficients, as well as the near body flow field, including the CRV effects. Section 5.5 compares the aerodynamic loads achieved with the ROM for the L-tab, to those attained with an analogous thin line model for a widely employed trailing edge solution, namely a classical plain flap. Section5.6 deals with further and concluding remarks.

5.1 Analytical formulation for the reduced order model

The analytical reduced order model developed in this chapter has its cornerstone in the theory of Küssner-Schwarz (KS) [43, 64]. This theory is based on the hypothesis of incompressible potential fluid flow, and so it is linear, and on thin-airfoil approach. In accordance to the small perturbation hypothesis, the aerodynamic solution of the unsteady flow around airfoils can be obtained as a linear combination of elementary solutions, corresponding to the separate contributions of the body angle of attack, camber and thickness distribution, under the further assumption that the coupling among these terms results is negligible, see Refs. [59, 43]. The KS formulation, allows for a straightforward and accurate computation of the pressure distribution, in terms of difference between the lower and the upper side, for an arbitrarily shaped mean line, subjected to any kind of motion, as far as the assumption of small perturbations is valid. The capability of the KS formulation to deal with arbitrary motions, comes directly from the theoretical foundation of the model. Since it is based on the Fourier decomposition of the velocity distribution along the mean line, a generic displacement law can be represented as sum of harmonics.

Let us consider an airfoil that moves according to a generic harmonic law:

$$z(x,t) = |\tilde{z}(\omega,x)| \mathrm{e}^{(\mathrm{j}\omega t + \varphi_z(\omega,x))}, \tag{5.1}$$

where $\tilde{(\cdot)}$ is the symbol used for the Fourier transformed variables and φ_z represents the phase of $\tilde{z}$. The upwash velocity due to the airfoil motion can be computed as:

$$v(x,t) = \frac{Dz}{Dt} = \frac{\partial z}{\partial t} + \frac{\partial z}{\partial x}\frac{\partial x}{\partial t} = \frac{\partial z}{\partial t} + U\frac{\partial z}{\partial x}. \tag{5.2}$$

The Fourier series of the spatial velocity distribution, allows for the computation of the upwash coefficients P_0, $...P_n$:

$$v(\theta,t) = g(\theta)\mathrm{e}^{(\mathrm{j}\omega t + \varphi(\theta))} = -U\mathrm{e}^{\mathrm{j}\omega t}\left(P_0 + 2\sum_{n=1}^{\infty} P_n \cos n\theta\right), \tag{5.3}$$

where θ is an angular abscissa that corresponds to the position x along the airfoil chord, through the classical transformation $x = b\cos\theta$, with $2b$ the chord of the airfoil. The upwash coefficients hence read:

$$P_n = -\frac{1}{U\pi}\int_0^{\pi} g(\theta)\mathrm{e}^{\mathrm{j}\varphi(\theta)} \cos n\theta \mathrm{d}\theta \tag{5.4}$$

Küssner and Schwarz shown that the difference of pressure coefficient can be expressed as a Fourier series:

$$\Delta C_P(\theta,t) = \mathrm{e}^{\mathrm{j}\omega t}\left(4A_o \tan\frac{\theta}{2} + 8\sum_{n=1}^{\infty} A_n \sin n\theta\right), \tag{5.5}$$

with the A_n coefficients that can be easily expressed as function of the upwash coefficients

$$\begin{aligned} A_0 &= C(k)\left(P_0 + P_1\right) - P_1 \\ A_n &= P_n + \frac{\mathrm{j}k}{2n}\left(P_{n-1} - P_{n+1}\right) \qquad \forall n > 0 \end{aligned} \tag{5.6}$$

In this equation k is the reduced frequency $k = \frac{\omega b}{U}$ and $C(k)$ is the Theodorsen's function [59], already introduced in chapter 2. The aerodynamic lift and moment result from the integration of the difference of pressure along the mean line, that is:

$$L(t) = \frac{1}{2}\rho U^2 b \int_0^{\pi} \Delta C_P(\theta,t) \sin\theta \mathrm{d}\theta \tag{5.7}$$

$$M_0(t) = -\frac{1}{2}\rho U^2 b^2 \int_0^{\pi} \left(\cos\theta - \bar{x}_0\right) \Delta C_P(\theta,t) \sin\theta \mathrm{d}\theta \tag{5.8}$$

where the moment is computed with respect to the point $\bar{x}_0 = x_0/b$. For pitch and plunge harmonic motions, the KS theory leads to results that are analytically equivalent to the classical Theodorsen's theory [64]. A general overview on the Küssner Schwarz formulation is reported in appendix B.

There are few studies on the physical mechanism of the GF lift enhancement, but there is a general agreement on the fact that the couple of counter-rotating vortices that appear in the flow behind the GF causes a shift of the Trailing Edge (TE) Kutta condition [2]. This vortical region on the TE can be considered an extension of the airfoil that increases the effective chord and modifies the camber, resulting in experienced lift and moment magnitude enhancements [8]. For subsonic flows the GF causes an increase of the pressure coefficient C_P along the entire airfoil.

Chapters 3 and 4 show that also for the present L-shaped Gurney configuration, both the numerical simulations and the experiments highlight the two CRV close to the TE, for upward and downward rotations of the tab, reported again for completeness in figure 5.1 . As a consequence the velocity and the pressure undergo local changes along the entire airfoil, see chapter 3.

The approach herein followed to build the ROM starts from the definition of a parametric model, that can be analyzed exploiting the KS theory, followed by a numerical optimization to identify the appropriate values of the parameters, through a comparison with CFD virtual experiments.

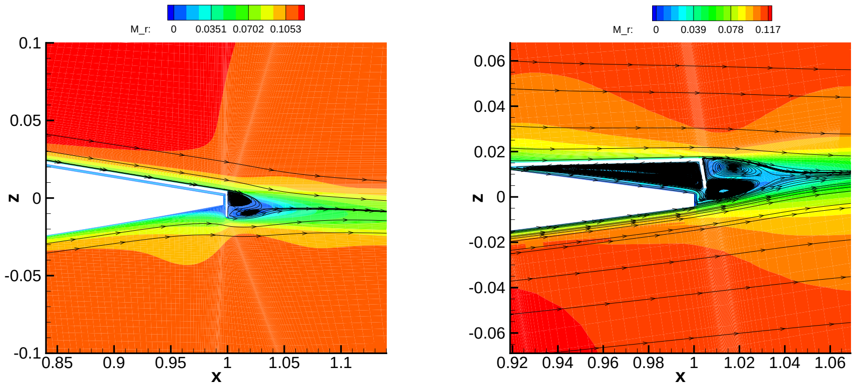

Figure 5.1: Mach number field and streamlines close to the L-tab downward deployed (left) and 9 deg. upward deflected (right); angle of attack $\alpha = 0$ degrees, freestream Mach number $\mathrm{M} = 0.117$, Reynolds number $\mathrm{Re} = 1 \cdot 10^6$.

Exploiting an approach similar to the one used by Liu and Montefort [39], the airfoil is represented by a piece-wise-linear mean-line composed by a fixed part plus two movable surfaces: a flap and a tab, see figure 5.2. The first segment represents the airfoil, the second segment models the flap portion of the L-tab, while the last one accounts for the effect of the CRV generated by the tab and it extends beyond the TE of the airfoil. This last portion represents a virtual movable surface that can explain the different loads experienced by the airfoil equipped with the L-tab with respect to the clean one. In the following, the first segment of the piece-wise mean line will be referred to as Equivalent Rigid Airfoil (ERA), the second segment as Equivalent L-Tab (ELT) and the third segment as counter-rotating Vortices Equivalent Trim Tab (VETT).

The geometrical and motion parameters considered for the model order reduction are reported in figure 5.2. The parameter x_f indicates the starting point of the ELT along the chord of the equivalent KS model, and it is expressed through an angle as $\theta_f = \arccos(x_f/b)$. The parameter x_c, and the corresponding angle $\theta_c = \arccos(x_c/b)$, indicates the TE of the airfoil along the chord of the equivalent KS model. The complex parameter $\beta_f \in \mathbb{C}$ represents the amplitude and phase of the ELT rotation relative to the ERA, whereas $\beta_w \in \mathbb{C}$ represents the amplitude and phase of the VETT rotation with respect

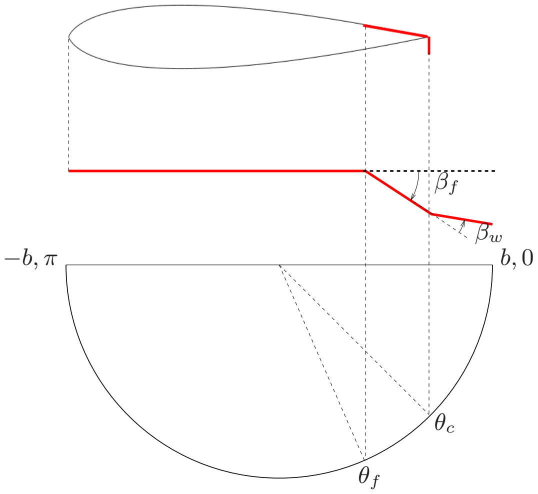

Figure 5.2: Thin line geometry and motion parameters of the physically based ROM for the NACA 0012 blade section equipped with the L-tab.

to the ELT. All of the geometrical parameters of the KS model are expressed as non-dimensional, using the thin airfoil chord $c_k = 2b$ as reference quantity. The position θ_c is an extremely important parameter, since it represents the fact the the KS thin airfoil equivalent model has a longer chord with respect to the reference airfoil, or in other words, that the point where the Kutta condition must be enforced is not at the airfoil TE. However, to compute the lift and moment to be compared with the CFD simulations, the pressure coefficient in the KS thin airfoil model is integrated from the leading edge to θ_c, since the last portion of the KS equivalent model is only virtual and does not correspond to a solid structure that can carry loads.

The L-tab equipped airfoil, is herein modeled as a linear system of three degrees of freedom. These are: the pitch of the airfoil, the plunge of the airfoil and the rotation of the L-tab. According to the assumption of linearity of the model, it is possible to study the system response in terms of aerodynamic loads, for each of the three aforementioned forcing motions, separately. Furthermore, under the hypotheses of small perturbations and linearity, the upwash velocity can be expressed as follows:

$$v = v_{\alpha_0}(x) + v_\alpha(x,t) + v_h(x,t) + v_{\beta_0}(x) + v_\beta(x,t) \tag{5.9}$$

where the subscript α represents the velocity terms due to the pitch motion, the subscript h indicates the velocity terms due to the plunge motion and the subscript β is related to the velocity terms due to the L-tab motion. The velocity contributions related to each of the degrees of freedom can be split into a steady term and a time dependent term, representative of the steady mean value and of unsteady oscillation amplitude, respectively. Accordingly, the aerodynamic forces can be expressed as:

$$F = F_{\alpha_0}(x) + F_\alpha(x,t) + F_h(x,t) + F_{\beta_0}(x) + F_\beta(x,t) \tag{5.10}$$

In the present work pitch oscillations are considered with zero mean value, hence $v_{\alpha_0}(x) = 0$ in equation (5.9). Consistently, it results that $F_{\alpha_0}(x) = 0$ in equation (5.10). A model order reduction procedure is performed separately for each of the remaining terms of equations (5.9) and (5.10). The analysis to compute the unsteady loads associated with pitch and plunge motion is not reported here, since it is equivalent to the standard approach presented in Ref. [64], Chapter 13. For the computation of the lift and moment associated with the ELT and VETT rotations, the equivalent geometry for the ROM takes the following mathematical form:

$$z(x,t) = \begin{cases} 0 & \text{if} \quad x \le x_f \\ -(x-x_f)\tilde{\beta}_f \mathrm{e}^{\mathrm{j}\omega t} & \text{if} \quad x_f < x \le x_c \\ -(x-x_f)\tilde{\beta}_f - (x-x_c)\tilde{\beta}_w \mathrm{e}^{\mathrm{j}\omega t} & \text{if} \quad x > x_c. \end{cases} \tag{5.11}$$

The upwash velocity is computed according to equation (5.2) and expressed as a function of θ. It reads

$$v(\theta,t) = \begin{cases} 0 & \text{if} \quad \theta > \theta_f \\ -U\left(\mathrm{j}k\cos\theta - \bar{x}_f + 1\right)\tilde{\beta}_f \mathrm{e}^{\mathrm{j}\omega t} & \text{if} \quad \theta_f > \theta \ge \theta_c \\ -U\Big(\left(\mathrm{j}k\cos\theta - \bar{x}_f + 1\right)\tilde{\beta}_f + \left(\mathrm{j}k\cos\theta - \bar{x}_c + 1\right)\tilde{\beta}_w\Big)\mathrm{e}^{\mathrm{j}\omega t} & \text{if} \quad \theta < \theta_c. \end{cases} \tag{5.12}$$

The adoption of relative rotations as degrees of freedom allows to build an incremental model for the lift and moment. Consider initially the upwash coefficients and the aerodynamic loads for the ELT, extending from θ_f to θ_c, oscillating with respect to its initial point θ_f, see figure 5.2.

The vertical displacement $z(x,t)$ of the ELT reads:

$$z(x,t) = -(x-x_f)\tilde{\beta}_f \mathrm{e}^{\mathrm{j}\omega t}, \qquad x_f < x < x_c \tag{5.13}$$

where $\tilde{\beta}_f \in \mathbb{C}$ is a complex parameter representing the Fourier transform of the ELT rotation at frequency ω. The vertical perturbation velocity is expressed as:

$$v(\theta,t) = -U\left(\mathrm{j}k\left(\cos\theta - \bar{x}_f\right) + 1\right)\tilde{\beta}_f \mathrm{e}^{\mathrm{j}\omega t} = g(\theta)\mathrm{e}^{\mathrm{j}\omega t}, \qquad \theta_c < \theta < \theta_f \tag{5.14}$$

with $\bar{x}_f = x_f/b$. The upwash coefficients P_n are then computed through the Fourier transformation of the vertical perturbation velocity, within the interval $[\theta_c \quad \theta_f]$.

$$P_n = -\frac{\tilde{\beta}_f}{U\pi}\int_{\theta_c}^{\theta_f} g(\theta)\mathrm{e}^{\mathrm{j}\varphi(\theta)}\cos n\theta \,\mathrm{d}\theta, \quad \text{where} \tag{5.15}$$

$$\begin{aligned}
P_0 &= \frac{\tilde{\beta}_f}{\pi}\left(\mathrm{j}k(\sin\theta_f - \bar{x}_f\theta_f) + \theta_f\right) - \frac{\tilde{\beta}_f}{\pi}\left(\mathrm{j}k(\sin\theta_c - \bar{x}_c\theta_c) + \theta_c\right), && (5.16)\\
P_1 &= \frac{\mathrm{j}k\tilde{\beta}_f}{\pi}\left(\frac{\sin\theta_f}{2} + \frac{\sin 3\theta_f}{6}\right) + \frac{\tilde{\beta}_f}{2\pi}\left(\sin 2\theta_f(1-\mathrm{j}k\bar{x}_f)\right) + && (5.17)\\
&\quad -\frac{\mathrm{j}k\tilde{\beta}_f}{\pi}\left(\frac{\sin\theta_c}{2} + \frac{\sin 3\theta_c}{6}\right) - \frac{\tilde{\beta}_f}{2\pi}\left(\sin 2\theta_c(1-\mathrm{j}k\bar{x}_c)\right), \\
P_n &= \frac{\tilde{\beta}_f}{\pi}\left(1-\mathrm{j}k\bar{x}_f\right)\left(\frac{\sin n\theta_f}{n}\right) + \frac{\tilde{\beta}_f}{\pi}\left(\frac{\sin(n+1)\theta_f}{2(n+1)} - \frac{\sin(1-n)\theta_f}{2(n-1)}\right) + && (5.18)\\
&\quad -\frac{\tilde{\beta}_f}{\pi}\left(1-\mathrm{j}k\bar{x}_c\right)\left(\frac{\sin n\theta_c}{n}\right) - \frac{\tilde{\beta}_f}{\pi}\left(\frac{\sin(n+1)\theta_c}{2(n+1)} - \frac{\sin(1-n)\theta_c}{2(n-1)}\right)
\end{aligned}$$

It is easy to see that the series of P_n is convergent toward zero, so it can be truncated after N terms, where N is selected as the first coefficient where the order of magnitude is at least three order of magnitude smaller than the leading term of the series.

The A_0 and A_n coefficients are easily computed through equation (5.6). The computation of ΔC_P through equation (5.5) is also straightforward. The aerodynamic loads can be obtained by substituting the resulting expression of ΔC_P in equations (5.8) and integrating the ΔC_P between the leading edge at π and the the trailing edge at θ_c, i.e.

$$\begin{aligned}
C_L &= \frac{1}{2}\int_{\theta_c}^{\pi}\left(4A_0\tan\frac{\theta}{2}+8\sum_{n=1}^{N}A_n\sin n\theta\right)\sin\theta\mathrm{d}\theta \qquad (5.19)\\
&= 2A_0\left(\pi-\theta_c+\sin\theta_c\right)+A_1 2\pi+A_1\frac{\sin 2\theta_c}{4}-A_1 2\theta_c+\\
&\quad +4\sum_{n=2}^{N}A_n\left(\frac{(n-1)\sin\left(n+1\right)\theta_c+(n+1)\sin\left(1-n\right)\theta_c}{2n^2-2}\right)
\end{aligned}$$

The moment coefficient with respect to the mid-chord reads:

$$\begin{aligned}
C_m &= -\frac{1}{4}\int_{\theta_c}^{\pi}\left(4A_0\tan\frac{\theta}{2}+8\sum_{n=1}^{N}A_n\sin n\theta\right)\sin\theta\cos\theta\mathrm{d}\theta \qquad (5.20)\\
&= A_0\left(\frac{\pi}{2}-\frac{\sin 2\theta_c}{4}+\sin\theta_c-\frac{\theta_c}{2}\right)+\\
&\quad +2A_1\frac{\sin^3\theta_c}{3}-A_2\frac{\pi}{2}+A_2\frac{\sin 4\theta_c}{8}-A_2\frac{\theta_c}{2}+\\
&\quad -2\sum_{n=3}^{N}\left(\frac{(n-2)\sin\left(n+2\right)\theta_c-(n+2)\sin\left(n-2\right)\theta_c}{4n^2-16}\right)
\end{aligned}$$

An identical approach can be used to compute the lift and moment coefficient due to the rotation of the VETT.

The ROM is determined by means of an optimization procedure performed at a fixed reduced frequency. The objective of the optimization is the minimization of the error between the steady mean value or the first harmonic component of the CFD-computed lift and moment coefficients, and the corresponding quantities computed using the KS model of figure 5.2. Namely, the numerical results presented in chapters 3 and 4 are used as a reference for the identification procedure. The higher harmonic content due to nonlinear effects (see Ref. [42]) is not considered here since the linear KS approach does not allow to model such effects. In fact, the response at the same frequency of the tab activation is the main concern when harmonic vibration control algorithms, such as the classical Higher Harmonic Control (HHC) [16], are considered in rotorcraft applications, see also chapter 6. A least squares-based optimization algorithm is used for the minimization procedure. In particular, the function to be minimized is written as follows:

$$\begin{aligned}
f(\mathbf{p}) = {}& \frac{1}{\Re(C_{L_{\mathrm{NUM}}})^2}\,\Re(C_{L_{\mathrm{NUM}}}-C_{L_K}(\mathbf{p}))^2+\frac{1}{\Im(C_{L_{\mathrm{NUM}}})^2}\,\Im(C_{L_{\mathrm{NUM}}}-C_{L_K}(\mathbf{p}))^2+ \qquad (5.21)\\
&+\frac{1}{\Re(C_{m_{\mathrm{NUM}}})^2}\,\Re(C_{m_{\mathrm{NUM}}}-C_{m_K}(\mathbf{p}))^2+\frac{1}{\Im(C_{m_{\mathrm{NUM}}})^2}\,\Im(C_{m_{\mathrm{NUM}}}-C_{m_K}(\mathbf{p}))^2
\end{aligned}$$

where $C_{L_{\mathrm{NUM}}}$ and $C_{m_{\mathrm{NUM}}}$ are the first harmonic components of lift and moment coefficients computed through CFD simulations. The array $\mathbf{p}$ contains the geometrical and motion free parameters of the KS model discussed in the above, see also figure 5.2, i.e. $\mathbf{p} = [\theta_c, \theta_f, \tilde{\beta}_f, \tilde{\beta}_w]$. Therefore it is composed of six independent scalar parameters.

For steady simulations, the solver output loads are directly used in equation (5.21), which, of course, has no imaginary terms. On the other hand, $C_{L_K}(\mathbf{p})$ and $C_{m_K}(\mathbf{p})$ are the KS aerodynamic loads to be computed by the optimization algorithm, according to the free parameters in $\mathbf{p}$. Depending from the sectional degree of freedom under consideration, different sets of free parameters are selected among all those of the KS formulation. A multistart approach is used to perform the minimization, to avoid the identification of a local minimum that does not correspond to the global one, since the objective function is not expected to be regular in the parameters space. Additionally, to achieve physically consistent solutions, constraints are imposed a priori to the free parameters. The values employed for these constraints will be given in the following sections.

5.2 Reduced order model for steady airfoil with fixed L-tab

The present section develops the ROM for the L-tab in fixed position and the airfoil at constant angle of attack. Section 5.1 illustrates how the ROM is achieved by means of an optimization procedure, where the difference in the aerodynamic loads between the numerical computations and the KS formulation has to be minimized. With this aim a least squares based optimization procedure is carried out. The functional to be minimized is the one of equation 5.21, where the imaginary terms are equal to zero.

The numerical results reported in chapters 3 and 4 highlight how the steady aerodynamic loads undergo significant shifts, according to the rotation angle of the L-tab, which indeed causes an alteration of the sectional geometry. Modifications in the effective aerodynamic shape are shown to be twofold. First, as for a classical TE flap, the solid geometry is modified in terms of camber, with respect to the baseline configuration. Secondly, the CRV lead to an additional change in camber and increase the effective chord.

To develop a ROM that can keep these effects into account, the extension of the KS model to steady flows is employed, obtaining a formulation analytically equivalent to the the classical thin airfoil theory. For a constant rotation of the L-tab, a time independent velocity distribution is adopted, to compute the upwash coefficients of the KS formulation. As a consequence $v(x)$ is computed using equation (5.2) with the partial derivative with respect to the time equal to zero.

According to the approach outlined in section 5.1 and referring to equations (5.9) and (5.10), the transfer function between $v_{\beta_0}(x)$ and $F_{\beta_0}(x)$ is herein derived. To keep into account both the flap-like effects and the Gurney flap-like effects, two free parameters in the KS model are employed in the optimization algorithm. These are $\beta_f = \tilde{\beta}_f \in \mathbb{R}$ and $\beta_w = \tilde{\beta}_w \in \mathbb{R}$, namely the rotations of the ELT and of the VETT in the piece-wise mean line of the KS model. So, the functional is minimized with respect to these two variables. Preliminary investigations showed that the functional is far from regular and features several local minima, therefore additional constraints have to be added to the free parameters. Such constraints fix the range of the parameters, allowing for the achievement of a physically consistent solution. Namely, β_f and β_w are constrained to belong to the range $[-20 \quad 20]$ degrees. The remaining geometrical parameters, involved in the KS formulation, are fixed according to the numerical results reported in chapter 3, a priori with respect to the optimization procedure. The chord-wise position of the ELT hinge is set to $x_f = 0.6c_k$, so that the ELT covers the 20% of the mean line length, consistently with the numerical geometry.

The numerical results show that the first intersection point of the upper and lower side streamlines is located approximately 5%c past the TE for the present L-tab. As a consequence $\cos\theta_c = 0.9c_k$ is imposed.

Figures 5.3(a) and 5.3(b) show the values of the ROM parameters obtained through the optimization procedure, performed separately at several deflections of the L-tab. β_f is found to increase with the L-tab upward deflection. The attainment of a negative β_f for the L-tab downward deflected, correctly reproduces the local increase of camber in TE area due to the presence of the GF. A change of slope is visible at β around 2 deg., for both the free parameters. The switch from the first to the second regime occurs when the L-tab deflection is such that the present device does no longer protrude from the airfoil lower side. When this happens, the stagnation flow region upsteam the L-tab disappears, with consequent changes in the flow field and in the circulation. As a result the pressure distribution and in turn the aerodynamic loads are modified. On the other hand β_w is always negative. In the range $\beta = [0 \quad 2]$ degrees, the slope of the β_w-β curve is positive, whereas the opposite is observed for larger rotations of the tab.

The two linear trends of the aerodynamic loads and the smoothness of the geometrical parameters with respect to the L-tab deflection –except for the sharp points at $\beta = 2$– suggest that these ROMs may be easily interpolated to compute the equivalent thin geometry and the aerodynamic loads for an arbitrary value of β in the range of tested angles.

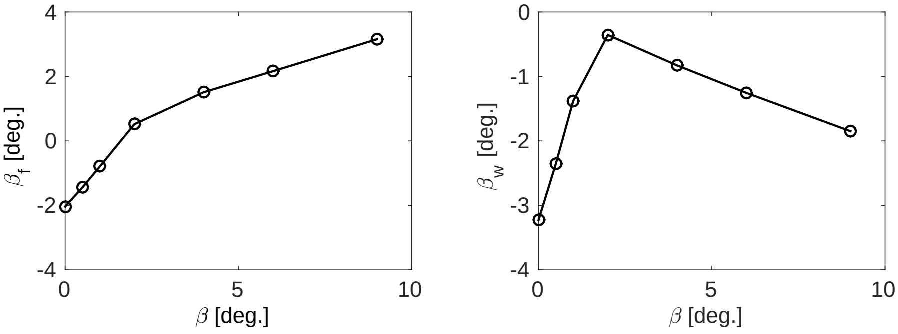

(a) Deflection angle of of the ELT

(b) Deflection angle of of the VETT

Figure 5.3: Rotation angles of the ELT and of the VETT for the physically based thin airfoil ROM, at several angular positions of the L-tab; $\alpha = 0$ degrees, M $= 0.117$, Re $= 1 \cdot 10^6$.

Figures 5.4(a) and 5.4(b) show the lift and mid-chord moment coefficients computed through the ROM, compared to the corresponding numerical loads, for several deflections of the L-tab. A very good accuracy of the ROM, in reproducing the numerical loads, is found, both in terms of C_L and C_m. A regular trend of C_L and C_m is achieved with respect to the L-tab deflection. Again, two almost linear regimes are observed.

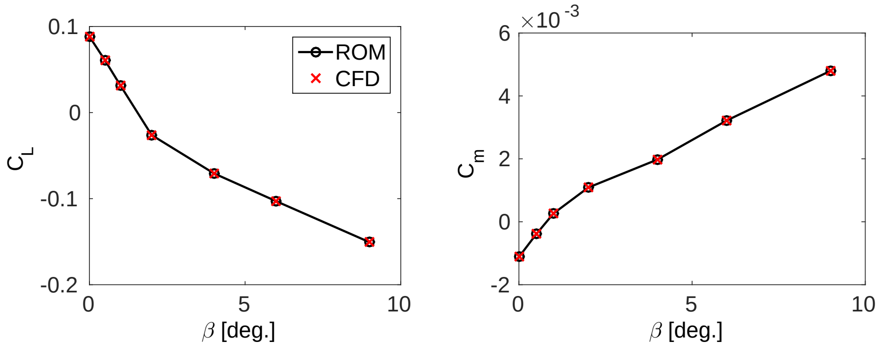

(a) Lift coefficient

(b) Mid-chord moment coefficient

Figure 5.4: Lift and mid-chord moment coefficients from the ROM, compared to the reference numerical values, for several deflections of the L-tab; $\alpha = 0$ degrees, M $= 0.117$, Re $= 1 \cdot 10^6$.

Figure 5.5 reports the equivalent thin line geometry, overlapped to the numerical flow field, close to the TE. The dotted line represents the direction parallel to the longitudinal edge of the numerical L-tab, whereas the dashed line is the linear approximation of the zero vorticity line in the CRV region. This latter segment is used to locate the mean line of the CRV wake. The two segments just mentioned are useful to catch the mean line modification effects resulting from the numerical computations, due to the L-tab. Moreover two streamlines, one from the upper and one from the lower side, are reported to further facilitate the visualization of the CRV region. The dash-dotted line represents the ELT, whereas the solid line is related to the VETT. The equivalent geometry well captures the flow physics near the body. Indeed the absolute slopes, as well as the relative inclination of the two KS segments, resemble the mean line effects observed in the simulations, even in terms of the CRV. Results, from both numerical computations and the ROM, highlight how the CRV is almost aligned to the L-tab, as expected for steady state configurations. Notice that a good matching, between the numerical and the analytical mean line, is found for all of the L-tab rotations herein considered.

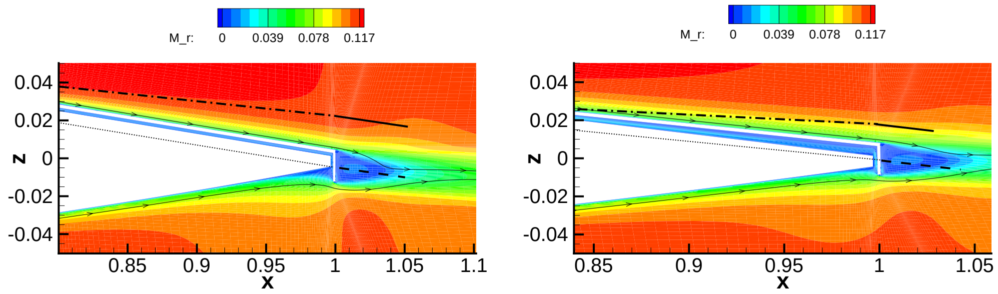

(a) $\beta = 0$ deg. (b) $\beta = 1$ deg.

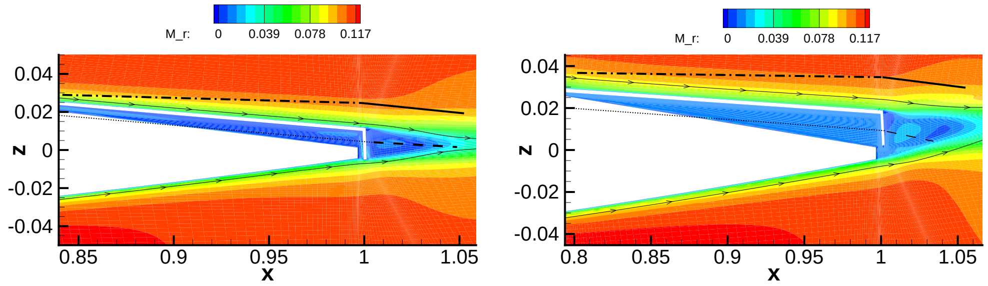

(c) $\beta = 2$ deg. (d) $\beta = 4$ deg.

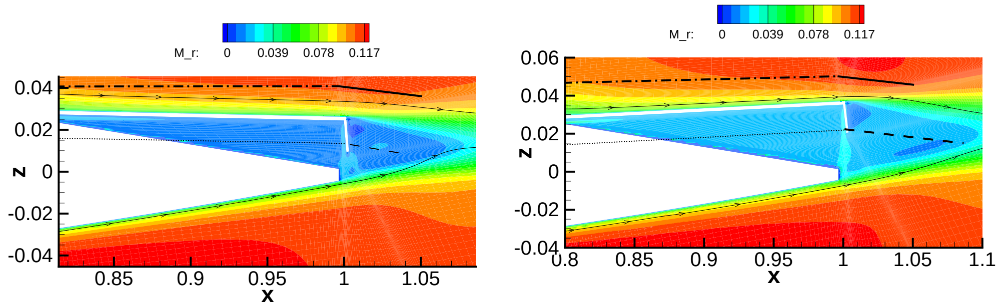

(e) $\beta = 6$ deg. (f) $\beta = 9$ deg.

Figure 5.5: Equivalent geometry of the physically based thin airfoil ROM, overlapped to the numerical model and to the Mach number field, together with two streamlines, for several deflections of the L-tab; $\alpha = 0$ degrees, $\mathrm{M} = 0.117$, $\mathrm{Re} = 1 \cdot 10^6$; dotted: direction parallel to the longitudinal edge of the numerical L-tab, dashed: linear approximation of the zero vorticity iso-line in the wake region, dash-dotted: ELT, solid: VETT.

The predictive capabilities of the present ROM are tested for $\beta = 7$ degrees. The mean line geometry is computed by extracting the values of the ELT and VETT from the curves reported in figures 5.3(a) and 5.3(b). The aerodynamic loads are extracted from the curves of figures 5.4(a) and 5.4(b). Numerical computations are carried out and compared to the ROM. Table 5.1 shows that the developed ROM accurately predicts aerodynamic loads due to an arbitrary L-tab deflection. A 2.24% error is attained in terms of the lift coefficient, whereas a 5% error results in terms of the mid-chord moment coefficient. Moreover figure 5.6 highlights that the ROM realistically represents the solid body mean line, as well as the mean shape of the CRV. These results further confirm the suitability of the present ROM for preliminary design studies of L-tab equipped aerodynamic sections. Indeed, not only the model allows for a straightforward computation of aerodynamic loads, but also

Airloads	ROM	CFD	% error
C_L	-0.1178	-0.1205	2.24%
C_m	0.0038	0.0040	5%

Table 5.1: Lift and mid-chord moment coefficient predicted with the ROM compared to the numerically computed values, together with the percent relative error; $\alpha = 0$ degrees, $\beta = 7$ degrees, M $= 0.117$, Re $= 1 \cdot 10^6$.

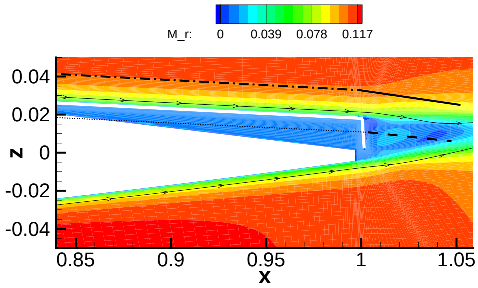

Figure 5.6: Equivalent geometry predicted by the physically based thin airfoil ROM, overlapped to the numerical model and flow field; $\alpha = 0$ degrees, $\beta = 7$ degrees, M $= 0.117$, Re $= 1 \cdot 10^6$; dotted: direction parallel to the longitudinal edge of the numerical L-tab, dashed: linear approximation of the zero vorticity iso-line in the wake region, dash-dotted: ELT, solid: VETT.

the near body-flow field can be reasonably predicted.

5.3 Reduced Order Model for pitching and plunging airfoil with L-tab in fixed position

The results reported in section 4.1 highlight that, for oscillating motions of the airfoil with the L-tab in fixed position, the first harmonic of the unsteady airloads is primarily affected by thickness effects, rather than by the camber shape. As a consequence no significant improvements are expected by modifications of the mean line, as those proposed in section 5.2 for constant angle of attack. It appears uselessntroduce camber modifications due to the L-tab or to the CRV, in that no improvements are expected in reproducing the first harmonic of the aerodynamic loads.

Therefore the KS model for a one-piece straight mean line is retained appropriate, to be used as ROM for the airfoil in pitch or in plunge motion, with the L-tab kept at constant deflection. Actually the chord of the model is rescaled by taking into account the mean chord enlargement effects caused by the CRV, as anticipated in section 4.1. No additional segments are used for the mean line representation and no optimization procedures are required for their sizing. Furthermore, since the formulation herein employed deals with a straight segment in unsteady motion, no physical interpretations in terms of effective camber are possible.

Further improvements could eventually be gained by trying to take into account the thickness effects, by means of a fitting procedure analogous to that presented in chapter 2 for the Theodorsen's model. That is, a modified KS model, accounting for the unsteady thickness effects, could be developed. Notice that, whereas in chapter 2 inviscid computations are used as a reference for the fitting procedure, viscous numerical simulations should be here employed. This appears mandatory to keep the consistency with the characterization of the L-tab equipped blade section reported in chapters 3 and 4, in which the viscosity has shown to have a primary role. Since the primary aim of this part of the work is to characterize and reproduce the effects of the L-tab, such fitting is left as a possible future step.

5.4 Reduced order model for steady airfoil with harmonically oscillating L-tab

The final degree of freedom of the ROM for the blade section equipped with the TE device is necessary to represent the effect of the moving L-tab, that drags the CRV created behind its vertical prong. Since the L-tab is subject to an oscillating motion, it is expected that also the CRV beside the movable device undergo an oscillatory movement.

The KS-based ROM is composed of a three segments piece-wise lifting line, where the first segment represents the airfoil in fixed position, the second segment is associated to the harmonic motion of the L-tab and the third segment is related to the harmonic motion of the CRV. The parameters of the ROM are computed through a least squares-based optimization algorithm. In this case the array $\mathbf{p}$ reads: $\mathbf{p} = [\tilde{\beta}_f,\ \tilde{\beta}_w,\ \theta_c]$, with $\tilde{\beta}_f = \beta_f \in \mathbb{R}$ and $\tilde{\beta}_w \in \mathbb{C}$ to account for the possible phase shift of the CRV motion, with respect to that of the L-tab. The length of the ELT is kept fixed at the 20% of the KS model chord, that is $\theta_f = 0.6c_k$, where $c_k = 2$, while the length of the VETT, and so the θ_c parameter, is defined through the optimization. Hence there are four scalar parameters of the KS model to be determined through the minimization algorithm. Constraints on the parameters are imposed to drive the minimization algorithm toward a physically consistent solution. Namely, the angle β_f has to lie in the range $[-90, 90]$ degrees; the magnitude of the angle β_f has to lie in the range $[-15, 15]$ degrees; the length of the VETT is constrained to lie in the range 1–10%c.

Figure 5.7 shows the free parameters obtained after the optimization procedure performed at different reduced frequencies, separately. In figure 5.7(a) the length of the VETT is rescaled with respect to the unitary chord of the numerical geometry. Hence, the shift of $\chi_w = \chi_w(x_c)$ with respect to the unity, directly quantifies the effect of chord extension. Overall this parameter doesn't undergo significant excursions, and on average the chord enlargement is equal to 2.5%c. Figures 5.7(b) and 5.7(c) represent the deflection amplitude of the ELT and of the VETT, respectively. Both these angles grow in magnitude, with opposite sign, for increasing values of k. The range of both $\tilde{\beta}_\mathrm{f} = \beta_\mathrm{f}$ and $\tilde{\beta}_\mathrm{w}$ is found to be smaller than six degrees. Figure 5.7(d) reports the oscillation phase of the VETT, i.e. of the movement of the CRV, with respect to the ELT. The regular shape of the curves reported in figure 5.7 –apart from a change in sign of $\varphi(\beta_w)$ between $k = 0.1$ and $k = 0.2$– allows to approximate such quantities with a low order polynomial. Therefore it should be possible to compute the mean line shape and the aerodynamic loads with the present ROM for an arbitrary k in the range [0.1 0.6].

Figure 5.8 compares the first harmonic of the CFD numerical aerodynamic lift and moment, to the results obtained with the linear ROM at $k = 0.1$, $k = 0.2$, $k = 0.4$ and $k = 0.6$. A good matching is found in terms of both the lift and moment coefficients for each of the reduced frequencies.

To highlight the physical consistency of the present model, the thin-line of the ROM is represented over the geometry and the flow field of the numerical model. Figures 5.9 and 5.10 show the shape of the identified KS-based flat-plate geometry, at four different time instants in the oscillation cycle, for $k = 0.1$ and $k = 0.6$, respectively.

The slope of the ELT is in reasonable agreement with the angular position of the numerical L-tab, for each of the time steps. A qualitatively good matching with the numerical physics is found in terms of length and rotation of the VETT as well. Indeed the absolute mean inclination and extension of the CRV are very well captured by the the third segment of the piece-wise mean line of the ROM. Furthermore, also the relative inclination of the two KS segments shows a good agreement with the numerical mean line effects. The ROM is capable to represent with reasonable accuracy the out-of-phase

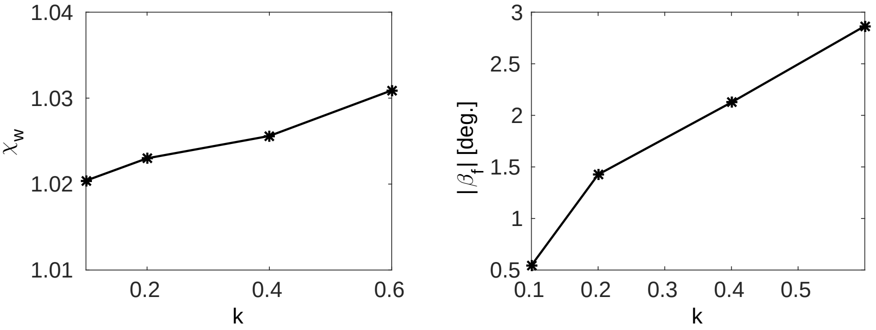

(a) Chord enlargement, function of the VETT length

(b) Deflection amplitude of the ELT

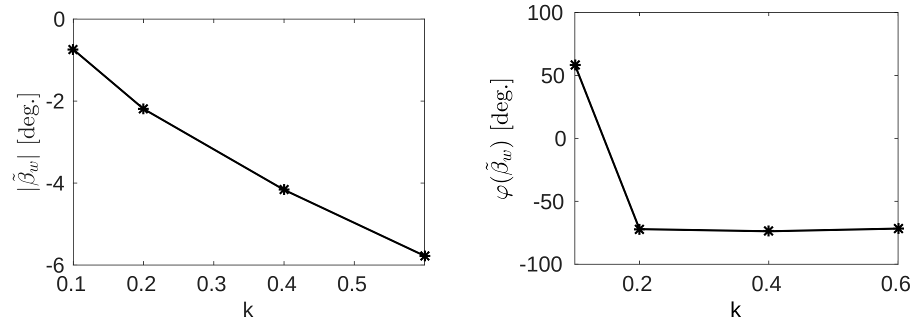

(c) Deflection amplitude of the VETT

(d) Deflection phase of the VETT

Figure 5.7: Values of the free parameters achieved after the optimization procedure at several reduced frequencies. The first parameter represents the effect of chord augmentation due to the CRV; $\beta = 1 + \sin(\omega t)$ degrees, $\alpha = 0$ degrees, M $= 0.117$, Re $= 1 \cdot 10^6$.

oscillation of the CRV with respect to the L-tab reported in figure 5.7(d). It can be observed that the angle between the L-tab and the CRV, both in numerical computations and in the ROM, is found to be significantly greater than what found for the steady state, discussed in section 5.2. So it can be stated that lead effects, with respect to the input motion law are visible both in the flow field and in the airloads.

Finally the predictive capabilities on the model in computing the unsteady airloads and the equivalent geometry, are tested at arbitrary reduced frequencies in the range [0.1 0.6]. A spline interpolation is applied to the coefficients reported in figure 5.7 and the resulting functions are evaluated at $k = 0.3$ and $k = 0.5$. The corresponding equivalent geometry, as well as the unsteady loads, are computed and compared to the flow field and to the airloads attained by means of numerical computations. Figure 5.11 reports the lift and the moment coefficient hysteresis curves achieved with the ROM vs. the numerical computations at $k = 0.3$ and $k = 0.5$. A good matching between the analytical low order model and the numerical results is observed. Both the amplitude and the slopes of the hysteresis cycles are well captured, giving feasibility to the model in predicting the first harmonic of the unsteady loads.

The equivalent KS thin-line, computed for $k = 0.3$, is depicted in figure 5.12, together with the numerical geometry and flow field. The dash-dot line, corresponding to the ELT, is found in good agreement with the inclination of the tab, represented by the dotted line, at each of the time instants herein considered. Moreover the solid line, which represents the VETT, is found to reasonably capture the mean slope of the zero-vorticity iso-line, corresponding to the dashed line. Therefore the ROM appears also capable to correctly predict the mean line modification introduced by the L-tab, given the reduced frequency of the motion.

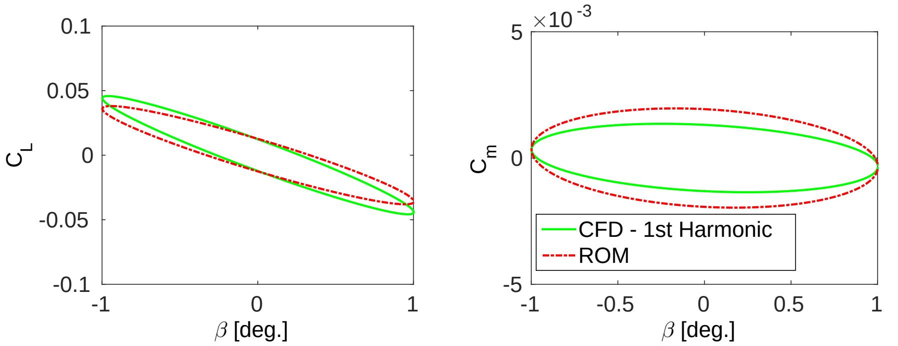

(a) Lift coefficient, $k = 0.1$ (b) Mid-chord moment coefficient, $k = 0.1$

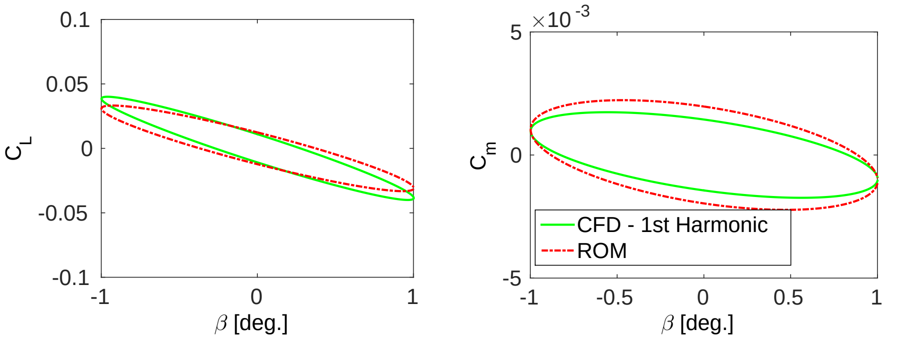

(c) Lift coefficient, $k = 0.2$ (d) Mid-chord moment coefficient, $k = 0.2$

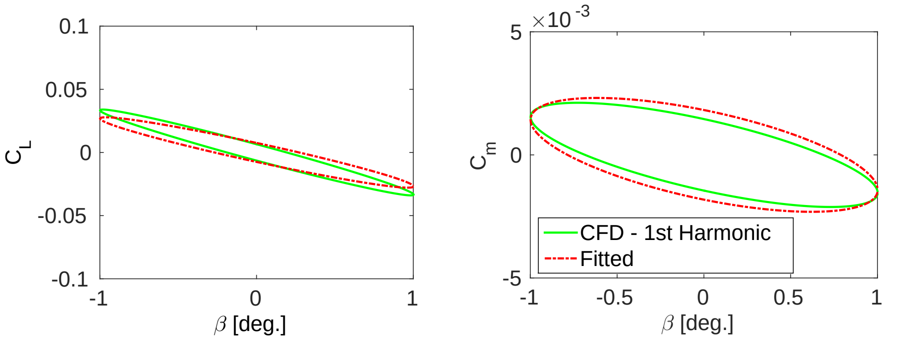

(e) Lift coefficient, $k = 0.4$ (f) Mid-chord moment coefficient, $k = 0.4$

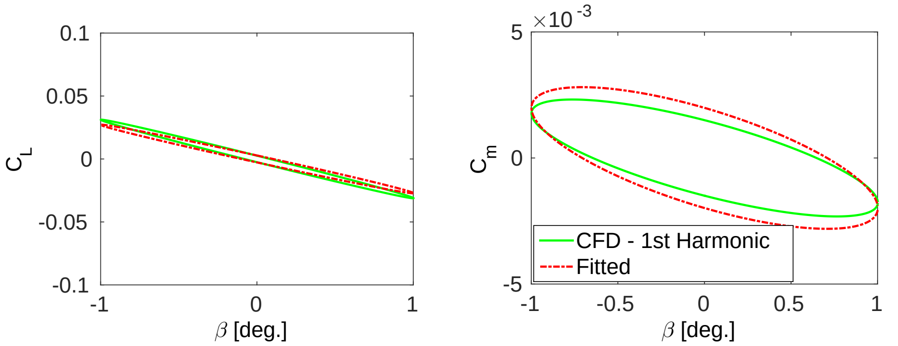

(g) Lift coefficient, $k = 0.6$ (h) Mid-chord moment coefficient, $k = 0.6$

Figure 5.8: Comparison between the numerical 1st harmonic components of the aerodynamic loads and their counterparts from the KS-based ROM at $k = 0.1$, $k = 0.2$, $k = 0.4$ and $k = 0.6$; $\beta = 1 + \sin(\omega t)$ degrees, $\alpha = 0$ degrees, $\mathrm{M} = 0.117$, $\mathrm{Re} = 1 \cdot 10^6$.

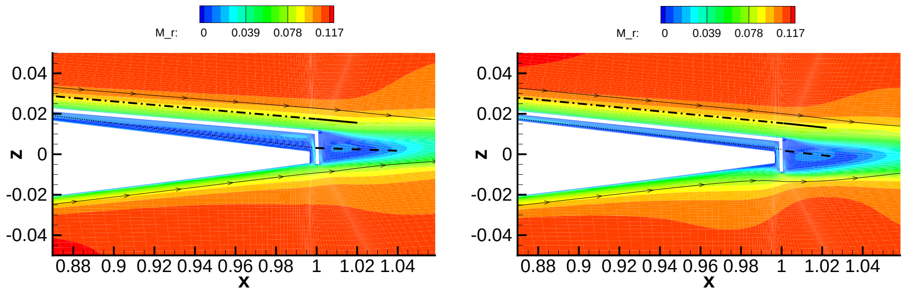

(a) $\beta = 2$ deg. (b) $\beta = 1$ deg., downstroke

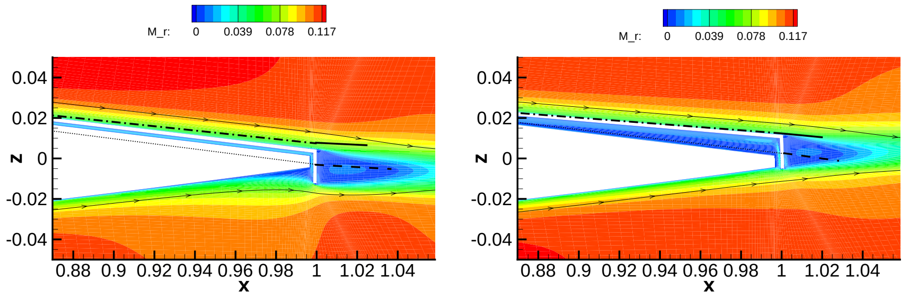

(c) $\beta = 0$ deg. (d) $\beta = 1$ deg., upstroke

Figure 5.9: Equivalent geometry for the physically based thin airfoil ROM, overlapped to the numerical section and to the Mach number field, together with two streamlines. Four time steps along the tab oscillation period are depicted; $\beta = 1 + \sin(\omega t)$ degrees, $k = 0.1$, $\alpha = 0$ degrees, $\mathrm{M} = 0.117$, $\mathrm{Re} = 1 \cdot 10^6$; dotted: direction parallel to the longitudinal edge of the numerical L-tab, dashed: linear approximation of the zero vorticity iso-line in the wake region, dash-dotted: ELT, solid: VETT.

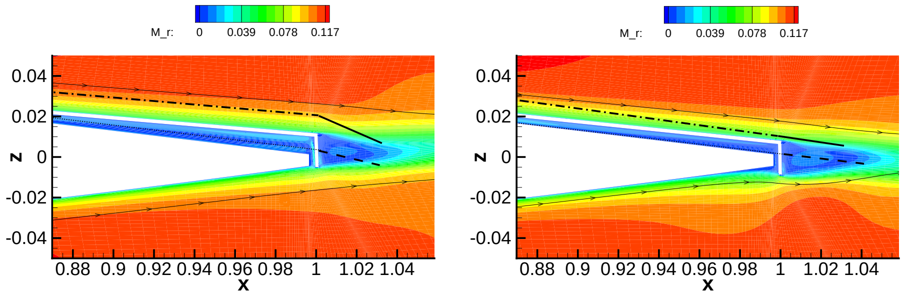

(a) $\beta = 2$ deg.

(b) $\beta = 1$ deg., downstroke

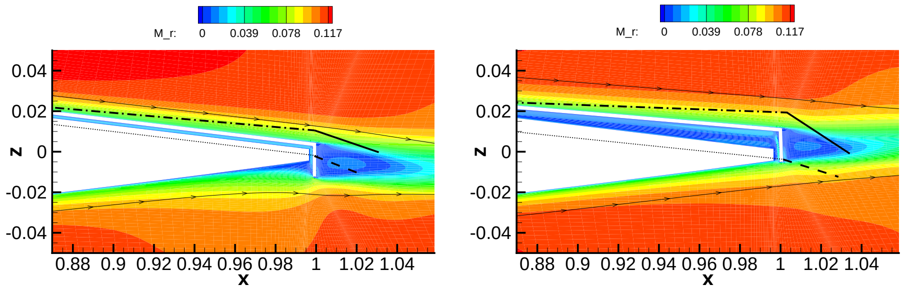

(c) $\beta = 0$ deg.

(d) $\beta = 1$ deg., upstroke

Figure 5.10: Equivalent geometry for the physically based thin airfoil ROM, overlapped to the numerical section and to the Mach number field, together with two streamlines. Four time steps along the tab oscillation period are depicted; $\beta = 1 + \sin(\omega t)$ degrees, $k = 0.6$, $\alpha = 0$ degrees, $\mathrm{M} = 0.117$, $\mathrm{Re} = 1 \cdot 10^6$; dotted: direction parallel to the longitudinal edge of the numerical L-tab, dashed: linear approximation of the zero vorticity iso-line in the wake region, dash-dotted: ELT, solid: VETT.

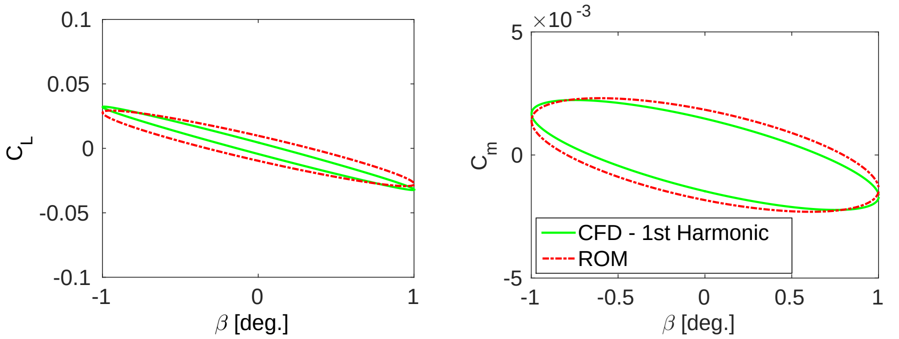

(a) Lift coefficient, $k = 0.3$ (b) Mid-chord moment coefficient, $k = 0.3$

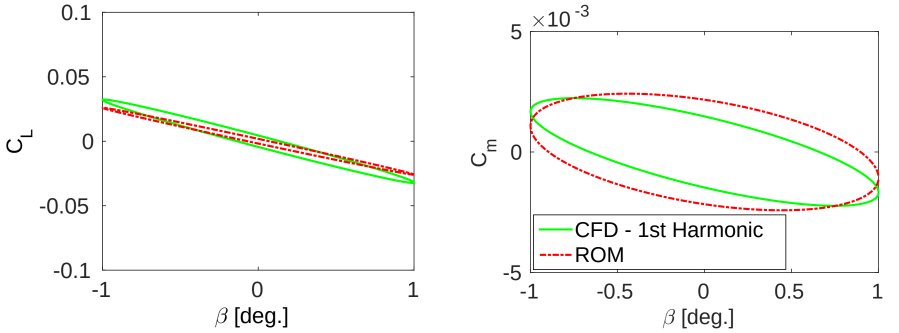

(c) Lift coefficient, $k = 0.5$ (d) Mid-chord moment coefficient, $k = 0.5$

Figure 5.11: Comparison between the numerical 1st harmonic components of aerodynamic loads and their counterparts from the KS-based ROM at $k = 0.3$ and $k = 0.5$; $\beta = 1 + \sin(\omega t)$ degrees, $\alpha = 0$ degrees, $\mathrm{M} = 0.117$, $\mathrm{Re} = 1 \cdot 10^6$.

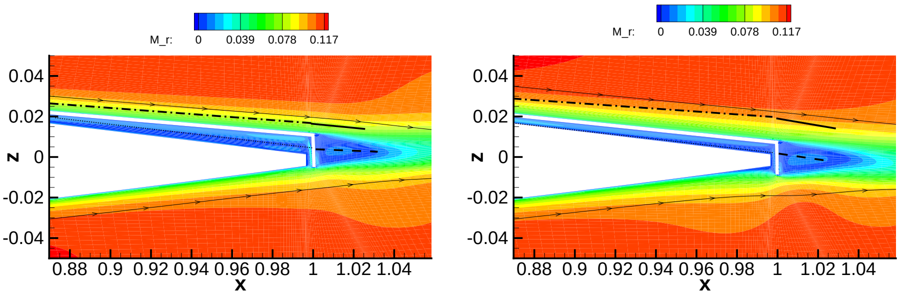

(a) $\beta = 2$ deg.

(b) $\beta = 1$ deg., downstroke

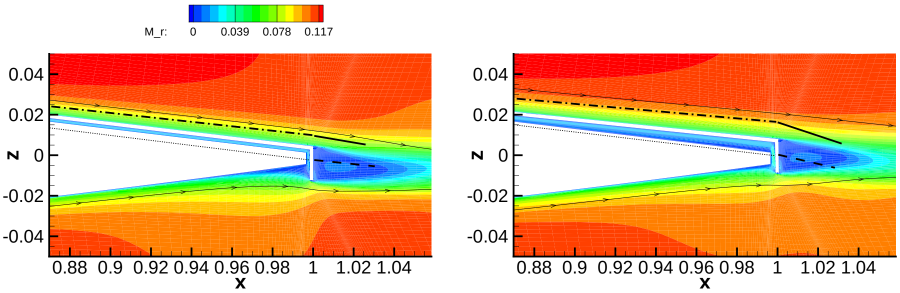

(c) $\beta = 0$ deg.

(d) $\beta = 1$ deg., upstroke

Figure 5.12: Equivalent geometry predicted by the physically based thin airfoil ROM, overlapped to the numerical section and to the Mach number field, together with two streamlines. Four time steps along the tab oscillation period are depicted; $\beta = 1 + \sin(\omega t)$ degrees, $k = 0.3$, $\alpha = 0$ degrees, $\mathrm{M} = 0.117$, $\mathrm{Re} = 1 \cdot 10^6$; dotted: direction parallel to the longitudinal edge of the numerical L-tab, dashed: linear approximation of the zero vorticity iso-line in the wake region, dash-dotted: ELT, solid: VETT.

5.5 Comparison between the L-tab and a classical trailing edge flap by means of thin line models

The L-tab, in fixed position as well as in oscillating motion, acts primarily on the effective camber line. In particular such camber modifications are found to be twofold. That is, on one hand the longitudinal edge of the movable device causes a change of the effective shape in the trailing edge area. On the other hand, the vertical prong of the tab generates two Counter Rotating Vortical structures past the trailing edge. As extensively reported in chapter 3, such vortical structures allow for a finite difference of pressure between the upper and the lower side. As a consequence, the Kutta condition is shifted downstream the trailing edge, leading to an effective longer and more cambered airfoil. In particular, being the flow entirely subsonic, these phenomena significantly affect the loads distribution on the whole airfoil.

Chapters 3 and 4 highlight that modifications in the effective camber, equivalent to those induced by the L-tab, could be attained with a classical trailing edge flap, a solution widely employed in literature, see e.g. Refs [106, 17, 107, 18, 19, 20]. Nevertheless, whereas the same shape of the mean line could be attained both with a Gurney flap like device, as the present L-tab, and with a classical trailing edge flap, the loads generated by the two configurations are expected to be quite different. Indeed the CRV past the L-tab do not directly contribute to the generation of the aerodynamic loads, that is such vortical structures do not act as a lifting surface, not being a solid body. Rather the CRV modify the pressure distribution along the rear airfoil, ultimately affecting the resulting aerodynamic loads. On the other hand a classical trailing edge flap behaves indeed as a lifting surface, capable to generate aerodynamic loads by itself. As a consequence, also the upstream affection in the pressure distribution is expected to be different, when dealing with a trailing edge flap, rather than with a Gurney flap like device.

It appears interesting to gain an overview on the aerodynamic loads potentially developed by these two different trailing edge configurations, when the airfoil is kept at constant angle of attack, therefore when the control surfaces have a primary affection on the flow field. This allows to preliminary estimate which solution among the present L-tab and a classical flap is more suitable for specific purposes, e.g. the vibration reduction at a reduced frequency of interest.

Thin line analytical low order models, as the one presented in this chapter, are found appropriate for this purpose, since these allow for a rapid and straightforward computation of the aerodynamic loads, given the reference geometry and the motion law. For the L-tab the KS based ROMs discussed in sections 5.2 and 5.4 are of course employed, and the related geometrical and motion parameters are evaluated at the reduced frequencies of interest. For the classical trailing edge flap similar ROMs are developed to reproduce the steady and unsteady force coefficients. In particular, the thin line geometry for the flapped blade section is composed of two segments, see the bottom of figure 5.13. The former is thought to represent the airfoil, whereas the latter, referred to as equivalent flap, is meant to reproduce the effects of the trailing edge flap. Figure 5.13 shows a schematic comparison between the two movable devices under consideration, performed with the corresponding thin line geometry. Notice that the flap, as well as its thin counterpart, is though to reproduce also the chord enlargement caused by the CRV past the L-tab. Therefore the second segment in the equivalent geometry of the flapped section has length equal to that of the ELT plus the VETT, as it is shown in figure 5.13. The hinge of the flap has the same location of that of the L-tab. The values of β_f and θ_c computed with the identification procedures performed on the L-tab are used for the model of the trailing edge flap as well. Of course this latter configuration does not present the DOF related to β_w, i.e. the additional motion of the VETT.

It appears useful to remark that the second segment for the trailing edge flap model is meant to be entirely a solid body. Therefore, whereas for the L-tab model the pressure distribution is integrated from the leading edge LE up to x_c only, for the trailing edge flap the integration domain ranges from LE up to the trailing edge TE, see again figure 5.13.

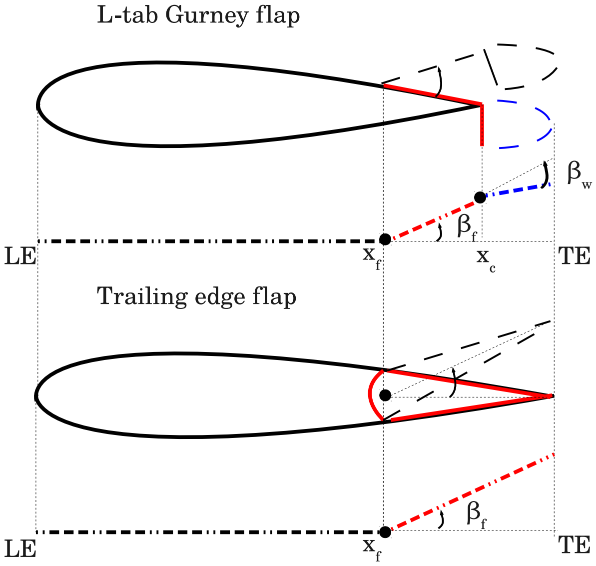

Figure 5.13: Thin line geometry for the KS based models; L-tab Gurney flap with the CRV (top) and classical trailing edge flap (bottom).

Once the resultants of the pressure distributions for the two configurations are computed, the aerodynamic loads have to be properly rescaled on the same chord length, to make them consistent and therefore comparable. Indeed the chord for the L-tab force coefficients ranges from $x = \cos\pi = -1$ to $x_c = \cos\theta_c < 1$, being the total length $1 + \cos\theta_c < 2$. With regard to the chord used as a reference for the trailing edge flap force coefficients, it ranges from $x = \cos\pi = -1$ to $x = \cos 0 = 1$, being 2 the total length. Therefore the scaling factor between the lift coefficient of the trailing edge flap model $C_{L_{\text{flap}}}$ and that of the L-tab model $C_{L_{\text{tab}}}$ reads

$$\frac{C_{L_{\text{flap}}}}{C_{L_{\text{tab}}}} = \frac{x_c + 1}{2} \tag{5.22}$$

For the pitching moment coefficient the scaling factor is computed as the square of the right hand side of equation (5.22). Figure 5.14 reports the magnitude and the phase of the properly scaled airloads, computed with the thin line models for the L-tab and for the trailing edge flap, at several values of k. The force coefficients are also computed for fixed positions of the tab, i.e $k = 0$, namely at $\beta = 1$ degree, which is the mean angle of oscillation for the unsteady motions herein taken into account. To this specific purpose the steady state ROM discussed in section 5.2 is used. The parameters of the model for the steady trailing edge flap are selected consistently with the approach adopted for the unsteady model. Figure 5.14(a) reports the magnitude of the lift coefficient versus the reduced frequency, including $k = 0$, attained with the corresponding KS based models, for the two trailing edge configurations. Notice that, whereas the L-tab grants larger lift in the range $0.05 \leq k \leq 0.125$, the trailing edge flap seems to provide higher values of normal force for $k < 0.05$ and for $0.125 <$ k < 0.6. A slightly larger value of lift seems to be achieved with the trailing edge flap for $k = 0$ as well. Figure 5.14(b) highlights that no significant differences are encountered in the phase of the lift coefficient for the two configurations at $k < 0.5$. Within this range the phase keeps almost constant with k and close to 90 degrees. At $k \geq 0.5$ the lift phase of the flapped section changes in sign, assuming values near to -90 degrees. The lift coefficient phase is of course zero at $k = 0$. Figure 5.14(c) reports the magnitude of the mid-chord moment coefficient for the L-tab and the flap models. Notice that for k > 0.0125 the moment magnitude attained with the L-tab is significantly larger with respect to the trailing edge flap. At $k = 0.0125$

the two trailing edge configurations seem to provide the same pitching moment. A larger pitching moment is attained at $k = 0$ with the trailing edge flap. The phase of the moment coefficient, reported in figure 5.14(d), is found to lie in the range [-90 90] degrees. At $k \geq 0.125$ the pitching moment phase is larger for the L-tab. The opposite occurs at $0 < k < 0.125$, whereas, again, the pitching moment phase is equal to zero at $k = 0$. At $k = 0.0125$ the pitching moment phase presents a local minimum for the L-tab and a local maximum for the trailing edge flap. In general the curve of the pitching moment phase related to the L-tab appears to be almost symmetrical to that of the trailing edge flap with respect to the $\varphi(C_m) \approx 10$ deg. horizontal axis.

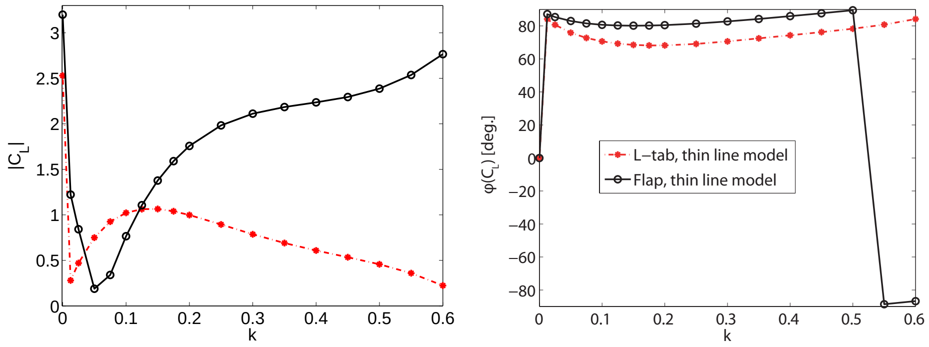

(a) Lift coefficient, magnitude

(b) Lift coefficient, phase

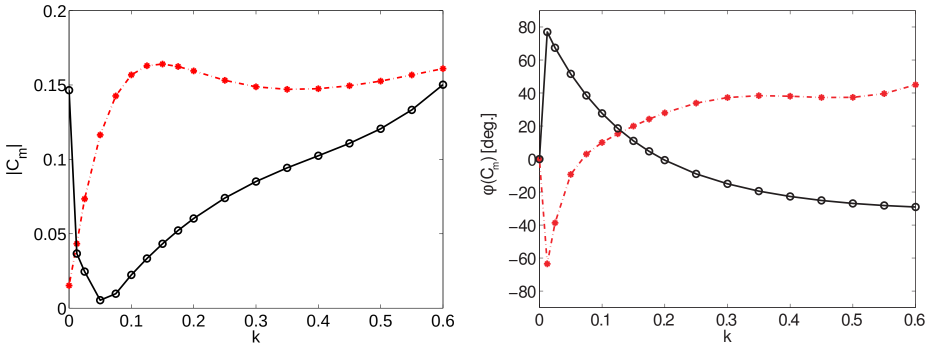

(c) Mid-chord moment coefficient, magnitude

(d) Mid-chord moment coefficient, phase

Figure 5.14: Magnitude and phase of the lift and pitching moment coefficients vs. the reduced frequency. Comparison between the L-tab and the flap models for $\beta = 1$ deg. and for $\beta = 1 + \sin(\omega t)$ degrees; M = 0.117, Re = $1 \cdot 10^6$.

It appears also interesting to look at the loads distribution along the chord and again to compare the trailing edge configurations herein investigated. With this regard, for consistency purposes, a proper rescaling has to be performed on the chord-wise domain used to plot the pressure distribution on the L-tab model. Indeed, the VETT segment actually lies downstream the trailing edge TE of the solid body. Therefore, the LE has to be kept at $x = -1$, whereas the TE has to be enlarged downstream. Starting from x_0 ranging from -1 to 1, the desired domain x_{plot} to correctly plot the pressure distribution for the L-tab model is attained with the following transformations:

$$
\begin{aligned}
x_0 &= \cos\theta && \in [-1\ \ 1] \\
x_1 &= (x_0+1) && \in [0\ \ 2] \\
x_2 &= x_1 \left[1 + \frac{1-\cos\theta_c}{1+\cos\theta_c}\right] && \in \left[0\ \ \left(2 + \frac{1-\cos\theta_c}{1+\cos\theta_c}\right)\right] \\
x_{\text{plot}} &= x_2 - 1 && \in \left[-1\ \ \left(1 + \frac{1-\cos\theta_c}{1+\cos\theta_c}\right)\right]
\end{aligned}
\tag{5.23}
$$

Figure 5.15 reports the magnitude of the pressure distributions for the L-tab and the flap models, at $k = 0.1$ and $k = 0.6$. In particular figure 5.15(a) clearly shows that the area subtended by the red curve, related to the L-tab model, is larger that that covered by the black line, associated to the trailing edge flap. Therefore the resulting lift generated by the L-tab is larger with respect to that provided by the trailing edge flap, see the points at $k = 0.1$ in figure 5.14(a). The opposite occurs at $k = 0.6$ in that figure 5.15(b) shows that the overall area subtended by the black curve, related to the flap model, is larger than that covered by red curve, associated to the L-tab. As shown in figure 5.14(a) at $k = 0.6$ the flap generates a larger normal force with respect to the L-tab.

For completeness, the lift coefficient hysteresis curves for the L-tab and the flap models, at $k = 0.1$ and $k = 0.6$, are reported in figure 5.16. These again confirm the results attained in terms of the pressure distribution. Moreover it is found that the ROM for the trailing edge flap gives reasonable results, in terms of behavior of the hysteresis loops, if compared, for example, to the computations performed by Liu [33] on a similar trailing edge movable device, or to the analytical and numerical data reported in the textbook of Leishman [66], pp. 500-502.

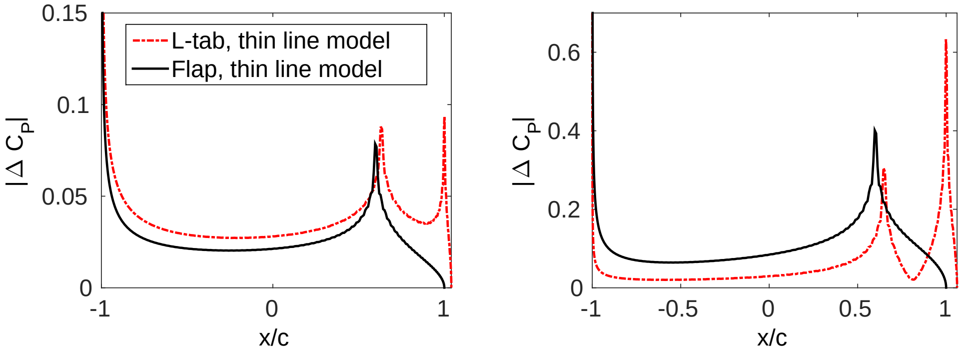

(a) k = 0.1

(b) k = 0.6

Figure 5.15: Pressure coefficient magnitude along the chord of the model. Comparison between the L-tab and the trailing edge flap models at $k = 0.1$ and $k = 0.6$; $\beta = 1 + \sin(\omega t)$ degrees, M = 0.117, Re $= 1 \cdot 10^6$.

Overall the comparisons between the loads generated by the L-tab and the trailing edge flap models highlight how, for some aspects the former configuration provides better performance, whereas for some others the trailing edge flap might be preferable. With regard to the lift and moment phase angles, these do not affect the performance of the movable devices, rather these give an useful information about the delay in the system response with respect to the input motion. Therefore the phase value is suitable e.g. when active control laws have to be defined.

With regard to the magnitude of the loads, the trailing edge flap solution is found to generate larger normal forces on a wider range of frequencies with respect to the L-tab. On the other hand the L-tab provides larger values of the pitching moment at each of the

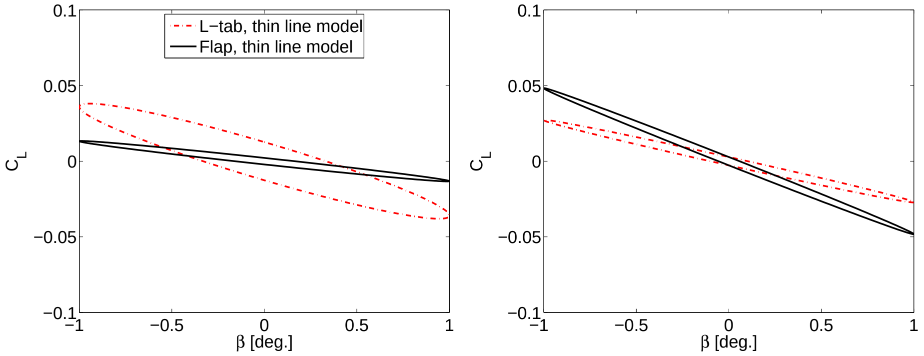

(a) k = 0.1 (b) k = 0.6

Figure 5.16: Lift coefficient hysteresis curves. Comparison between the L-tab and the trailing edge flap models at $k = 0.1$ and $k = 0.6$; $\beta = 1 + \sin(\omega t)$ degrees, M = 0.117, Re $= 1 \cdot 10^6$.

reduced frequencies taken under consideration, but at $k < 0.0125$.

The ultimate selection of the control surface to be employed is somehow tricky, since several aspects have to be taken together under consideration. Of course, the choice can not be based merely on the magnitude of lift and moment coefficients developed for steady state configurations or small amplitude oscillations, but must take into account also technological aspects. The preliminary comparison reported in this section has the primary aim of showing that both the steady and the unsteady airloads, developed by the present L-tab, are comparable, at least up to $k = 0.15$, to those generated by a classical trailing edge flap configuration, widely diffused in literature.

The capabilities of vibration reduction of both these devices will be investigated in the following. It appears useful to recall that, among the additional operations of such movable devices on rotor blades, the performance enhancement and the dynamic stall alleviation are of primary interest. With this regard, acting on the pitching moment appears to be more effective, rather than on the lift. Indeed, by acting directly on the blade twist, the angle of attack can be locally controlled and properly set to the values required e.g. for static load balance or to avoid the stall onset. Furthermore, considerations concerning actuation and stowage requirements, as those reported in the work of Palacios [34], affect the ultimate choice of the trailing edge device for the rotor blade. With this regard the employment of the L-tab appears to be very promising, since its small weight features should allow for lower power and in turn smaller and lighter actuation systems with respect to those required for classical trailing edge flaps.

5.6 Concluding remarks

The steady state and the unsteady numerical simulations discussed in chapters 3 and 4 highlight that the L-tab under consideration primarily acts by modifying the effective camber and length of the baseline section. Additionally, it is found that such device is potentially suitable for load balance improvement, performance enhancement and vibration reduction on helicopter rotor blades, if a proper control system is designed. With this specific purpose the development of a ROM, to rapidly couple the aerodynamic system with the dynamic counterpart, is mandatory.

Since the ultimate aim of the present work concerns the assessment of the L-tab capabilities in reducing vibration, the assumption of small perturbation regime is suitable. In this context, the aerodynamic section with the movable device is approximated as a linear system with three DOFs, that is the harmonic pitch and plunge motions of the airfoil and the harmonic oscillation of the L-tab, consistently with the aerodynamic characterization proposed in chapters 3 and 4. On the basis of the numerical simulations, a physically consistent ROM, derived from the analytical Küssner and Schwarz [43] linear flat plate theory, is developed for fixed rotations and unsteady harmonic motions of the L-tab, separately. The KS based ROM is thought to realistically capture the changes in the mean line shape introduced by the L-tab. Notice that, for unsteady motions, the ROM is meant to correctly reproduce the first harmonic of the aerodynamic loads, which is in fact the main concern of the HHC control system preliminarily designed in chapter 6. The ROM is attained through an optimization procedure, aimed to minimize the difference between the numerical and analytical aerodynamic loads, with respect to the geometrical and motion parameters of the three segments piece-wise mean line of figure 5.2. For pitch and plunge motions of the airfoil with the L-tab in arbitrary fixed position, the classical KS model for a straight flat plate is found to be appropriate. Indeed, for these specific motion laws, the prevailing effects on the first harmonic are attributed to the airfoil thickness, rather than to the shape of the mean line, which is far primarily affected by the L-tab. Actually, to improve the accuracy in reproducing the unsteady airloads developed by the blade in oscillating motion with the L-tab at fixed rotations, the chord of the flat plate model is rescaled by taking into account the enlargement effects due to the CRV, namely approx. 5% of the clean airfoil

A very good agreement is found between the loads computed with the KS-based ROM and the numerical results. Furthermore, the equivalent mean line of the ROM is found to accurately reproduce the reference mean line of the numerical geometry, both for fixed positions and harmonic motions of the L-tab. The length and the inclination of the CRV behind the L-tab are also very well reproduced by the ROM. Moreover the predictive capabilities of the ROM are verified for fixed positions of the L-tab and for oscillating motions of the movable device. Additionally, appendix C shows how the identification procedure performed for the oscillating movable device can be successfully applied, also when changing the parameters of the motion law. In particular no irregular changes in the free parameters of the thin line model are encountered, with respect to the oscillation law employed in section 5.4. The physical consistency of the present model is a distinguishing mark with respect to black box identification procedures, e.g. rational functions approximations. Indeed, with few parameters, the model is capable to realistically reproduce the near body physics, in addition to providing the correct aerodynamic loads as a response to steady state or harmonic inputs. The availability of a such much more complete information is of manifold suitability in the helicopter blades design process, dealing with e.g. aerodynamic shape studies or realizations of active control systems.

The present ROM is used to preliminarily compare the loads generated by the L-tab, to those provided by a trailing edge flap thin line model, with length equal to that of the ELT plus that of the VETT. The ROM for the trailing edge flap has the same geometrical and motion parameters of those computed for the L-tab, but the VETT relative motion, which is of course absent. It is found that the trailing edge flap configuration provides higher values of lift at large reduced frequencies, whereas larger pitching moments are generated by the L-tab. Moreover the L-tab is expected to have lower power requirements, with respect to a classical flap, in addition to yielding less drawbacks in terms of drag rise, as suggested in chapter 3 and in Ref. [15]. These remarks find further confirmations in the works of Liu [33] and Palacios [34]. Of course much deeper studies lead to the final selection of the more proper solution to be employed on a rotor, and taking under consideration several aspects at the same time is mandatory. The preliminary comparison herein reported has the primary aim of proving that the novel L-shaped trailing edge configuration has capabilities comparable to those of a well known solution, as a classical trailing edge flap.

Chapter 6

Active control on helicopter blades with the L-tab

The ROMs discussed in chapter 5, are exploited to build up two separate three degrees of freedom linear aerostructural models, for a blade equipped with a partial span L-tab and trailing edge flap, respectively. At first the results of a test CFD computation performed on the blade section moving in pitch and in plunge, equipped with the L-tab also in unsteady motion, are compared to those attained by superimposing the ROMs for each of these DOFs. Such comparison allows to ultimately prove the linearity of the aerodynamic behavior of the blade and to confirm the actual suitability of such ROMs for the aeroelastic model. Classical analytical formulations are used to build up the mass and stiffness matrices for the aerostructural systems. A higher harmonic control algorithm is then developed for the L-tab or flap equipped blade models, with the aim of computing proper control inputs for each of the two trailing edge configurations, in order to reduce separately the 2/rev, 3/rev, 4/rev and 5/rev harmonics of the blade root rotating frame vertical force, flapping and feathering moments. Overall a successful reduction of the vibratory loads is attained, by imposing proper motion laws to the L-tab. Moreover the attainment of similar results with a well known trailing edge device, such the classical flap taken under consideration, is a further confirmation of the potential feasibility of this novel L-tab as an effective alternative mean for vibration reduction on rotor blades. Section 6.1 illustrates how the linear analytical aerostructural models for a rotor blade equipped with the L-tab and the TE flap respectively, are built up. The derivation of the aerodynamic transfer function, as well as the assembling of the mass and stiffness matrices, are discussed in detail. The linearity check for the aerodynamic behavior of the blade with a three DOFs CFD computation is also reported at the beginning of the section. Subsequently section 6.2 describes the formulation of the HHC algorithm, by providing the matrices included in the figure of merit, in addition to the resulting expression of the control input. The vibratory flapping and feathering moments and the vertical force, obtained with the application of the control inputs computed at 2/rev, 3/rev, 4/rev and 5/rev, are compared to those of the uncontrolled system. The effectiveness of both the L-tab and the TE devices in load alleviation is discussed. Section 6.3 contains concluding remarks and proposes future developments to further improve the control action.

6.1 Aeroelastic model for the blade section with the L-tab

An analytical formulation based on the typical section model [45] is used to investigate the aeroelastic response of the blade section equipped either with the L-tab or with the

TE flap introduced in section 5.5. Details of this largely employed analytical approach can be found, for instance, in the textbook of Johnson [44], chapter 16. Consistently with the ROM developed for the aerodynamic loads, the aerostructural model has three DOFs, namely pitch and plunge oscillations of the airfoil, in addition to the rotation of the trailing edge movable device. Since three motions of the blade are involved together, it appears proper to ultimately demonstrate that the application of a linear model for the aerodynamic behavior of the L-tab equipped blade is in fact feasible. Actually other authors [106, 107, 33] employed in fact linear aerodynamic models to investigate the aeroelastic behavior of helicopter blades equipped with trailing edge control surfaces, making this approach far to be novel. With this purpose CFD test computations are carried out on the L-tab equipped blade section model, undergoing both pitch and plunge oscillations, in addition to a harmonic motion of the movable device. The first harmonics of the resulting lift and moment coefficients are then compared to those attained by the superimposition of the ROMs related to each of these motions separately, see chapter 5. Indeed small amplitude oscillations are imposed for the input motions, since these are appropriate in the context of vibratory loads, which are indeed the focus of this chapter. The input motion laws are $\alpha = 0.5\sin(\omega t)$ deg. for the pitch, $h/c = 0.005\sin(\omega t)$ for the plunge and $\beta = 0.1 + 0.1\sin(\omega t)$ deg. for the L-tab oscillation. The circulatory frequency ω is defined according to k $= \omega c/2U = 0.1$, being $c = 1$ m and $U = 40$ m/s. With regard to the ROM for the L-tab in harmonic oscillation, the geometrical and motion parameters reported in figure 5.7 are used. These are computed for $\beta = 1 + \sin(\omega t)$ degrees but, due to the linear assumption for the model, not significant variations on such quantities are expected by varying the parameters of the motion laws. With this regard in appendix C the identification procedure discussed in chapter 5 is applied for a different oscillation of the L-tab. The geometrical and motion parameters of the resulting thin line geometry are found reasonably similar to those attained in chapter 5 for oscillations with amplitude and mean value equal to one degree. Therefore it appears feasible to approximate the parameters of the thin line model as invariant with respect to the motion law parameters, at least as a first approximation.

Table 6.1 reports the CFD computed first harmonic of the lift and the quarter chord moment coefficients, compared to their counterparts attained with the ROMs of chapter 5.

Loads computation	$\lvert C_L \rvert$	$\varphi(C_L)$ [deg.]	$\lvert C_m \rvert$	$\varphi(C_m)$ [deg.]
CFD–first harmonic	0.0762	65.7836	0.0285	133.1010
ROMs	0.0788	61.2122	0.0224	134.3476

Table 6.1: First harmonics of the CFD computed lift and quarter chord moment coefficients compared to the corresponding quantities achieved with the linear superimposition of the ROMs of chapter 5.

A good agreement is found between the results of the linear superimposition of the single DOF ROMs and the three DOFs numerical computations. Namely 3% and 7% errors are observed for the lift coefficient magnitude and phase respectively. With regard to the moment coefficient, errors of 20% and 0.9% are observed for the magnitude and the phase respectively. Overall such matching confirms that the assumption of linearity for the development of the ROMs reported in chapter 5 is actually appropriate, to describe the aerodynamic behavior of the L-tab equipped blade section, of course within the small perturbation regime. Moreover, the good agreement observed between the ROMs and the CFD suggests how the assumption of thin line geometrical and motion parameters almost invariant, with respect to the motion law, is in fact feasible.

The derivation of the aerostructural models for a rotor blade with a trailing edge L-tab or flap is discussed hereinafter. According to classical approaches adopted to model the blade dynamics [44], the plunge motion is written as a function of the local bending, namely

$h = -\beta_{\mathrm{bl}}\, r$, being β_{bl} the flapping angle and r the local radius on the blade. Consistently with the classical notation, the pitch of the blade is referred to as θ, i.e. $\theta = \alpha$. Moreover the rotation of the control movable device is herein referred to as $\beta_{\mathrm{cont}} = \beta$, positive upward. The resulting 3x1 complex array of the blade DOFs is therefore $[\beta_{\mathrm{bl}}\ \ \theta\ \ \beta_{\mathrm{cont}}]^T$.

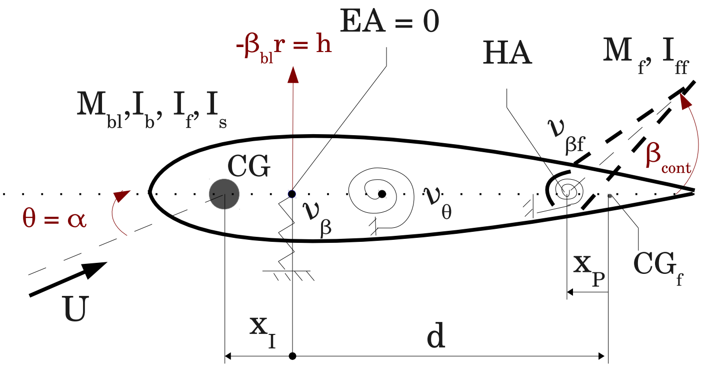

Figure 6.1: Sketch of a typical section model with a trailing edge flap

The aeroelastic model, thought as a simple flapped hingeless rotor helicopter blade, is sketched in figure 6.1. The bending stiffness is represented a translational spring of non-dimensional stiffness ν_β, equivalent to the rotating natural frequency of flap mode for the blade model. On the other hand, the torsional stiffness is represented by means of a torsional spring of non-dimensional stiffness ν_θ, equivalent to the rotating natural frequency of the torsion mode for the blade model. The trailing edge movable device has non-dimensional torsional stiffness $\nu_{\beta\mathrm{f}}$, herein assumed negligible with respect to ν_β and ν_θ. The blade mass is referred to as M_{bl}, whereas its flap and feathering moments of inertia are referred to as I_b and I_f, respectively. The bending static moment of the blade is referred to as I_s. To keep the consistency with the stiffness quantities, the blade mass properties are made dimensionless with respect to the flap moment of inertia [44]. The mass M_{f} and moment of inertia I_{ff} of the TE control surface are herein assumed negligible with respect to those of the blade.

The origin of the x chord-wise coordinate is located on the blade elastic axis EA, namely at the airfoil quarter-chord. The center of gravity CG is located at distance x_I upstream the elastic axis. The center of gravity of the control surface CG$_{\mathrm{f}}$ is located at distance d from the elastic axis. The offset of the flap hinge axis HA with respect to its center of gravity corresponds to x_P.
The control surface is supposed to cover the 12% of the blade length and to be centered at the 75% of the blade span, as shown in figure 6.2.

The resulting aeroelastic system for a single rotor blade with TE control surface is written in non-dimensional form as:

$$[-\omega^2 \mathbf{M}^{3\mathrm{x}3} + \mathbf{K}^{3\mathrm{x}3} - \gamma {\mathbf{H}_{\mathbf{am}}}^{3\mathrm{x}3}]\ [\mathbf{q}(\mathrm{j}\omega)]^{3\mathrm{x}1} = [\mathbf{Z}(\mathrm{j}\omega)]^{3\mathrm{x}3}\ [\mathbf{q}(\mathrm{j}\omega)]^{3\mathrm{x}1} = \begin{bmatrix} \bar{M}_{\beta_{\mathrm{bl}}} \\ \bar{M}_\theta \\ \bar{M}_{h_{\beta_{\mathrm{cont}}}} \end{bmatrix}^{3\mathrm{x}1} \tag{6.1}$$

being $\mathbf{M}$ the mass matrix, $\mathbf{K}$ the stiffness matrix, $\mathbf{H_{am}}$ the aerodynamic transfer matrix, $\mathbf{q} = [\beta_{\mathrm{bl}}\ \ \theta\ \ \beta_{\mathrm{cont}}]^T$ the array of the blade DOFs, ω an integer multiple of the blade angular velocity and γ the Lock number, i.e. the ratio between the aerodynamic forces and the inertial forces (here the blade flap moment of inertia I_b). Moreover $M_{\beta_{\mathrm{bl}}}$, M_θ, $M_{h_{\beta_{\mathrm{cont}}}}$ correspond to the blade flapping moment, pitching moment and hinge moment, respectively. No damping terms are introduced in the model, and no gust or additional

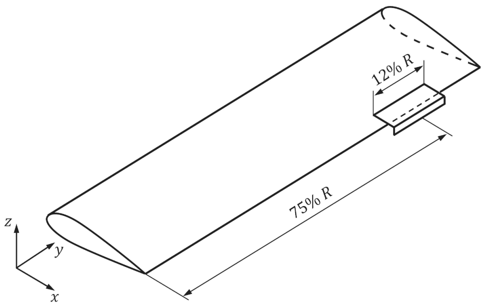

Figure 6.2: Sketch of the blade model equipped with the L-shaped control surface.

external forcing are considered at this stage.

The 3x3 non-symmetrical full aerodynamic transfer matrix $\mathbf{H_{am}}$ is meant to provide the 3x1 array of the root airloads, resulting from pitch and plunge oscillations of the blade and from harmonic motions of the control surface. The elements of $\mathbf{H_{am}}$ are computed with the thin-line based ROMs provided in section 5.4, considering unitary amplitude input motions. The sectional lift L, quarter-chord pitching moment $M_{\mathrm{c}/4}$ and hinge moment M_h attained with the ROMs have to be then integrated along the whole blade. Namely 833 stations along the blade span –100 on the control surface sketched in figure 6.2– are used to compute the local airloads. Notice that the local airspeed U changes on the blade sections according to the law $U = \Omega r$, being r the local radius and Ω the rotor angular velocity. Therefore the local reduced frequency, required to compute the unsteady airloads on the corresponding section, reads:

$$k = \frac{\omega c}{2\Omega r} = \frac{\omega b}{\Omega r}, \tag{6.2}$$

being c the span-wise uniform blade chord and b the corresponding semi-chord. Section 5.4 shows that the geometrical and motion parameters of the ROM slightly change with the reduced frequency. As a result it is required to evaluate these quantities for each of the stations on the span. With this aim the curves of figure 5.7 are interpolated at the local reduced frequency to properly compute the sectional airloads. Notice that, consistently with the most widely diffused approaches [44], the Theodorsen's function [59] C(k) involved in the computation of the local unsteady loads is kept constant along the blade span. Namely a reference value corresponding to the reduced frequency evaluated at $\bar{r} = 0.75R$ is used, so that $k = \frac{\omega b}{\Omega \bar{r}} \Rightarrow \mathrm{C} = \bar{\mathrm{C}}(k)$. Once the load distribution on the blade is obtained, the resulting non-dimensional forces at the blade root are computed as follows:

$$\bar{M}_{\beta_{\mathrm{bl}}} = \frac{1}{\rho 2\pi c \Omega^2 R^4} \int_0^R rL \, dr \tag{6.3}$$

$$\bar{M}_{\theta} = \frac{1}{\rho 2\pi c \Omega^2 R^4} \int_0^R M_{\mathrm{c}/4} \, dr \tag{6.4}$$

$$\bar{M}_{h_{\beta_{\mathrm{cont}}}} = \frac{1}{\rho 2\pi c \Omega^2 R^4} \int_0^R M_h \, dr, \tag{6.5}$$

where R is the blade radius and ρ is the freestream density. Notice that no offset is herein assumed for the aerodynamic center with respect to the elastic axis. Therefore the resulting aerodynamic system can be written in non-dimensional form as:

$$\begin{bmatrix} \bar{M}_{\beta_{\mathrm{bl}}} \\ \bar{M}_{\theta} \\ \bar{M}_{h_{\beta_{\mathrm{cont}}}} \end{bmatrix} = \begin{bmatrix} h_{\beta_{\mathrm{bl}}\beta_{\mathrm{bl}}} & h_{\beta_{\mathrm{bl}}\theta} & h_{\beta_{\mathrm{bl}}\beta_{\mathrm{cont}}} \\ h_{\theta\beta_{\mathrm{bl}}} & h_{\theta\theta} & h_{\theta\beta_{\mathrm{cont}}} \\ h_{\beta_{\mathrm{cont}}\beta_{\mathrm{bl}}} & h_{\beta_{\mathrm{cont}}\theta} & h_{\beta_{\mathrm{cont}}\beta_{\mathrm{cont}}} \end{bmatrix} \begin{bmatrix} \beta_{\mathrm{bl}} \\ \theta \\ \beta_{\mathrm{cont}} \end{bmatrix} = [\mathbf{H_{am}}]^{3\mathrm{x}3}[\mathbf{q}]^{3\mathrm{x}1} \tag{6.6}$$

The symmetrical mass matrix reads [44]:

$$\mathbf{M} = \frac{1}{\Omega^2} \begin{bmatrix} 1 & -\frac{3}{2}\frac{x_I}{R} & 0 \\ -\frac{3}{2}\frac{x_I}{R} & \bar{I}_f & 0 \\ 0 & 0 & 0 \end{bmatrix}, \tag{6.7}$$

where x_I is the offset of the blade center of gravity with respect to its feathering axis (negative upstream the feathering axis) and $\bar{I}_f$ is the ratio between the feather moment of inertia I_f and the flap moment of inertia I_b.

The symmetrical stiffness matrix, also made dimensionless with respect to the blade flap moment of inertia, reads [44]:

$$\mathbf{K} = \begin{bmatrix} \nu_\beta^2 & -\frac{3}{2}\frac{x_I}{R} & 0 \\ -\frac{3}{2}\frac{x_I}{R} & \bar{I}_f \nu_\theta^2 & 0 \\ 0 & 0 & 0 \end{bmatrix}, \tag{6.8}$$

recalling that ν_β is the rotating natural frequency of the flap mode and ν_θ is the rotating natural frequency of the pitch mode, both expressed in /rev.

Since β_{cont} is actually a control input, the aeroelastic transfer matrix $\mathbf{Z}(\mathrm{j}\omega)$ of equation (6.1) is split as follows:

$$\mathbf{Z}(j\omega) = \begin{bmatrix} [\mathbf{Z}_{\beta_{\mathrm{bl}}\theta}]^{2\mathrm{x}2} & [\mathbf{Z}_{(\beta_{\mathrm{bl}}\theta)\beta_{\mathrm{cont}}}]^{2\mathrm{x}1} \\ [\mathbf{Z}_{\beta_{\mathrm{cont}(\beta_{\mathrm{bl}}\theta)}}]^{1\mathrm{x}2} & [\mathbf{Z}_{\beta_{\mathrm{cont}}\beta_{\mathrm{cont}}}]^{1\mathrm{x}1} \end{bmatrix} \tag{6.9}$$

This leads to:

$$\left[\mathbf{Z}_{\beta_{\mathrm{bl}}\theta}\right] \begin{bmatrix} \beta_{\mathrm{bl}} \\ \theta \end{bmatrix} = -\left[\mathbf{Z}_{(\beta_{\mathrm{bl}}\theta)\beta_{\mathrm{cont}}}\right] \beta_{\mathrm{cont}} \tag{6.10}$$

$$\left[\mathbf{Z}_{\beta_{\mathrm{cont}(\beta_{\mathrm{bl}}\ \theta)}}\right] \begin{bmatrix} \beta_{\mathrm{bl}} \\ \theta \end{bmatrix} + \left[\mathbf{Z}_{\beta_{\mathrm{cont}}\beta_{\mathrm{cont}}}\right] \beta_{\mathrm{cont}} = \bar{M}_{h_{\beta_{\mathrm{cont}}}} \tag{6.11}$$

Commonly equation 6.11 is used to check the suitability of the control input, computed by means of the two scalar equations (6.10), with respect to the operating capabilities of the actuation system. The system response array $[\beta_{\mathrm{bl}}\ \ \theta]^T$ may be then expressed as [46, 47]:

$$\begin{bmatrix} \beta_{\mathrm{bl}} \\ \theta \end{bmatrix} = \begin{bmatrix} \beta_{\mathrm{bl}_0} \\ \theta_0 \end{bmatrix} + \begin{bmatrix} \beta_{\mathrm{bl}} \\ \theta \end{bmatrix} = [\mathbf{z}_0] + [\mathbf{z}], \tag{6.12}$$

being $\mathbf{z}_0$ the uncontrolled response and $\mathbf{z}$ the system response to the control input.

Accordingly, equation 6.10 is written as:

$$\left[\mathbf{Z}_{\beta_{\mathrm{bl}}\theta}\right] \begin{bmatrix} \beta_{\mathrm{bl}} \\ \theta \end{bmatrix} = -\left[\mathbf{Z}_{\beta_{\mathrm{bl}}\theta}\right] \begin{bmatrix} \beta_{\mathrm{bl}_0} \\ \theta_0 \end{bmatrix} - \left[\mathbf{Z}_{(\beta_{\mathrm{bl}}\theta)\beta_{\mathrm{cont}}}\right] \beta_{\mathrm{cont}} \tag{6.13}$$

For further convenience the matrices of equation 6.13 may be renamed as follows:

$$[\mathbf{X}]^{2\mathrm{x}2}[\mathbf{z}]^{2\mathrm{x}1} = -[\mathbf{X}]^{2\mathrm{x}2}[\mathbf{z}_0]^{2\mathrm{x}1} - [\mathbf{F}]^{2\mathrm{x}1}\beta_{\mathrm{cont}} \tag{6.14}$$

On the right hand side in equation (6.14) the first term represents the uncontrolled loads on the blade, whereas the second term is the input control force. The state variables of the aerostructural system, i.e. the system response, can ultimately be expressed as:

$$[\mathbf{z}] = -[\mathbf{z}_0] - [\mathbf{X}]^{-1}[\mathbf{F}]\beta_{\mathrm{cont}} \tag{6.15}$$

For completeness notice that, according to the classical notation employed for the HHC formulations [16, 46, 47], equation (6.15) can be written as

$$[\mathbf{z}] = -[\mathbf{z}_0] - [\mathbf{T}]\beta_{\text{cont}}, \tag{6.16}$$

where $[\mathbf{T}]^{2\text{x}1} = [\mathbf{X}]^{-1}[\mathbf{F}]$.

As a result the control force $\bar{\mathbf{F}}_{\mathbf{c}}^{2\text{x}1}$ in terms of the blade root flap and pitch moments, developed by the trailing edge device, reads

$$\bar{\mathbf{F}}_{\text{c}} = -[\mathbf{X}]^{-1}[\mathbf{F}]\beta_{\text{cont}} \tag{6.17}$$

Consistently, the flap and pitch moments at the blade root for the uncontrolled system can be written as

$$\bar{\mathbf{F}}_{\text{uc}} = -[\mathbf{X}]^{-1}[\mathbf{z}_0] \tag{6.18}$$

Among the load components which most affect the vibration transmitted from the blades to the rotor hub there is the vertical force F_z. This quantity is herein added as the output equation of the linear aeroelastic system described by the state equation (6.14). The aerodynamic vertical force on the blade is computed by assuming the lift as almost parallel to the yaw z axis. The lift, computed with the ROMs of chapter 5 for each of the blade sections, by taking into account the local speed and reduced frequency, is integrated along the span to obtain the blade root non-dimensional vertical aerodynamic force $\bar{F}_{z_{\text{a}}}$:

$$\bar{F}_{z_{\text{a}}} = \frac{1}{\rho\pi R^4\Omega^2}\int_0^R L\,dr = \frac{1}{\rho\pi R^4\Omega^2}\left(-[F_{z_{\beta_{\text{bl}}}}\;\; F_{z_\theta}]^{1\text{x}2}[\mathbf{z}]^{2\text{x}1} + F_{z_{\beta_{\text{cont}}}}^{1\text{x}1}\beta_{\text{cont}}\right). \tag{6.19}$$

The 1x3 array $[F_{z_{\beta_{\text{bl}}}}\;\; F_{z_\theta}\;\; F_{z_{\beta_{\text{cont}}}}]^{1\text{x}3}$ is indeed the aerodynamic transfer matrix for the blade root vertical force. Namely $F_{z_{\beta_{\text{bl}}}}$ gives the vertical force for a unitary bending rotation of the blade, F_{z_θ} provides the vertical force for a unitary pitch rotation of the blade, whereas $F_{z_{\beta_{\text{cont}}}}$ determines the vertical force for a unitary rotation of the control surface. Notice that the first term of the right hand side in equation (6.19) is opposite in sign with respect to the second term. Indeed by imposing e.g. a downward rotation to the control surface, the blade undergoes an upward flapping motion, which in turn leads to negative aerodynamic forces generated by plunge and pitch oscillations. That is the aerodynamic vertical force related to flapping and pitching motions of the blade is opposite in sign with respect to the vertical force generated by deflecting the control surface.
The complete expression for the non-dimensional vertical force $\bar{F}_z$ at the blade root includes the blade bending inertial force. Therefore

$$\bar{F}_z = \frac{1}{\rho\pi R^4\Omega^2}\left(-[F_{z_{\beta_{\text{bl}}}}\;\; F_{z_\theta}]^{1\text{x}2}[\mathbf{z}]^{2\text{x}1} + F_{z_{\beta_{\text{cont}}}}^{1\text{x}1}\beta_{\text{cont}} - \Omega^2 I_s\,\beta_{\text{bl}}\right), \tag{6.20}$$

where the bending inertial force $\Omega^2 I_s\,\beta_{\text{bl}}$ is again opposite in sign with respect to the blade flapping induced by the rotation of the control surface.

6.2 Higher harmonic control for the blade vibration reduction

An HHC approach [16, 46, 47] is herein employed to investigate the vibration reduction capabilities of the L-tab compared to those provided by the trailing edge flap described in section 5.5. According to Johnson [46] three primary features characterize HHC algorithms: a linear, quasi-static frequency domain model of the helicopter response; an identification procedure carried out by means of a least squares or a Kalman filter method; the employment of a quadratic-form figure of merit. The HHC algorithm herein proposed presents indeed all of these properties.

Since the HHC approach is conceived to minimize vibratory loads for one specific frequency at time [16], proper control inputs are computed separately for the 2/rev, 3/rev, 4/rev and 5/rev loads. A figure of merit including the blade root flap and pitch moments, in addition to the vertical shear, is employed for computing the optimal control input β_{cont} to be applied. Namely the functional contains the 3x1 array $\mathbf{L} = [\bar{M}_{\beta_{\text{bl}}} \;\; \bar{M}_{\theta} \;\; \bar{F}_z]^T$ as follows:

$$J = \begin{bmatrix} \bar{M}_{\beta_{\text{bl}}} \\ \bar{M}_{\theta} \\ \bar{F}_z \end{bmatrix}^T [\mathbf{W}]^{3\text{x}3} \begin{bmatrix} \bar{M}_{\beta_{\text{bl}}} \\ \bar{M}_{\theta} \\ \bar{F}_z \end{bmatrix} + \beta_{\text{cont}}^T R_{\text{cont}}^{1\text{x}1} \beta_{\text{cont}} \tag{6.21}$$

where, dealing with complex quantities, the transpose operation involves also the computation of the complex conjugate of the single elements. Therefore β_{cont}^T is the complex conjugate of $\beta_{\text{cont}} \in \mathbb{C}$. The diagonal 3x3 matrix $\mathbf{W}$ specifies the weights for the controlled variables, whereas the scalar R_{cont} weights the control input authority. The array of loads in equation (6.21) has to be expressed as a function of the control input β_{cont}. For convenience the following matrices are introduced:

$$[\tilde{\mathbf{F}}_{\mathbf{z}}]^{1\text{x}2} = \frac{1}{\rho \pi R^4 \Omega^2} \left([F_{z_{\beta_{\text{bl}}}} \;\; F_{z_{\theta}}]^{1\text{x}2} + [\Omega^2 I_s \;\; 0]^{1\text{x}2} \right) \tag{6.22}$$

$$[\mathbf{B}]^{3\text{x}2} = \begin{bmatrix} [\mathbf{0}]^{2\text{x}2} \\ [\tilde{\mathbf{F}}_{\mathbf{z}}]^{1\text{x}2} \end{bmatrix}^{3\text{x}2}, \tag{6.23}$$

$$[\mathbf{C}]^{3\text{x}1} = \begin{bmatrix} [-\mathbf{F}]^{2\text{x}1} \\ F_{z_{\beta_{\text{cont}}}}^{1\text{x}1} \end{bmatrix}^{3\text{x}1}, \tag{6.24}$$

where the matrix $\mathbf{F}^{2\text{x}1}$ appears in equation (6.14). The following matrices are also introduced, to conveniently express J.

$$[\mathbf{L}_0]^{3\text{x}1} = \begin{bmatrix} [\mathbf{F}_{\text{uc}}]^{2\text{x}1} \\ 0^{1\text{x}1} \end{bmatrix}^{3\text{x}1} - [\mathbf{B}]^{3\text{x}2} \, [z_0]^{2\text{x}1}, \tag{6.25}$$

$$[\mathbf{L}_{\text{cont}}]^{3\text{x}1} = -[\mathbf{B}]^{3\text{x}2} [\mathbf{X}]^{-1} [\mathbf{F}]^{2\text{x}1} + [\mathbf{C}]^{3\text{x}1}, \tag{6.26}$$

where the array of the uncontrolled flap and pitch moments $\mathbf{F}_{\text{uc}}^{2\text{x}1}$ is introduced in equation (6.18). The 3x1 array $\mathbf{L}$ containing the loads to be minimized can be now written as a function of β_{cont} as follows:

$$[\mathbf{L}] = [\mathbf{L}_0] + [\mathbf{L}_{\text{cont}}] \beta_{\text{cont}} \tag{6.27}$$

As a result the figure of merit of equation (6.21) reads:

$$J = \left([\mathbf{L}_0]^T + \beta_{\text{cont}}^T [\mathbf{L}_{\text{cont}}]^T \right) [\mathbf{W}] \left([\mathbf{L}_0] + [\mathbf{L}_{\text{cont}}] \beta_{\text{cont}} \right) + \beta_{\text{cont}}^T R_{\text{cont}} \beta_{\text{cont}} \tag{6.28}$$

By imposing $\frac{dJ}{d\beta_{\text{cont}}} = 0$ the control input can be computed as follows:

$$\beta_{\text{cont}} = -\left([\mathbf{L}_{\text{cont}}]^T [\mathbf{W}] [\mathbf{L}_{\text{cont}}] + R_{\text{cont}} \right)^{-1} \left([\mathbf{L}_0]^T [\mathbf{W}] [\mathbf{L}_0] \right) \tag{6.29}$$

Notice that equations (6.27), (6.28) and (6.29) have indeed the same form of those of the HHC classical formulation, see e.g. Refs. [16, 46, 47].

A blade model for a hingeless Bo-105 rotor is herein used as test application for the present control system. The values of the blade model properties, used to evaluate the matrices of the aeroelastic system, are reported in table 6.2.

It's worth noting that the control input β_{cont} has to be computed by properly selecting the weighing factors for the control outputs and input, i.e. the elements of $\mathbf{W}$ and the value of R_{cont}. In particular the ratios between the weighing factors on the state variables and the weight on the control input should leave reasonable authority to the controller and at the same time keep the control input within the operating limits of the actuation

Table 6.2: Geometrical, inertial and elastic main properties of the blade for a Bo-105 rotor model.

Parameters	Values
R	4.9000 m
M_{bl}	50.6061 kg m
I_b	209.9097 kg m^2
I_f	0.1059 kg m^2
Ω	44.4010 rad/s
ν_β	1.1080 /rev
ν_θ	3.8210 /rev
γ	5.5
c	0.27 m
EA	0
feathering axis	$0 \equiv$ EA
aerodynamic center	$0 \equiv$ EA
CG	-0.5439 m
HA	$0.8c$
x axis origin	$c/4 \equiv$ EA
μ	0.2

system. Several tests are run to select the weights which best satisfy such compromise, by changing the ratios between $\mathbf{W}$ and R_{cont} and evaluating the resulting control input, as well as the developed control loads. It appears useful to recall that β_{cont} is ultimately a complex parameter, therefore the control input results in a single harmonic input law in the form $\beta_{\text{cont}}(t) = |\beta_{\text{cont}}|\mathrm{e}^{(\mathrm{j}\omega t+\varphi(\beta_{\text{cont}}))}$. Notice that the frequency ω of the control input is meant to be the same of the load harmonic to control, consistently with the HHC approach [16, 46, 47]. The results in terms of vibration reduction at 2/rev, 3/rev, 4/rev and 5/rev respectively, obtained with the aerostructural models for the L-tab and the trailing edge flap, are reported hereinafter. The baseline loads for the Bo-105 rotor are taken from data of the HART-II program [32].

Figure 6.3 reports the vibratory rotating frame blade root loads corresponding to the baseline and controlled configurations—with both the L-tab and the TE flap models—for the 2/rev and 3/rev harmonic components. The values of the control input magnitude and phase, obtained by minimizing the figure of merit in equation (6.28), are also reported. Both the L-tab and the TE flap appear to break down almost the 100% of the vertical force and of the bending moment. On the other hand, the root pitching moment appears substantially unaffected by the movable device. The optimal control input of the L-tab is slightly smaller than that of the TE flap. Notice that such values of the control inputs are not dissimilar to those obtained by Chopra [106, 18], with analogous trailing edge solutions. The phase angle of the control input lies in the range [-125 -75] degrees, for both the L-tab and the TE flap.

Figure 6.4 shows the vibratory rotating frame blade root loads corresponding to the baseline and to the configuration with the L-tab and TE flap models, for the 4/rev and 5/rev harmonic components. The control input magnitude and phase, obtained by minimizing the figure of merit of equation (6.28), are also reported. The rotating frame blade root flapping moments are almost completely canceled, whereas the vertical forces undergo reductions higher than 90%. Similarly to what observed for the 2/rev and 3/rev harmonics, no effect of the control devices on the blade root pitching moment is observed. The optimal control input amplitude obtained for the L-tab is slightly larger with respect to that of the TE flap. The input control amplitude is again not dissimilar to the values computed by Chopra [106, 18] on a TE flap for rotorcraft vibration reductions.The phase angle of the control inputs is positive for the 2/rev harmonic and negative for the 3/rev component.

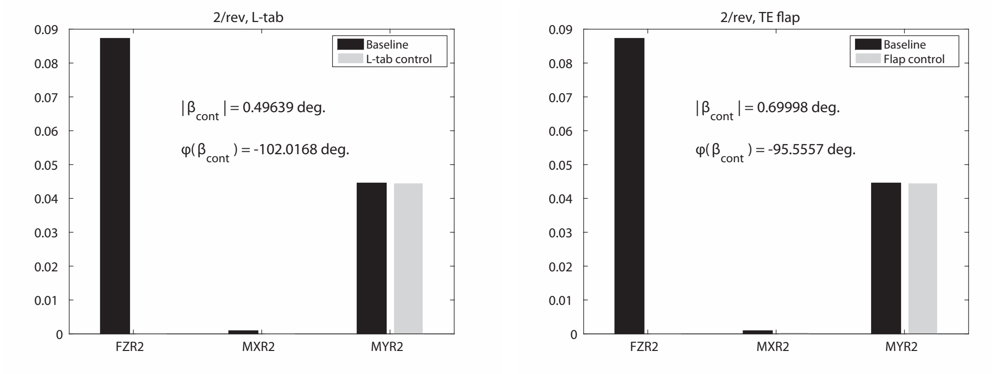

(a) 2/rev, control with the L-tab (b) 2/rev, control with the TE flap

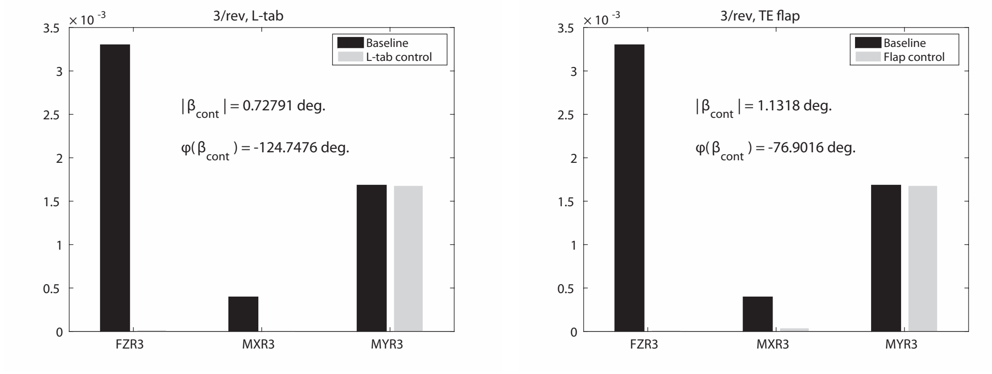

(c) 3/rev, control with the L-tab (d) 3/rev, control with the TE flap

Figure 6.3: Rotating frame blade root 2/rev and 3/rev harmonic components of vertical force (FZ), bending (MX) and pitching (MY) moments with and without the addition of the movable device, controlled with the HHC approach; $\mu = 0.2$.

As expected, both the L-tab and the TE flap are found not capable to alleviate the blade root pitching moment. This is due to the large torsional stiffness, typical of most the blades. Namely, whereas the local flapping caused by the rotation of the movable device propagates along the entire span, providing a significant magnification factor to the action of the control surface, this does not occur for the blade torsion. That is, the magnification effects due to the propagation of the blade twisting induced by the rotation of the movable device are almost negligible, being the torsional stiffness much greater than the bending counterpart, see table 6.2. To obtain a more effective action on the blade twist, which in turn is transmitted to the main rotor through the pitch links, a distribution of several L-tabs or TE flaps along the span should be employed, see for instance the work of Lemmens [108]. Alternatively a new blade, with a significantly smaller torsional stiffness, should be conceived, to allow for the propagation of the local blade torsion, induced by the control surface, along the entire span. Nevertheless a more flexible blade in twist could cause potential aeroelastic issues, ultimately even anticipating the onset of flutter phenomena.

Table 6.3 reports the values of the reference reduced frequency, computed at the 75% of the blade span as $k = \frac{\omega c}{2\,\Omega\, 0.75R}$, being ω the /rev frequency, ranging from 2/rev to 5/rev. In this way it is possible to immediately relate the results discussed in this section with those reported in figures 5.14(a), 5.15(a) and 5.16. Notice that for 2/rev and 3/rev $k < 0.125$. Therefore, according to figure 5.14(a) the L-tab provides larger values of lift, for equal rotations of the movable device. This is consistent with the results reported in figure 6.3, in terms of the computed control input amplitude. Indeed, to achieve almost the same control force –and in turn load alleviation– the TE flap requires a larger rotation amplitude

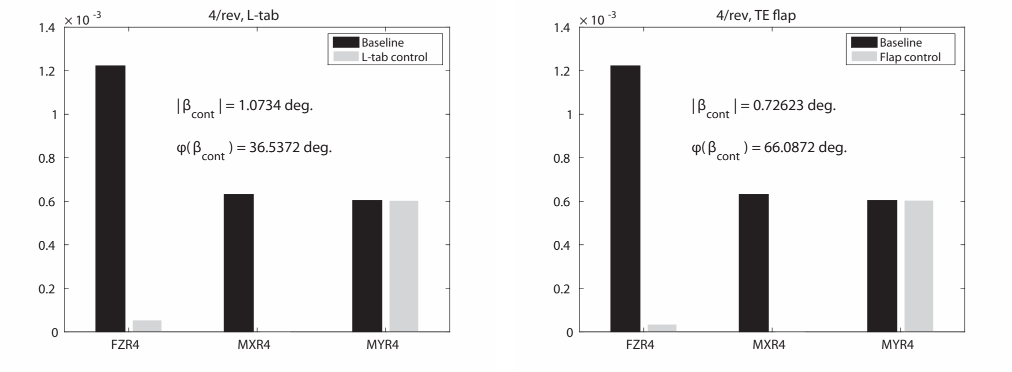

(a) 4/rev, control with the L-tab

(b) 4/rev, control with the TE flap

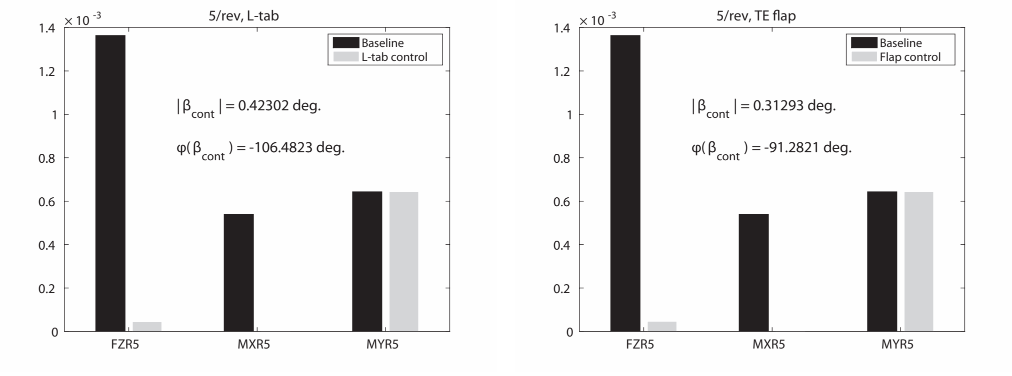

(c) 5/rev, control with the L-tab

(d) 5/rev, control with the TE flap

Figure 6.4: Rotating frame blade root 4/rev and 5/rev harmonic components of vertical force (FZ), bending (MX) and pitching (MY) moments with and without the addition of the movable device, controlled with the HHC approach; $\mu = 0.2$.

with respect to the L-tab. On the other hand, for 4/rev and 5/rev the corresponding reference k is greater than 0.125. Consistently, almost analogous reductions in the vertical force and in the bending moment are obtained with slightly larger rotations of the L-tab with respect to the flap. The magnitude of the computed control inputs for the L-tab and the TE flap models at N/rev are reported versus the related harmonics in figure 6.5. These last remarks give further confirmation to what observed by simply considering the aerodynamic forces developed by the two TE devices, see section 5.5. That is, by coupling the aerodynamic models to the blade dynamics, no unexpected or undesired effects are encountered.

Parameters	Values			
harmonics	2/rev	3/rev	4/rev	5/rev
k	0.0735	0.1102	0.1469	0.1837

Table 6.3: Reference 0.75R reduced frequency corresponding to the N/rev harmonics.

In general the present results demonstrate that the L-tab is potentially capable to significantly reduce the rotating frame vertical force and bending moment. Moreover substantially analogous results are found by employing either the L-tab or a classical TE flap, being this latter a widely employed solution in literature. This agreement appears ultimately a further confirmation of the potential feasibility of such L-tab on actual rotor environments, with the additional advantage of an actuation system expected to be lighter and less complex, with respect to those commonly employed for classical TE flaps.

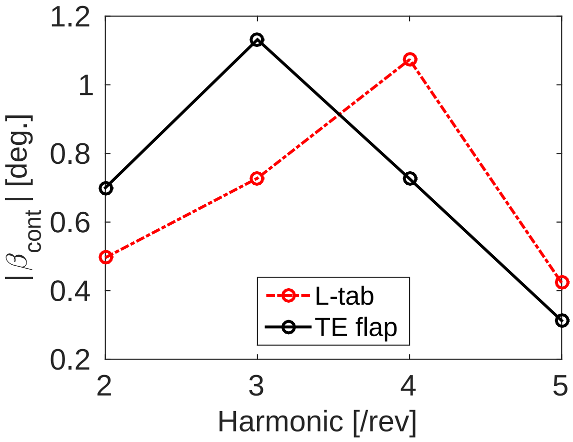

Figure 6.5: Amplitude of the HHC computed control inputs versus the minimized harmonic. The results attained for both the L-tab and the TE flap are reported.

6.3 Conclusions

The capabilities of the present L-tab in alleviating vibration on helicopter blades are investigated and compared to the performance provided by a classical TE flap. The physically based ROM for the L-tab, in addition to that developed for a TE flap, are exploited to build up the aerostructural model. At first the actual feasibility of the linear superimposition of the airloads, generated by pitch and plunge oscillations of the airfoil, in addition to harmonic motions of the tab, is checked by means of a comparison with CFD results attained on a L-tab equipped airfoil undergoing these three movements at the same time. A reasonable agreement is found between the summation of the unsteady pitch, plunge and L-tab motion forces, computed separately with the related linear ROMs, and the first harmonic of the CFD airloads. Such matching ultimately confirms the feasibility of the linear aerodynamic behavior assumption employed in chapter 5, at least for the first harmonic of the loads. Two analytical three DOFs typical section aerostructural models are then developed for a helicopter blade equipped with the L-tab and the TE flap, respectively. The rotating frame blade root aerodynamic loads are computed by integrating along the span the airloads achieved with the physically based ROMs just mentioned. The mass and the stiffness matrices are built up exploiting the bending and pitching equilibrium equations of the blade. The resulting aerostructural three DOFs system relates the blade root flapping, feathering and movable device hinge moments to the blade flapping, to the blade pitching and to the motion of the control surface. Additionally the blade root vertical force, is expressed as output equation for the aeroelastic system.

A higher harmonic control approach is used to compute single-frequency control inputs, to reduce the bending moment, the pitching moment and the vertical force at the blade root, in terms of the 2/rev, 3/rev, 4/rev and 5/rev harmonics, respectively. It is found that both the L-tab and the TE flap are capable to alleviate almost completely the vertical force and of the bending moment at N/rev.

With regard to the blade root pitching moment no alleviations are obtained with the L-tab as well as with the TE flap, for each of the harmonics under consideration. This is in fact not surprising, since the torsional stiffness of the blade is much larger than the bending stiffness for most rotors. Indeed, due to the significantly lower flexibility of the blade with respect to the elastic axis, the blade torsion does not propagate along the span, remaining almost limited to the sections were the devices are installed. To overcome such limitation more than a single TE device could be installed on the blade, thus enlarging the span-wise extension of the control surfaces. Alternatively, a blade with lower torsional stiffness could be designed, but in this case care should be used to avoid anticipate onsets of aeroelastic instabilities, more likely to occur if the twist flexibility is increased.

Overall, this preliminary aeroelastic assessment shows that the present L-tab is potentially suitable to be used as a vibration reduction system on rotor blades. A confirmation of such feasibility is also found in the very similar behavior –both in terms of load alleviation and of control input values– encountered with a widely used trailing edge solution, such a classical flap is. It appears useful to remark that the blade aerostructural model herein employed is representative only of low advance ratio conditions, since the freestream is assumed uniform and no inflow is introduced. On the contrary when dealing with large advance ratios, the freestream unsteadiness can not be neglected. With this regard coupled CFD-CFS computations on complete rotor models are indeed recommended as future step, to assess with more detail the L-tab vibration reduction capabilities, as well as to extend the investigation to high speed forward flight conditions.

Chapter 7

Conclusions and recommendations

The present work deals with the aerodynamic assessment of a L-shaped Gurney flap for rotorcraft applications. At first the behavior of oscillating airfoils, representative of clean blade section models, is characterized numerically and analytically with linear low order formulations. Inviscid numerical computations, verified a priori with experimental data, are performed on symmetrical airfoils, with maximum thickness ranging between 4% and 24% of the chord, undergoing small amplitude oscillations in pitch. The computed lift and pitching moment coefficient exhibit increasing detachments, with respect to the classical flat plate Theodorsen's model, for growing values of the airfoil thickness. By exploiting the numerical results, a modification of the Theodorsen's formulation is developed, which allows to take into account the unsteady thickness effects in the analytical computation of the aerodynamic forces. Such formulation is indeed found capable to significantly improve the accuracy in predicting the unsteady airloads, on airfoils of arbitrary maximum thickness, in the range 4–24% of the chord. Additionally aeroelastic computations performed on a typical section model are found to provide different predictions of the flutter velocity onset, if the unsteady thickness effects in the aerodynamic transfer matrix are taken into account, rather than neglected. A better comprehension of the unsteady geometrical effects on clean blade section models is found ultimately helpful, to get more clearly the phenomena directly induced by the L-tab on the flow field, as well as on the aerodynamic loads.

A steady state characterization of the aerodynamic behavior of the L-tab is then carried out. This allows to investigate the potential suitability of the tab in adapting the rotor asset, according to the flight conditions. The reliability the of steady state numerical computations is supported by comparisons with experimental data measured on the same device, as well as on a common trailing edge Gurney Flap (GF). Numerical computations, performed both at small and at static stall angles of attack, highlight how the L-tab under consideration features a twofold effective operation, which makes it an hybrid between a Gurney flap and a classical trailing edge (TE) plain flap. Namely, when the L-tab is downward deployed, it acts as a Gurney flap, allowing for lift and lift to drag ratio enhancements, without in turn severely affecting the drag coefficient. On the other hand, upward deflections of the L-tab are shown capable to reduce the blade airloads, in terms of both lift and pitching moment magnitude. In particular, qualitative numerical results, attained in the static stall regime highlight how upward deflections of the L-tab around 20 degrees appear effective in significantly alleviate the static stall negative effects.

Unsteady computations are then performed for small amplitude oscillations either of the airfoil or of the L-tab, to ultimately assess the feasibility of such movable device in reducing vibration on rotor blades. Convergence analyses of the numerical solution are performed, to ensure the accuracy of the attained results. Notice that, dealing within the small perturbation regime, the aerodynamic behavior of the blade can be assumed to be linear. This hypothesis allows to investigate separately the airfoil pitch, the airfoil plunge and harmonic oscillations of the L-tab. Unsteady motions, either of the airfoil or of the L-tab, exhibit shedding phenomena of the Counter Rotating Vortical structures (CRV) generated past the vertical prong of the control surface. The CRV convection leads to secondary small amplitude oscillations in the resulting airloads, also experimentally observed in literature on similar devices [27, 26, 34]. A spectral analysis of such multi-harmonic airloads highlights that the frequency of the secondary oscillations is around twenty-two times that of the input motion. This substantial regularity, common to pitch, plunge and L-tab oscillations, allows to know a priori at which frequency eventual secondary vibration have to be expected. By the way, it is remarkable that the exact shedding frequency is not actually an integer multiple of the rotor angular velocity, therefore avoiding unwanted resonance effects on the blade. Additionally, the amplitude of the secondary oscillations, observed in the unsteady airloads is much lower than the magnitude of the primary counterpart.

Overall the steady and unsteady characterization of the L-tab shows that the primary effect induced by such device consists of a modification in the effective camber and chord length, with respect to those of the clean airfoil. Such effects are due to the generation of the aforementioned counter rotating vortical structures, which yield a shift of the Kutta condition application point downstream the TE.

Having gained some insight into the behavior of the L-tab installed on a blade section, a physically based Reduced Order Model (ROM) is built up, with the aim to avoid issues concerning the computational burden of CFD evaluations. The developed ROM is capable to correctly reproduce the mean line modifications induced by steady state or oscillating motions of the L-tab –with the airfoil at constant angle of attack– in addition to accurately predict the resulting lift and moment coefficients. For unsteady motions, either of the airfoil or of the L-tab, only the first harmonic of the airloads is taken under consideration for the model order reduction, being this component by far the main concern, when dealing with control systems for vibration reduction on rotor blades. Specifically for oscillating motions of the airfoil a flat plate analytical model is employed, where the reference chord of the equivalent thin line is rescaled according to the mean enlargement effects due to the CRV. Indeed the first harmonic of the unsteady airloads, for pitching and plunging oscillations of the airfoil, is found almost not affected by the steady rotation angle of the L-tab.

The development of a physically consistent ROM has several potential advantages, with respect to commonly used black box identification procedures, e.g. Rational Function Approximations (RFA). Indeed, whereas for these latter approaches CFD simulations –or alternatively experimental measurements– are a necessary step for the identification, these are no longer mandatory for a physically consistent ROM, as the one herein proposed. That is, when dealing with a fixed or movable GF-like device, the preliminary computation of the developed airloads can be performed immediately, without involving CFD evaluations. Namely, once the size of the GF-like surface has been estimated, the ROM developed in this work, is capable to provide the corresponding equivalent mean line and in turn the resulting aerodynamic forces. In particular it is found that, at least for Reynolds number around 10^6, the medium extension of the CRV is approx. four times the height of the GF device for steady state configurations and scales linearly with the oscillation amplitude for unsteady motions of the tab. The remaining parameters of the equivalent geometry can be immediately estimated with the approach discussed in chapter 5. Additionally steady state CFD computations can be performed a posteriori, to ultimately adjust the sizing parameters of the thin line model. The remarkable difference with respect to black box or indicial response identification procedures, is that CFD computations are not a compulsory step in the derivation of the ROM, being rather an optional choice, to be meant as an ultimate refinement. As a result, a significant speed up in the preliminary design procedure is attained. Indeed the immediate availability of the equivalent geometry allows, for instance, to proceed in parallel with the general aerodynamic sizing and control system realization, and in the meanwhile eventually refine the ROM with unsteady CFD computations.

The potential capabilities of the L-tab in reducing vibration on rotor blades are then investigated by employing the developed ROM in assembling the aerodynamic transfer matrix of a three DOF aerostructural typical section model. The mass and stiffness matrices of the aeroelastic model are analytically built up with the equilibrium equations of the blade bending and torsion. The resulting aerostructural system relates the rotating frame blade root flapping, feathering and hinge moments to the bending, pitching and control surface motions. The control input, meant in terms of deflection law of the trailing edge device, is computed with an Higher Harmonic Control algorithm (HHC), conceived to control vibratory loads at discrete frequencies. This approach is indeed appropriate for rotorcraft applications, due to the highly tonal nature of the vibration, which occur at known specific frequencies, integer multiples of the rotor angular velocity. The quadratic form of the cost function, minimized to compute the control inputs at specific frequencies, involves the blade root vertical shear, in addition to the flapping and feathering moments. In fact the vertical force has a primary affection in transmitting the vibratory loads from the rotating to the fixed reference frame of the hub. The control inputs at 2/rev, 3/rev, 4/rev and 5/rev, respectively are computed. In addition, the control inputs at the same frequencies are evaluated considering analytical aerodynamic and aerostructural models of a classical TE plain flap, built in parallel to the L-tab counterparts. This allows to compare the results achieved with the novel L-tab configuration –in terms of both aerodynamic performance and vibration reduction– with those attained with a widely tested configuration such a TE plain flap. The preliminary aeroelastic assessment shows that the L-tab and the TE flap, are capable to effectively reduce the N/rev blade root vertical force and flapping moment, with comparable control inputs.

In conclusion the general targets of this work, concerning the characterization of a novel L-shaped Gurney flap for rotorcraft applications, have been achieved. Namely the steady state aerodynamic assessment, highlights that the L-tab under consideration appears feasible for load balance, to optimize the rotor asset according to the flight configuration. These findings show the the present device could be additionally employed to improve the aerodynamic performance. The unsteady aerodynamic characterization within the small perturbation regime, together with the subsequent aeroelastic assessment, shows that the L-tab is also potentially capable to reduce vibratory loads at the blade root, when actuated with proper control laws. The employments of the L-tab for the load balance on the rotor and for vibration reduction at the blade root have to be added to the applications of such device in alleviating dynamic stall effects. This latter operation of the L-tab was investigated experimentally by Gibertini et al. [35, 36].

Recommendations to the present work concern experimental assessments of the unsteady aerodynamic behavior of the L-tab, to ultimately validate the numerical results for small amplitude oscillations of the airfoil and of the movable device. Moreover the acoustic behavior of the L-tab should be assessed. In fact the noise generated by the shedding phenomena induced by the tab could be a potential drawback related to such device. Additionally, measurements tests for the actual performance of the active control system herein designed are recommended. With this regard, as well as in the context of noise studies, coupled nonlinear CFD-CFS investigations of the aerostructural behavior on a comprehensive rotor model, actively controlled with the L-tab, appear to be proper as well.

Bibliography

[1] J. Katz. Aerodynamics of race cars. *Annual Review of Fluid Mechanics*, 38(1):27–63, 2006.

[2] R. H. Liebeck. Design of Subsonic Airfoils for High Lift. *Journal of Aircaft*, 15(9):547–561, 1978.

[3] J. Kentfield. The potential of Gurney flaps for improving the aerodynamic performance of helicopter rotors. In *International Powered Lift Conference, Santa Clara, CA, USA*. American Institute of Aeronautics and Astronautics, December 1993.

[4] B. L. Storms and C. S. Jang. Lift Enhancement of an Airfoil Using a Gurney Flap and Vortex Generators. *Journal of Aircraft*, 31(3):542–547, 1994.

[5] R. Y. Myose, M. Papadakis, and I. Heron. Gurney Flap Experiments on Airfoils, Wings, and Reflection Plane Model. *Journal of Aircaft*, 35(2):206–211, 1998.

[6] M. Papadakis, R. Y. Myose, I. Heron, and B. L. Johnson. An experimental investigation of Gurney flaps on a GA(W)-2 airfoil with 25% slotted flap. In *14th AIAA Applied Aerodynamic Conference, AIAA Paper 1996-2437*, 1996.

[7] W. Zhang, J. J. Wang, and Z. Wu. Experimental investigations on the application of lift enhancement devices to forward-swept aircraft model. *The Aeronautical Journal*, 110(1108):361–367, June 2006.

[8] J. J. Wang, Y. C. Li, and K. S. Choi. Gurney flap–Lift enhancement, mechanisms and applications. *Progress in Aerospace Sciences*, 44(1):22–47, January 2008.

[9] J. P. Baker, K. J. Standish, and C. P. van Dam. Two-Dimensional Wind Tunnel and Computational Investigation of a Microtab Modified Airfoil. *Journal of Aircraft*, 44(2):563–572, 2007.

[10] M. D. Maughmer and G. Bramesfeld. Experimental Investigation of Gurney Flaps. *Journal of Aircraft*, 45(6):2062–2067, 2008.

[11] P. Giguère, J. Lemay, and G. Dumas. Gurney Flap Effects and Scaling for Low-Speed Airfoils. *AIAA Paper 95-1881-CP*, 1995.

[12] C. S. Jang, J. C. Ross, and R. M. Cummings. Numerical investigation of an airfoil with a Gurney flap. *Aircraft Design*, 1(2):75–88, June 1998.

[13] D. Jeffrey, X. Zhang, and D. Hurst. Aerodynamics of Gurney Flaps on a Single-Element High-Lift Wing. *Journal of Aircaft*, 37(2):295–301, 2000.

[14] K. J. Standish and C. P. van Dam. Computational analysis of a microtab-based aerodynamic load control system for rotor blades. In *AHS 4th Decennial Specialist's Conference on Aeromechanics*, January 2004.

[15] V. Motta, A. Guardone, and G. Quaranta. Numerical investigation of an L-shaped deployable Gurney flap for rotorcraft vibration control. In *International Forum on Aeroelasticity and Structural Dynamics, Bristol, UK*, 24–26 June 2013.

[16] P. P. Friedmann and T. A. Millott. Vibration Reduction in Rotorcraft Using Active Control: A Comparison of Various Approaches. *Journal of Guidance, Control, and Dynamics*, 18(4):664–673, 1995.

[17] J. Milgram, I. Chopra, and F. Straub. Rotors With Trailing Edge Flaps: Analysis and Comparison With Experimental Data. *Journal of the American Helicopter Society*, 43(4):319–332, 1998.

[18] B. Roget and I. Chopra. Control of Dissimilar Rotor Vibration. In *43rd AIAA/ASME/ASCE/AHS/ASC Structures, Structural Dynamics and Materials Conference, Denver, CO*, 22–25 April 2002.

[19] J. Shen, M. Yang, and I. Chopra. Swashplateless Helicopter Rotor System with Active Trailing-Edge Flaps for Primary and Vibration Controls. In *45th AIAA/ASME/ASCE/AHS/ASC Structures, Structural Dynamics and Materials Conference, Palm Springs, CA*, 19–22 April 2004.

[20] B. Roget and I. Chopra. Wind-Tunnel Testing of Rotor with Individually Controlled Trailing-Edge Flaps for Vibration Reduction. *Journal of Aircraft*, 45(3):868–879, 2008.

[21] D. Greenblatt, B. Nishri, A. Darabi, and I. Wygnanski. Dynamic Stall Control by Periodic Excitation, Part 2: Mechanisms. *Journal of Aircaft*, 38(3):439–447, 2001.

[22] D. Feszty, E. A. Gillies, and M. Vezza. Alleviation of Airfoil Dynamic Stall Moments via Trailing-Edge Flap Flow Control. *AIAA Journal*, 42(1):17–25, January 2004.

[23] H. Lee and Y. Y. Su. Unsteady airfoil with a harmonically deflected trailing-edge flap. *Journal of Fluids and Structures*, 27(27):1411–1424, 2011.

[24] T. Lee and P. Gerontakos. Oscillating Wing Loadings with Trailing-Edge Strips. *Journal of Aircaft*, 43(2):428–436, 2006.

[25] D. Tang and E. H. Dowell. Aerodynamic Flow Control of an Airfoil with Small Trailing-Edge Strips. *Journal of Aircraft*, 43(6):1854–1866, 2006.

[26] D. Tang and E. H. Dowell. Aerodynamic Loading for an Airfoil with an Oscillating Gurney Flap. *Journal of Aircaft*, 44(4):428–436, 2007.

[27] M. P. Kinzel, M. D. Maughmer, and E. P. N. Duque. Numerical Investigation on the Aerodynamics of Oscillating Airfoils with Deployable Gurney Flaps. *AIAA Journal*, 48(7):1457–1469, 2010.

[28] Y. Li, Wang J., and P. Zhang. Influences of Mounting Angles and Locations on the Effects of Gurney Flaps. *Journal of Aircraft*, 40(3):494–498, 2003.

[29] J. A. Cole, B. A. Vieira, J. G. Coder, A. Premi, and M. D. Maughmer. Experimental Investigation into the Effect of Gurney Flaps on Various Airfoils. *Journal of Aircaft*, 50(4):1287–1294, 2013.

[30] C. G. Matalanis, B. E. Wake, D. Opoku, B. Min, N. Yeshala, and L. Sankar. Aerodynamic Evaluation of Miniature Trailing-Edge Effectors for Active Rotor Control. *Journal of Aircraft*, 48(3):995–1004, 2011.

[31] B. Y. Min, L. Sankar, and O. A. Bauchau. A CFD-CSD Coupled-Analysis of HART-II Rotor Vibration Reduction using Gurney Flaps. In *Proceedings of the American Helicopter Society 66th Forum and Technology Display, Phoenix, AZ*, 2010.

[32] Y. H. Yu, C. Tung, B. G. van der Wall, H. Pausder, C. Burley, T. Brooks, P. Beaumier, Y. Delrieux, E. Mercker, and K. Pengel. The HART-II Test: Rotor Wakes and Aeroacoustics with Higher-Harmonic Pitch Control (HHC) Inputs – The Joint German/French/Dutch/US Project. In *American Helicopter Society 58th Annual Forum, Montreal, Canada*, 11–13 June 2002.

[33] L. Liu, A. K. Padthe, and P. P. Friedmann. Computational Study of Microflaps with Application to Vibration Reduction in Helicopter Rotors. *AIAA Journal*, 49(7), July 2011.

[34] J. Palacios, M. P. Kinzel, and A. Overmeyer. Active Gurney Flaps: Their Application in a Rotor Blade Centrifugal Field. *Journal of Aircaft*, 51(2):473–489, 2014.

[35] A. Zanotti and G. Gibertini. Experimental investigation of the dynamic stall phenomenon on a NACA 23012 oscillating aerofoil. *Proceedings of the Institution of Mechanical Engineers, Part G: Journal of Aerospace Engineering*, 227(9):1375–1388, 2013.

[36] A. Zanotti, G. Grassi, and Gibertini. G. Experimental investigation of a trailing edge L-shaped tab on a pitching airfoil in deep dynamic stall conditions. *Part G: Journal of Aerospace Engineering*, (12), December 2013.

[37] K. Richter and H. Rosemann. Experimental investigation of trailing-edge devices at transonic speeds. *The Aeronautical Journal*, (2621):183–193, April 2002.

[38] Y. Li, J. Wang, and J. Hua. Experimental investigations on the effects of divergent trailing edge and Gurney flaps on a supercritical airfoil. *Aerospace Science and Technology*, (11):91–99, December 2006.

[39] T. Liu and J. Montefort. Thin-Airfoil Theoretical Interpretation for Gurney Flap Lift Enhancement. *Journal of Aircraft*, 44(2):667–671, 2007.

[40] M. P. Kinzel. Miniature Trailing-Edge Effectors for Rotorcraft Applications. Master's thesis, August 2004.

[41] N. Hariharan and J. G. Leishman. Unsteady Aerodynamics of a Flapped Airfoil in Subsonic Flow by Indicial Concepts. *Journal of Aircraft*, 33(5):855–868, 1996.

[42] B. A. Vieira, M. P. Kinzel, and M. D. Maughmer. Unsteady aerodynamics of miniature trailing-edge effectors based on indicial methods. In *49th AIAA Aerospace Sciences Meeting, AIAA Paper 2011-1049*, January 2011.

[43] H. G. Küssner and L. Schwarz. The oscillating wing with aerodynamically balanced elevator. TM 991, NACA, 1941. Translated from Luftfahrtforschung, vol. 17, pp. 337–354, 1940.

[44] W. Johnson. *Rotorcraft Aeromechanics.* Cambridge University Press, New York, 2013.

[45] R. L. Bisplinghoff, H. Ashley, and R. L. Halfman. *Aeroelasticity.* Addison–Wesley Publishing Company, Cambridge, Mass., 1955.

[46] W. Johnson. Self-Tuning Regulators for Multicyclic Control of Helicopter Vibrations. Technical report, NASA TP, 1996.

[47] D. Patt, L. Liu, J. Chandrasekar, Bernstein. D. S., and P. P. Friedmann. Higher-Harmonic-Control Algorithm for Helicopter Vibration Reduction Revisited. *Journal of Guidance, Control, and Dynamics*, 28(5):918–930, 2005.

[48] I. E. Garrick. Propulsion of a Flapping and Oscillating Airfoil. TR 567, NACA, May 1936.

[49] P. Freymuth. Propulsive vortical signature of plunging and pitching airfoils. *AIAA Journal*, 26(7):881–883, 1988.

[50] J. M. Anderson, K. Streitlien, D. S. Barrett, and M. S. Triantafyllou. Oscillating foils of high propulsive efficiency. *Journal of Fluid Mechanics*, 360:41–72, 1998.

[51] M. Kurosaka. On the flow field of a rapidly oscillating airfoil in a supersonic flow. *Journal of Fluid Mechanics*, 62(04):811–827, 1974.

[52] Y. S. Baik, L. P. Bernal, K. Granlund, and M. V. Ol. Unsteady force generation and vortex dynamics of pitching and plunging aerofoils. *Journal of Fluid Mechanics*, 709:37–68, 2012.

[53] J. P. Uldrick and J. Siekmann. On the swimming of a flexible plate of arbitrary finite thickness. *Journal of Fluid Mechanics*, 20(01):1–33, 1964.

[54] J. Panda and K. B. M. Q. Zaman. Experimental investigation of the flow field of an oscillating airfoil and estimation of lift from wake surveys. *Journal of Fluid Mechanics*, 265:65–95, 1994.

[55] T. Lee and P. Gerontakos. Investigation of flow over an oscillating airfoil. *Journal of Fluid Mechanics*, 512:313–341, 2004.

[56] D. G. Bohl and M. M. Koochesfahani. Mtv measurements of the vortical field in the wake of an airfoil oscillating at high reduced frequency. *Journal of Fluid Mechanics*, 620:63–88, 2009.

[57] W. J. McCroskey. Unsteady airfoils. *Annual Review of Fluid Mechanics*, 14(1):285–311, 1982.

[58] H. Wagner. Über die Entstehung des dynamischen Auftriebes von Tragflügeln. *Zeitschrift für Angewandte Mathematic und Mechanik*, 5(1):17–35, 1925.

[59] T. Theodorsen. General Theory of Aerodynamic Instability and the Mechanism of Flutter. TR 496, NACA, 1935.

[60] H. G. Küssner. Zusammenfassender Bericht über den instationären Auftrieb von Flügeln. *Luftfahrtforschung*, 13(12):410–424, 1936.

[61] P. Cicala. Le azioni aerodinamiche sul profilo oscillante. *Aerotecnica*, 16:652–655, 1936.

[62] I. E. Garrick. On Some Reciprocal Relations in the Theory of Nonstationary Flows. TR 629, NACA, March 1938.

[63] M. Gennaretti, C. Testa, and G. Bernardini. An unsteady aerodynamic formulation for efficient rotor tonal noise prediction. *Journal of Sound and Vibration*, 332(25):6743–6754, December 2013.

[64] Y. C. Fung. *Theory of Aeroelasticity*. John Wiley and Sons, Inc., New York, 1955.

[65] W. Johnson. *Helicopter Theory*. Princeton University Press, 1980.

[66] J. G. Leishman. *Principles of Helicopter Aerodynamics*. Cambridge University Press, 2006.

[67] R. L. Barger. Adaptation of the Theodorsen Theory to the Representation of an Airfoil as a combination of a Lifting Line and a Thickness Distribution. TN D-8117, NASA, 1975.

[68] H. G. Küssner. Nonstationary theory of airfoils of finite thickness in incompressible flow. In W.P. Jones, editor, *AGARD Manual on aeroelasticity. Part 2*, chapter 5. 1960.

[69] W. J. McCroskey. Inviscid Flowfield of an Unsteady Airfoil. *AIAA Journal*, 11(8), 1973.

[70] I. H. Abbott and A. E. von Doenhoff. *Theory of Wing sections*. Dover Publication, Inc., New York, NY, 1949.

[71] M. E. Goldstein and H. Atassi. A complete second-order theory for the unsteady flow about an airfoil due to a periodic gust. *Journal of Fluid Mechanics*, 74:741–765, March 1976.

[72] M. D. Van Dyke. On second-order supersonic flow past a slowly oscillating airfoil. *Journal of the Aeronautical Sciences (Institute of the Aeronautical Sciences)*, 20(1):61, 1953.

[73] S. A. L. Glegg and W. Davenport. Unsteady loading on an airfoil of arbitrary thickness. *Journal of Sound and Vibration*, 319, 2009.

[74] J. Katz and A. Plotkin. *Low-speed aerodynamics: from wing theory to panel methods*. McGraw-Hill, New York, NY, 1991.

[75] L. Morino. A General Theory of Compressible Potential Aerodynamics. CR 2464, NASA, 1974.

[76] L. Morino, L. T. Chen, and E. O. Suciu. Steady and Oscillatory Subsonic and Supersonic Aerodynamics Around Complex Configurations. *AIAA Journal*, 13(3):368–374, 1975.

[77] J. A. Esfahania, E. Baratib, and H. R. Karbasiana. Fluid structures of flapping airfoil with elliptical motion trajectory. *Computers & Fluids*, 108:142–155, 2015.

[78] L. Morino. Is There a Difference Between Aeroacoustics and Aerodynamics? An Aeroelastician's Viewpoint. *AIAA Journal*, 41(7):1209–1223, July 2003.

[79] T. Theodorsen. Theory of Wing Sections of Arbitrary Shape. Technical report, Langley Memorial Aeronautical Laboratory, October 1931.

[80] M. Biava. *RANS computations of rotor/fuselage unsteady interactional aerodynamics*. PhD thesis, Politecnico di Milano, April 2007.

[81] B. van Leer. Towards the ultimate conservative difference scheme. IV. A new approach to numerical convection. *Journal of Computational Physics*, 23:276–299, 1977.

[82] B. van Leer. Towards the ultimate conservative difference scheme. V. A second order sequel to Godunov's method. *Journal of Computational Physics*, 32:101–136, 1979.

[83] V. Venkatakrishnan and D. J. Mavriplis. Implicit method for the computation of unsteady flows on unstructured grids. *Journal of Computational Physics*, 127(2):380–397, 1996.

[84] D. Drikakis, B. Zhong, G. Barakos, R. Steijl, M. Biava, L. Vigevano, A. Brocklehurst, O. J. Boelens, M. Dietz, M. Embacher, W. Khier, and A.F. Antoniadis. Methods Against Experimental Flow Measurements for Helicopter Flows. *Aerospace Science and Technology*, 19(1):86–100, 2012.

[85] W. Khier, L. Vigevano, and M. Biava. Prediction of Air Flow Past a Full Helicopter Configuration. *Aerospace Science and Technology*, 19(1):3–18, 2012.

[86] R. L. Halfman. Experimental aerodynamic derivatives of a sinusoidally oscillating airfoil in two-dimensional flow. Report 1108, NACA, 1952.

[87] P. T. Lin, T. J. Baker, L. Martinelli, and A. Jameson. Two-dimensional implicit time-dependent calculations on adaptive unstructured meshes with time evolving boundaries. *International Journal for Numerical Methods in Fluids*, 50(2):199–218, 2006.

[88] P. R. Spalart and S. R. Allmaras. A one-equation turbulence model for aerodynamic flows. *La Recerche Aérospatiale*, 1:5–21, 1994.

[89] VV. AA. Compendium of unsteady aerodynamic measurements. Report no. 702, AGARD, 1982.

[90] A. G. Rainey. Measurement of aerodynamic forces for various mean angles of attack on an airfoil oscillating in pitch and on two finite-span wings oscillating in bending with enphasis on damping in the stall. Report 1305, NACA, 1957.

[91] I. G. Currie. *Fundamental Mechanics of Fluids, Fourth Edition.* CRC Press, 2012.

[92] P. R. Spalart and S. R. Allmaras. A One Equation Model For Aerodynamic Flows. 6–9 January 1992.

[93] V. Motta and G. Quaranta. Physically-based reduced order model for unsteady aerodynamic loads of a L-shaped Gurney flap. In *32nd AIAA Applied Aerodynamics Conference, Atlanta, GA*, 16–21 June 2014.

[94] M. P. Kinzel, M. D. Maughmer, and G. L. Lesieutre. Numerical Investigation of Miniature Trailing-Edge Effectors on Static and Oscillating Airfoils. 43rd AIAA Aerospace Sciences Meeting and Exhibit, Reno, NV, 10–13 January 2005.

[95] M. Sarioglu and T. Yavuz. Vortex Shedding From Circular and Rectangular Cylinders Placed Horizontally in a Turbulent Flow. *Turk. J. Engin. Environ. Sci.*, 24:217–228, 2000.

[96] A. A. Cusher. *A Design and Analysis Approach for Drag Reduction on Aircraft with Adaptive Lifting Surfaces* . PhD thesis, 2008.

[97] D. H. Neuhart and Pendergraft O. C. Jr. A water study of Gurney Flaps. *NASA TM 4071*, November 1988.

[98] P. M. H. W. Vijgen, C. P. van Dam, B. J. Holmes, and F. G. Howard. Wind-Tunnel Investigations of Wings with Serrated Sharp Trailing Edges. In *Proceedings of the Conference on Low Reynolds Number Airfoil Aerodynamics, University of Notre Dame, USA*, 1989.

[99] B. L. Storms and J. C. Ross. An Experimental Study of Lift-Enhancing Tabs on a Two-Element Airfoil. *AIAA Paper 94-1868-CP*, 1994.

[100] L. W. Traub and G. Agarwall. Exploratory Investigation of Geometry Effects on Gurney Flap Performance. *Journal of Aircaft*, 44(1):349–351, 2007.

[101] Y. C. Li, J. J. Wang, and J. Hua. Experimental investigations on the effects of divergent trailing edge and Gurney flaps on a supercritical airfoil . *Aerospace Science and Technology*, 11:91–99, 2007.

[102] T. Yu, J. J. Wang, and P. F. Zhang. Numerical Simulation of Gurney Flap on RAE-2822 Supercritical Airfoil. *Journal of Aircaft*, 48(5):1565–1575, 2011.

[103] A. Zanotti, D. Grassi, and G. Gibertini. Experimental Investigation of a Trailing Edge L-shaped Tab on a Pitching Airfoil in Deep Dynamic Stall Conditions. *Proceedings of the Institution of Mechanical Engineers, Part G: Journal of Aerospace Engineering*, in press.

[104] Zanotti A., Nilifard R., Gibertini G., Guardone A., and Quaranta G. Assessment of 2d/3d numerical modeling for deep dynamic stall experiments. *Journal of Fluids and Structures*, 51:97–115, 2014.

[105] J. C. Tyler and J. G. Leishman. Analysis of Pitch and Plunge Effects on Unsteady Airfoil Behavior . *Journal of the American Helicopter Society*, July 1992.

[106] J. Milgram and I. Chopra. Helicopter Vibration Reduction with Trailing Edge Flaps. In *36th AIAA/ASME/ASCE/AHS/ASC Structures, Structural Dynamics and Materials Conference, New Orleans, LA*, 10–12 April 1995.

[107] N. A. Koratkar and I. Chopra. Analysis and Testing of Mach Scaled Rotor Model with Piezoelectric Bender Actuated Trailing-Edge Flaps for Helicopter Vibration Control. *AIAA Paper 99-1501*, 1999.

[108] Y. Lemmens, H. Erdelyi, and T. Olbrechts. Design Study of an Active Gurney Flap System for Helicopter Rotor Blades. In *28th International Congress of the Aeronautical Sciences, Brisbane, AUS*, 23–28 September 2012.

Appendix A

Sensitivity of the thickness effects to the pitch amplitude

Chapter 2 deals with the assessment of the unsteady thickness effects on symmetric airfoils oscillating in pitch with motion law $\alpha = \sin(\omega t)$ degrees. It appears interesting to show how the main findings reported in chapter 2 apply also when considering a different oscillating law, e.g. $\alpha = 2\sin(\omega t)$ degrees. This allows to check if, at least as a first approximation, the phenomena related to the unsteady thickness effects are linear. As a consequence considerations consistent with those of chapter 2 could be drawn when dealing with arbitrary pitch motion laws, of course under the small perturbation assumption.

With this regard, inviscid numerical computations are performed on the NACA 0004 and on the NACA 0024 sections, at several values of the reduced frequency. The Mach number is kept at M = 0.117. The behavior of the numerical lift coefficient is again compared to the results achieved with the flat plate Theodorsen's model [79]. In particular the orientation of the C_L hysteresis path and its phase inversion reduced frequency are taken under consideration.

Figure A.1 reports the lift coefficient hysteresis curve obtained at $k = 0.1$. The curve of the NACA 0004 is almost indistinguishable from that computed with the Theodorsen's model. For the NACA 0024 section the amplitude of the hysteresis cycle is larger. The opposite behavior, reported in figure A.2, is observed at $k = 0.5$. Indeed the increase of thickness causes a reduction of the amplitude of the hysteresis cycles. Moreover, as observed for unitary amplitude motion laws, the orientation cycle of the hysteresis curve is counter-clockwise at $k = 0.1$ and clockwise at $k = 0.5$, suggesting how the phase inversion occurs again for $0.1 < k < 0.5$.

Recalling equation (2.22), the airfoil thickness is found to enhance the unsteady contribution of the flat-plate model in the expression of the boundary condition at the body. In particular, during the down-stroke phase, $\frac{d\alpha}{dt} > 0$ and the potential difference between the upper and the lower side on a thick airfoil is greater with respect to a flat-plate. As a result during the downstroke, at the same angle of attack, the airfoil with thickness develops a lift coefficient larger with respect to the flat-plate. Moreover at the maximum and minimum angles of attack ($\alpha = \pm 2$ deg.), where $d\alpha/dt = 0$ and the thickness-related term in (2.17) is zero, the overall effect of thickness is still almost null, thus confirming that the main effect of thickness is due to the kinematic angle of attack and not to the geometric angle of attack. Additionally, the main effect is found related primarily to the circulatory part of the lift, rather than to the added mass, proportional to the airfoil acceleration. For the upstroke the opposite occurs. Indeed $\frac{d\alpha}{dt} < 0$ and the potential difference is larger for thin airfoils. The net effect is a smaller lift coefficient for the airfoils with thickness, with respect to that developed by the flat-plate, at the same angle of attack during the upstroke.

Figures A.3 and A.4 show the effects of the thickness on the amplitude and the phase of the lift coefficient transfer function. Both the amplitude and the phase retain a qualitative

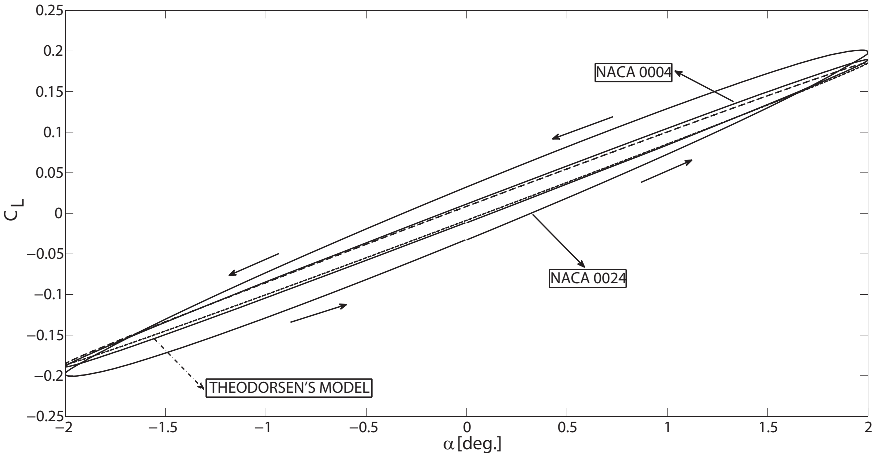

Figure A.1: Lift coefficient hysteresis curve below the phase inversion point, $k = 0.1$; $\alpha = 2\sin(\omega t)$ degrees, M = 0.117.

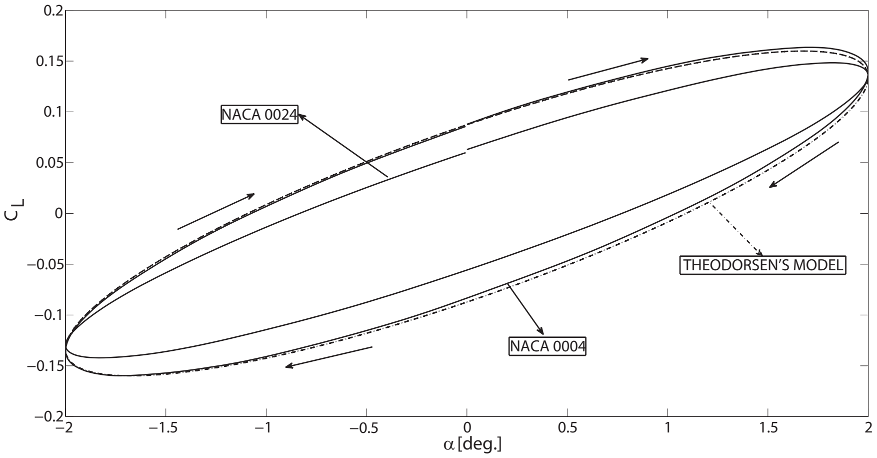

Figure A.2: Lift coefficient hysteresis curve above the phase inversion point, $k = 0.5$; $\alpha = 2\sin(\omega t)$ degrees, M = 0.117.

dependence on the reduced frequency, which is similar to the flat-plate case, as also shown in figures 2.2(a) and 2.2(b). Moreover the amplitude is found again to grow at small k by increasing the thickness and to decrease at large reduced frequencies. On the other hand, as observed for unitary amplitude oscillations, the phase curves shift to the right, moving the phase inversion point to higher values of k, as the thickness is increased.

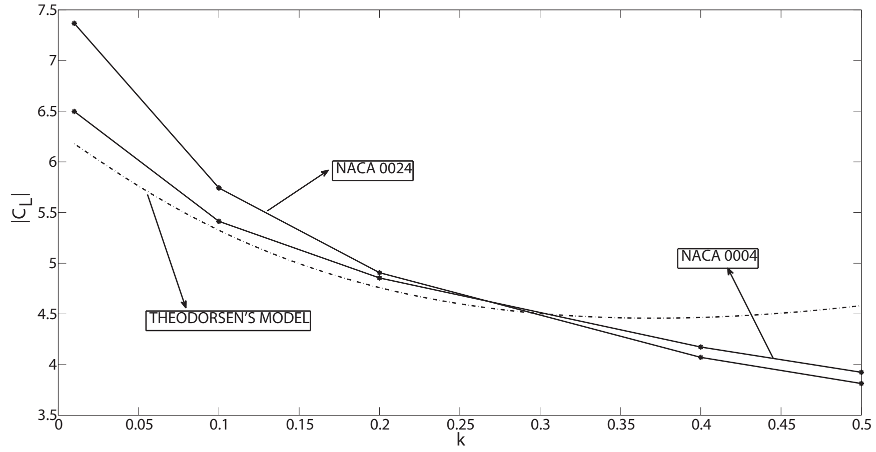

Figure A.3: Numerical lift coefficient magnitude versus k compared to Theodorsen's model; $\alpha = 2\sin(\omega t)$ degrees, M = 0.117.

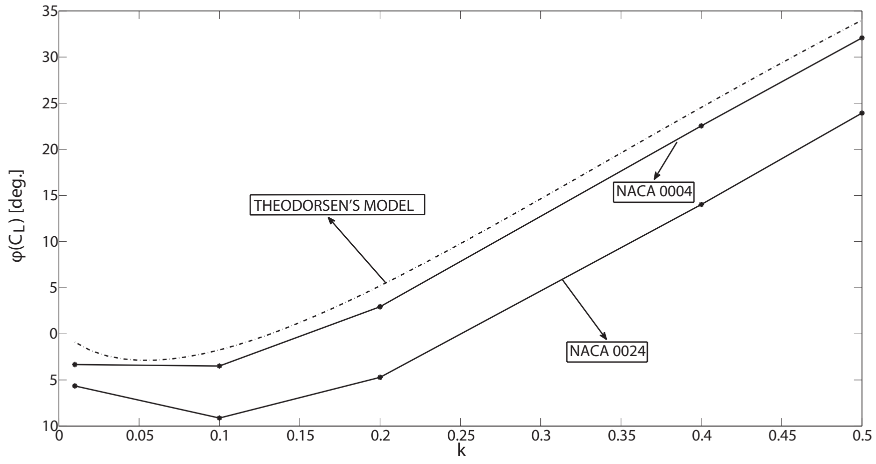

Figure A.4: Numerical lift phase angle versus k compared to Theodorsen's model; $\alpha = 2\sin(\omega t)$ degrees, M = 0.117.

Such behavior is consistent with the previous remarks on the lift coefficient hysteresis curve. Indeed, because of the enlargement of the lift coefficient hysteresis loop due to the thickness, the phase inversion is observed at larger k, also for oscillation amplitude of two degrees. In particular the values of the phase inversion k are almost the same of those observed in chapter 2.

Overall no significant changes are encountered in the lift coefficient behavior by doubling the pitch oscillation amplitude, with respect to what reported in chapter 2. Indeed the lift coefficient is found to behave similarly, both in the time and in the frequency domain, in which in particular it is found that the inversion phase occurs at approx. the same values of k observed for unitary amplitude oscillations. This empirically confirms the linearity of the unsteady thickness effects on symmetric airfoils oscillating in pitch, of course as far as the small perturbation hypothesis is valid.

Appendix B

General Küssner Schwarz theory

B.1 General overview on the analytical formulation

The benchmark of the physically based ROM presented in chapter 5 is the analytical Küssner and Schwarz (KS) model [43]. A brief overview on the mathematical formulation of such model is given hereinafter.

The Küssner and Schwarz theory allows to compute the difference of pressure coefficient between the upper and the lower sides of a thin airfoil, subject to an unsteady periodic motion. Additionally such formulation allows to modify the shape of the mean line while moving.

The airfoil is represented as a thin line with no initial camber. The reference frame is placed at the center of such line, with the x axis aligned to the chord and the z axis perpendicular to it, directed toward the upper side of the airfoil. The chord goes from $[-b, b]$ and the asymptotic air velocity is directed in the x direction, with module U.

Let us consider to express the perturbation velocity of a periodic movement with frequency ω as

$$v(x,t) = g(x)\mathrm{e}^{\mathrm{j}(\omega t+\varphi(x))} \tag{B.1}$$

where $g(x)$ is the amplitude of the perturbation velocity and $\varphi(x)$ is the phase, both dependents on the position x.

It is useful to perform a change of variables $x = b\cos\theta$, so that the interval goes from $[\pi, 0]$, therefore

$$v(\theta,t) = g(\theta)\mathrm{e}^{\mathrm{j}(\omega t+\varphi(\theta))} \tag{B.2}$$

The function $v(\theta, t)$ can be expressed as a Fourier series with respect to the spatial variable θ, that is:

$$v(\theta,t) = -U\mathrm{e}^{\mathrm{j}\omega t}\left(P_0 + 2\sum_{n=1}^{\infty} P_n \cos n\theta\right), \tag{B.3}$$

where the *upwash coefficients* $P_n \in \mathbb{C}$ are equal to

$$P_n = -\frac{1}{U\pi}\int_0^{\pi} f(\theta)\mathrm{e}^{\mathrm{j}\varphi(\theta)}\cos n\theta \mathrm{d}\theta \tag{B.4}$$

Küssner and Schwarz [43] showed that the difference of pressure coefficient, between the upper and the lower side, can be expressed as the Fourier series

$$\Delta C_P(\theta,t) = \mathrm{e}^{\mathrm{j}\omega t}\left(4A_0\tan\frac{\theta}{2} + 8\sum_{n=1}^{\infty} A_n \sin n\theta\right), \tag{B.5}$$

where the A_n coefficients can be easily expressed as function of the upwash coefficients

$$A_0 = C(k)\left(P_0 + P_1\right) - P_1 \quad \text{and} \tag{B.6}$$

$$A_n = P_n + \frac{\mathrm{j}k}{2n}\left(P_{n-1} - P_{n+1}\right) \tag{B.7}$$

In equation B.6 $k = \omega b/U$ is the reduced frequency and $C(k)$ is the Theodorsen function [59].

B.1.1 Computation of the forces

The global forces can be computed given the ΔC_P. The total lift is equal to

$$L(t) = \frac{1}{2}\rho U^2 \int_{-b}^{b} \Delta C_P(x,t)\mathrm{d}x \tag{B.8}$$

However only the expression of $\Delta C_P(\theta, t)$ is known, therefore a change of variable has to be performed, ultimately leading to

$$L(t) = \frac{1}{2}\rho U^2 b \int_0^{\pi} \Delta C_P(\theta,t)\sin\theta \mathrm{d}\theta \tag{B.9}$$

Exploiting the fact that

$$\int_0^{\pi} \sin n\theta \sin m\theta \mathrm{d}\theta = 0, \qquad \text{if} \quad m \neq n, \tag{B.10}$$

it can be seen that the global lift depends only on the coefficients A_0 and A_1. Using the following formulae

$$\int_0^{\pi} \tan\frac{\theta}{2}\sin\theta\mathrm{d}\theta = \pi, \tag{B.11}$$

$$\int_0^{\pi} \sin n\theta \sin n\theta\mathrm{d}\theta = \frac{\pi}{2} - \frac{\sin 2n\pi}{4n} \tag{B.12}$$

it can be seen that

$$L(t) = \frac{1}{2}\rho U^2 b 4\pi\left(A_0 + A_1\right)\mathrm{e}^{\mathrm{j}\omega t} \tag{B.13}$$

$$L(t) = \frac{1}{2}\rho U^2 (2b) 2\pi\left(C(k)\left(P_0 + P_1\right) + \frac{\mathrm{j}k}{2}\left(P_0 - P_2\right)\right)\mathrm{e}^{\mathrm{j}\omega t} \tag{B.14}$$

This result is very interesting because it is independent from the type of spatial law applied to the airfoil during the movement: in any case the lift depends only from the first three coefficients of the Fourier series used to represent the velocity.

The moment about the point x_0, positive in the nose-down sense, reads

$$M_0(t) = -\frac{1}{2}\rho U^2 \int_{-b}^{b} (x - x_0)\Delta C_P(x,t)\mathrm{d}x \tag{B.15}$$

By performing again the change of variable from x to θ, one gets

$$M_0(t) = -\frac{1}{2}\rho U^2 b^2 \int_0^{\pi} \left(\cos\theta - \bar{x}_0\right)\Delta C_P(\theta,t)\sin\theta\mathrm{d}\theta, \tag{B.16}$$

with $x_0/b = \bar{x}_0$. Therefore

$$\begin{aligned} M_0(t) = & -\frac{1}{2}\rho U^2 b^2 4A_0 \int_0^{\pi} \frac{1}{2}\sin 2\theta \tan\frac{\theta}{2}\mathrm{d}\theta \ \mathrm{e}^{\mathrm{j}\omega t} + \ ... \\ & -\frac{1}{2}\rho U^2 b^2 8A_n \sum_{n=1}^{\infty}\int_0^{\pi} \frac{1}{2}\sin 2\theta \sin n\theta\mathrm{d}\theta \ \mathrm{e}^{\mathrm{j}\omega t} + \ ... \\ & ... \ + b\bar{x}_0 L(t) \ \mathrm{e}^{\mathrm{j}\omega t} \end{aligned} \tag{B.17}$$

Since

$$\int_0^\pi \tan\frac{\theta}{2}\sin 2\theta \mathrm{d}\theta = -\pi, \tag{B.18}$$

the pitching moment can be ultimately written as

$$M_0(t) = \left(\frac{1}{2}\rho U^2 b^2 2\pi \left(A_0 - A_2\right) + \frac{1}{2}\rho U^2 \bar{x}_0 b^2 4\pi \left(A_0 + A_1\right)\right) \mathrm{e}^{\mathrm{j}\omega t} \tag{B.19}$$

Expressing the A_n in terms of the P_n, it results

$$\begin{aligned} M_0(t) &= \frac{1}{2}\rho U^2 b^2 2\pi \left(1 + 2\bar{x}_0\right)\left[C(k)\left(P_0 + P_1\right) - P_1\right] + \ \ldots \\ &\ldots \ + \frac{1}{2}\rho U^2 b^2 2\pi \left[2\bar{x}_0 \left(P_1 + \frac{\mathrm{j}k}{2}\left(P_0 - P_2\right)\right) - P_2 - \frac{\mathrm{j}k}{4}\left(P_1 - P_3\right)\right] \mathrm{e}^{\mathrm{j}\omega t} \end{aligned} \tag{B.20}$$

Consistently with the Theodorsen's model the moment with respect to the quarter chord (i.e. $\bar{x}_0 = -1/2$), has no terms depending on $C(k)$:

$$M_{c/4}(t) = -\frac{1}{2}\rho U^2 b^2 2\pi \left(P_1 + P_2 + \frac{\mathrm{j}k}{2}\left(P_0 - P_2 + \frac{P_1 - P_3}{2}\right)\right) \mathrm{e}^{\mathrm{j}\omega t} \tag{B.21}$$

B.2 Moving airfoil

Let us consider an airfoil that moves according to the following law:

$$z(x,t) = z(x)\mathrm{e}^{\mathrm{j}\omega t}. \tag{B.22}$$

The corresponding velocity vector is equal to

$$v(x,t) = \frac{Dz}{Dt} = \frac{\partial z}{\partial t} + \frac{\partial z}{\partial x}\frac{\partial x}{\partial t} = \frac{\partial z}{\partial t} + U\frac{\partial z}{\partial x}, \quad \text{that is} \tag{B.23}$$

$$v(x,t) = \left(\mathrm{j}\omega g(x) + U g'(x)\right)\mathrm{e}^{\mathrm{j}\omega t} \tag{B.24}$$

Using the reduced frequency $k = \omega b/U$ the velocity can be written as

$$v(x,t) = \frac{U}{b}\left(\mathrm{j}k g(x) + b g'(x)\right)\mathrm{e}^{\mathrm{j}\omega t} \tag{B.25}$$

Applying again the transformation $x = b\cos\theta$ one gets

$$\begin{aligned} v(\theta,t) &= \frac{U}{b}\left(\mathrm{j}k g(\theta) + b g'(\theta)\frac{\mathrm{d}\theta}{\mathrm{d}x}\right)\mathrm{e}^{\mathrm{j}\omega t} \\ &= \frac{U}{b}\left(\mathrm{j}k g(\theta) - \frac{1}{\sin\theta}g'(\theta)\right)\mathrm{e}^{\mathrm{j}\omega t}, \end{aligned} \tag{B.26}$$

$$\text{therefore} \quad g_v(\theta) = g(\theta)\mathrm{e}^{\mathrm{j}\varphi(\theta)} = \frac{U}{b}\left(\mathrm{j}k g(\theta) - \frac{1}{\sin\theta}g'(\theta)\right) \tag{B.27}$$

B.2.1 Rigidly moving airfoil

If one considers a vertical translation (using the Theodorsen convention positive toward the bottom)

$$z(x,t) = \bar{h}b\mathrm{e}^{\mathrm{j}\omega t}, \tag{B.28}$$

where $z(x) = z(\theta) = \bar{h}b = h$, the velocity with respect to the spatial variable θ is

$$v(\theta,t) = \mathrm{j}kU\bar{h}\mathrm{e}^{\mathrm{j}\omega t}. \tag{B.29}$$

The upwash coefficients are written as:

$$P_n = -\frac{\mathrm{j}k}{\pi}\bar{h}\int_0^{\pi}\cos n\theta \mathrm{d}\theta. \tag{B.30}$$

Therefore all of the P_n coefficients are zero but P_0, namely

$$\begin{aligned} P_0 &= -\mathrm{j}k\bar{h} && \text{(B.31)}\\ P_n &= 0 \qquad \text{for} \quad n \neq 0 && \text{(B.32)} \end{aligned}$$

The resulting aerodynamic loads are given by

$$\begin{aligned} L(t) &= \frac{1}{2}\rho U^2(2b)2\pi\left(\frac{k^2}{2} - \mathrm{j}kC(k)\right)\bar{h}\,\mathrm{e}^{\mathrm{j}\omega t} && \text{(B.33)}\\ M_{c/4}(t) &= \frac{1}{2}\rho U^2 b^2 2\pi\frac{k^2}{2}\bar{h}\,\mathrm{e}^{\mathrm{j}\omega t} && \text{(B.34)} \end{aligned}$$

Using the fact that $k^2\bar{h} = -b\ddot{h}/U^2$ and $\mathrm{j}k\bar{h} = \dot{h}/U$, the force coefficients can be written as

$$\begin{aligned} L(t) &= -\rho U^2 b2\pi\left(\frac{b}{2}\frac{\ddot{h}}{U^2} + \frac{\dot{h}}{U}C(k)\right)\mathrm{e}^{\mathrm{j}\omega t} && \text{(B.35)}\\ M_{c/4}(t) &= -\frac{1}{2}\rho b^3\pi\ddot{h}\,\mathrm{e}^{\mathrm{j}\omega t} && \text{(B.36)} \end{aligned}$$

For a pure rotation with respect to the point x_p the vertical displacement reads

$$z(x,t) = -(x - x_p)\alpha\mathrm{e}^{\mathrm{j}\omega t} \tag{B.37}$$

and by performing the variable change from x to θ one gets $z(\theta) = -b(\cos\theta - \bar{x}_p)\alpha$, being $\bar{x}_p = x_p/b$. Therefore the velocity with respect to the spatial variable θ is

$$v(\theta,t) = -U\left(\mathrm{j}k\left(\cos\theta - \bar{x}_p\right) + 1\right)\alpha\mathrm{e}^{\mathrm{j}\omega t}. \tag{B.38}$$

The corresponding upwash coefficients are

$$P_n = \frac{1}{\pi}\alpha\int_0^{\pi}\left(\mathrm{j}k\left(\cos\theta - \bar{x}_p\right) + 1\right)\cos n\theta\mathrm{d}\theta. \tag{B.39}$$

Notice that only P_0 and P_1 are not zero, namely

$$\begin{aligned} P_0 &= \left(1 - \mathrm{j}k\bar{x}_p\right)\alpha && \text{(B.40)}\\ P_1 &= \frac{jk}{2}\alpha && \text{(B.41)}\\ P_n &= 0 \qquad \text{for} \quad n > 1. && \text{(B.42)} \end{aligned}$$

Using this movement, the lift generated by a thin line oscillating in pitch can be computed as

$$\begin{aligned} L(t) &= \frac{1}{2}\rho U^2(2b)2\pi\left(C(k)\left(P_0 + P_1\right) + \frac{\mathrm{j}k}{2}\left(P_0 - P_2\right)\right)\mathrm{e}^{\mathrm{j}\omega t} && \text{(B.43)}\\ &= \frac{1}{2}\rho U^2(2b)2\pi\left(C(k)\left(\left(1 - \mathrm{j}k\bar{x}_p\right) + \frac{\mathrm{j}k}{2}\right) + \frac{\mathrm{j}k}{2}\left(1 - \mathrm{j}k\bar{x}_p\right)\right)\alpha && \text{(B.44)}\\ &= \rho U^2 b2\pi\left(C(k)\left(\alpha + \frac{b}{U}\left(\frac{1}{2} - \bar{x}_p\right)\dot{\alpha}\right) + \frac{b}{2U}\left(\dot{\alpha} - \frac{b}{U}\bar{x}_p\ddot{\alpha}\right)\right) && \text{(B.45)} \end{aligned}$$

In the same way it is possible to compute the moment with respect to $c/4$, i.e. $\bar{x}_0 = -1/2$, as

$$\begin{aligned} M_{c/4}(t) &= -\rho U^2 b^2 \pi \left(P_1 + P_2 + \frac{\mathrm{j}k}{2} \left(P_0 - P_2 + \frac{P_1 - P_3}{2} \right) \right) \mathrm{e}^{\mathrm{j}\omega t} && \text{(B.46)} \\ &= -\rho U^2 b^2 \pi \left(\frac{\mathrm{j}k}{2} + \frac{\mathrm{j}k}{2} \left((1 - \mathrm{j}k\bar{x}_p) + \frac{\mathrm{j}k}{4} \right) \right) \alpha \mathrm{e}^{\mathrm{j}\omega t} && \text{(B.47)} \\ &= -\rho b^2 \pi \left(Ub\dot{\alpha} + b^2 \left(\frac{1}{8} - \frac{\bar{x}_p}{2} \right) \ddot{\alpha} \right) && \text{(B.48)} \end{aligned}$$

B.2.2 Flap rotation

Let us consider a flap movement

$$z(x,t) = \begin{cases} 0, & x \leq x_f \\ -(x - x_f)\beta \mathrm{e}^{\mathrm{j}\omega t}, & x > x_f \end{cases} \tag{B.49}$$

$$v(\theta,t) = \begin{cases} 0, & \theta \leq \theta_f \\ -U\left(\mathrm{j}k\left(\cos\theta - \bar{x}_f\right) + 1\right)\beta \mathrm{e}^{\mathrm{j}\omega t}, & \theta > \theta_f \end{cases} \tag{B.50}$$

with $\bar{x}_f = x_f/b$ and $\theta_f = \arccos\left(\bar{x}_f\right)$.

Also in this case it is possible to compute the upwash coefficients as

$$\begin{aligned} P_n &= \frac{1}{\pi}\beta \int_0^{\theta_f} \left(\mathrm{j}k\left(\cos\theta - \bar{x}_f\right) + 1\right) \cos n\theta \mathrm{d}\theta && \text{(B.51)} \\ &= \frac{1}{\pi}\beta \left(\int_0^{\theta_f} \mathrm{j}k \cos\theta \cos n\theta \mathrm{d}\theta + \int_0^{\theta_f} \left(1 - \mathrm{j}k\bar{x}_f\right) \cos n\theta \mathrm{d}\theta \right) \end{aligned}$$

It results that

$$\begin{aligned} P_0 &= \left(\frac{\mathrm{j}k}{\pi} \sqrt{1 - \bar{x}_f^2} + \left(1 - \mathrm{j}k\bar{x}_f\right) \frac{\theta_f}{\pi} \right) \beta && \text{(B.52)} \\ &= \frac{\mathrm{j}k}{\pi(n^2-1)} \left(n\bar{x}_f \sin n\theta_f - \sqrt{1 - \bar{x}_f^2} \cos n\theta_f \right) \beta + \ \dots \\ &\dots \ + \frac{1}{n\pi} \left(1 - \mathrm{j}k\bar{x}_f\right) \sin n\theta_f \ \beta \end{aligned}$$

The series is composed by an infinite number of terms that decay as $1/n$ and $1/n^2$. Nevertheless only the first three terms are important to evaluate the lift, whereas only four terms are required to consider also the aerodynamic moment. It appears useful to evaluate also the hinge moment, which is equal to

$$\begin{aligned} M_0(t) &= -\frac{1}{2}\rho U^2 b^2 \int_0^{\theta_f} \left(\cos\theta - \bar{x}_f\right) \Delta C_P(\theta,t) \sin\theta \mathrm{d}\theta && \text{(B.53)} \\ &= -\frac{1}{2}\rho U^2 b^2 \int_0^{\theta_f} \left(\cos\theta - \bar{x}_f\right) \left(4A_0 \tan\frac{\theta}{2} + 8\sum_{n=1}^{\infty} A_n \sin n\theta \right) \sin\theta \mathrm{d}\theta \ \mathrm{e}^{\mathrm{j}\omega t} \end{aligned}$$

Solving this integral it results

$$\begin{aligned} M_0(t) &= -\frac{1}{2}\rho U^2 b^2 2A_0 \left(\left(2 + \bar{x}_f\right) \sqrt{1 - \bar{x}_f^2} + \left(1 + 2\bar{x}_f\right) \theta_f \right) \mathrm{e}^{\mathrm{j}\omega t} + \ \dots && \text{(B.54)} \\ &\dots \ + \frac{1}{2}\rho U^2 b^2 \frac{8A_n \bar{x}_f}{n^2 - 1} \left(\bar{x}_f \sin n\theta_f - n\sqrt{1 - \bar{x}_f^2} \cos n\theta_f \right) \mathrm{e}^{\mathrm{j}\omega t} + \ \dots \\ &\dots \ + \frac{1}{2}\rho U^2 b^2 2A_n \left(\frac{\sin\left((n+2)\theta_f\right)}{n+2} - \frac{\sin\left((n-2)\theta_f\right)}{n-2} \right) \mathrm{e}^{\mathrm{j}\omega t} \end{aligned}$$

B.2.3 Flap rotation + trim tab

Let us consider a movement of the type

$$z(x,t) = \begin{cases} 0, & x \leq x_f \\ -(x - x_f)\beta_f \mathrm{e}^{\mathrm{j}\omega t}, & x_f < x \leq x_w \\ -(x - x_f)\beta_f \mathrm{e}^{\mathrm{j}\omega t} - (x - x_w)\beta_w \mathrm{e}^{\mathrm{j}\omega t}, & x > x_w \end{cases} \tag{B.55}$$

with $x_w > x_f$. This expression could model the movement of an airfoil equipped with a flap and a trim tab. In particular the trim tab is meant to be in relative motion with respect to the flap.

$$v(\theta,t) = \begin{cases} 0, & \theta \leq \theta_f \\ -U\left(\mathrm{j}k\left(\cos\theta - \bar{x}_f\right) + 1\right)\beta_f \mathrm{e}^{\mathrm{j}\omega t}, & \theta_f < \theta \leq \theta_c \\ -U\left(\left(\mathrm{j}k\left(\cos\theta - \bar{x}_f\right) + 1\right)\beta_f + \left(\mathrm{j}k\left(\cos\theta - \bar{x}_w\right) + 1\right)\beta_w\right)\mathrm{e}^{\mathrm{j}\omega t}, & \theta > \theta_c \end{cases} \tag{B.56}$$

with $\bar{x}_f = x_f/b$, $\bar{x}_w = x_w/b$, $\theta_f = \arccos(\bar{x}_f)$ and $\theta_c = \arccos(\bar{x}_w)$, consistently with the definitions given in chapter 5.

The upwash coefficients related to β_f are identical to those already computed for the variable β with regard to the flap rotation, since the velocity distribution is a composition of the effect of two rotations, with the second relative to the first one. Therefore for the β_w rotation is easy to see that the upwash coefficients have the same form as those already computed, if changing $\bar{x}_f$ into $\bar{x}_w$. That is

$$P_0 = \left(\frac{\mathrm{j}k}{\pi}\sqrt{1-\bar{x}_w^2} + \left(1 - \mathrm{j}k\bar{x}_w\right)\frac{\theta_w}{\pi}\right)\beta_w \tag{B.57}$$

$$\begin{aligned} P_n = {} & \frac{\mathrm{j}k}{\pi(n^2-1)}\left(n\bar{x}_w \sin n\theta_w - \sqrt{1-\bar{x}_w^2}\cos n\theta_w\right)\beta_w + \ \ldots \\ & \ldots + \frac{1}{n\pi}\left(1 - \mathrm{j}k\bar{x}_w\right)\sin n\theta_w \, \beta_w \end{aligned} \tag{B.58}$$

Using this approach it is possible to represent the airfoil as a sequence of N straight lines each one that rotates with respect to the previous one by a relative angle β_i. As a result any camber variation can be approximated by using closed form analytical solutions which tend to the exact solution as $N \to \infty$.

It appears useful to remark that the KS model gives analytical formulae for the lift and the moment which are identically equal to those provided by the formulation of Theodorsen [59]. This can be immediately verified by the looking at equations (B.35), (B.36), (B.45) and (B.48), which indeed match exactly the classical Theodorsen's formulae reported in equations (2.23) and (2.24). Notice that the exact correspondence between the formulations of KS and Theodorsen was analytically proved by Fung [64].

The KS model is specifically used for the present work, since it allows to handle directly the velocity distribution and therefore the local loads. On the contrary the formulation of Theodorsen provides the expressions of the global aerodynamic loads, given the parameters of the motion law. The possibility to act explicitly on the velocity distribution, and therefore on the shape of the mean line, is found more appropriate, to get the desired physical consistency of the ROM for the blade section with the L-tab. The primary effects of the present device consist indeed of local camber modifications, as well as enlargements of the chord length.

Appendix C

Sensitivity of the L-tab ROM to the motion law

Chapter 5 reports the development of a physically based ROM for the NACA 0012 blade section model, equipped with the L-tab. Recalling that the assumption of linearity is used to this purpose, separate ROMs are proposed for: fixed positions of the tab and the airfoil, pitch and plunge oscillations of the airfoil with the tab in fixed position and oscillating motions of the L-tab with the airfoil at constant angle of attack. This latter ROM results the most challenging to develop, due to the high complexity of the phenomena which have to be correctly reproduced, to keep the consistency with the physics of the problem. Section 5.4 presents the derivation of the ROM for motion laws of the tab expressed as $\beta = 1 + \sin(\omega t)$ degrees. The same procedure is here applied on the L-tab oscillating according to the law $\beta = 2 + 2\sin(\omega t)$ degrees, with k in the range [0.1 0.6], M = 0.117 and Re = $1 \cdot 10^6$. Figure C.1 reports the lift and moment coefficients computed numerically for this latter oscillating law. Again, as expected, clearly visible oscillations appear in the unsteady airloads. Consistently with the approach discussed in chapter 5, the identification procedure is performed on the first harmonic component of the force coefficients, reported for completeness in figure C.1.

The free parameters of the optimization algorithm are those reported in section 5.4, namely the oscillation amplitude of the Equivalent L-Tab (ELT), and the length and the oscillation amplitude and phase of the counter-rotating Vortices Equivalent Trim Tab (VETT). The results of the identification procedure are reported in figure C.2. The hysteresis curves of the numerical first harmonic of the lift and moment coefficients are represented together with the corresponding airloads computed with the ROM. The unsteady loads computed with the ROM are found in good agreement with the reference numerical computations, both at $k = 0.1$ and at $k = 0.6$.

Figure C.3 reports the free parameters of the ROM computed for the L-tab with motion law $\beta = 2 + 2\sin(\omega t)$ degrees, versus the related reduced frequency. The corresponding geometrical and motion parameters achieved for the reference motion $\beta = 1 + \sin(\omega t)$ degrees, see section 5.4, are added for comparison. Notice at first that a smooth and quite regular behavior of the free parameters with respect to k is achieved, also for the present oscillating law. Additionally a reasonably similar dependence on k of the curves concerning the two oscillation laws is observed. This suggests how the assumption of linearity of the ROM parameters, with respect to those of the oscillation law, is acceptable for preliminary investigations. Indeed no significant modifications in the behavior of such curves have to be expected by changing the oscillation laws of the tab, within the small perturbation regime.

Moreover it is found that, when doubling the mean angle and the amplitude of the oscillation law, the geometrical and motion parameters of the ROM exhibit only small shifts in their absolute value. With this regard, it appears eventually feasible the employment of the mean of the values of the free parameters computed for the two oscillation

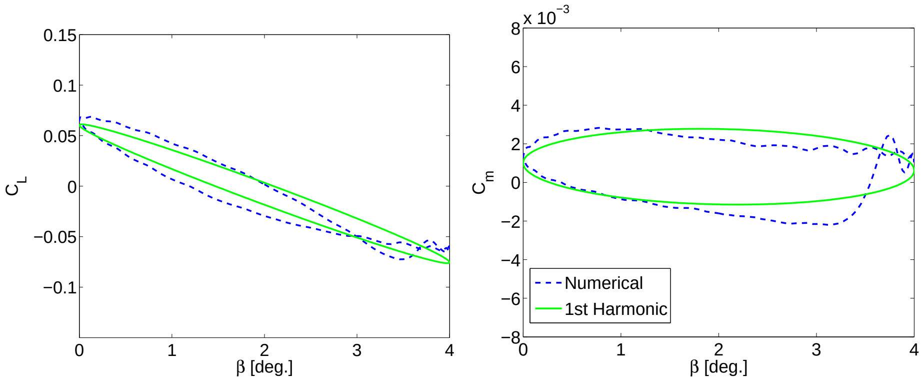

(a) Lift coefficient, $k = 0.1$ (b) Mid-chord moment coefficient, $k = 0.1$

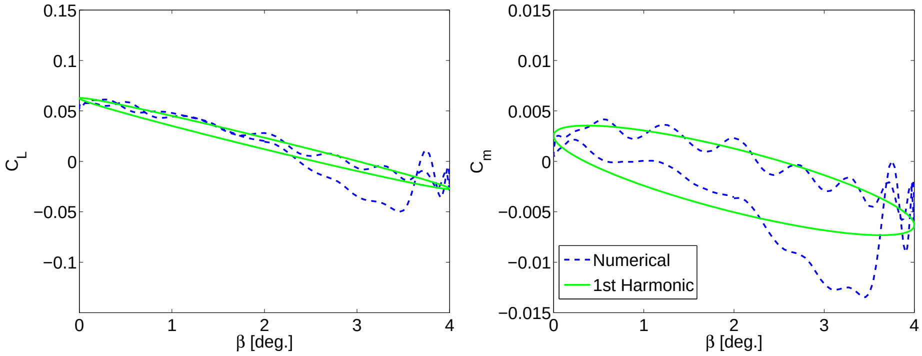

(c) Lift coefficient, $k = 0.6$ (d) Mid-chord moment coefficient, $k = 0.6$

Figure C.1: Numerical aerodynamic loads together with the related 1st harmonic component, computed at $k = 0.1$ and $k = 0.6$; $\beta = 2 + 2\sin(\omega t)$ degrees, $\alpha = 0$ degrees, $\mathrm{M} = 0.117$, $\mathrm{Re} = 1 \cdot 10^6$.

laws of the tab. The resulting curves with respect to k would have general validity in the range $\beta = [0 \;\; 4]$ degrees and therefore no further identification procedures would be required to compute the equivalent geometry, as well as the unsteady airloads. Of course, for larger values of the oscillation mean value and amplitude, greater shifts are expected in terms of the geometrical parameters. The development of general laws describing the dependence of the geometrical quantities, and therefore of the aerodynamic loads, on the motion parameters is left as a future step for this work.

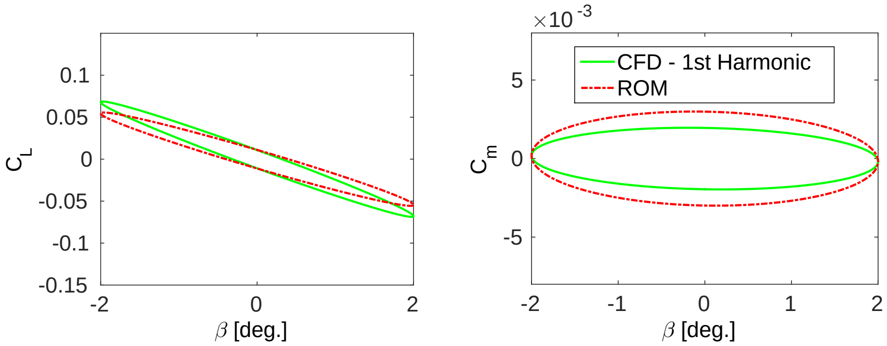

(a) Lift coefficient, $k = 0.1$ (b) Mid-chord moment coefficient, $k = 0.1$

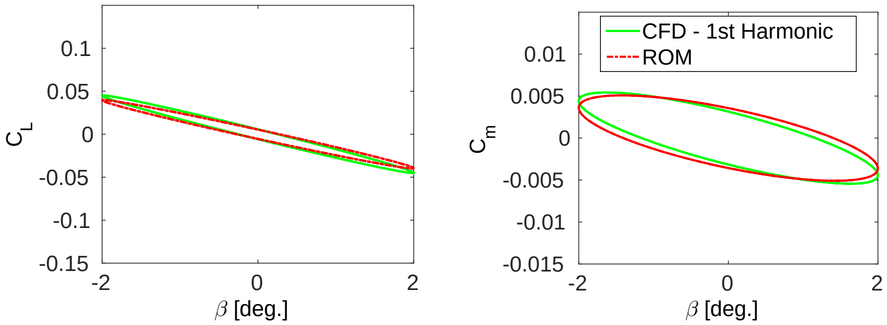

(c) Lift coefficient, $k = 0.6$ (d) Mid-chord moment coefficient, $k = 0.6$

Figure C.2: Comparison between the numerical 1st harmonic components of the aerodynamic loads and their counterparts from the KS-based ROM at $k = 0.1$ and $k = 0.6$; $\beta = 2 + 2\sin(\omega t)$ degrees, $\alpha = 0$ degrees, $\mathrm{M} = 0.117$, $\mathrm{Re} = 1 \cdot 10^6$.

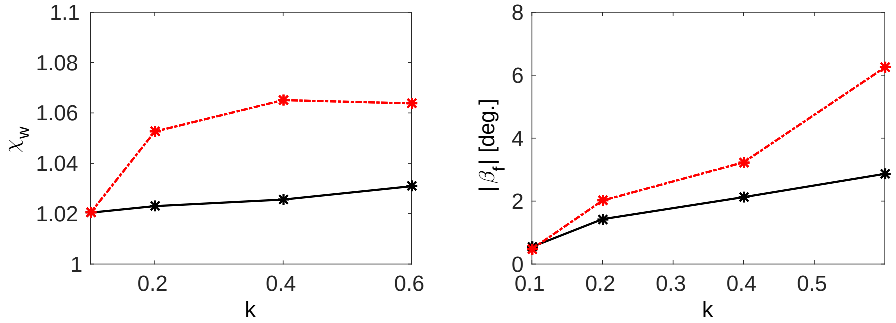

(a) Chord enlargement, function of the VETT length

(b) Deflection amplitude of the ELT

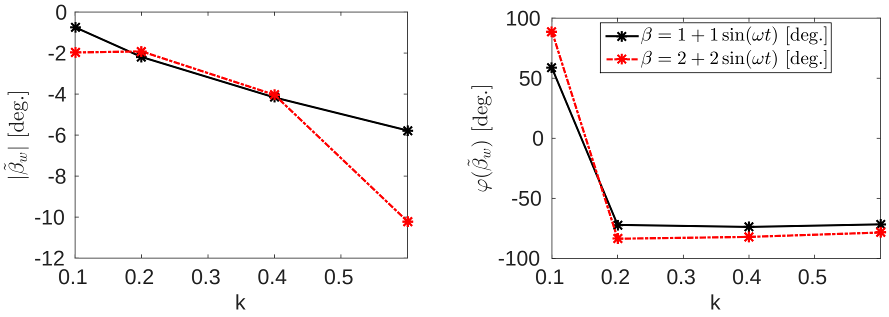

(c) Deflection amplitude of the VETT

(d) Deflection phase of the VETT

Figure C.3: Sensitivity of the ROM free parameters to the oscillation law. The comparison between $\beta = 2 + 2\sin(\omega t)$ deg. and $\beta = 1 + \sin(\omega t)$ deg. is reported. The first parameter represents the effect of chord augmentation due to the CRV; $\alpha = 0$ degrees, $\mathrm{M} = 0.117$, $\mathrm{Re} = 1 \cdot 10^6$.